LIQUID-PHASE OPERATION OF MEMS RESONATORS FOR BIOCHEMICAL SENSING IN POINT OF CARE AND EMBEDDED APPLICATIONS

A Dissertation
Presented to
The Academic Faculty

by

Luke A. Beardslee

In Partial Fulfillment
of the Requirements for the Degree
Doctor of Philosophy in the
School of Electrical and Computer Engineering

Georgia Institute of Technology
August 2011

LIQUID-PHASE OPERATION OF MEMS RESONATORS FOR BIOCHEMICAL SENSING IN POINT OF CARE AND EMBEDDED APPLICATIONS

Approved by:

Dr. Oliver Brand, Advisor
School of Electrical and Computer Engineering
Georgia Institute of Technology

Dr. Pamela Bhatti
School of Electrical and Computer Engineering
Georgia Institute of Technology

Dr. Mark Allen
School of Electrical and Computer Engineering
Georgia Institute of Technology

Dr. A. Bruno Frazier
School of Electrical and Computer Engineering
Georgia Institute of Technology

Dr. Hang Lu
School of Chemical and Biomolecular Engineering
Georgia Institute of Technology

Date Approved: 07/06/2011

To my family for all their love and support.

ACKNOWLEDGEMENTS

First I would like to express my deepest thanks to my advisor, Dr. Oliver Brand. Dr. Brand's door is always open and he has been a source of great inspiration, encouragement and support during my PhD work. In addition, he has allowed me to tackle challenges myself and to suggest my own solutions. This experience along with the advice he has offered along the way have been invaluable in helping me to learn (and continue to learn going forward) how to conduct engineering research and development.

Along the same lines I would like to thank Dr. Mark Allen, Dr. Pamela Bhatti, Dr. Bruno Frazier, and Dr. Hang Lu for serving on my dissertation committee and for their guidance and their review of my work.

And Dr. Fabien Josse and Dr. Stephen Heinrich, both at Marquette University. Through my collaborations with Dr. Josse and Dr. Heinrich I was able to learn a great deal about microcantilevers and was also able to learn about some aspects of cantilever modeling which I would have not seen otherwise.

I also owe immense gratitude to my other groups members and collaborators. I would like to thank my fellow group mates past and present: Dr. Jae Seo, Dr. Kianoush Naeli, Dr. Kemal Safak Demirci, Juan Cesaretti, Stuart Truax, Jin-Jyh Su, Christopher Carron, Spyridon Pavlidis, and Jonathan Lehman. These individuals have been extremely helpful in both helping me with measurements in the lab, with cleanroom work, and also in discussions about where to go with my research. I would also like to thank Dr. Yulia Luzinova for her help with liquid-phase chemical sensing experiments and Dr. Shyam Aravamudhan and Dr. Paul Joseph for help with biosensor experiments. Along the same

lines I am also grateful to the other students whom I've worked with in the cleanroom and the NRC technical staff for their help with microfabrication. Also, I would like to thank Pradeep Hothur and Assim Addous who are two undergraduate students whom I had the opportunity to work with, and also Mary Render, Linda Newton, and Sharon Lawrence for their help with administrative matters.

I am also immensely grateful to the National Science Foundation and Air Force Research Lab for funding during the course of my PhD work. The research into both of the resonant sensing concepts that are presented as part of this thesis were funded by the National Science Foundation.

I would like thank all the guys at Old Time Garage in Newton, MA and in particular PJ Ayotte, Michael Bontempo, Al Valentino, and Sam Hurwitz. Thanks for showing me the importance of paying attention to the details and the importance of doing things right the first time. Finally, last but not least I need to thank my parents William and Barbara Beardslee, my brother Dan Beardslee, and my sisters Eliza and Anna Beardslee for their endless love, support and encouragement.

TABLE OF CONTENTS

LIST OF TABLES

LIST OF FIGURES

Page

LIST OF SYMBOLS AND ABBREVIATIONS

MEMS	Microelectromechanical Systems
CMOS	Complimentary Metal Oxide Semiconductor
UV	Ultraviolet
POCT	Point of Care Testing
EPA	Environmental Protection Agency
μGC	Micro Gas Chromatography
ASIC	Application Specific Integrated Circuit
ELISA	Enzyme-linked Immunosorbent Assay
SDS	Sodium Dodecyl Sulfate
IR	Infrared
NMR	Nuclear Magnetic Resonance
DNA	Deoxyribonucleic Acid
SNP	Single Nucleotide Polymorphism
PCR	Polymerase Chain Reaction
REDOX	Oxidation-Reduction
GMR	Giant Magneto Resistance
SPR	Surface Plasmon Resonance
SERS	Surface Enhanced Raman Spectroscopy
TIRF	Total Internal Reflection Fluorescence
LED	Light Emitting Diode
CMUT	Capacitive Micromachined Ultrasonic Transducer
QCM	Quartz Crystal Microbalance
SAW	Surface Acoustic Wave

ppb	Parts Per Billion
ppm	Parts Per Million
PSA	Prostate Specific Antigen
FEM	Finite Element Method
Q	Quality Factor
LOD	Limit of Detection
KOH	Potassium Hydroxide
IP	In-Plane
OOP	Out-Of-Plane
SOI	Silicon On Insulator
ICP	Inductively Coupled Plasma
BOE	Buffered Oxide Etch
PECVD	Plasma Enhanced Chemical Vapor Depostion
SLA	Stereolithography
DIL	Dual In Line
CAD	Computer Aided Design
SEM	Scanning Electron Microscope
SAM	Self Assembled Monolayer
PEEK	Polyetheretherketone
ALD	Atomic Layer Deposition
HF	High Frequency
RF	Radio Frequency
DI	Deionized
PIB	Polyisobutylene
PDMS	Polydimethylsiloxane

PECH	Polyepichlorohydrin
EPCO	Ethylene-propylene Copolymer
HMDS	Hexamethyldisilazane
EDC	N-(3-Dimethylaminopropyl)-N′-ethylcarbodiimide
NHS	N-Hydroxysuccinimide
MES	2-(N-Morpholino)ethanesulfonic Acid Hydrate, 4-Morpholineethanesulfonic Acid
PBS	Phosphate Buffered Saline
BSA	Bovine Serum Albumin
BSA-FITC	Fluorescein Isothiocyanate Conjugated Bovine Serum Albumin
XPS	X-Ray Photoelectron Spectroscopy
PBS	Phosphate Buffered Saline
AFM	Atomic Force Microscopy
CNTs	Carbon Nanotubes
VOC	Volatile Organic Compound
IgG	Immunoglobulin G
IgG-FITC	Fluorescein Isothiocyanate Conjugated Immunoglobulin G
LPCVD	Low Pressure Chemical Vapor Deposition
HARPSS	High Aspect Ratio Combined Poly and Single-Crystal Silicon

SUMMARY

The purpose of this work is the development of MEMS-based resonant sensors for liquid-phase biochemical sensing applications. Specifically, the sensors developed here are aimed at embedded or point-of-sampling applications: (1) when there is not enough time to send a sample to a lab for analysis, (2) in resource-poor settings, (3) when collecting analyte and shipping it to a lab would damage the sample, or (4) for in-situ monitoring. To this end, two new transducers, a bulk-micromachined resonant cantilever sensor vibrating in an in-plane flexural mode and a surface-micromachined sensor based on the spring-softening effect, are investigated.

Resonant biochemical sensors directly measure the mass of molecules absorbed/attached to their surface. While there has been a great deal of work concerning gas-phase resonant chemical sensing, few studies have investigated resonant sensing in the liquid-phase with the resonator operated continuously. Continuous sensor operation in the fluid alleviates challenges associated with washing steps and also allows for measurement of the transient signals, which can yield additional information about the identity of an analyte.

The cantilever resonators studied in this work utilize the fundamental in-plane flexural mode, in contrast to the commonly employed first out-of-plane flexural mode. In-plane mode operation reduces the viscous damping and the mass loading by the surrounding fluid, which results in reduced (improved) detection limits in liquid-phase sensing applications. An integrated excitation and detection scheme has been developed for exciting the first in-plane flexural mode. More than seventy cantilever geometries

varying in length, width and thickness have been tested in air and water to derive design guidelines for optimal device dimensions for liquid phase operation. The tested in-plane cantilevers have quality factors as high as 86 in liquid. This is in contrast to quality factors in the range of 10-20 (in liquid) for previously investigated out-of-plane mode cantilevers. In addition, the frequency drop upon immersion in liquid is only between 5-10%, in comparison to values as high as 30-50 % for out-of-plane mode cantilevers. The improvements in both the quality factor and frequency shift upon liquid immersion enable lower limits of detection in liquid-phase chemical sensing applications.

Furthermore, a microfluidic packaging scheme has been implemented enabling efficient liquid-phase biochemical testing Thereby, part of the microfluidic packaging packaging is done at the wafer level, thus largely improving device reproducibility and yield. The fabricated mass-sensitive microsensors have been tested in two distinct application scenarios: (1) as chemical sensors for detecting organic pollutants in water samples and (2) as biosensors for detecting antibodies/antigens and thus targeting medical diagnostics.

The implemented liquid-phase biochemical sensors based on in-plane mode cantilevers show a significant improvement over previously investigated systems that are operated continuously in liquid and use integrated excitation and readout schemes. Microresonators coated with polymeric sensing films for the detection organic compounds in water samples yielded estimated limits of detection below 100 ppb without any pre-concentration. In addition, biosensor tests for the detection IgG antibodies gave estimated limits of detection around 100 ng/ml. For ground water monitoring applications detection limits in the low ppb range are generally needed, while for clinical diagnostics,

biosensors with detection limits in the low ng/ml range are desirable. Further optimization of the resonator geometry and improvements in ligand surface coverage are two methods that will be discussed, which can lower the limits of detection. Both the biosensors and chemical sensors implemented with the in-plane mode cantilevers give detection limits that are within an order of magnitude of the needed levels and viable strategies are suggested to further improve these limits of detection. The achieved limits of detection for the liquid-phase chemical sensors represent roughly an order of magnitude improvement over previously investigated platforms utilizing out-of-plane silicon cantilevers with an integrated excitation and detection scheme. On the biosensors side, the results are within an order of magnitude of the needed detection limit and special emphasis has been put on implementing suitable controls to account of nonspecific binding and on properly characterizing the surface functionalization protocol.

In an attempt to further improve sensor reliability and to further lower the limits of detection, a second sensing concept has been investigated. The developed scheme isolates the resonator from the liquid to reduce viscous losses, which limit sensor resolution. Isolating the resonator from the fluid also prevents possible damage to the resonator itself from the pressure of the fluid or from corrosive substances in solution. The presented sensing scheme is capacitive with the resonator acting as an analog-to-digital converter. The resonator and the sensing capacitors are coupled via the spring softening effect, i.e. a change in the sensing capacitance ultimately causes a shift in resonant frequency. The proposed sensor concept has been extensively modeled and a fabrication process has been developed allowing for fabrication and on-chip packaging of the sensor structures.

CHAPTER 1

INTRODUCTION

Quantification of liquid-phase analytes is essential in biomedical and environmental sample analysis. Example applications include, but are not limited to: (1) detection of harmful water contaminants, (2) point-of-care quantification of serum proteins, (3) chemical-process monitoring, and (4) studying interactions between molecules (i.e., binding kinetics). These four examples all require that quantitative results be obtained, preferably in real time, or if not, with short measurement times (i.e., several minutes). For the most part, these analyses are currently performed by automated analytical instruments such as mass spectrometers and UV spectrophotometers. While these instruments can provide a wealth of useful information about a sample, they are expensive and complicated to operate. Thus, they are not suited to point-of-sampling use such as a patient's bedside or on-site monitoring of pollutants.

The current state-of-the-art in both environmental monitoring and biomedical testing applications is taking samples and then sending them to a lab for analysis. Three main disadvantages of this method are: the costs of the analyses [1], the time required for sample analysis [2], and possible sample degradation from the time the sample is collected to when it is analyzed [1, 3]. In fact, in clinical sample analysis, the main cause of measurement errors is in the pre-analytical phase, between the time the sample is obtained and when it is analyzed [3, 4]. In addition, if repeated sampling and analysis is necessary using the current methods can add significant cost to a project [1]. Sampling and measurement at the patient's bedside or in the field (in the case of environmental

monitoring) can help eliminate errors thus also reduce costs.

In time-critical applications, the current methods also fall short. It can take days to sample, ship, and test environmental specimens using mass spectroscopy, which is problematic when results are needed faster [2]. In biomedical applications, time can be critical and sometimes a test cannot be done fast enough, leaving doctors without important information for making a decision on a course of treatment [5]. Time is also essential in security applications, e.g. in the detection of biochemical warfare agents. Cheap and reliable tests are needed for potential bio/chemical warfare agents that can be done at the point-of-sampling with a fast turnaround time [6].

Point-of-care testing is a growing market that is projected to keep growing for some time [7], fueled in large part by the need for cheaper and more efficient tests in healthcare. Along the same lines, early disease detection and prevention of chronic illnesses can lead to huge cost savings and gains in quality of life [8]. Currently, most available point-of-care tests are based on lateral-flow assays, the classic example being at-home pregnancy tests. In addition, commercialized point-of-care tests exist for many analytes and disease markers [9]. In large part, these assays only provide qualitative information (i.e., a positive or negative result); at best these assays provide semi-quantitative responses [7]. If quantitative information is needed, the current technology falls short, and there are few examples of compact platforms appropriate for bedside or field use (i.e., by a paramedic). Point-of-care tests (POCT) are, of course, only appropriate for certain applications, some questions to keep in mind when looking for appropriate point-of-care applications include [10]: (1) “What clinical question is being asked when requesting this test?” (2) “Why isn’t the laboratory able to deliver the

required service?" (3) "Are there economic benefits to the POCT strategy?" (4) "Are there adequate facilities to perform the test and store the reagents?" , a full list of such considerations can be found in [10].

Requirements for in-situ environmental monitoring, i.e., detection of biochemical analytes in aqueous solutions, are similar to those for point-of-care applications. The current standard in such measurements is the use of bench-top analytical instruments, such as gas-chromatography-mass-spectroscopy. An example of the use of such systems for groundwater analysis can be found in [11]. These laboratory instruments are inappropriate for in-field use, and there is a need for portable devices for continuous monitoring [12]. The need for in-situ water monitoring, particularly the detection of heavy metals and volatile organics is directly related to human health. A recent President's Cancer Panel report stated: "organic water contaminants are an underappreciated cause of cancer that is inflicting grievous harm on Americans [13]." A full list of contaminants of interest is available from the US Environmental Protection Agency (EPA) [14]. The recent oil spill in the Gulf of Mexico and groundwater contamination from gas-well drilling have also highlighted the need for tests on environmental samples that can give quantitative results in the field [2, 15]. Although there has been work in this direction, particularly efforts targeting micro-gas chromatography systems (μGC) [16, 17], further miniaturization and cost reductions are possible and necessary.

One consideration for liquid-phase sensing systems is whether to label the analytes of interest to facilitate detection. Labeling with fluorescent tags or other markers adds extra preparation steps and additional cost. On the other hand, the addition of tags to

analytes of interest can make them easier to detect by increasing their mass, enhancing their dielectric properties, or giving them new properties such as magnetic activity [18, 19]. Labeling can also change the properties of an analyte so that it no longer binds to detector molecules [9, 20]. Thus, label-free detection is preferred. A second consideration is whether to actually perform the measurement in liquid, or alternatively, to immerse the transducer, rinse, and dry it and then do the measurement. Actually measuring the sensor in liquid, in real time, has several advantages, including minimizing the use of extra reagents, decreasing the number of processing steps, and providing the ability to study binding kinetics and molecular interactions at the sensor surface. Additionally, capturing the transient sensor response can provide information helping to distinguish between analytes [21].

Microsensors have the potential to solve many of the problems associated with the current measurement technologies, especially when quantitative measurement of a targeted set of analytes is required on-site (i.e., point-of-care applications or in-situ environmental monitoring.) Specifically, Complimentary Metal Oxide Semiconductor (CMOS)-compatible MEMS resonators are an attractive solution for several reasons. First, they can readily be batch manufactured and fabricated using the same tooling as integrated circuits. CMOS-compatible batch manufacturing leads to reductions in cost per unit and also allows system-on-a-chip or system-on-a-package solutions, which are low-cost and have a small footprint [22]. Resonators are also of particular interest because they can produce a semi-digital output, which can be tracked with a digital counter; this greatly simplifies system integration. Continuous operation of MEMS resonators in liquid is possible and can be achieved using an approach that can be ported to a hand-held

system. Finally, MEMS resonators are easily integrated with an Application Specific Integrated Circuit (ASIC) driving/read-out circuit that can be incorporated into a system-on-a-package solution.

To this end, micromachined mass-sensitive resonant cantilevers have attracted considerable research interest. Yet, few studies actually operate cantilevers in liquid and continuously track the resonator's frequency (the advantages of this measurement strategy are outlined above.) Two reasons for this are that (1) viscous damping can severely limit the resolution of cantilevers operated in liquid, and (2) when operated in the traditionally utilized out-of-plane flexural modes there is a significant amount of mass loading on the cantilever as evidenced by the frequency shift when the devices are immersed in liquid. This leads to a higher starting mass, and thus lower mass sensitivity [23, 24]. This work utilizes a cantilever's first in-plane mode, demonstrating that label-free biochemical measurements are possible in liquid, and that this approach can be competitive with other technologies for the development of hand-held platforms for point-of-care testing and in-situ environmental monitoring.

In addition to the cantilever work, a new resonant sensing concept will be presented that aims to improve upon device reliability and resolution in liquid-phase sensing applications. The proposed configuration isolates the resonator from the fluid and uses an electrical-to-mechanical-to-electrical transducer effect where the resonator serves essentially as an analog-to-digital converter. A small capacitance change due to the presence of the analyte alters the amount of charge stored on a floating intermediate electrode, and thus the DC voltage on a that electrode (the floating electrode drives the resonator). This causes a shift in resonator frequency via the spring-softening effect. This

sensor concept allows isolation of the resonator from the fluid, letting it operate in air or even vacuum. The proposed system could possibly lead to lower limits of detection because of the high resolution of the resonator, which is not subject to viscous losses from the fluid, and due to the sensitivity of the spring-softening effect to changes in stored charge.

A review of previous liquid-phase biochemical sensor work can be found in Chapter 2. Chapters 3, 4, 5 and 6 all contain information about the in-plane cantilevers. Chapter 3 outlines the theory of cantilever operation in a viscous fluid, Chapter 4 describes the fabrication process and packaging for the in-plane cantilevers, Chapter 5 contains mechanical characterization data for the in-plane cantilevers in both air and water, and Chapter 6 outlines the liquid-phase biochemical testing that has been performed with the cantilevers. Chapter 7 and 8 are concerned with the theory and implementation of the spring-softening resonators with Chapter 7 outlining the modeling if this new device and Chapter 8 describing the fabrication and initial characterization of the spring-softening sensor. Chapter 9 contains some concluding thoughts and outlook.

CHAPTER 2

REVIEW OF PREVIOUS LIQUID-PHASE BIOCHEMICAL SENSOR WORK

2.1 Current State of the Art in Laboratory Diagnostics/Biochemical Analysis

Measurement of a variety of analytes is needed in clinical and environmental sample analysis. In clinical laboratories a wide range of compounds in solution are quantified including but not limited to (1) proteins, (2) nucleotides, (3) metal ions and dissolved gases. In environmental analysis many of the same analytes are of interest including metal ions and volatile organic compounds, as well a contaminates such as pesticides and hormones. Currently, the state of the art is collecting a sample in the field (or in a hospital) and shipping it to a central laboratory where it can be analyzed. This takes time, which can result in sample degradation [4]. In addition, the instruments that are currently used have long turn-around times causing problems if results are needed rapidly (as mentioned in Chapter 1).

Currently, clinical laboratories rely on bench-top instruments in order to obtain quantitative results [10]. Point-of-care tests are also used, but can only provide qualitative, or at best semi-quantitative information [7]. The specific instrument or technique employed is dependant on the analyte and the nature of the sample. For example, immunoblotting is a common method to separate and identify serum proteins. While, electrochemical techniques might be used to detect metal ions in a blood sample, or to measure blood glucose concentration [10]. For each test, important considerations include: the probability of a false result (either negative or positive) and also the needed

detection limit. Specifically, detection limits are determined by statistical studies (randomized clinical trials), and a given test result needs to be compared to what is statistically normal within a given population [10].

In terms of point-of-care assays, one of the most commonly employed configurations is a lateral-flow assay. In a typical lateral-flow assay, a nitrocellulose membrane (or other material) is used to wick the sample through different zones of labeled antibodies creating a unique signal-mostly a color change-if the analyte of interest is present [9]. More specifically, a drop of sample is placed on the device and begins to flow by capillary action. It first passes through a filter, which separates out blood cells or other unwanted components. The sample then flows through a reagent region where proteins (or other analytes) from the sample bind to a labeled recognition molecule (i.e., an antibody that is tagged with gold or latex particles for easy visualization). Further down the membrane the bound antigen-antibody complex binds to another antibody in a detection region where the labeled antibodies can be seen. The sample keeps flowing and unbound labeled antibodies then bind to a control strip, which is used to indicate that the device functioned properly [7, 10].

Point-of-care technologies are often benchmarked against the commonly used enzyme linked immunosorbent assay (ELISA). An ELISA assay starts with absorbing a sample onto some sort of surface such as a polystyrene plate. Then, antibodies specific to the protein of interest are added and bind to the analyte (if it is present). Secondary antibodies conjugated to an enzyme (the enzyme produces a colored product) are added and bound to the first antibody. Addition of the enzyme's substrate produces a fluorescent signal, which can be analyzed with a spectrophotometer. The strength of the fluorescent

signal is proportional to the amount of analyte in the sample [10, 25] (See Figure 2.1). In state-of-the-art clinical laboratories, automated sampling and measurements tools are used to analyze fluorescent samples such as ELISA assays [10]. Although low detection limits are possible, ELISA requires multiple process steps, many reagents, and an optical reader. This can limit its use in time-critical, point-of-care, or embedded applications [7, 26, 27].

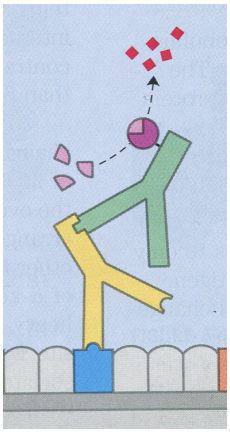

Figure 2.1: Diagram of and ELISA assay with the analyte shown in blue, the primary antibody shown in yellow, the secondary antibody shown in green, the enzyme shown in purple and the reporter molecules shown in red. Image is reproduced from [25].

A more detailed analysis of proteins in a solution can be performed with *electrophoresis followed by immunoprecipitation*. This combination of methods can both separate and identify proteins. Electrophoresis relies on the difference in size between molecules and also on their charge-to-mass ratio. In electrophoresis, a sample is first exposed to a heavily charged medium (sodium dodecyl sulfate (SDS)) which binds to proteins in the sample. This is done to even out any differences in shape and charge between proteins so that they will only migrate through the gel based on mass. The samples are then loaded into a gel (usually made from polyacrimide) with a fixed pore size. An electric potential is applied across the gel, and the distance that each species will

move is directly proportional to its mass [25]. An immunoprecipitation assay can be used to identify proteins that have been separated by electrophoresis. In this assay, a trough next to the electrophoresis gel is loaded with antibodies to the protein of interest and the gel is left to sit overnight. Formation of linked antibody-antigen complexes cause the proteins to precipitate out of the gel in a pattern that is characteristic for different proteins [10].

If the chosen medium does not lend itself easily to immunoprecipitation, or the antigens present cannot easily be precipitated [10], blotting can be used to identify the proteins in the sample. In *immunoblotting*, the electrophoresis gel is blotted onto a nitrocellulose membrane, and primary antibodies to the protein of interest are added. Next, in similar fashion to ELISA, secondary antibodies linked to an enzyme are introduced. Addition of the enzyme's substrate generates a fluorescent signal which can be used to identify which proteins are present [25]. (This technique is also called western blotting.) *Isoelectric focusing* is an example of a more advanced method yielding better separation. A solution containing proteins is loaded onto a gel that has an electrically established pH gradient. The proteins migrate in an electrical field, stopping when they reach the pH of their isoelectric point. This is the pH where they have no net charge; and thus, will not migrate further [25]. Subsequently, the isoelectric focusing gel is loaded onto a polyacrylamide gel and electrophoresis followed by immunoblotting is performed. Isoelectric focusing combined with immunoblotting allows for separation by isoelectric point and molecular weight giving further information for protein identification.

Chromatography is a separation method that fundamentally differs from electrophoresis in that analytes migrate through a vertical column at different rates based

on their interaction with the material in the column (the fixed or stationary phase). Types of chromatography include: affinity chromatography where analytes selectively bind to receptors on the fixed phase, size exclusion chromatography where analytes attach and detach to pores in the fixed phase based on size, and ion exchange chromatography where analytes bind to the stationary phase because of charge interactions [25]. Chromatography is only a separation technique. After separation, the different fractions must be identified by mass-spectroscopy or some other method.

Proteins are not the only analytes of interest in biomedical and environmental samples. For example, organic water contaminants pose a great threat to human health. Different contaminants can be separated from a water sample by gas-chromatography and then identified by mass spectroscopy, infrared (IR) spectroscopy, or nuclear magnetic resonance (NMR) [28]. These tools are highly specific, but are large and require extensive training to operate and to interpret the results. Advantageously, each spectroscopic technique gives different information, which can be combined and used to identify an organic compound. For example, NMR provides data on the connectivity and local chemical environment of a functional group within a molecule while, IR spectroscopy will yield information on what functional groups are present [28]. The combination of the data from different spectroscopies can lead to highly specific identification of organic molecules. These spectroscopic tools also have biomedical uses. Recently, a miniaturized NMR system has been created that can be used to identify malignant tumors thus, helping to eliminate problems with long wait times for results (minutes vs. days), and also alleviating errors associated with sample degradation between the time the biopsy is done and when it reaches the lab [29]. Similarly, a Raman

spectroscopy (a type of IR spectroscopy) system has been developed that can measure glucose concentrations in the field for better diabetes management [30].

Deoxyribonucleic acids (DNA) are a third class of molecules that are currently identified with analytical instruments in the lab. An example of a DNA analysis procedure comes from a clinical study where one might want to identify different single nucleotide polymorphisms (SNPs) within a population. (SNPs are base pair differences in a DNA strand that code for the same protein.) One method for doing this is using DNA microarrays which utilize array spotting methods and mass spectroscopy. First, a sample is split and then mixed with different tags for each SNP of interest; the sample is loaded with each tag onto a 384 well plate (see Figure 2.2 for an example of a tool that does this). The samples then undergo amplification using polymerase chain reaction (PCR) followed by further processing steps. Each well, containing the sample and tags is then spotted onto a special chip (a very small sample volume from each well is used). A mass spectrometer then analyzes each spot. A different signal is obtained based on whether or not the SNP of interest is present in the DNA sequence in each well [31]. (Protein microarrays using similar technology are also possible for the identification of proteins instead of DNA.)

In addition to array spotting followed by mass spectroscopy, the electrophoresis methods outlined above can also be used to separate and sequence DNA. For electrophoresis, the DNA molecules are first cleaved with enzymes and then sent through an electrophoresis gel. Tagging before electrophoresis causes each different sequence to create a unique pattern when run through a gel [25]. Through the use of appropriate cleaving enzymes and radiolabels, separation of DNA strands that differ by only one

nucleotide is possible [25].

Figure 2.2: Commercial pipetting tool used for placing samples in well-plates for analysis. Image reproduced from [31].

Micromachining techniques have been used to miniaturize, or develop new tests that are not available with current analytical instruments, and these devices are beginning to make their way into clinical laboratories. There is a great deal of research on using micromachining techniques (especially microfluidics) to create point-of-care tests [4, 7]. In order to get more quantitative results, additional features have been added to lateral-flow assays, or new microscale techniques are employed. For example, hand-held devices using fluorescent tags and an optical reader have been commercialized for the detection of cardiac markers for diagnosis of a heart attack [7]. A second example that uses microfluidics but not lateral-flow technology is a product being developed by Artemis Health. This company manufactures a patterned flow channel to separate fetal cells from maternal blood for the diagnosis of genetic disorders in the fetus (see Figure 2.3). Separating fetal cells from maternal blood poses significantly less risk to the developing child than the traditionally used amneocentesis [32].

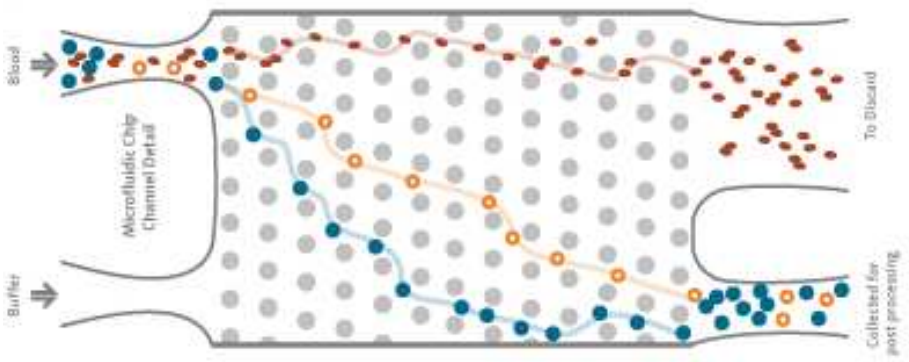

Figure 2.3: Diagram of the microfluidic system made by Artemis Health to isolate fetal cells from maternal blood. Reproduced from [32].

Although the laboratory instruments described above provide quantitative results and can measure a broad range of analytes effectively they area inappropriate for use in low-cost systems that can be used in the field. Microsensors have the potential to replace bench top instruments for in-field or point of care use. In particular, for medical diagnostic applications if a system that yields quantitative results rapidly could be cheaply manufactured it could particularly useful as molecular diagnostics become more prevalent. Allowing for accurate quantification of a number of disease markers at once [4]. For environmental sensors, particularly for the detection of volatile organics in water, a field useable measurement system would save time and could even allow consumers to test their own water. Detection of contaminants by the consumer could allow them to avoid ingestion of harmful contaminants. The next section offers a summary of different microsensor approaches.

2.2. Review of Microsensor/Microanalysis Systems

Many microscale sensor technologies exist for quantifying liquid-phase analytes. Each technology has advantages and disadvantages. For example, optical sensors offer

very low detection limits, but require components that are difficult/expensive to miniaturize. Alternatively, MEMS-based sensors can be relatively simple to batch manufacture and integrate, but may not be as sensitive. There is not a perfect technology that works for every application, rather a technology needs to be matched to an appropriate application. For sensors, key considerations include: (1) Limit of detection: ng/ml are generally required for biosensors in medical diagnostic applications and low-ppb range limits of detection are required for sensing organic contaminants in drinking water. (2) Reliability: how well does the sensor hold-up in the environment in which it will be used? (3) Cost/ease of manufacture: does the technology require exotic materials? Can the sensors be easily batch manufactured and packaged? (4) Environmental sensitivity: how sensitive is the sensor output to environmental factors such as temperature or solution properties such as pH? Choosing the appropriate sensor technology for a given liquid-phase application will depend on balancing the trade-offs of a given technology for these four considerations among others.

2.2.1 Electrochemical Sensors

Electrochemical sensors utilize interactions of electric charges and electric fields with analytes in order to detect them. There are many different electrochemical sensing schemes including: amperometric, impedimetric, magnetic, and capacitive. Electrochemical sensors can be highly sensitive, and in some cases are inherently selective. It is also possible to directly integrate many types of electrochemical sensors with CMOS technology. This integration gives advantages in terms of batch fabrication and the creation of single-chip systems.

There are several types of electrochemical sensors, each with its own advantages and drawbacks. For example amperometry and voltammetry offer high selectivity but require a REDOX active species. Alternatively, capacitive sensors can be easily integrated with CMOS but often offer lower selectivity. The choice of the appropriate electrochemical sensor depends on the application.

i. Voltammetry and Amperometry

Voltammetry and amperometry, are two of the most basic electrochemical sensing configurations. These sensing schemes use oxidation-reduction (REDOX) reactions at electrodes immersed in solution in order to detect dissolved species. In voltammetry the voltage on a set of electrodes is swept, and species in solution begin to be oxidized or reduced at a certain potential in the voltage sweep. The resulting current can be measured using a transimpedance amplifier. Different analytes undergo oxidation/reduction at a characteristic potential [10]. In amperometry, a fixed voltage is applied and the resulting current is proportional to the concentration of analyte in solution. Amperometry and voltammetry have been employed in the detection of many types of molecules including: dissolved metal ions [10], gases in solution [10], dissolved organic compounds [33], glucose, and proteins [20].

An analyte must undergo a REDOX reaction to be measured with amperometry and voltammetry. Unfortunately, not all compounds will be readily oxidized or reduced. Also, many proteins and enzymes have REDOX centers that are not readily accessible, or require large potentials in order to be oxidized or reduced. These difficult-to-measure molecules require a “REDOX active” label in order to be measured with voltammetry or

amperometry [34]. In the case of biosensors, this can be accomplished by a sandwich assay where antibodies are immobilized on a surface, antigen from solution binds to the antibody, and then a labeled antibody is bound to the antibody-antigen complex. The label on the second antibody contains a REDOX active compound (which will be oxidized or reduced) allowing for quantification by amperometry or voltammetry [20]. For environmental monitoring of volatile organics the same problem is encountered, i.e., volatile organics are not readily oxidize/reduced. In this instance, a measurement of the dissolved oxygen content can be correlated with the amount of dissolved organic compounds. In an example configuration, a TiO_2 catalyst and UV lamp are used to degrade dissolved organic compounds. As organic molecules are broken down by the catalyst they consume oxygen. The oxygen concentration can be measured amperometrically and correlated back to the amount of dissolved organics originally in the sample [33].

Microscale fabrication techniques have been used to miniaturize and to enhance amperometric sensors. In one such configuration, a monolayer of silver is deposited on the surface of a gold electrode and the gold is further modified with a recognition element (i.e. an antibody or DNA). Sweeping the current on the electrode oxidizes and reduces the silver monolayer. Binding of analytes to the recognition element causes a decrease in the observed current because the bound species make it more difficult for electrons to reach the underlying silver. This technique can give detection limits in the pg/ml range [34]. In addition to metal monolayers, metal nanoparticles can be used as a REDOX active species in an electrochemical immunoassay [34]. Microfabrication methods have also been used to create on-chip electrode arrays for amperometry and voltammetry; as

examples such systems can be used to detect DNA and antibody-antigen binding [35-37].

ii. Capacitive and Impedimetric Sensors

Capacitive and impedimetric sensors are alternative electrochemical methods that lend themselves well to miniaturization and CMOS compatibility [38, 39]. Capacitive and impedimetric sensors operate by measuring the change in the capacitance or impedance of a structure in response to the presence of an analyte. A typical configuration consists of a set of electrodes with some method of biasing. A biomolecule or organic compound will have a different dielectric constant than the surrounding solution. Thus, if that biomolecule binds to one of the capacitor electrode surfaces and displaces water molecules, the capacitance will change due to the change in dielectric constant. Capacitance can be measured by several methods, including: charging and discharging of capacitors [38], switched capacitor circuits [38], or measuring with an AC signal in a capacitive divider configuration [40]. If an AC signal is used then the entire impedance is measured not just the capacitance. Both of these sensor types can be used in label free formats, in contrast to volammetry or amperometry, which often require attaching some electroactive species to the analyte to generate a current.

There is a great deal of literature on capacitive sensors and they have been demonstrated for the detection of a wide range of analytes including: C-reactive protein [41], allostatin [42], many different compounds based on antibody-antigen interactions (see Figure 2.4 for an example of a capacitive device) [38], and volatile organic compounds [43]. In an interesting approach, a commercially available fingerprint sensor containing many electrodes in an array was modified and used as an immunosensor [18]. To increase the sensitivity of the device, antigen labeling was required. But, never-the-

less it shows the simplicity of the capacitive approach and how an array of such sensors can be built. Capacitive and impedimetric sensors are easy to miniaturize and integrate and can give detection limits in the ng/ml range [41]. As an example of a point-of-care system, impedimetric sensors have even been demonstrated for use in a lateral-flow assay format integrated with a sample delivery system [44]. A drawback of capacitive and impedimetric sensors is that they do not have inherent selectivity and also may require labeling to increase their sensitivity.

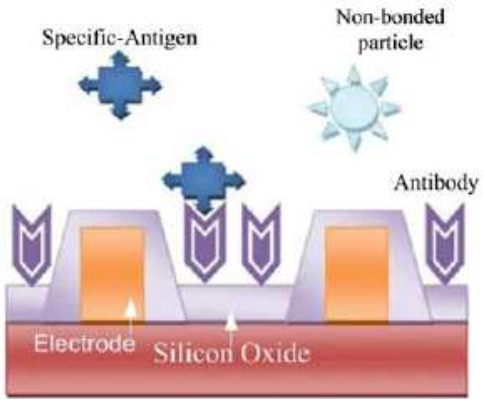

Figure 2.4: Diagram of a CMOS-based capacitive biosensor. Image is reproduced from [38].

iii. Field-Effect and Conductometric Sensors

A third class of electrochemical sensors is conductometric/field-effect sensors. These transducers convert a chemical absorption or an analyte binding event into a change in resistance or conductance. The analyte binding can either directly change the amount of current flowing through a structure or induce an electric field change which alters the current flow. A simple example of a conductometric sensor is a resistive chemical sensor for detecting volatile organics. In this system, a polymer impregnated with conductive nanoparticle is placed on top of an array of electrodes. Analyte

absorption swells the polymer. This changes the distance between the conductive nanoparticles, and thus, the measured conductivity [45]. A possible field-effect configuration uses the interaction of nanowires with biomolecules to detect analytes in solution. The exact mechanism of transduction is not clear, but it is thought that biomolecules induce electric field changes within the nanowire altering the conductivity [46-48]. On similar lines, field-effect transistors can also be employed as biochemical sensors. These devices are CMOS-compatible, and thus, can be readily batch fabricated. The source and drain of the transistor are biased, and analyte binding to the gate (which is functionalized with a sensitive layer) generates an electric field, which modifies the conduction within the channel [49, 50]. Field-effect devices and nanowires offer high sensitivity to analyte binding, yet can be greatly affected by a surrounding aqueous solution (i.e., by charged ions in the solution) [46]. In some cases more research may be needed to fully understand the operation of these devices and the effects analytes have on them.

iv. Magnetic Biosensors

Finally, magnetic biosensors are a fourth class of electrochemical sensors, which can give high sensitivities (in some cases high enough for single molecule detection). In addition, they are also capable of providing real-time binding information. On the other hand, magnetic sensors require labeling of analytes with magnetic nanoparticles (which can lead to higher costs) [51]. A commonly used magnetic sensing scheme is giant magnetoresistance (GMR). In GMR devices the interaction with a magnetic bead attached to an analyte causes a resistance change in the sensing structure. In one

configuration, GMR sensors are based on spin-valves, where a local change in the magnetic field induces spin dependant scattering, changing the resistance in a magnetic material. This technique can yield limits of detection in the femtomolar range for DNA and proteins (for a 150 kDa antibody this is well below ng/ml) but requires the integration of exotic magnetic materials [19]. GMR sensors have also been integrated with lateral-flow assays with detection limits in the pg/ml range [52]. An additional example of a magnetic biosensor is a micro Hall-effect sensor, where a miniaturized Hall-effect sensor is fabricated in silicon. The interaction of a magnetically tagged molecule with the Hall-effect device facilitates analyte detection. This device has detection limits down to a single molecule [53].

2.2.2 Optical Techniques

Optical sensing methods use the interaction of visible, ultraviolet (UV), or infrared light (IR) with a sample to produce a useful sensor output. Optical sensors have the major advantage of high sensitivity. On the other hand, optical components can be difficult to integrate on a single chip platform because they often require laser sources and other optical components, which utilize expensive materials [38]. In addition, optical sensors are highly sensitive to environmental changes (i.e., they often require vibrational isolation) and can be highly sensitive to the optical properties of a sample [7]. Many different optical sensor topologies have been investigated including: surface plasmon resonance (SPR) [54], surface enhanced Raman spectroscopy (SERS) [55], optical gratings [56], and waveguide-based sensors [57]. There has been a great deal of work on optical sensors, and commercialized platforms are available [20, 58].

Optical biosensors offer the advantage of high sensitivity and have even been commercialized. Their drawbacks include high temperature sensitivity [26], sensitivity to optical properties of a solution (i.e., some samples auto fluoresce or are difficult to pass light through) [7], and high costs associated with integration of optical materials [38] (e.g., III-V materials for the fabrication of on-chip lasers). Despite these drawbacks, optical sensors make effective sensing platforms and have found widespread use.

i. Surface Plasmon Resonance Based Sensors

SERS and SPR are both methods that employ light propagation along a surface. SERS is the most sensitive surface technique and is even capable of single molecule detection. It relies on Raman spectroscopy where a photon is absorbed by a material and then re-emitted at a different wavelength. The frequency of the emitted photon is characteristic for different compounds [59]. For reasons that are not completely clear, the Raman effect is greatly enhanced at metal surfaces allowing for detection of single molecules [55]. Sensing using SERS involves binding or absorbing analytes to a metal surface and then exciting the surface with IR light. This technique is highly sensitive but is not widely reported in the literature for miniaturized sensors.

Although not as sensitive as SERS, SPR has found widespread use. Surface plasmons exist at a metal surface when an electromagnetic wave in an insulator (i.e., a dielectric material above the metal) is strongly coupled to a plasma wave on the surface of the metal [60]. SPR sensors require a thin metal coating, which has a negative dielectric constant at the frequencies of light used for excitation. Charges on the metal surface are responsible for the propagation of the plasma wave, and thus, the surface

plasmon is highly sensitive to changes on the metal surface. Analyte binding to the thin metal layer induces changes in the dielectric constant at the surface, shifting the SPR resonant frequency (frequency of light at which surface plasmons will be excited) [20].

When light is properly coupled to the thin metal layer, a surface plasmon is excited (resonance occurs), and a dip in reflectance is observed. Thus, SPR requires a method of coupling light to the metal surface in order to excite a surface plasmon. In one configuration, a prism is used and light is focused at the correct angle, exciting surface plasma waves. With the prism coupling method, sensing can be accomplished by varying the angle of incident light and observing changes in the angle that gives resonance (analyte binding changes the angle that gives resonance). Alternatively, the structure can be illuminated at a constant angle and the changes in wavelength or intensity of light reflected through the structure can be measured [20, 58]. Alternative coupling methods (as opposed to prism coupling) utilize optical fibers (Figure 2.5 contains a diagram of an SPR sensor with light coupled from an optical fiber) [61], waveguides [58], or optical gratings [60] to generate surface plasmons. In the waveguide and optical fiber techniques, light traveling through the waveguide generates an evanescent field, which excites surface plasmons in similar fashion to the prism coupling method [58, 61].

SPR sensors have been commercialized, though mostly relying on non-integrated components [20]. In addition, miniaturized SPR sensors have been demonstrated for in-field use [54]. SPR techniques have yielded detection limits in the tenths of ng/ml range for proteins [58] and have been utilized for a variety of applications including detection of markers for Alzheimer's disease [62], nucleic acids [63], and many different proteins [58]. Despite several advantages, SPR sensors do have some drawbacks including: (1) the

often used prism couplers are difficult to integrate, (2) alternative coupling methods require a transparent analyte solution or waveguide structure in order to be used, and (3) there is no method to differentiate between refractive index changes at the device surface due to analyte binding and index changes due to variations in the bulk solution [58].

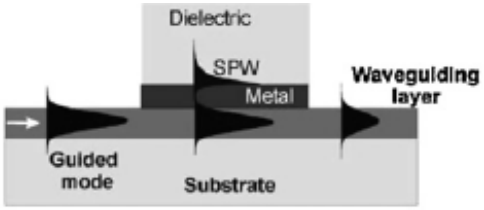

Figure 2.5: Diagram of the basic operation of an SPR sensor. There are several possible sensor configurations. In the one depicted light from a waveguide excites surface plasmons in the metal layer. The surface plasmons are then sensitive to material bound to the metal layer. Image is reproduced from [58].

ii. Waveguide Sensors

A second optical sensing method employs optical waveguides and optical fibers. These devices are again sensitive to refractive index changes at a surface where analyte binds, but a different mechanism is used to detect these changes. The main method of sensing utilizes the interaction of the evanescent field of a guided wave with a surface where analyte has been captured. Different sensing schemes are possible including integrated Mach-Zehnder interferometers [64] and total internal reflection fluorescence (TIRF) [65]. Interferometer configurations rely on a structure where a laser beam is split into two different branches, each of which is routed onto waveguides. One branch has an exposed surface where analyte binds. Through interaction with the evanescent field of the guided wave, the analyte changes the phase of the guided wave in one of the branches of the interferometer. The two beams are recombined and the intensity is measured to determine if the analyte is present (when the beams are out-of-phase due to phase-shifts

as a result of analyte binding the beam intensity decreases). The interferometer used for this approach can be integrated into a small handheld format, but off-chip laser excitation and off-chip detection are still used [64].

In TIRF, total internal reflection is used to guide light in an optical fiber. The evanescent field of the guided wave excites fluorescence in labeled detector molecules. The signal from those molecules can be tracked as analyte binds, giving a sensor output [65]. Direct detection is also possible by measuring the fluorescent signal when a sample is excited with a laser beam, such an approach is presented in [66] for the detection of procalcitonin. Both of the schemes presented above exhibit low detection limits, well into the ng/ml range for proteins and hormones [58, 65]. Additionally, TIRF sensors have been applied for the detection of environmental water contaminants [65, 67]. In order to enhance the interaction of the evanescent waves used for sensing in optical fiber sensors and the analytes being bound to the outer surface of the fiber, the optical fibers themselves can be tapered by thinning the cladding on the outside of the fiber. Such a structure has recently been demonstrated for the detection of biomolecules, in this case the interaction of the evanescent field with the analyte shifts the frequency of the optical wave in the fiber [68].

Additional waveguide sensing approaches are possible, relying on similar principles as those presented above. For example, fiber IR sensors are a type of waveguide sensor that is appropriate for in-field environmental applications. They rely on the interaction of an absorbing layer that binds volatile organics from the environment with evanescent waves from within the fiber (in this case the absorbent material is deposited on the fiber surface). Alternatively, the absorbing layer can be contained within

the fiber itself and directly interact with the guided light. By measuring the transmitted optical signal at a given wavelength, absorbance information at a given wavelength can be obtained [69]. These sensors have been used to detect volatile organic compounds in water. Since IR absorbance at a wavelength is measured, these systems can also give information about the identity of the molecules that are present, similar to conventionally used IR spectroscopy [69].

iii. Optical Resonators and Optical Gratings

Optical resonators and diffraction gratings are simple to manufacture and have also been used as sensors. Optical resonators shift their resonance frequency as analyte binds to their surface because the analytes induce changes in dielectric constant on the resonator surface [70]. In some cases, these structures can be fabricated in silicon using widely available semiconductor processes, and can offer limits of detection well into the ng/ml range or lower for proteins. An important note is that although the resonant structures can be made in silicon, the system still requires the use of an off-chip laser source [71]. Diffraction gratings are another simple to manufacture structure (they can be fabricated using screen printing). Recently, a biosensor was demonstrated that used screen-printed gratings, with changes in diffraction efficiency being tracked in order to sense analyte binding [56].

iv. Paper-Based Optical Sensors

There has been recent work on integration of optical sensors with microfluidics [72], and optical detectors/readers can also be employed in paper-based assay or lateral-

flow assays [9, 73]. There is a great deal of interest in paper-based and lateral-flow types of systems because they require small sample volumes and provide a compact platform that can be used in a resource poor environment. In one such configuration, a miniaturized electrophoresis system is used to separate the components within a sample. Fluorescent labeling allows for the identification of different fragments (that have been separated by electrophoresis). This system gives detection limits in the ng/ml range for several disease markers but as presented requires a bench-top microscope [74]. Ellerbee et. al. demonstrated a fully integrated colorimetic detection scheme that uses a paper-based assay. The colorimetric detection system features an integrated photodetection setup, consisting of a tricolor light emitting diode (LED) for illumination, and photodetector for quantification of the transmitted light that passes through the sample-laden paper (see Figure 2.6) [75].

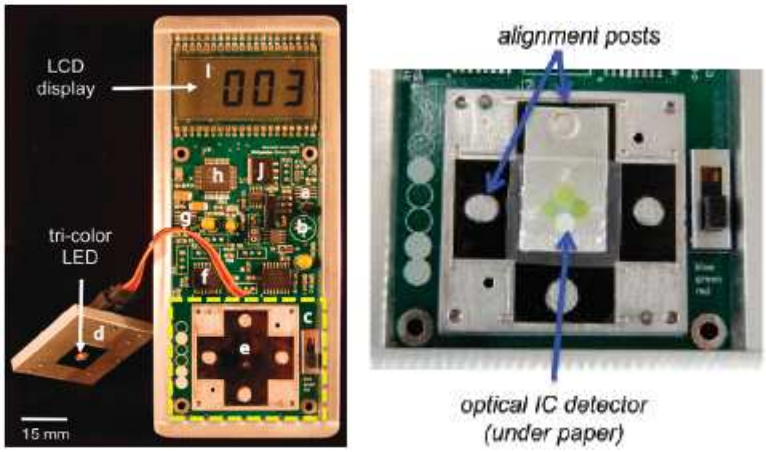

Figure 2.6: Image of the optical detector used with paper based assay (right). The entire hand-held optical detection system (left). A sample can be dipped in solution and then inserted into the detector for quantification of the analytes present. Image is reproduced from [75].

A similar concept has been developed for a portable paper-based ELISA essay, the results of which can be read using a standard document scanner [76]. One downside of these

microfluidic and paper-based assays is that the employed optical detection schemes can be sensitive to other properties of the sample besides the concentration of analyte, leading to possible erroneous results [9].

2.2.3 Acoustic Sensors

Acoustic wave sensors detect analyte binding through the use of mechanical waves generated within or on the surface of a solid. There are several different types of acoustic sensors and they are categorized by the type of mechanical wave that is excited in the device. Figure 2.7 displays some examples of different modes of operation for these types of structures. Generally, piezoelectric materials are used to generate a mechanical excitation from an applied voltage [50]. An exception are capacitive micromachined ultrasonic transducers (CMUT), which use capacitive excitation to excite vibrations in a thin membrane [77]. Acoustic sensors operate at high frequencies, generally in the megahertz range or higher, and offer the advantage of high sensitivity. But, acoustic sensors use exotic piezoelectric materials that can make integration with excitation/read-out circuitry more challenging and increase fabrication costs [78].

The classic example of an acoustic sensor is the quartz crystal microbalance (QCM) [79]. This device utilizes a quartz crystal as a resonator. Mass loading on the device surface causes the frequency to drop. (For a mechanical resonator, the resonant frequency is proportional to the square-root of the effective stiffness divided by the mass.) These devices have been commercialized and are available in bench-top instruments (i.e., the Q-Sense system). The main disadvantages of QCM's for creating microscale sensors is that they can't easily be integrated with CMOS circuitry; and that

they have a footprint on the order of tens of millimeters, limiting where they could potentially be placed.

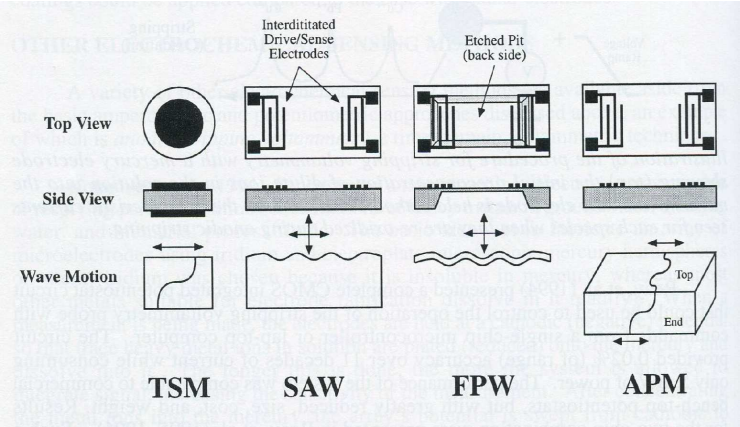

Figure 2.7: Diagram showing some commonly used acoustic modes and the electrodes used for their excitation. Image is reproduced from [50].

Extensive research exists on creating miniaturized sensors utilizing acoustic wave devices for operation in both air and liquid [80]. The devices themselves can be fabricated using the following methods: (1) from piezoelectric crystals and combined with oscillator circuitry [81], (2) by deposition of piezoelectric materials onto CMOS oscillator circuitry [78], (3) or by fabrication of extremely thin membranes in a post-CMOS process in the case of CMUTs [77]. In a typical excitation and detection configuration, interdigitated electrodes excite and detect an acoustic wave in the transducer. The transit time of the generated wave is altered by the binding of analytes onto the device, which alters the resonant frequency of the sensor (the resonant frequency can be tracked with an oscillator circuit) [50].

One of the most common employed modes for sensing applications is the surface acoustic wave (SAW). Surface acoustic waves propagate along the surface of the

transducer, and thus, are highly sensitive to changes that occur when an analyte attaches to the device surface. SAW devices have been extensively investigated as biochemical sensors [82]. For liquid operation, the typically used Raleigh waves are too severely damped. The damping is a result of the dielectric constants of the acoustic materials in the device being significantly lower than that of water, causing the electric fields needed for wave excitation to be drawn into solution. Two possible remedies to this problem are to use piezoelectric materials with a higher dielectric constant, or to use Love-wave devices where the acoustic energy is confined to a coating on the device's surface [82]. Love-wave chemical sensors have been able to detect volatile organics in water down to the low parts per billion (ppb) range [81]. In addition, arrays of SAW devices have been integrated with CMOS circuitry to create sensor arrays for the detection of cancer biomarkers in the ng/ml range [83]. Flexural plate wave devices are a third example of acoustic transducer that has been investigated for liquid-phase applications [84]. These devices use a piezoelectric material deposited on a thin membrane in order to excite the membrane into resonance. An example application is the detection of IgE antibodies for applications in allergy diagnosis and management [85].

Acoustic transducers offer low detection limits for compounds in water. On the other hand, they require the integration of nonstandard materials into CMOS processes increasing fabrication costs; and they can be highly sensitive to properties of the surrounding medium (i.e., viscosity of the solution in which the are operated) [80], [78]. In addition, the frequencies that they operate at can lead to issues with interferences requiring shielding or other techniques, making system design more difficult [86]. Despite these challenges, acoustic wave devices have been used to create robust sensors,

and work has even been done in integrating them into handheld platforms [87].

2.2.4 Cantilever-based Sensors

The term cantilever generally refers to a beam of rectangular cross-section that is either clamped at one or both ends. Cantilevers have been widely used in scanning probe microscopy [88], and have been extensively investigated as biochemical sensors in both the gas and liquid-phase [23, 89]. There are many possible actuation and detection configurations to make sensors from cantilevers, and many different materials from which the beams themselves can be fabricated [23]. There are two main sensing schemes that are utilized with cantilevers, either dynamic mode or static mode. In dynamic mode, the cantilever is used as a resonator, and changes in either the mechanical stiffness of the beam or its mass induce frequency shifts (the resonant frequency is proportional to the square-root of the effective stiffness divided by the mass). Thus, in dynamic mode, analyte detection is accomplished by tracking the cantilevers frequency [23]. The frequency can either be tracked closed-loop with the resonator operating continuously in real-time at its resonant frequency or open-loop where the frequency transfer characteristic is measured at discrete time points. Alternatively, in the static mode configuration, analyte attachment induces surface stress on a thin cantilever beam causing the cantilever to bend. The deflection of the beam can be measured using a variety of transduction principles [90].

i. Excitation and Detection Methods

Many examples of cantilever biochemical sensors are available [23, 91], and they

employ a variety of transduction mechanisms including: piezoelectric [92], static mode with optical detection [93], static mode with piezoresistive detection [94], dynamic (resonant) mode with piezoresistive [24], and also capacitive transduction [95].

Piezoelectric cantilevers rely on a piezoelectric material which deforms in response to an applied voltage. The deformation is the result of an anisotropic arrangement of atoms in a crystal that allows a dipole to exist when the material is deformed [50]. This deformation upon application of an electric potential allows for a piezoelectric material to excite a beam into resonance, and can also be used as a static mode detection method.

As mentioned above, piezoresistive and capacitive sensing schemes are two additional examples of integrated methods that can be used to obtain signals from cantilevers. Piezoresistive devices utilize changes in resistance in response to mechanical stress. In semiconductor materials this change is due to variations in the bandgap energy in response to material deformation. When the piezoresistive material is stressed the arrangement of atoms in the crystal is modified, thus changing the bandgap energy [96]. Piezoresistance can be used as a detection method in either static or dynamic mode. Alternatively, capacitive transduction methods rely on using the capacitance between a set of fixed electrodes and the movable beam to electrostatically excite and sense cantilever static deflection or dynamic vibration [89].

In addition to integrated detection methods, off-chip optical detection of static or dynamic mode cantilever operation is possible. One such technique relies on the use of interferometers, which utilizes a set of interdigitated beams. A laser is focused on the beams and deflection of the cantilevers changes the intensity of the observed interference

pattern [89]. A second optical technique is called an optical lever, where a laser beam pointed at the end of the cantilever is deflected onto an array of detectors, and the deflection of the cantilever changes the location of the beam on a detector [89].

As chemical sensors, cantilevers have been employed extensively in the gas-phase to detect a variety of analytes [86, 95, 97]. Both the in-plane and out-of-plane flexural modes of resonant cantilevers have been explored. Bedair et al demonstrated a capacitively actuated in-plane mode cantilever fabricated in a CMOS process for gas-phase sensing applications [95]. Static mode cantilevers have also be investigated as chemical sensors. A sensitive polymer layer is deposited on the surface of the beam, this layer swells when it absorbs vapor, causing the cantilever to bend. The bending induces a surface stress that can be detected using a piezoresistive Wheatstone bridge [98].

Beam surfaces can be readily functionalized and used in the liquid-phase for biosensing applications. For static mode cantilevers, detection limits below 1 ng/ml have been demonstrated for prostate specific antigen ((PSA), a biomarker used for diagnosis of prostate cancer) in a background of serum protein (with optical detection) [99]. More recently, fg/ml detection limits have been demonstrated for biotin (with optical detection) [23]. Arrays of static mode cantilevers utilizing piezoresistive detection have been proposed as a means of looking at several disease markers at once (see Figure 2.8 for an image of these cantilevers) [100]. Additionally, dynamic mode cantilevers have demonstrated detection limits in the ng/ml range for integrated operation, and have been able to detect a single strand of DNA using an optical detection scheme [23].

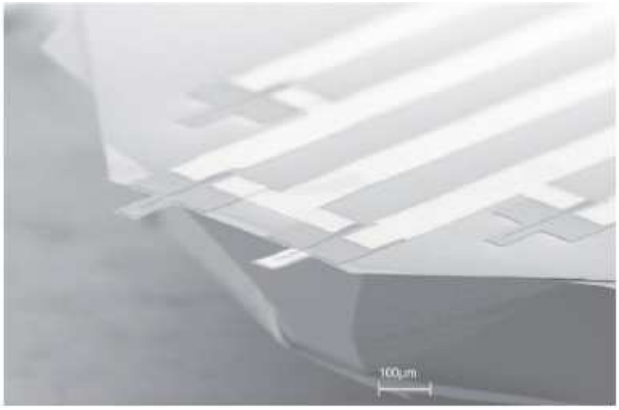

Figure 2.8: Image of a piezoresistive static mode cantilever; a gold layer is deposited on the beam for attachment of biomolecules. Image is reproduced from [100].

ii. Liquid Phase Operation of Resonant Cantilevers

Few studies of cantilevers operated in the liquid-phase exist, mostly because the surrounding fluid severely damps the cantilever response limiting sensor resolution. Often the chosen sensing strategy is to measure a baseline sensor output (i.e. resonant frequency, piezoresistor resistance ect.). Then, expose the sensor surface to liquid-phase analytes, which are absorbed by a sensitive layer or coating applied to the beam. Finally, the device is dried and re-measured [101]. This strategy is problematic in practical applications because a washing step is required, which necessitates additional reagents, and also during the drying process particles can contaminate the device surface. Drying the device is also not appropriate for real-time or in-situ measurements. Despite these issues, this technique has been used to achieve ng/ml range limits-of-detection for cancer biomarkers [102].

For continuous operation in liquid, Vancura et al. investigated cantilevers operated in their first out-of-plane flexural mode to create resonant chemical sensors [24]. These devices are CMOS-compatible and use a magnetic excitation mechanism and

piezoresistive detection scheme to achieve parts per million (ppm) range limits of detection for volatile organic compounds in water [24]. Microdisk resonators supported by a clamped-clamped beam and utilizing thermal actuation and piezoresistive detection are a second example of a CMOS compatible strategy that has been used to make liquid-phase sensors [103]. Direct resonator operation in liquid has also been demonstrated for heavy metal sensors, where the metal ions are plated onto a mass-sensitive resonator altering its mass, and thus, the resonance frequency [104]. The same research group has been able to develop thermally excited high-frequency resonators, which give high-Q (on the order of a few hundred) in liquid [105]. Although they offer high-Q, these resonators have the drawback of high power consumption and large temperature rise along their surface.

A sensing scheme that uses direct cantilever operation in a fluid but utilizes an optical instead of integrated read-out has been demonstrated to detect ng/ml quantities of protein in fluid. In this technique, a cantilever beam is piezoelectrically actuated into resonance and the resonator frequency is measured using a laser. This method gives good detection limits, but requires equipment that is too complex for a point-of-care setting [106]. Although, optical detection schemes require more components than an integrated (i.e. piezoresistive or capacitive) read-out, they have been implemented with discrete components to give single nanogram per milliliter detection limits for detection of biomarkers for hepatitis [107]. A final example of resonator operation in fluid is for the mass-sensitive detection of ethanol using piezoresistive cantilevers [108].

A promising alternative strategy for liquid-phase sensing using cantilevers has been presented in [109]. In this work, a fluid channel is routed through the interior of the

cantilever itself. This allows the beam to operate in air or even vacuum giving quality factors as high as 15000, mitigating the damping problem in fluids (Figure 2.9 contains a diagram of this device). This strategy makes extremely low limits of detection possible. Quantities as small as a single cell/particle can be measured using this approach. Recently, an integrated piezoresistive read-out has been implemented for the embedded fluid channel cantilevers [110]. Although the embedded fluid channel resonator offers single molecule resolution, it requires a complicated fabrication process and can only tolerate very low fluid flow-rates.

Along the same lines, electrostatically actuated flexural plate resonators have been developed that allow for fluid to be routed through the resonator while it is operated in vacuum. The flexural plate resonators are fabricated using a wafer bonding process and can be on-chip packaged [111]. Alternatively, a system has been developed that allows a cantilever resonator be placed in a flow cell such that only one side of the cantilever is immersed yielding Q-factors in the hundreds [112]. It is expected that the improved Q-factor from this approach will improve sensor resolution.

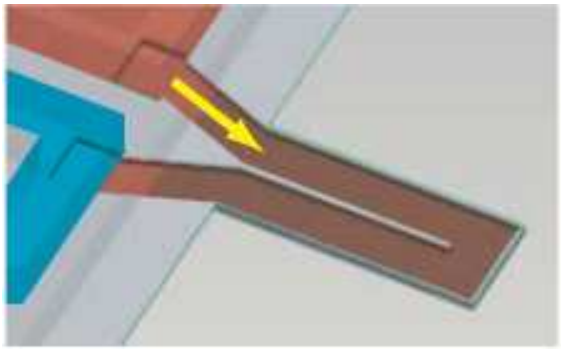

Figure 2.9: Diagram of a suspended microchannel resonator, the fluid channel can be seen inside the cantilever allowing for operation of the device in vacuum. Image is reproduced from [109].

In summary, cantilever-based sensors rely on a wide range of transduction

mechanisms and utilize a variety of transducer effects to convert beam deflections into usable signals. With high-end optical setups, very low detection limits are possible with cantilever-based sensors [23]. On the other hand, CMOS compatibility and liquid operation are possible with cantilever-based sensors, opening the way for their uses as inexpensive sensors for disposable point-of-care or embedded applications [24, 100]. Table 2.1 below contains a summary of different liquid-phase microsensor approaches.

Table 2.1: Summary of liquid-phase microsensor techniques.

	Limit of Detection	**IC Compatible**	**Selectivity**	**Notes**
Electrochemical	ng/ml	Yes	Inherent/Depends on method	-Simple systems -Very sensitive to solution properties
Optical	.1 ng/ml (Best)	No	Inherent/Depends on method	-Highly sensitive -Expensive to miniaturize lasers
Static Cantilevers	ng/ml (w/ Optical readout)	Yes/varies	Receptor Dependant	-Often requires optical read out for low LOD
Resonant Sensors	ng/ml	Yes/varies	Receptor Dependant	-Mass sensitive/Every molecule has mass. -Lower LOD Needed

CHAPTER 3

IN-PLANE CANTILEVER CONCEPT AND DESING

In contrast to previous investigations, the cantilevers studied here utilize the first in-plane flexural mode, instead of either an out-of-plane flexural or torsional mode. The original motivation for this was that in a fluidic environment, the magnitude of the viscous damping would be reduced because the cantilever would move laterally through the fluid, instead of pushing against it. It should be noted that for cantilevers operated in air, energy loss through the anchor can be considerable, while in liquid the anchor loss is generally negligible compared to that of the viscous losses to the surrounding fluid. Intuitively, the lower damping of the first-in-plane mode compared to the first out-of-plane mode makes sense to anyone who has used a canoe paddle; i.e. it is much easier to move the narrow face of the paddle through the water than the broad face (the part of the paddle which is normally used to propel a canoe). Figure 3.1 shows a schematic of cantilever beam with the variables used for the different dimensions in the formulas presented here. The cantilevers in this thesis vibrate in width (b) direction (the in-plane direction). Figure 3.2 displays FEM (finite element method) simulations of the first out-of-plane and first in-plane cantilevers modes.

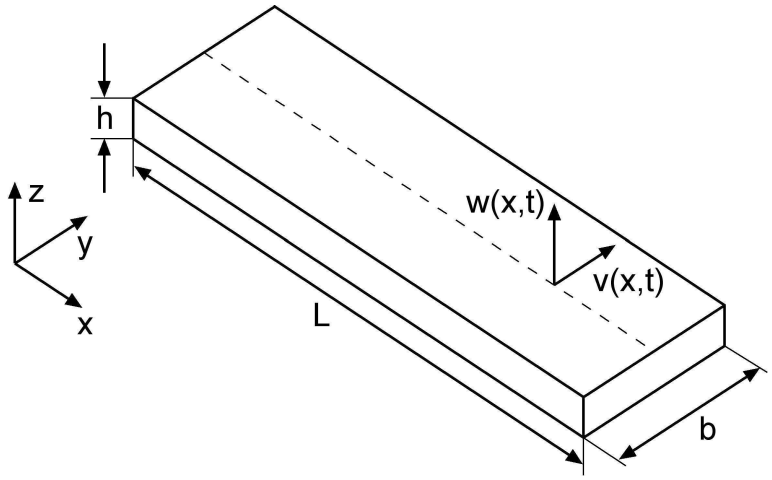

Figure 3.1: Schematic of cantilever beam with length L, width b, and thickness h.

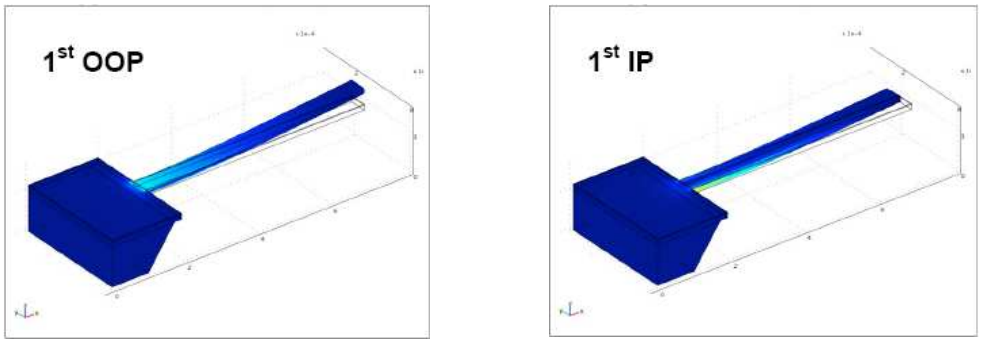

Figure 3.2: FEM simulation of fundamental out-of-plane (1st OOP) and fundamental in-plane (1st IP) vibration mode of a 600 µm long silicon cantilever. The colors correspond to the y-directed stress distribution in the beam as it deflects.

Two parameters of particular interest when examining resonator designs or resonant modes for operation in liquid are the quality factor (Q) and the amount of mass added to the device by the fluid as the cantilever vibrates. The quality factor is a measure of the ratio of the energy stored by a vibrating structure to that of the energy lost by the structure over one cycle of oscillation, and can be written as:

$$Q = 2\pi \frac{E_{stored}}{E_{diss}} = \frac{f}{\Delta f} \tag{3.1}$$

In Equation 3.1, E_{stored} is the energy stored by the resonant structure, and E_{diss} is the energy dissipated over the course of a single cycle. In the alternative form displayed in

Equation 3.1, f is the resonant frequency of the structure and Δf is the bandwidth of the resonant peak. Δf is defined by the full width at half maximum (the frequency difference between the -3dB points on each side of the peak). Q increases as dissipation decreases, or in other words by decreasing the amount of energy loss by damping mechanisms such as the viscous loss to the surrounding fluid. Through the course of this study, it was found that utilizing the in-plane mode leads to lower viscous loss because of a lower amount of fluid damping.

In addition, and equally important from a sensor design perspective, use of the in-plane flexural mode induces less mass-loading from the surrounding fluid, improving the mass-sensitivity of the device because the effective starting mass of the cantilever is lower. In the following, the basic governing equations for the operation of cantilever beams with a uniform cross-section will be reviewed for the case of both out-of-plane and in-plane flexural mode vibration.

3.1 Operation of Out-of-Plane Mode Cantilevers in a Viscous Fluid

There have been both theoretical [113] and experimental [24, 114] investigations of the operation of cantilevers excited in one of their flexural out-of-plane modes in liquid for the implementation of biochemical sensors. A brief review of this work is presented before in-plane mode operation is introduced.

The flexural vibrations of a cantilever beam in vacuum can be described using the 1-D Euler-Bernoulli equation [115]:

$$E_{eff} I \frac{\partial^4 w(x,t)}{\partial x^4} + \rho_{eff} A \frac{\partial^2 w(x,t)}{\partial t^2} = F(x,t) \qquad (3.2)$$

In Equation 3.2 E_{eff} is beam's (effective) Young's Modulus, I the beam's moment of

inertia, $w(x,t)$ is the vibration amplitude of the beam, ρ_{eff} is the beam's (effective) density, A is the beam's cross-sectional area, and $F(x,t)$ is the driving force used to excite the beam. It should be noted that Equation 3.2 does not include any damping term and that the beam is subject to pure bending. In solving Equation 3.2, the effective Young's modulus and density are used because the beams studied here are composite structures of silicon and dielectric layers (see Chapter 4). The additional dielectric layers need to be considered when calculating the (effective) material properties. Assuming a beam with uniform rectangular cross-section (i.e. $I = b \cdot h^3/12$), the characteristic resonance frequencies of the vibrating structure can be found by solving the homogeneous part of Equation 3.2 (i.e., right hand side is equal to zero) [115], yielding

$$\omega_i = \frac{\lambda_i^2}{\sqrt{12}} \frac{h}{L^2} \sqrt{\frac{E_{eff}}{\rho_{eff}}} , \qquad (3.3)$$

where h is the thickness of the beam, L is the beam's length, E_{eff} is the effective Young's modulus of the beam, and ρ_{eff} is the effective density of the beam. The mode coefficient λ_i of the i-th flexural mode depends on the boundary conditions; for an ideal clamped-free beam, one finds $\lambda_1 = 1.875$, $\lambda_2 = 4.694$, and $\lambda_3 = 7.855$ [115].

As mentioned earlier, Equation 3.2 does not consider damping or any mass loading by the surrounding fluid. When the vibrating cantilever moves through the fluid, the fluid offers resistance to the motion of the beam, which can be described by an external force acting on the cantilever [113]. This fluidic force (per unit length) F_{fluid} is generally considered to have a damping term proportional to the beam's velocity (associated with the viscous losses) and an inertial part proportional to the beam's acceleration (associated with fluid mass accelerated by the moving beam):

$$F_{fluid} = -c_f \frac{\partial w(x,t)}{\partial t} - m_f \frac{\partial^2 w(x,t)}{\partial t^2}\,, \qquad (3.4)$$

In Equation 3.4, c_f denotes the (frequency-dependent) fluid damping coefficient and m_f the (frequency-dependent) added fluid mass per unit length of the beam.

To account for the fluidic effects, this fluidic force must be included in Equation 3.2, yielding:

$$E_{eff} I \frac{\partial^4 w(x,t)}{\partial x^4} + c_f \frac{\partial w(x,t)}{\partial t} + (\rho_{eff} A + m_f) \frac{\partial^2 w(x,t)}{\partial t^2} = F(x,t) \qquad (3.5)$$

It should be noted that Equation 3.5 assumes that the viscous damping by the surrounding fluid is the only (or the dominating) damping effect, which is generally the case in liquids but not necessarily in air, where e.g. anchor losses can play an important role as well. Considering that fluid damping is the dominant damping effect, the resonance frequency for a cantilever operating in its (fundamental) out-of-plane mode can be expressed as [24]:

$$\omega_{fluid} = \omega_0 \frac{1}{\sqrt{1 + \left[\frac{L\, m_f}{m}\right]}} \sqrt{1 - \frac{1}{2\, Q_{fluid}^2}} \qquad (3.6)$$

ω_0 is the resonance frequency of the beam without any fluid loading (i.e. in vacuum), L and $m = \rho_{eff} \cdot A \cdot L$ are the length and mass of the cantilever, respectively. Q_{fluid} is the quality factor of the cantilever in the fluid, and can be expressed as [24]:

$$Q_{fluid} = \frac{\omega_0 \sqrt{1 + (L m_f / m)}}{L c_f / m} \qquad (3.7)$$

Considering that the most suitable cantilevers for liquid operation have Q_{fluid} > 10, the

effect of the Q-factor on the resonance frequency (see Equation 3.6) is minimal and the frequency change will be dominated by the added mass term m_f. Thus m_f should be minimized, which is achieved in this work by operating the cantilevers in an in-plane flexural mode. On the other hand, the fluid contribution to the quality factor Q_{fluid} is maximized by minimizing the fluid damping coefficient c_f, which again is achieved in this work by operating the cantilevers in an in-plane flexural mode.

It should be noted that Q_{fluid} is the fluid contribution to the quality factor; if the cantilever beam has an intrinsic Q-factor Q_{in} when operated in vacuum, the measured Q-factor Q_{total} in the fluid will be

$$\frac{1}{Q_{total}} = \frac{1}{Q_{in}} + \frac{1}{Q_{fluid}} \qquad (3.8)$$

The fluid-damping term (c_f) and added-mass term (m_f) per unit length, for a cantilever operated in the out-of-plane mode are[24]:

$$c_f = \pi \eta \,\mathrm{Re}\, \Gamma_i(\mathrm{Re}) \qquad (3.9)$$

$$m_f = \frac{\pi \eta \,\mathrm{Re}}{\omega_o} \Gamma_r(\mathrm{Re}) \qquad (3.10)$$

As above, ω_o is the beam's vibration frequency in vacuum, Re is the Reynolds number, η is the fluid viscosity, and Γ_r, Γ_i are the real and imaginary parts of the hydrodynamic function, which is used to correlate the beam deflection and the resulting force on the beam from the surrounding fluid [113]. The hydrodynamic function is different for beams of different geometries and a detailed discussion of it can be found in [113]. The hydrodynamic function exhibits the following asymptotic behavior for beams of rectangular cross section, in case of Re approaching 0 or infinity [113]:

$$\Gamma(\omega) = 1 \qquad \text{as the Reynolds number approaches 0} \qquad (3.11)$$

$$\Gamma(\omega) = \frac{-4i}{Re\ln(-i\sqrt{Re})} \qquad \text{as the Reynolds number approaches infinity}$$

The Reynolds number Re of a beam vibrating at a frequency ω in a fluid of density ρ_f is given by

$$\mathrm{Re} = \frac{\rho_f\, b^2\, \omega}{4\,\eta}. \qquad (3.12)$$

The above models assume that the beam's length is at least five times greater than its width and that the deflection during vibration is much smaller than any of the beam dimensions. In other words, simple beam bending is assumed and shear forces and rotational effects are neglected.

3.2 Operation of In-Plane Mode Cantilevers in a Viscous Fluid

In the most general sense, one can think of in-plane mode operation as the same as out-of-plane vibration but with the cantilever's width (b) swapped with its thickness (h). In fact, directly swapping these quantities in Equation 3.3 will yield the correct resonant frequencies for in-plane operation (in vacuum)

$$\omega_i = \frac{\lambda_i^2}{\sqrt{12}}\,\frac{b}{L^2}\sqrt{\frac{E_{eff}}{\rho_{eff}}}, \qquad (3.13)$$

as long as L >> b, i.e. the conditions for pure beam bending are fulfilled. While a theoretical understanding of the dependence of ω and Q in case of transverse beam bending in fluid is provided by the work of Sader [113] (see Chapter 3.1), that model is not applicable to in-plane flexural vibrations.

However, the general approach followed when investigating the out-of-plane

flexural vibration of the beam is also applicable for in-plane flexural vibration, i.e. the vibrating beam is subject to a fluidic force that has two components, one being proportional to beam velocity, the other being proportional to beam acceleration. Thus, similar to Equation 3.5, a differential equation can be established for the in-plane deflection of the cantilever beam [116]:

$$E_{eff} I \frac{\partial^4 v(x,t)}{\partial x^4} + c_f \frac{\partial v(x,t)}{\partial t} + (\rho_{eff} A + m_f) \frac{\partial^2 v(x,t)}{\partial t^2} = F(x,t) \qquad (3.14)$$

In Equation 3.14, $v(x,t)$ now represents the in-plane deflection of the beam, and c_f and m_f denotes the (frequency-dependent) fluid damping coefficient and the added fluid mass per unit length of the beam vibrating in plane. Assuming that the fluid resistance under in-plane vibration is due solely to shear stresses and that those shear stresses are given by Stoke's classical solution for an oscillating infinite plate, the fluid properties are given by [116]:

$$m_f = \frac{\sqrt{2\eta\rho_f b^2}}{\sqrt{\omega}} \qquad (3.15)$$

$$c_f = \sqrt{2\eta\rho_f b^2}\sqrt{\omega} \qquad (3.16)$$

In equations 3.15 and 3.16, η is the viscosity of the fluid, ρ_f is the density of the fluid, b is the width of the beam, and ω is the frequency of the beam's vibration. Thus, c_f increases with the square-root of frequency, while m_f decreases with the square-root of frequency. Experimental evidence for both of these trends will be presented later (see Chapter 5).

Assuming that the beam's vibration mode in the fluid can be approximated by the vibration mode in vacuum and assuming a harmonic tip force as the excitation force,

Heinrich et al. [116] have derived a simple equation for the quality factor of the fundamental in-plane resonance mode:

$$Q \approx 0.7124 \left[\frac{E_{eff}\, \rho_{eff}^3}{\eta^2 \rho_f^2} \right]^{1/4} \frac{h\sqrt{b}}{L} \qquad (3.17)$$

Equation 3.17 indicates that Q increases proportional to $b^{0.5}/L$, i.e. proportional to the square-root of the in-plane resonance frequency (see Equation 3.17). Moreover, Q increases with increasing beam thickness h because of the increased beam inertia. Again, Equation 3.17 represent the Q due to fluid damping only; the experimental data will show that this is a good approximation in liquid, while in air at least the anchor loss must be considered as well. The model used to derive Equation 3.17 has subsequently been refined [116] by accounting for a more realistic excitation force; the resulting Q-factor, however, closely matches the values obtained from Equation 3.17.

3.3 Figures of Merit for Resonant Biochemical Microsensors

The ultimate performance metric for any (bio)chemical sensor is its limit of detection (LOD), i.e. the smallest detectable analyte concentration. In the case of a resonant (mass-sensitive) biochemical sensor, the limit of detection (LOD) (in ppm) of a is generally defined as three times the noise-equivalent analyte concentration, which itself is given by the ratio of the short-term frequency stability Δf_{min} (in Hz), determined e.g. via the Allan variance method [117], and the chemical sensor sensitivity S (in Hz/ppm):

$$LOD = 3\frac{\Delta f_{\min}}{S}, \qquad (3.18)$$

Alternatively, the LOD might be expressed as three times the ratio of the relative

frequency stability σ_{min} to the relative chemical sensor sensitivity S_R:

$$LOD = 3\frac{\sigma_{min}}{S_R} = 3\frac{\Delta f_{min} / f}{S / f}\ , \tag{3.19}$$

As described in [86], the chemical sensitivity S (or relative chemical sensitivity S_R) may be written as the product of the gravimetric sensitivity G (or the relative gravimetric sensitivity G_R) of the coated resonant sensor, i.e., the absolute or relative change in frequency f due to a change in coating density ρ_m, and the analyte sensitivity S_A, i.e., the change in coating density ρ_m due to a change in analyte concentration c_A in the surrounding medium:

$$S = G \cdot S_A = \frac{\partial f}{\partial \rho_m}\frac{\partial \rho_m}{\partial c_A},\ S_R = G_R \cdot S_A = \left(\frac{1}{f}\frac{\partial f}{\partial \rho_m}\right)\frac{\partial \rho_m}{\partial c_A}, \tag{3.20}$$

If the analyte concentration in the surrounding liquid is given in ppm (v/v), the analyte sensitivity S_A may be calculated as

$$S_A = \frac{\partial \rho_L}{\partial c_A} = \rho_A \cdot K \cdot 10^{-6}\ , \tag{3.21}$$

where ρ_A is the density of the analyte absorbed into the sensitive layer, and K is the partition coefficient of the particular analyte/membrane combination, i.e., the ratio of the analyte concentration in the sensitive film to the analyte concentration in the surrounding matrix. The factor 10^{-6} accounts for the fact that c_A is given in ppm.

The sensor's limit of detection given in Equation 3.18 is particularly affected by the geometrical dependence of the minimal detectable frequency change Δf_{min}. Δf_{min} is generally improved (i.e., reduced) by increasing the quality factor of the resonance, which is the main motivation behind investigating in-plane rather than out-of-plane

cantilever modes. In addition, as stated earlier, utilizing the in-plane mode (in comparison to the fundamental out-of-plane mode) gives much lower mass-loading due to the surrounding fluid, which helps to reduce the cantilever's starting mass and thus improves its gravimetric sensitivity [23].

The use of the cantilever's in-plane flexural mode reduces the resistance of the surrounding fluid to that associated with shear stresses at the cantilever-fluid interface along the direction of motion [118]. Advantageously, the drop in resonant frequency upon immersion into liquid, and thus, the drop in the gravimetric sensitivity due to the surrounding fluid are greatly reduced, as the effective mass of the accelerated fluid is much smaller during in-plane flexural vibrations. Immersion of the devices tested in this work into liquid results only in a 5-10% reduction in resonant frequency, while for cantilevers operated in out-of-plane bending modes 30-50% frequency shifts are typically observed [24]. Due to the smaller accelerated fluid mass, the starting mass of the cantilever is reduced in the case of in-plane mode operation in water, thus increasing the gravimetric sensitivity of the device. In addition, the decreased damping associated with the in-plane flexural modes results in quality factors that are up to five times larger than those reported for devices operated in out-of-plane modes in liquid. In fact, for in-plane mode cantilevers quality factors as high as 86 have been measured in fluid. As will be shown (see Chapters 5 and 6), the combination of lower damping and less added fluid mass yields an improved limit of detection for liquid-phase cantilever-based chemical sensors operating in in-plane flexural modes.

3.4 Design of Actuation and Detection Schemes for In-Plane Mode Operation

Thermal actuation and piezoresistive detection were chosen for exciting the first in-plane flexural mode of single crystal silicon cantilevers. Thermal actuation and piezoresistive detection both rely on resistors as transducer elements, which are straightforward to integrate with the proposed silicon-based bulk-micromachining process. Moreover, thermal excitation produces relatively large actuation forces, which is advantageous especially in a liquid environment. In order to reject common mode signals and also possible signals from unwanted modes, the piezoresistors are arranged in a Wheatstone bridge configuration.

Figure 3.3 shows the layout of the excitation and Wheatstone bridge resistors as well as the simulated bending stress component σ_y (in the length direction of the cantilever) for the first out-of-plane and the first in-plane bending mode. It should be noted that, for both modes, σ_y is the dominant stress component. The implemented Wheatstone bridge has a U shape, with piezoresistors 1 and 4 experiencing —to first order— a longitudinal stress, while piezoresistors 2 and 3 are subject to a transverse stress. Using the longitudinal and transverse piezoresistive coefficients π_l and π_t, respectively, one finds:

$$\frac{\Delta R}{R}\Big|_{1,4} \approx \pi_l \sigma_y \quad \frac{\Delta R}{R}\Big|_{2,3} \approx \pi_t \sigma_y \qquad (3.22)$$

Considering that the piezoresistors are p-type (implemented by boron diffusion) and arranged parallel/perpendicular to the <110> crystal direction of the (100) wafer, π_l and π_t have similar magnitude but opposite signs [96]. Figure 3.3 shows the resulting signs of the resistance changes in the Wheatstone bridge (the resistance change of resistor 1 is assumed to be positive) for both the in-plane and out-of-plane mode; from these

considerations, it becomes clear that the stress distribution characteristic for the fundamental in-plane mode will result in an output signal of the Wheatstone bridge, while the stress distribution associated with the fundamental out-of-plane mode –to a first order– yields no output signal, i.e. the detection of this mode is suppressed. This is essential for the proper operation of the cantilevers presented in this work: as will be shown in Chapter 6, the cantilevers are operated in an amplifying feedback loop, and proper locking to the in-plane mode requires that this mode generates the strongest piezoresistive output signal.

For excitation, the heating resistors are placed at the high stress region near the clamped-edge of the cantilever. The excitation resistors are driven with a DC voltage superimposed on an AC voltage to prevent frequency doubling. The most efficient excitation occurs when a single resistor is used.

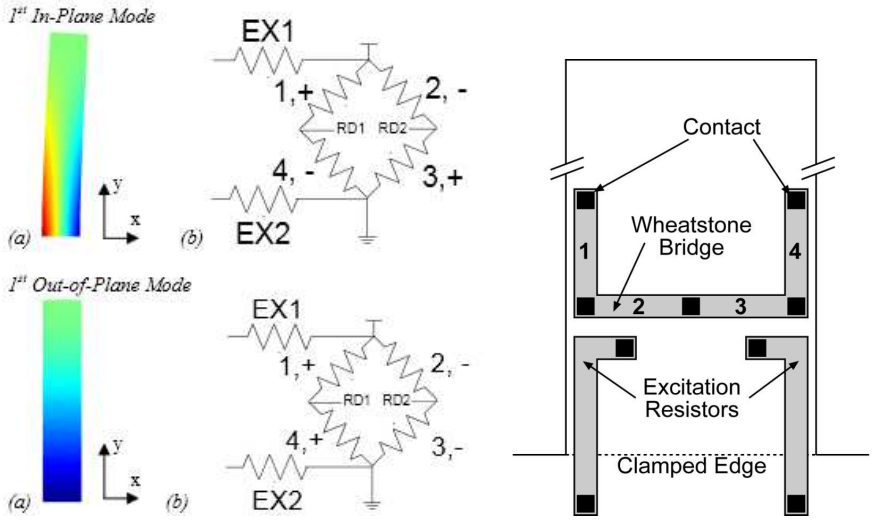

Figure 3.3: (Left) Simulated longitudinal stress components for both the 1st in-plane and 1st out-of-plane flexural modes along with the signs of the resistance changes for each resistor in the Wheatstone bridge. (Right) Schematic of the Wheatstone bridge resistor and the heating resistor layout.

In total, twenty different cantilever geometries with lengths ranging from 200 to

1000µm and widths ranging from 45 to 90µm were designed (Figure 3.5(a)). The resulting in-plane mode resonance frequencies range from 50 kHz to 2.2 MHz (in air). Open-loop frequency transfer characteristics were recorded (see also Chapter 5) to determine if the excitation scheme was working properly. As an example, Figure 3.4 shows the open-loop frequency response for a 600 µm long and 45 µm wide cantilever in air.

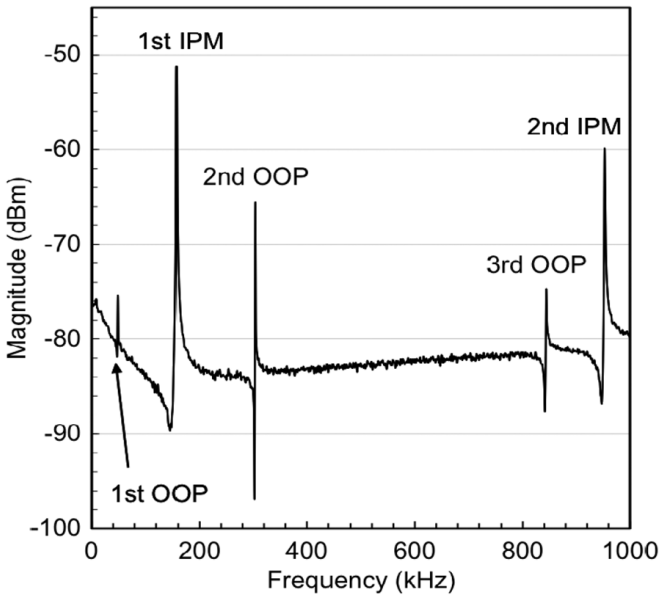

Figure 3.4: Piezoresistive output signal of a 45µm wide, 600µm long and 12µm thick cantilever in air as a function of the frequency.

The resonance modes were identified with accompanying finite-element method (FEM) simulations, and as expected from the bridge design, the first in-plane resonance at 157 kHz yields the strongest piezoresistive output signal. When placed in an amplifying feedback loop, the cantilever is excited at this mode. Short-term frequency stability measurements based on the Allan variance method yield values in the 10^{-8} range in air and 10^{-6} range in water.

Besides simple rectangular cantilever structures, a new “hanmerhead” structure (Figure 3.5(b)) has been implemented in the mask design. The hammerheads have a clamped-free beam support, which is attached to a larger “wing” structure. Initially, it was thought that this “wing” would provide a larger area for mass binding, thus increasing the sensitivity of the resonant sensor. As will be discussed in Chapter 5, this is in fact not the case because it can be shown that the normalized gravimetric sensitivity of the fundamental in-plane mode only depends on the device thickness (and the layer stack), but is independent of the lateral beam geometry (see Chapter 5). Hammerheads behave as a simple cantilever beam with a mass at the end, thus the stress distribution for the fundamental in-plane mode is very similar to that of a cantilever. The designed hammerhead structures have an anchor beam that is 45 μm wide, and the same resistor layout was used as for the standard 45 μm wide cantilevers.

(a) 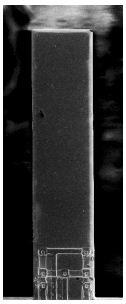 (b) 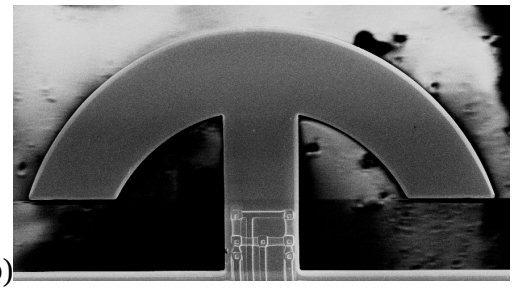

Figure 3.5: SEM micrographs of (a) a 45 wide, 200μm long cantilever and (b) a hammerhead device with a 45μm wide and 100μm long support cantilever and a circular wing with a radius of 150μm. The piezoresistive Wheatstone bridge and thermal excitation resistors can be seen at the base of each device.

In addition to the hammerheads, tuning fork structures with integrated thermal excitation and piezoresistive detection were designed. Tuning forks have been previously used in quartz resonators [50, 119] and also in MEMS-based force and inertial sensors

[120-122]. Figure 3.6 displays simulated mode shapes of the desired tuning fork mode (where the tines vibrate against each other out of phase), as well the lowest-frequency out-of-plane and torsional modes of the structure.

As is evidenced by Figure 3.6, the tuning forks have a different stress distribution compared to the simple cantilevers, and thus require a different heating resistor and Wheatstone bridge layout in order to excite/detect the tuning fork mode and suppress as much as possible all other vibration modes. Figures 3.7 and 3.8 show the resistor layout for the tuning fork structure and also the electrical connections for those resistors. In addition, Figure 3.8 depicts the signs of the resistance changes that will be obtained for the tuning fork mode and the first torsional mode (the signs of the resistance changes can be determined by examining the FEM simulations in Figure 3.6, similar to the case of the simple cantilevers explained earlier). As before, Figure 3.8 assumes that resistor 1 sees a positive change in resistance. Again, the particular Wheatstone bridge layout ensures a strong output signal for the tuning fork mode, but e.g. ideally no signal for the first torsional mode. It should be noted that all piezoresistors in the tuning fork design primarily exhibit longitudinal stresses.

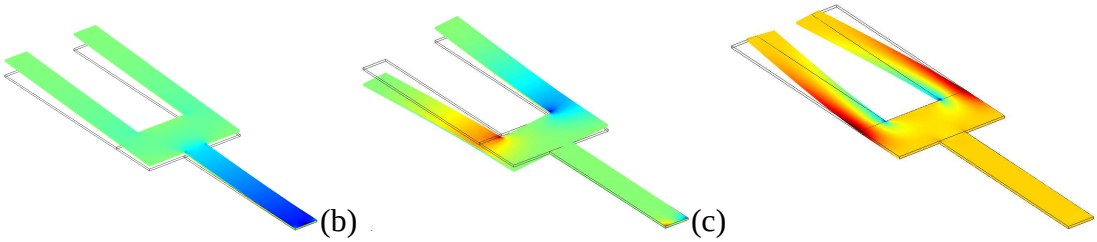

Figure 3.6: Simulated stress distribution in the length direction and mode shape for a tuning fork operated at (a) the first out-of-plane, (b) the first torsional mode shape, and (c) the desired tuning fork mode. The simulations were done using COMSOL. The colors correspond to the y-directed stress distribution in the structure.

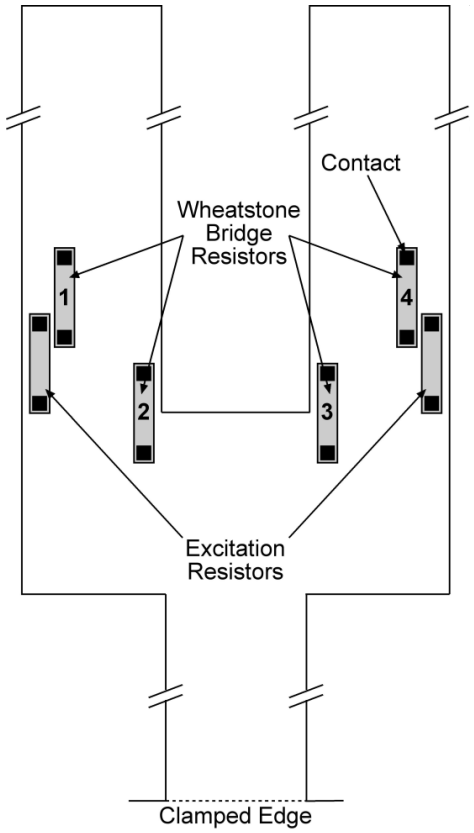

Figure 3.7: Layout of the piezoresistors and the excitation resistors in order to excite the tuning fork mode.

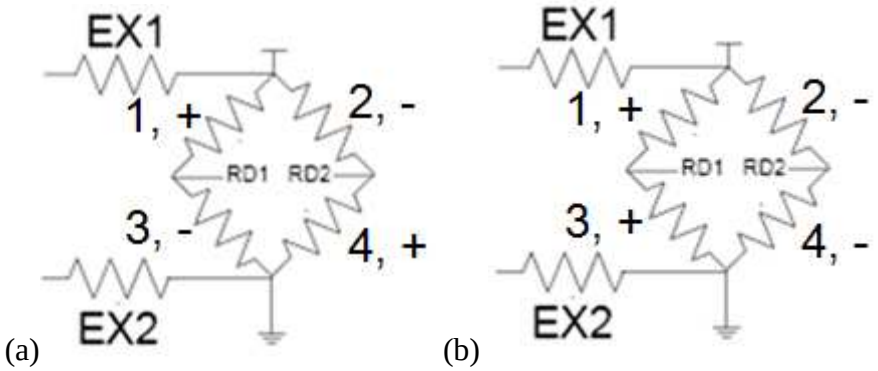

Figure 3.8: Signs of the resistance change in the piezoresistors for (a) the tuning fork mode and (b) the torsional mode of the tuning fork structure.

Examining the signs in the resistance changes from Figure 3.8, the tuning fork mode is the only mode that will produce a measureable output. The Wheatstone bridge resistors are also arranged so that the thermal signal from the excitation resistors will not give a

measureable output.

3.5 Layout Considerations

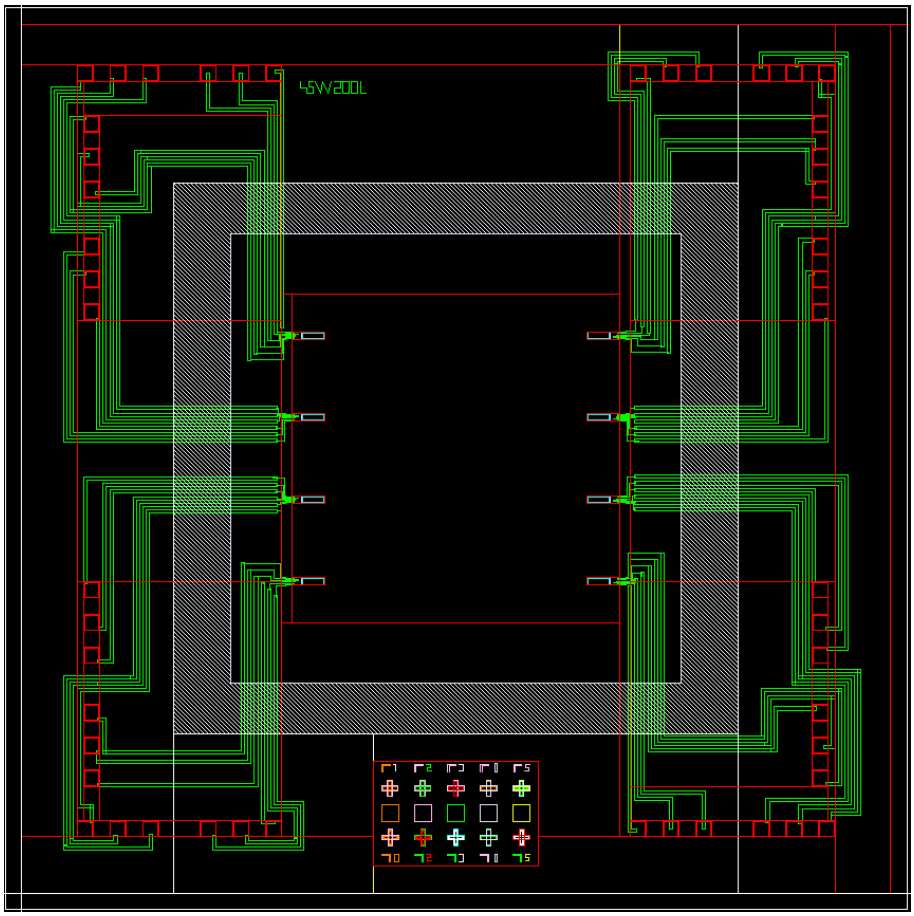

Figure 3.9: Sample die layout for the cantilever resonators. The aluminum lines are shown in green. The large white rectangular area is used for the on-chip packaging process, which will be discussed in Chapter 6.

The cantilever designs were drawn using Cadence (Cadence Design Systems, Berkshire, UK). The die size was approximately 5.5mm by 5.5mm, with a bulk-micromachined membrane size of 2mm by 2mm. Each die contains eight cantilevers. A sample die layout for the cantilever resonators is presented in Figure 3.9. To ensure that the layout was compatible with the in-house fabrication facilities, resistors were drawn to be at least 4μm from the edge of the beams. In addition, since the aluminum metallization

lines were to be wet etched (i.e., an isotropic etching step), the lines were drawn to be at least 4μm wide (the metal lines are roughly 0.6-0.7 μm thick). For most of the distance from the bond pads to the Wheatstone bridge, the metal lines were drawn with a 20 μm width to minimize their resistivity. On each resistor, at least 0.5μm was left between the contact opening and the edge of the diffusion opening (see Chapter 4) to account for alignment inaccuracy. For the same reason, the metal on the contact was drawn at least 0.5 μm wider than the contact itself. The resistors were drawn with a length to width ratio of 4 (at a maximum) to ensure that the fabricated resistors would not have too high of a resistance.

CHAPTER 4

IN-PLANE CANTILEVER FABRICATION AND PACKAGING

The in-plane mode cantilevers were fabricated using a bulk-micromachining fabrication process. Bulk-micromachining has the advantages in terms of reliability when compared to surface micromachining. Since the entire wafer is etched during a bulk micromachining process, there are no small gaps between the beams and the substrate, which can cause stiction or other problems. Bulk-micromachining also allows for the use of lower cost substrates if epitaxial wafers are used (compared to i.e. SOI wafers). In addition, for liquid-phase packaging and testing, the bulk-micromachined opening allows liquids to be routed through the entire die (vertically), minimizing the trapping of air bubbles. This helps to ensure that the cantilevers are fully immersed during testing. If a cantilever is not fully immersed, inaccurate quality factors will be measured and the device can fail to give a stable frequency during closed-loop testing.

The in-plane cantilevers are fabricated using a 7-mask bulk micromachining process that uses epitaxial silicon wafers as the starting material. The cantilever fabrication begins with the diffusion of resistors for the piezoresistive Wheatstone bridge and for thermal excitation. Subsequently, contacts are made to the resistors and a metal layer is patterned, etched, and passivated; creating electrical connections to the resistors. Finally, the bulk-micromachining step defines a membrane of fixed thickness dictated by the thickness of the epitaxial layer on the wafer's surface. Potassium hydroxide (KOH) is used for etching and an electrochemical etch stop technique stops the KOH etch at the p-n junction between the epitaxial layer and the p-type substrate. After etching of the

membrane, the cantilevers themselves are defined by ICP (inductively coupled plasma) etching the membrane using the BOSCH process. Figure 4.1(a),(b) below presents an image of the cantilever die and also a cross-section of the die. The second cross-section is the cross-section used to illustrate the fabrication process in Section 4.1.

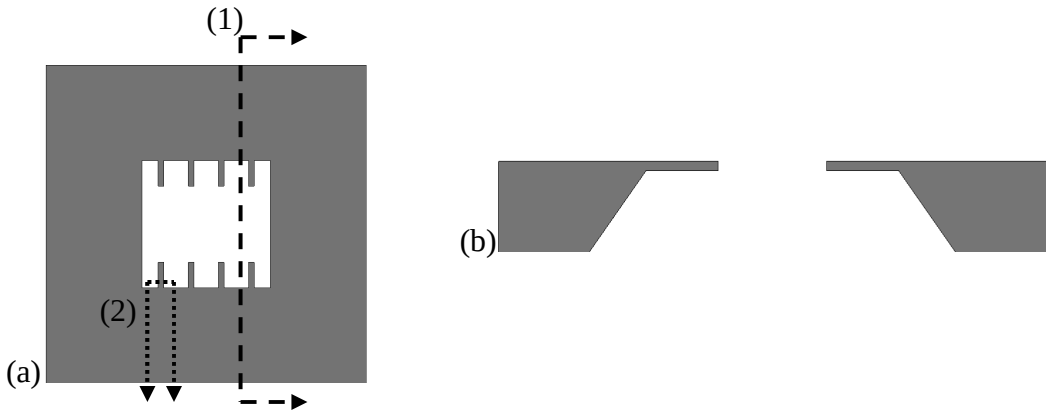

Figure 4.1: Top view of the cantilever die (a), cross-section of the cantilever die (b). The cross-section shown in (b) is the cross-section taken at (1). The cross-sections shown with the fabrication process in Section 4.1 are taken at (2).

4.1 Cantilever Fabrication Process

This section summarizes the major steps in the cantilever fabrication process (A detailed process flow can be found in Appendix 3). The process shown below is similar to the one presented in [103]. The fabrication is done on 525 µm thick, 100-mm p-type silicon wafers, which have an n-type epitaxial layer grown on their surface with a thickness between 5-20 µm. The epi-layer thickness ultimately defines the thickness of the cantilevers. The cross-sections shown are roughly taken across the width of the cantilever (at its base) and are not drawn to scale.

1. Start with a 525 µm thick p-type prime wafer with an n-type epitaxial layer
2. Grow 1 µm of thermal oxide using a wet oxidation process.

3. Pattern and etch diffusion openings. This step defines the piezoresistors.

Figure4.2(a): Cross-section showing the diffusion mask with the silicon shown in gray and the oxide shown in purple.

4. Diffuse piezoresistors and excitation resistors from solid boron sources. The target resistance of the completed resistors in the 500-1000 Ohm range.

Figure 4.2(b): Cross-section showing the diffused resistors the diffused areas are shown in brown.

5. Spin coat photoresist on the wafer backside, dip the wafer in BOE for 4 minutes to partially strip the doping oxide. (Photoresist on the backside preserves the high quality thermal oxide for use in the KOH etch mask.)

6. The piezoresistors are driven-in, and a thermal oxide is simultaneously grown over the resistors to passivate them. The oxide thickness is approximately 1500 A.

Figure4.2(c): Cross-section showing the resistors after drive-in and growing of a thermal oxide over the diffused regions. The oxide over the resistors is pictured in blue.

7. Pattern and etch contact openings through the passivation oxide, which covers the piezoresistors.

Figure4.2(d): Cross-section depicting the opening of contacts to the diffused resistors.

8. Clean the wafer using Pirhana etch and perform a BOE dip prior to metallization.

9. Evaporate 750 nm of aluminum onto the wafer.

10. Pattern and wet etch the aluminum to create metal lines.

Figure4.2(e): Cross-section depicting the cantilevers after the metallization step. The aluminum is shown in silver.

11. Sinter the wafer for 2.5 hours at 450 C. This step creates an alloy of aluminum and silicon, lowering the contact resistance.

12. Measure the contact resistance using a probe station. The contact resistance for 4x4 µm contacts should be in the 10-20 Ohm range. Test structures (Van der Pore structures) are placed on the wafer, which allow the contact resistance to be measured.

13. Passivate the metal lines using alternating silicon nitride and silicon dioxide layers. The oxide is deposited using a pulsed plasma enhanced chemical vapor deposition (PECVD) process in order minimize pinhole formation. The two films have opposite signs of residual stress and are alternated to minimize the induced stress on the wafer.

14. Deposit 1 µm of low-stress PECVD silicon dioxide on wafer backside.

15. Deposit 0.4 µm of low-stress PECVD silicon nitride on wafer backside, rotate wafer, deposit 0.6 µm of low-stress PECVD silicon nitride on wafer backside. The wafer rotation is done to partially mitigate the effects of pinholes.

Figure4.2(f): Cross-section showing the wafer after PECVD passivation on the topside (pink) and deposition of a PECVD KOH etch mask on the backside (green).

16. Pattern and etch KOH etch windows through the backside protection layers.

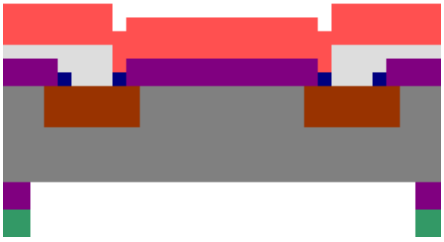

Figure4.2(g): Cross-section showing the wafer after etching openings in the PECVD etch mask on the wafer backside.

17. Pattern and etch the topside passivation layer. This opens both the bond pads and the membrane release openings.

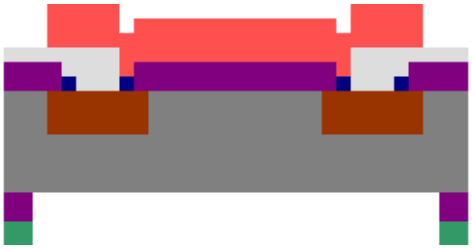

Figure4.2(h): Cross-section showing the wafer after etching the PECVD passivation off of the bond-pads on the wafer topside.

18. Pattern photoresist for a gold liftoff step, then deposit and liftoff gold (500 A). This creates a patterned surface for bio-functionalization. The gold is left as thin as possible because its added mass reduces the resonators mass-sensitivity.

Figure4.2(i): Cross-section depicting the result of the gold-liftoff step with the gold shown in gold.

19. KOH etch the wafer for 10 hours at 75 ˚C. Use an electrochemical etch-stop technique to stop the etching at the p-n junction between the n-type epitaxial layer and the p-type substrate.

Figure4.2(j): Cross-section showing the wafer after KOH etching from the backside.

20. Pattern and release cantilevers from the membrane using the BOSCH process (not shown in cross section).

21. Clean wafer thoroughly, and dice into individual dies.

Examples of the fabricated devices are shown in Figure 4.3.

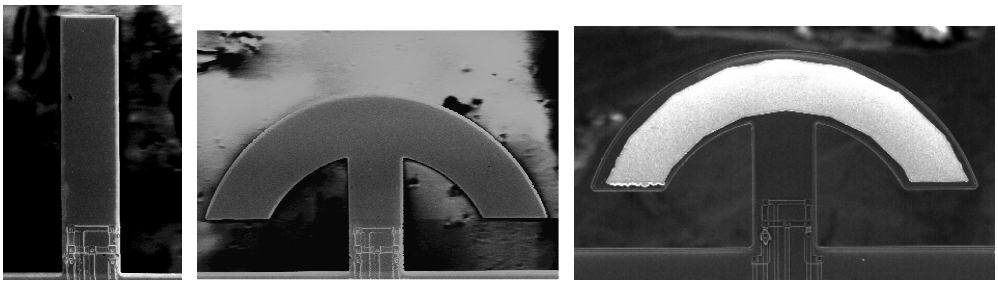

Figure 4.3: SEM image of a fabricated 45 μm Wide by 200 μm long cantilever (left). SEM image of a fabricated Small F150 hammerhead (middle) and a small F150 hammerhead with gold (right).The Wheatstone bridge and excitation resistors are visible at the base of each device.

For the process above to work properly a few precautions must be taken during key steps. First, for the etching of the diffusion openings, over-etching of about 15% is required to ensure that diffusion openings are actually etched through the oxide everywhere on the wafer surface. Second, for the contact openings, over-etching is also required. Since these openings are smaller, on the order of 4μm by 4μm, a long over-etch is required to ensure that good contacts are obtained (again, to ensure that the oxide is etched to the silicon over the entire wafer surface). The total etch time for the contact opening step is on the order of three times the etch time one would calculate based solely on the silicon dioxide etch rate. Third, for the KOH etch mask, the residual stress in the masking material and the pinholes in the film are extremely important. Too much stress can lead to film cracking allowing for KOH to reach the areas of the wafer that are supposed to remain untouched. Pinholes can have the same effect. To alleviate the effect of pinholes, double the amount of silicon nitride was deposited than was actually needed based on the KOH etch rate of silicon nitride. The nitride deposition was preformed in two steps, with the wafer rotated 90 degrees in between steps, in order to prevent pinholes from extending all the way through the film. In addition, the initial thermal oxide layer was kept on the back of the wafer, instead of being partially etched during the BOE dip after doping. The thermal oxide provides a smoother surface (than the unpolished wafer backside) on which to deposit the PECVD layers. Finally, the PECVD oxide layer was chosen and its thickness determined so that it cancels the stress induced by the silicon nitride layer. A method to choose appropriate PECVD films and film thicknesses to get as little stress as possible is described in Section 4.4.2.

A final note is that the cantilevers are actually thicker than the epitaxial layer thickness. For example, wafers with a target epitaxial layer thickness of 5 μm (based on the vendor specification) yield cantilevers that are between 7.5 and 8.5 μm's thick. It is thought that this effect is partly due to the depletion region that exists at the p-n junction between the p-type substrate and the n-type epi-layer. The epi-layer has a resistivity of roughly 1 ohm-cm and the substrate has a resistivity of 10-20 ohm-cm. The dopant concentration can be determined from resistivity vs. dopant concentration data. The width of the depletion region is given by [123]:

$$W_d = \sqrt{\frac{2\varepsilon_{si}(N_a + N_d)\psi_m}{qN_aN_d}} \qquad (4.1)$$

Where ε_{si} is the permittivity of silicon, N_a is the concentration of acceptor atoms, N_d is the concentration of donor atoms, q is the fundamental charge, and ψ_m is the total potential drop across the p-n junction at the epi-layer/substrate interface.

Using equation 4.1, N_a equal to 10^{15} cm^{-3}, N_d equal to $4.86*10^{15}$ cm^{-3}, and a built in voltage of .738 V, and a 1.8 V bias (this is the bias used for electrochemical etch stop), the depletion region width is roughly 2 μm's. The depletion region will lie mostly in the lower doped region, or in this case the P-type wafer. Since the dopant concentrations have a ratio of roughly 5:1, the depletion region width is approximately 1.66 μm in the p-type wafer. The extra thickness of the beams can also be partly attributed to the tolerance in the epitaxial layer thickness (the tolerance is +-.5 μm for a 5 μm thick epi-layer); and a possible slowing of the KOH etching as it reaches the depletion region (the depletion region does not have a sharp boundary as is approximated by using equation 4.1). It should also be noted that the thicker epi-layers have a larger

tolerance on the epi-thickness, i.e. +- 1-2 μm for the 10 μm wafers.

Table 4.1 summarizes the structures that were fabricated using the cantilever process, and also the range of dimensions that were fabricated for each structure.

Table 4.1: Summary of the different in-plane cantilever geometries that were fabricated along with relevant dimensions.

Device Name	**Basic Layout**	**Fabricated Dimensions**
Cantilever	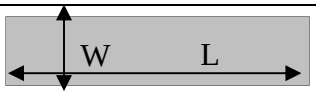	Length: 200-1000 μm Width: 45-90 μm Thickness: 5-20 μm
Tuning Fork	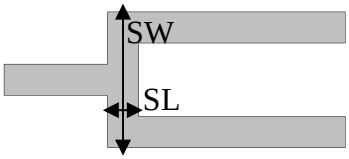	SW: 185 μm, 250 μm SL: 60um Anchor Beam: 60 μm X 200 μm, 60 μm X 400 μm Tines: 60 μm X 400 μm Thickness: 5-20 μm
Hammerhead	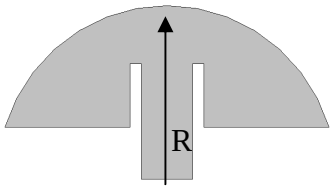	Radius: 150 μm, 200 μm, 300 μm Support Beam: 45 μm X 100 μm Thickness: 5-20 μm
Hammerhead Small	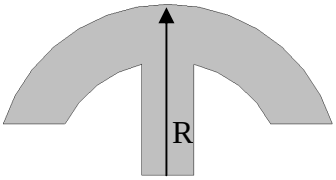	Radius: 150 μm, 200 μm Support Beam: 45 μm X 100 μm Thickness: 5-20 μm

4.2 Cantilever Packaging

After fabrication, the cantilevers were electrically connected to the excitation and read-out circuitry through wire-bonding in a 28-pin dual-in-line (DIL) package. Thus, for liquid-phase testing a method was needed to deliver fluid to the portion of the die containing the cantilevers (the KOH etch opening), while at the same time preventing fluid contact with the wire-bonds. It is also desirable that the bonding wires not be covered in epoxy to allow for re-bonding as needed. A method of injecting fluid that

minimizes the trapping of air-bubbles is also desired. Air-bubbles can lead to device instability or prevent sample delivery to the cantilever surface.

4.2.1 Flow Cell Design

Once fabricated and diced, the devices are wire-bonded and packaged using acrylic manifolds, which are fabricated with a VIPER stereolithography tool (the parts are first drawn in SolidWorks (Concord, MA) and then a file is generated that can be read by the stereolithography tool (SLA)).

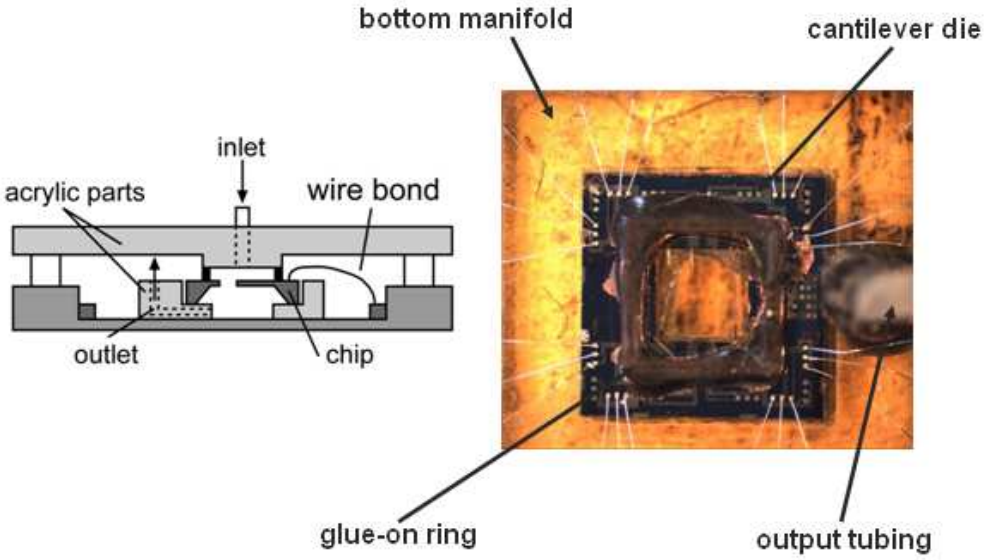

Figure 4.4: Diagram of the implemented packaging scheme (left), image of a packaged die (right). See Chapter 6 for images of the packaged devices in the manifold and testing setup.

For creating the flow cell, the bottom acrylic manifold (see Figure 4.5) is first glued into a standard 28-pin DIL package. The cantilever chip is placed over a silicone gasket (which seals to the bottom of the die when the entire system is assembled) in the bottom manifold. The die is then wire-bonded. Subsequently, an acrylic ring is glued to the surface of the chip. The top manifold (see Figure 4.6) screws down to threaded inserts

glued to the DIL package. This allows a gasket to seal against the acrylic ring, thereby creating a flow cell (Figure 4.4).

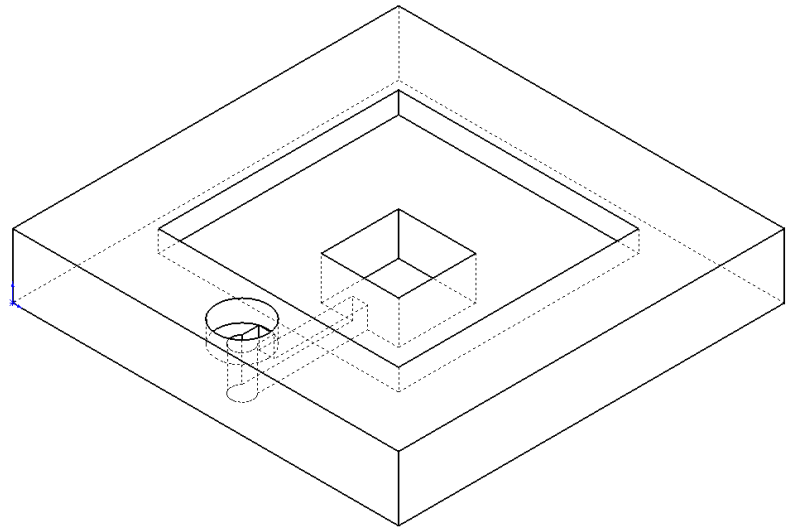

Figure 4.5: CAD drawing of the bottom microfluidic manifold. The die sits in the large rectangular opening in the center. The path of the fluid can be seen from the smaller square in the center to the circular opening to which the PEEK (or flexible) tubing is glued creating an outlet.

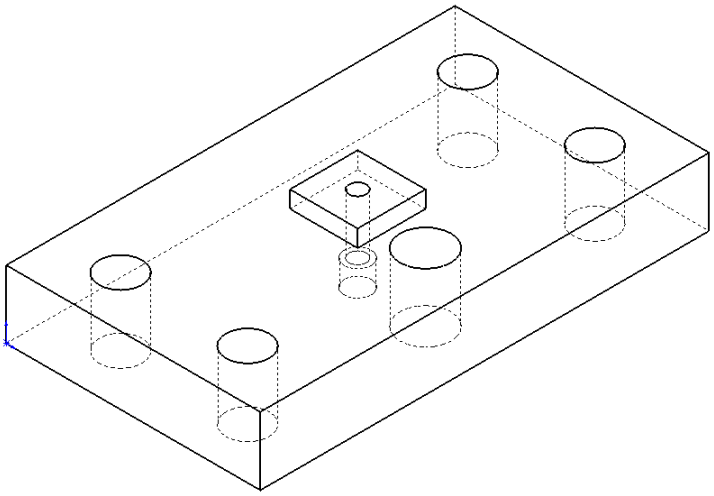

Figure 4.6: CAD drawing of the top manifold used for microfluidic packaging. The four large circular openings at the edges are for inserting screws to fasten the manifold to thermoplastic inserts on the DIL package. The extruded square in the middle is where the seal is made to the ring on the die, fluid flows from the circular opening in the center of the square.

The design of the packaging allows fluid flow from the top to the bottom of the sensor chip through the bulk-micromachined opening. This design helps to prevent the trapping of air bubbles, which can cause problems with measurements. Figure 4.7 presents an exploded cross-section showing the assembly of the cantilever flow cell.

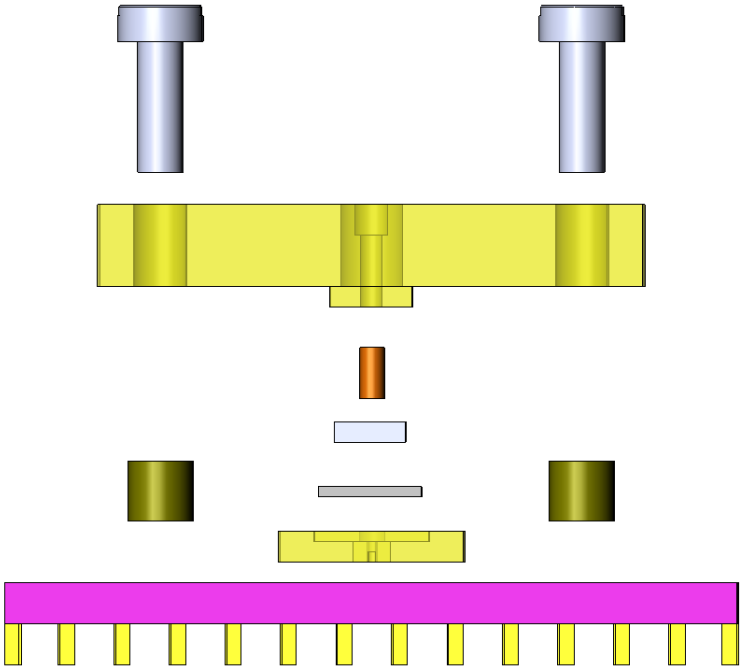

Figure 4.7: Exploded cross-section showing the assembly of the flow cell for the in-plane cantilevers. The only component not pictured is the silicone tubing that is slid over the PEEK tubing at the output.

It was found that the original packaging scheme implemented for chemical sensor testing (the one described above) was not reliable enough for biosensor testing. One of the main difficulties with the implementation of biosensors, in comparison to chemical sensors, is that for biosensing the antibody-antigen interactions are not easily reversible, making the chips one-time-use. Thus, greater device/packaging reliability is required to successfully test biosensors.

Three changes were made to improve reliability. First, the dies were glued into the bottom manifold. This provides a more reliable seal than using a gasket. Second, the

acrylic rings that were originally used (Fig. 4.4) were found to dissolve in the ethanol-based self-assembled monolayer (SAM) formation solution, which is applied during the first step of surface functionalization (see Chapter 6.). To correct the problem, a silicon ring (which is described in see section 4.3) was attached with a UV-curable epoxy, creating a solvent-resistant ring structure.

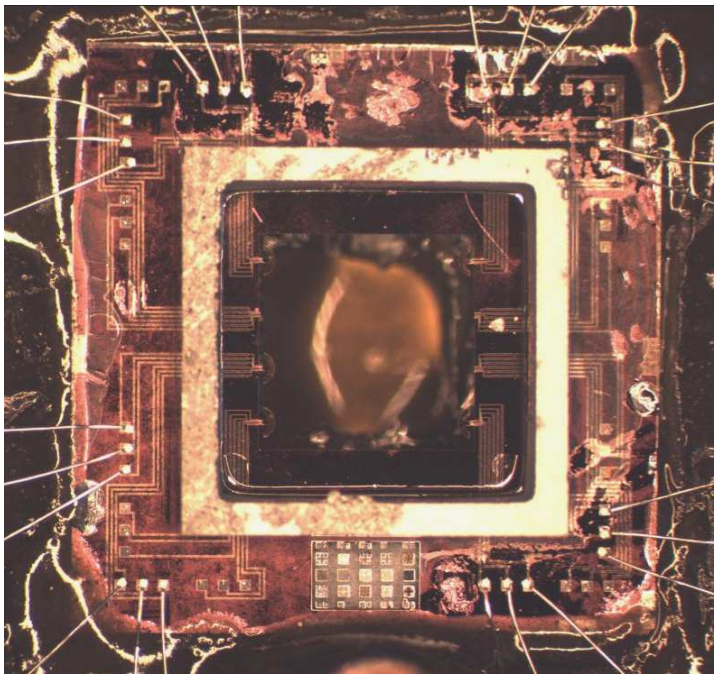

Figure 4.8: Package biosensor test chip with a silicon ring. Five small diameter hammerhead devices are visible inside the silicon ring.

Third, the output connection created by gluing a piece of flexible silicone tubing to the circular opening at the manifold outlet was found to be prone to leakage. This was problematic during sensor functionalization when the packaged device needed to be moved to several different locations, including a refrigerator (see Chapter 6). To make a more reliable fluid outlet, a section of polyetheretherketone (PEEK) tubing was glued into the bottom manifold. Then, a piece of flexible tubing could be slid over the PEEK

tubing making a good seal. Since PEEK is rigid, it does not move and cannot wiggle out of the hardened epoxy (See Figure 4.9).

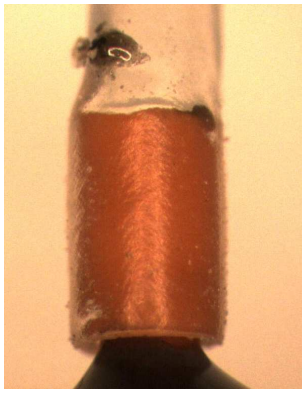

Figure 4.9: A piece of flexible silicone tubing placed over hard PEEK tubing which is glued into the bottom manifold. Simply placing the flexible tubing over the PEEK tubing provides an adequate seal for biosensor testing

4.2.2 Metal Line Passivation/Protection

For liquid-phase device operation, as opposed to gas-phase operation, the protection of the device's metal lines becomes a prime concern. Inadequate isolation of the metal lines from the solution can lead to both corrosion (depending on the material the traces are made with) and can also lead to shorting between connections in ionic solutions. Both of these problems can result in device failure. In considering possible passivations a few factors need to be considered: (1) will the proposed passivation react with the targeted analytes? (2) what is the film quality/density? (3) Will the passivation adversely effect device operation, i.e. by damping? (4) how much stress will the film induce? All four of these factors are important to consider when developing a process to create (resonant) MEMS devices for operation in liquid. For example, polymers might make a good liquid barrier, but can severely damp the oscillation of a resonant device and can also absorb analytes interfering with chemical measurements. For this reason, crystalline films were predominantly explored as possible passivations for the cantilevers.

crystalline films are non-reactive/corrosion resistant, can provide a good barrier between liquids and the metal lines, and are widely used in CMOS processes to protect and isolate metal layers. When considering potential passivations, two of the most important parameters to consider are pinholes and stress. Denser films will have a lower pinhole density, and thus will be less likely to let corrosive solutions reach the metal lines. But at the same time higher density films will have a higher stress.

Stress is a key concern, especially in cantilever design. Residual stress in a released micromechanical structure can cause the structure to bend, degrading performance or making it unusable. The deflection of a beam for a given structure due to residual stress is given by Stoney's formula [124]:

$$\sigma = \frac{1}{R}\frac{E}{6(1-v)}\frac{T^2}{t} \qquad (4.2)$$

In Stoney's formula, σ is the stress in the film deposited on the beam material, R is the microstructure's radius of curvature, v is the Poisson's ratio in the beam, E is the Young's modulus for the beam, T is the thickness of the beam, and t is the thickness of the deposited film. As an example, a 45μm wide 600μm long 8μm thick cantilever with 2μm of a thin-film passivation that has a residual stress of 400 MPa, will experience a tip deflection of 74.1μm. Such a deflection would be problematic for operation of the cantilever as a resonator. The residual stress in a film comprised of a series of different layers can be estimated by summing the product of thickness and the stress of each individual layer [96]. This method was used to determine what combination of PECVD layers would give as low a residual stress as possible.

In the course of this work, various liquid-phase passivations were tested (see Table 4.2) to determine which coating is most effective at preventing metal line

corrosion, and allowing for prolonged device operation in aqueous solution.

Table 4. 2: Resulting device lifetime in liquid with various passivation films.

Film Description	Thickness	Device Lifetime w/ Film
PECVD SiO_2/SiN_x	1.9 μm	10 hrs
Pulsed PECVD SiO_2/HF SiN_x	1.2 μm	>24 hrs
RF Sputtered SiO_2	.6 μm	4-5 hrs
Thermal ALD Al_2O_3	50 nm	3-7 hrs
Plasma ALD SiO_2	50 nm	***
Thermal ALD SiO_2	50 nm	Less than 24 hrs*
Plasma ALD TiO_2	50 nm	24 hrs
Thermal Al2O3/ZrO_2	50 nm	24 hrs
Parylene C	1 μm	24 hrs **

***Devices didn't stop operating, but there were spots of corrosion on metal lines after 24 hours.*
*** One device operated for 24 hours, on the second device the parylene delaminated, greatly degrading the device's performance.*
**** The deposition of this film was non-uniform, making accurate testing difficult. In addition, wire bonding through this ALD film was not reliable making prolonged testing impossible.*

PECVD, atomic layer deposition (ALD), and polymer coatings were tested, and it was found that either a stack of pulse-deposited low-frequency PECVD oxide and high-frequency PECVD nitride, ALD-deposited titanium dioxide, or an ALD deposited nanolaminate of zirconium oxide and aluminum oxide were most effective (see table 4.2). The tested resonators were fabricated using the process detailed in Section 4.1.

All of the passivations were deposited onto .6um-.75um of aluminum that had been evaporated in a CVC E-beam evaporator system at a rate of 1.5 A/sec, and with a base pressure in the range of 1-3*10^-6 T. Some of the devices had a thin PECVD SiO_2 layer already over the metal lines; based on previous results this layer is too thin to protect the devices from corrosion. Outside vendors (Cambridge Nanotech and Oxford

Instruments) deposited some of the ALD coatings that were not available in the NRC cleanroom at Georgia Tech.

For passivation testing, dies were packaged as shown in Section 4.2.1, and DI water was injected into the package using a 5cc syringe. The resonator was set into oscillation using a feedback loop described in [103]. Because the observed output waveform is different in air and aqueous solution, one can determine if the device is in fact immersed in liquid based on the shape of the resonator output signal. The devices were operated up to 24 hours in liquid, and were checked for corrosion periodically, or when a large change in resonant frequency or waveform shape was observed. For each coating, a minimum of two dies were tested. Based on the testing results and the film availability in the NRC cleanroom, a pulsed-PECVD SiO_2 (deposited using the low-frequency RF source) and high frequency (HF) SiN_x (deposited using the high-frequency RF source) passivation was chosen as the passivation for most of the devices tested here.

A diagram of the layered PECVD film that is deposited on the cantilever surface is shown below. Note that the thermal oxide layer (see Figure 4.10) is used to isolate the aluminum lines from the silicon substrate. The metal lines themselves are not shown. The stress for all three of the films on the silicon beams (thermal oxide, PECVD oxide and nitride) was measured using the wafer curvature method on a Tencor P15 Profilometer. The thermal oxide had a stress of -300 MPa, the PECVD oxide had a stress of -330 MPa, and the PECVD nitride had a stress of 350 MPa. The thicknesses of the two PECVD layers were chosen to give as little residual stress as possible in the final film stack. The total stress of the hybrid film was measured, also using the wafer curvature method, and was found to be 100 MPa or less. When fabricated the cantilevers had minimal bending

(which is the main goal of stress minimization.) Further, a stack of several alternating layers is used to minimize the effects of pinholes.

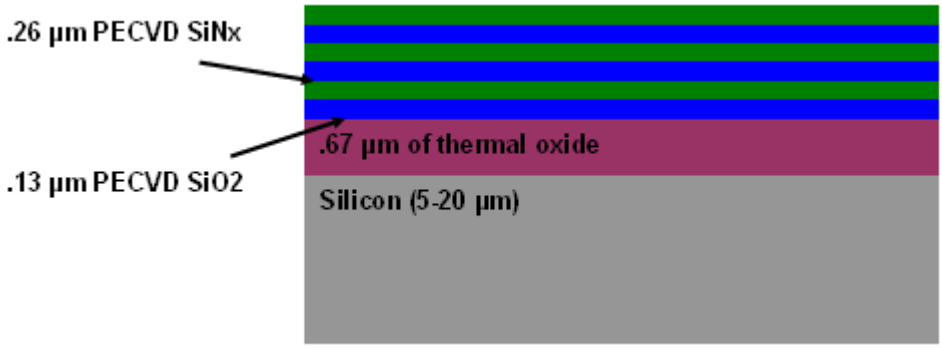

Figure 4.10: Cross section of the tested cantilevers.

4.2.3 On-Chip Packaging Process

The packaging scheme described in Section 4.2.1 provides a method for packaging resonators for liquid-phase testing, but still leaves room for improvement. First, placing the ring by hand on the die surface can result in epoxy or the ring being too close to the bond pads or on the resonators themselves, rendering the devices in question useless. Second, a water jet is used to cool and lubricate the blade of the dicing saw during the dicing step at the conclusion of the process. The water from the saw can hit the resonators with enough force that they break, greatly reducing the yield per wafer. In Figure 4.8, only 5 devices on the die (instead of 8) withstand the water from the dicing saw. Third, placing the rings by hand doesn't scale well if one wants to go to a production scale batch manufacturing process. One of the main advantages of MEMS-based sensors is that they can be batch manufactured relatively inexpensively, and thus finding a wafer-level packing solution is important if cantilever microsensors are to move out of the lab and become available commercially.

The concept of the wafer-level packaging process is to fabricate the rings from

silicon (or another materials) and to mount them to the device wafer using a wafer-bonding process. The on-chip packaging process utilizes two etching steps on a p-type prime wafer (the packaging wafer) to create the correct shapes (dicing completes the formation of the ring structure). SU-8 bonding is used to attach the packaging wafer to the wafer with cantilever devices [125]. The patterning of the packaging wafer only requires one additional mask because the mask for the KOH etch openings can also be used to define the openings on one side of that wafer. SU-8 is applied to the surface of the packaging wafer using a photoresist transfer process [126]. The subsequent bonding step is low-temperature, being performed at only 150 C, and also does not require a large amount of pressure to be applied to the wafer. Following bonding, a two step dicing process is used. The first dicing pass completes the creation of ring structures on the upper wafer (the packaging wafer) and then the device wafer underneath is diced as usual.

In developing the bonding process, two alternative bonding methods were tried in addition to the SU-8 bonding: (1) glass-frit bonding, (2) gold-eutectic bonding. The glass-frit process was problematic because the screen printing step used to deposit the glass-frit paste on the packaging wafer could actually crack the micromachined wafer. In addition, for screen printing, there is a limit on the aspect ratio of the features that can be implemented, which would place another constraint on the mask design. The gold-eutectic process provided a good bond, but the gold-silicon eutectic mixture destroyed the metal lines that run laterally under the ring.

In preparation for dicing, blue vacuum tape (Semiconductor Equipment Corp) is adhered to the exposed face of the packaging wafer (the part of the wafer that will face upwards during dicing and be exposed to water from the saw) after bonding. The dicing

saw cuts through the vacuum-tape without peeling it off the wafer surface. Thus, the openings in the packaging wafer are obscured by the vacuum-tape, preventing water from hitting the cantilevers and breaking them. Using this scheme the yield from the cantilever fabrication process could be substantially improved.

As mentioned above, the packaging wafer is a 100 mm p-type prime wafer that is approximately 525 μm thick. A brief description of the process steps for the on-chip packaging process are given below (more details can be found in Appendix 3).

1. Deposit 2μm of PECVD oxide on the top side and 4μm of PECVD oxide on the backside of a p-type prime wafer.

Figure 4.11(a): Cross-section showing a prime wafer with PECVD silicon dioxide (shown in purple) on both sides.

2. Pattern and etch the topside oxide using the properly designed packaging mask.

3. Pattern and etch the backside oxide using the same mask used to pattern the PECVD layers for the KOH etch mask.

Figure 4.11(b): Cross-section showing the patterned PECVD oxide creating an etch mask.

4. ICP etch the wafer, using the PECVD oxide layers as a mask. Etch approximately 170 μm into the wafer from the topside and the rest of the way through from the backside.

Figure 4.11(c): Cross-section showing the prime wafer after silicon etching.

5. Strip the oxide from the packaging wafer using HF, clean the packaging wafer

thoroughly.

6. Spin-coat SU-8 2025 on a blank wafer. The SU-8 layer has an approximate thickness of: 20 μm. Do NOT bake.

Figure 4.11(d): Cross-section depicting a prime wafer with an SU-8 layer.

7. Place the cleaned packaging wafer on top of the wafer with SU-8 with the topside down, move the wafers around gently to transfer SU-8 to the packaging wafer

Figure 4.11(e): Cross-section depicting the photoresist transfer process.

8. Use razor blades to remove the packaging wafer from the wafer with SU-8. Clean the SU-8 off the edge of the pattern, and also out of any of the openings (using a swab).

9. Align the device wafer and packaging wafer using the bond fixture and a microscope. Note: The device wafer is fully processed at this point including the membrane release step to define the cantilevers themselves.

10. Bond the two wafers for 70 minutes at 150 degrees C and 28 PSI of force; the process chamber in the bonder is pumped to high vacuum for bonding.

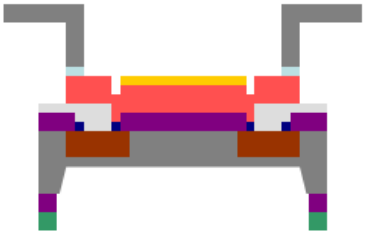

Figure4.11(f): Cross-section depicting the device wafer with packaging wafer bonded on top.

11. Place blue vacuum-tape on top of the openings on the packaging wafer.

12. Dicing Step 1: Dice through the partially etched areas of the packaging wafer, leaving the device wafer underneath untouched.

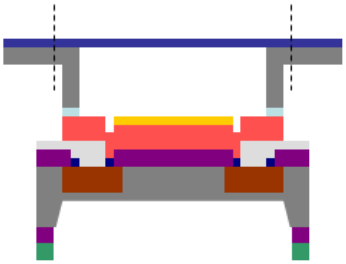

Figure 4.11(g): Cross-section showing the blue tape placed over the opening in the packaging wafer in order to protect the beams. The dicing streets are shown as dotted lines.

13. Dicing Step 2: Dice through the device wafer as normal.

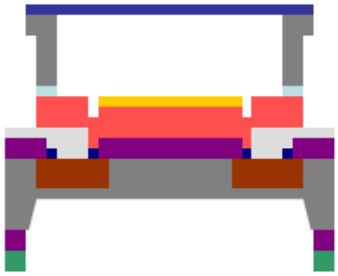

Figure 4.11(h): Cross-section depicting the device and packing wafers after the on-chip packaging process and dicing of the packing wafer.

14. Remove vacuum tape from dies before use.

Figure 4.12 shows a photograph of the entire wafer after the on-chip packing process and dicing.

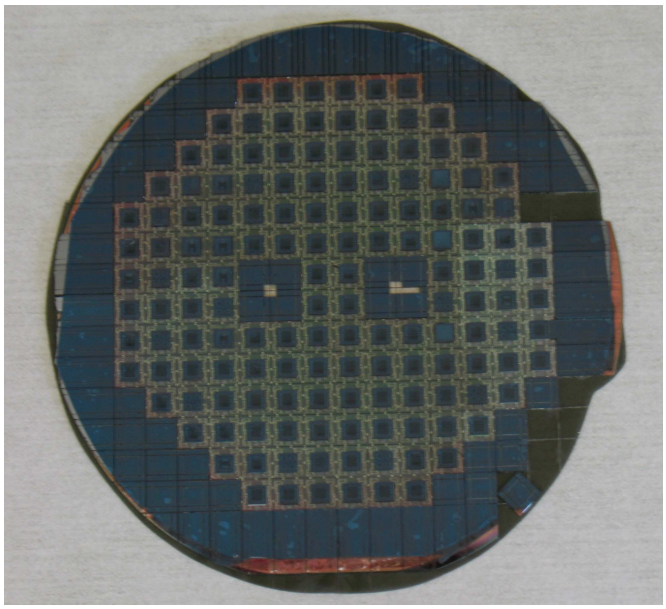

Figure 4.12: Wafer-level image after performing the on-chip packaging process. The blue vacuum-tape that prevents water from hitting the beams can be seen on the surface of the upper wafer.

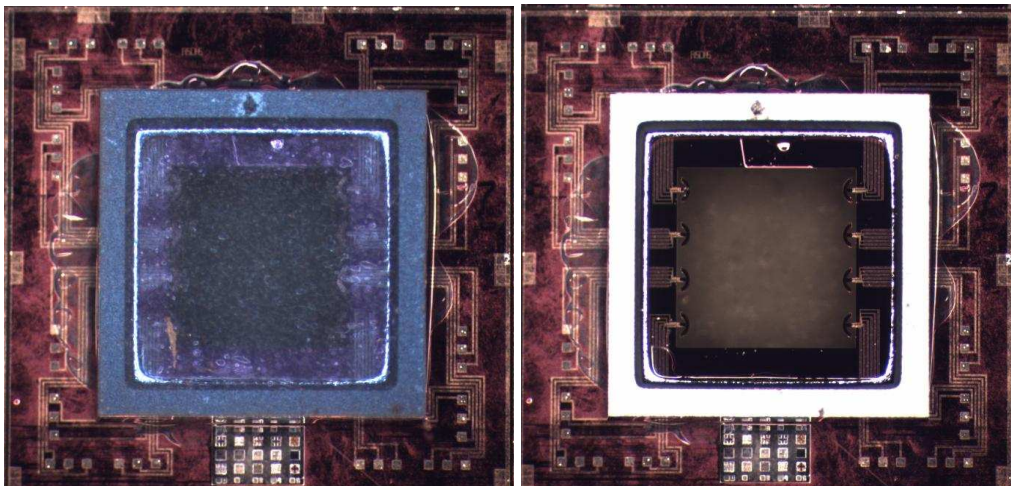

Figure 4.13: Close-up view of a hammerhead die protected by vacuum tape (left), with hammerhead resonators visible below the tape. After removal of the tape the unbroken hammerheads are visible inside the silicon ring that is used for packaging (right).

For the on-chip packaging process to work effectively, there are a few important layout considerations. First, in order to be able to wire-bond, enough room must be left between the bond pads and the packaging ring so that the wedge on the wire-bonder can contact the bond pad. In this case, 450 μm were sufficient between the edge of the

packaging structure and the edge of the bond-pad (this distance depends on the geometry of the wire-bonder wedge). Second, pressure is applied during the bonding process, and thus the packaging structure needs to be placed so that it is not over the membrane, or another part of the wafer that has been thinned by KOH etching. This is accomplished by using the KOH etch mask to define the inner ring opening, automatically ensuring that the ring is not over a thinned portion of the wafer.

With these layout concerns in mind, the on-chip packaging process has been successfully implemented for the cantilever, and allows the spacer ring that is necessary for creating a flow cell to be placed on all of the cantilever dies at once. In addition, the centering done during bond alignment provides better ring placement than what can be done with an individual ring by hand at the die level. Biosensor tests have been performed using devices packaged using this method and the devices and microfluidic packaging performed as expected. Although extensive mechanical testing of the SU-8 bond has not been performed, during the course of experiments it has been found that the silicon ring actually breaks before the SU-8 bond. This indicates that the SU-8 bond is robust.

One possible drawback of the SU-8 bonding process is that SU-8 can leak out from under the packaging wafer and cover devices and bond pads (this is visible in Figure 4.13). Leaking of SU-8 was not found to be a consistent problem, and did not occur on all of the wafers that were packaged in this manner. A baking step could possible be added after the SU-8 transfer to help harden the epoxy, however, doing so runs the risk of crosslinking the SU-8 too much so that it cannot form a good bond.

CHAPTER 5

CANTILEVER MECHANICAL CHARACTERIZATION IN AIR AND WATER

In sensing applications where cantilever dynamic mode operation is used, the short term frequency stability limits the sensor resolution. The stability is correlated with the quality factor, Q, of the resonance mode. For this reason, several recent studies have measured and modeled the Q-factors of cantilevers vibrating in out-of-plane bending modes in air [127], [128], [129], [130]. While Q-factors up to 1,500 have been measured for the first out-of-plane bending mode in air [130], liquid operation is challenging because of the substantial viscous damping by the fluid. Besides low Q-factors, typically not exceeding 10-20 in water [24], a substantial reduction of the out-of-plane resonance frequency (typically 50%) is caused by the large effective mass of the fluid. In addition, cantilevers that push against the fluid are more sensitive to viscosity and density changes in the liquid itself [24].

In this chapter, extensive mechanical characterization of cantilevers with twenty different length and width combinations, and four different thicknesses (eighty devices in total) vibrating in their fundamental in-plane resonance mode has been performed in both air and water. Combining these characterization data with FEM modeling to estimate the gravimetric sensitivity, allows one to approximate, using the equations derived in Chapter 3, which cantilever geometries would give the lowest detection limits (at least for the tested beams) if used as a liquid or gas-phase biochemical sensor. More broadly, examination of the characterization data allows one to examine the tradeoffs that exist in

the design of biochemical sensors using in-plane cantilevers.

5.1 Testing Setup and Methods

In order to investigate the effect of the beam dimensions on the resonance frequency and quality-factor of cantilevers operated in the their first in-plane flexural mode, thermally actuated and piezoresistively detected single-crystal silicon cantilevers were fabricated using the bulk-micromachining process presented in Chapter 4. For protection of the aluminum metal lines during liquid testing a passivation stack of PECVD (plasma enhanced chemical vapor deposition) oxide/nitride layers was used (see Figure 4.7 for a schematic of the beam cross section.) The target thickness of the PECVD passivation layer stack was 1.2 μm.

Cantilever mechanical characterization was performed in both air and water. The devices were packaged as presented in Chapter 4 with a gasket used underneath the cantilever die, allowing the packages to be re-used. Pressure exerted from the top manifold normally used as part of the flow cell can slightly alter the beam's resonant frequency. Consequently, the top manifold was not used during mechanical characterization. For characterization in liquid, a drop of DI water was placed inside the acrylic ring (which was glued to the surface of the die for testing, see Chapter 4) and allowed to percolate through the bulk-micromachined opening. Leaving the package open to the air allows one to confirm that that there are no air bubbles trapped next to the cantilevers, which could lead to inaccurate results. The amplitude of the observed signal provides further confirmation that there is no air trapped underneath the resonator. Cantilever mechanical characterization was performed in de-ionized water.

For mechanical characterization in air and water, the amplitude and phase response from the piezoresistive Wheatstone bridge [103] was captured using an Agilent HP4395A network/spectrum analyzer and a custom PCB board. The data was transferred to a computer for processing using a LabVIEW (Austin, Texas) program. The Wheatstone bridge bias voltage was kept at 3V for open-loop measurements in both air and water. In water, a single heating resistors was driven with a -10 dBm (70.7 mV @ 50 Ohms) AC excitation voltage superimposed on a 3V bias voltage [118]. In air, a single heating resistor was driven with a -20 dBm (22.4 mV @ 50 Ohms) AC excitation voltage superimposed on a 0.5 V bias voltage. In some cases, slightly higher voltages were needed to produce an output signal. In addition, the voltages were chosen/kept sufficiently small during the air measurements so that they did not excite the cantilevers into a nonlinear regime causing a reduction in Q. Typical resistor values for both the heating resistors and the piezoresistors are 500-700 Ohms. After measurement, the capacitive signal crosstalk between input and output signals was removed using Nyquist's method [131]. The quality factor and resonant frequency were extracted using the 3-dB method in MATLAB (Mathworks, Natick, MA).

In addition to transfer characteristic measurements using the piezoresistive Wheatstone bridge, select resonator transfer characteristics were also measured using a Polytec MSA-500 Micro System Analyzer (Polytec, Waldbronn, Germany). This tool allows measurement of the out-of-plane as well as the in-plane vibration amplitudes of the microstructures as a function of the driving frequency. Directly, capturing the vibration amplitude and mode shape provides further verification that the thermal excitation scheme is in fact exciting the in-plane mode as desired. Figure 5.1 gives the

piezoresistive transfer characteristic of a 90 μm wide, 400 μm long, 20 μm thick cantilever in air. Figure 5.2 shows the transfer characteristic of the same cantilever for the first in-plane mode in water, also captured using the piezoresistive Wheatstone bridge.

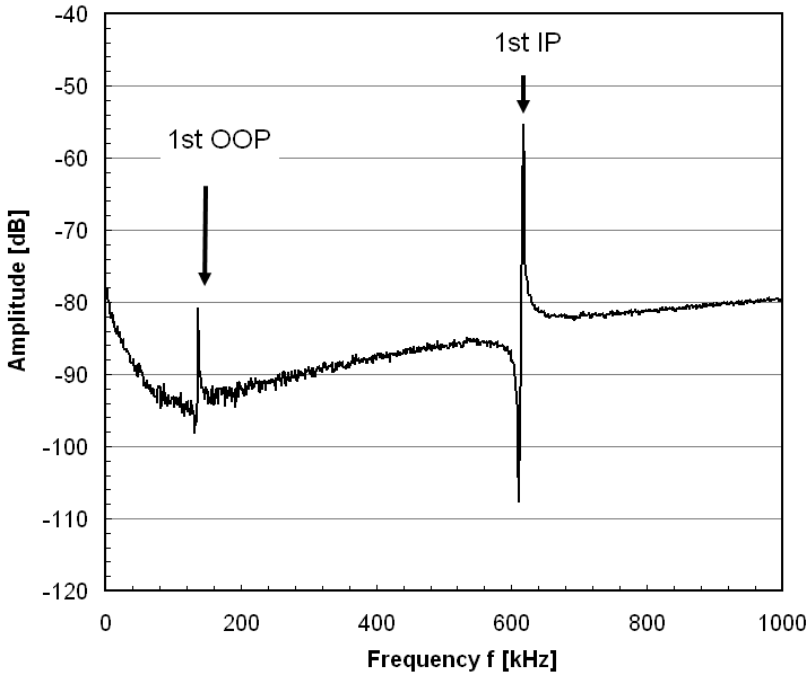

Figure 5.1: Open-loop amplitude transfer characteristic of a 90 μm wide, 400 μm long, 20 μm thick cantilever measured using the integrated piezoresistive Wheatstone bridge on the cantilever itself.

For Figure 5.2, a scan over the entire frequency range from 10 Hz to 1 MHz is not presented because the signal amplitudes are much smaller in liquid than in air. Showing the entire frequency range would make identifying the resonance peaks more difficult if not impossible.

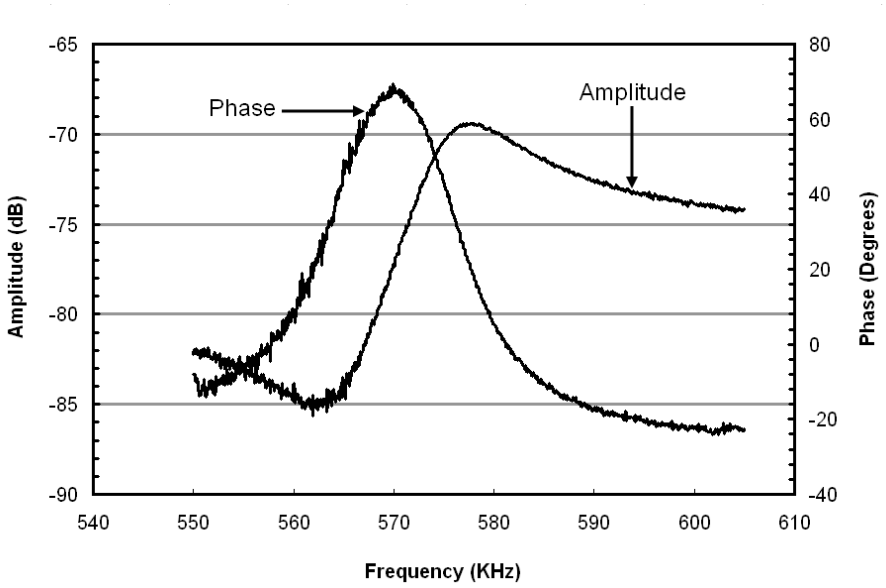

Figure 5.2: Open-loop amplitude and phase transfer characteristic of a 90 μm wide, 400 μm long, 20 μm thick cantilever measured using the piezoresistive Wheatstone bridge as a function of frequency in water. The frequency range is chosen to capture the fundamental in-plane mode.

Figure 5.3 plots the out-of-plane vibration amplitude (measured using a Polytec MSA-500 Micro System Analyzer at the beam's free-end corner) of a 90 μm wide, 400 μm long, 20 μm thick cantilever in air as a function of frequency, as well as the out-of-plane vibration mode shape at the in-plane resonance frequency. Comparing Figures 5.1 and 5.3, a large peak in the out-of-plane amplitude spectrum is observed around the frequency of the out-of-plane mode (as expected), while a much smaller peak is seen around the frequency of the first in-plane mode (in contrast, the piezoresistive transfer characteristic show the strongest signal for the in-plane resonant mode). This indicates that there is only a small out-of-plane vibration component at the in-plane mode and that the designed excitation scheme preferentially excites the fundamental in-plane mode. It should be further noted that the measured out-of-plane vibration component is not simply due to the fact that the beam is not perfectly normal to the optical measurement axis, but

rather resembles a torsional vibration component on top of the dominant in-plane vibration component. Going a step further, Figure 5.4 shows the in-plane vibration amplitude at the beam tip of a 90 μm wide, 400 μm long, 20 μm thick cantilever in air measured around the frequency of the first in-plane mode. The measurement was again performed using a Polytec MSA-500 Micro System Analyzer. The results show that the in-plane mode has a peak amplitude of around 900 nm for a 4 V AC excitation amplitude superimposed on a 4 V DC bias.

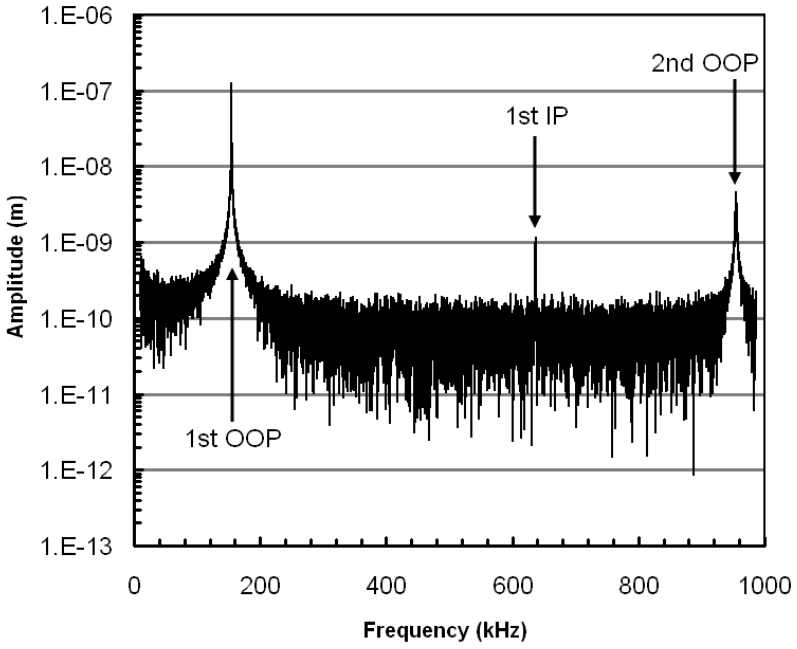

Figure 5.3: (a) Out-of-plane vibration amplitude at the corner of the beam tip of a 90 μm wide, 400 μm long, 20 μm thick cantilever as a function of frequency in air and (b) out-of-plane vibration component at the in-plane resonance frequency measured using a Polytec MSA-500 Micro System Analyzer as a function of frequency in air. Using a 1 V AC voltage superimposed on a 1 V DC bias, the maximum out-of-plane vibration amplitude at the in-plane resonance mode (f ≈ 637 kHz) is approx. 1 nm.

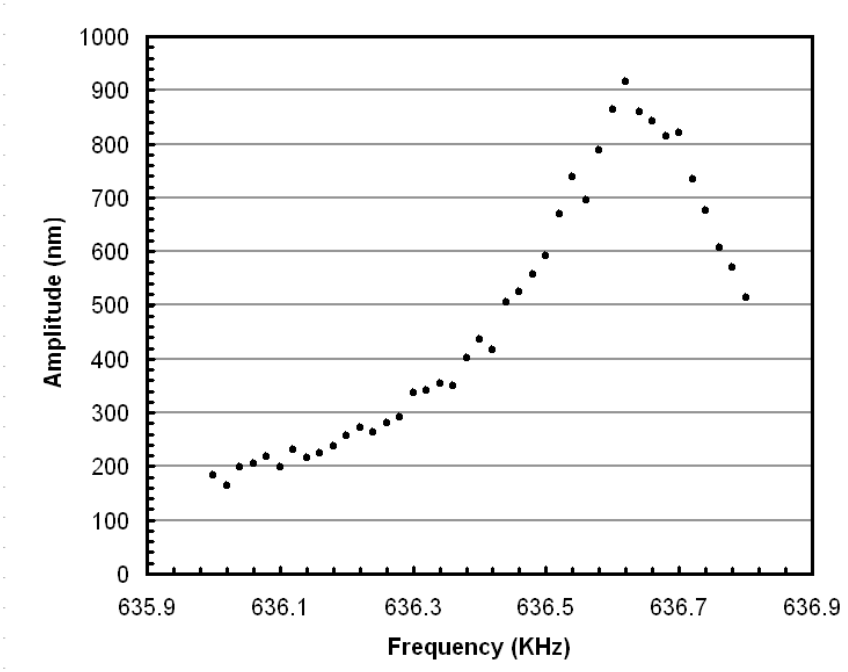

Figure 5.4: In-plane vibration amplitude of a 90 μm wide, 400 μm long, 20 μm thick cantilever measured using a Polytec MSA-500 Micro System Analyzer as a function of frequency in air for 4 V AC excitation superimposed on a 4 V DC bias. The frequency range is chosen to capture the fundamental in-plane mode.

5.2 Eigenmode Analysis in COMSOL

Cantilevers with a frequencies ranging from 50KHz to 2MHz were desired for mechanical characterization and sensor testing. While the resonance frequencies as a function of the beam dimension can be roughly estimated using Equation 3.3, the underlying assumptions of pure beam bending and an ideally clamped beam edge are not necessarily fulfilled for the micromachined cantilevers tested in this work. Thus, to better predict the in-plane resonance frequencies of the tested cantilevers, eigenmode simulations were carried out using the FEM (finite element modeling) software COMSOL. For more accurate simulation, a realistic representation of the actual support structure was drawn for the beams (see FEM model in Figure 5.5), including part of the anisotropically etched cavity and a 20 μm wide silicon rim that originates from

misalignment of the KOH etching mask with respect to the cantilever edge. A fixed boundary condition was applied to the bottom edges of the support structure and an eigenmode analysis was performed for each cantilever size. The simulations presented in this chapter were carried out for a silicon beam thickness of 20 µm and anisotropic material properties of silicon as implemented in COMSOL were applied. A 1.9 µm thick passivation film was added to the surface and averaged material properties for the SiO2/SiNx stack were applied as follows: a Young's modulus of 91 GPa, a density of 2350 kg/m^3, and a Poisson's ratio of 0.2. The simulated in-plane resonant frequencies for each beam size are given in Table 5.1.

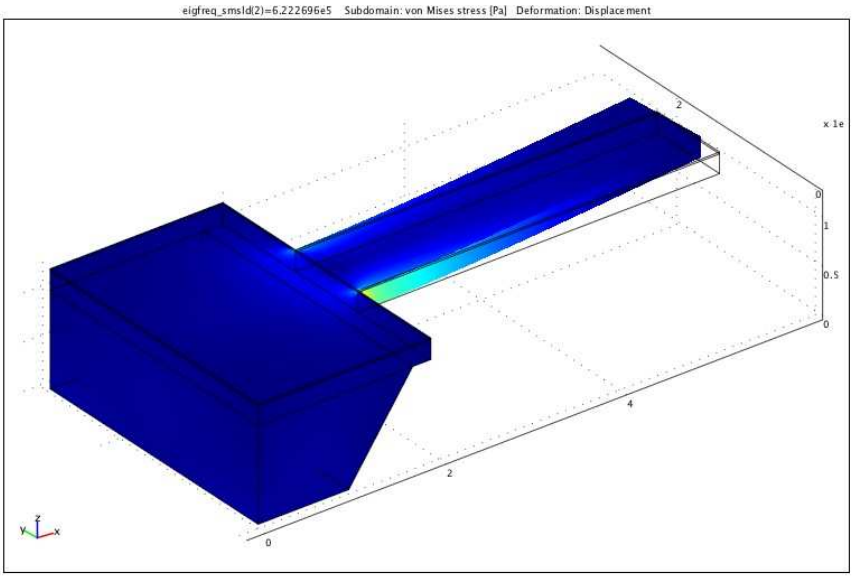

Figure 5.5: Fundamental in-plane mode of a 90 µm wide, 400 µm long, and 20 µm thick cantilever simulated using COMSOL. The color coding represents the von Mises stress distribution. Material properties are as discussed in the text.

Figure 5.5 and Table 5.2 presents the FEM model and the simulated lowest eigenfrequencies for a 90 µm wide, 400 µm long, 20 µm thick cantilever. In Figure 5.5 the support structure is shown along with the deformed shape of the cantilever. The colors correspond to the von Mises stress distribution along the deformed cantilever. Table 5.2

lists the simulated frequencies for modes of interest for the 90 μm wide, 400 μm long, 20 μm thick cantilever.

Table 5.1: Simulated resonant frequencies of the fundamental in-plane mode. For the simulations a silicon thickness of 20 μm was assumed.

Cantilever Width (μm)	Cantilever Length (μm)	In-Plane Mode Frequency (kHz)
45	200	1234.2
45	400	344.0
45	600	158.2
45	800	90.5
45	1000	58.5
60	200	1530.6
60	400	443.5
60	600	206.5
60	800	118.7
60	1000	77.0
75	200	1779.9
75	400	536.2
75	600	252.7
75	800	146.1
75	1000	95.1
90	200	1983.0
90	400	622.3
90	600	296.8
90	800	172.8
90	1000	112.8

Table 5.2: Simulated eigenfrequencies of a20 μm thick 90W400L cantilever between 1 KHz and 2 MHz.

Mode	**1st OOP**	**1st IP**	**2nd OOP**	**1st Torsional**
Frequency (kHz)	156.95	965.49	1263.8	622.27

The simulated resonance frequencies generally agree to within 5% of the measured resonance frequencies. The simulations were done assuming that the cantilevers have a 20 μm long “rim” of silicon. This “rim” is a result of underetching of the <111> plane during the KOH etching step and/or mask misalignment during the membrane release step of the fabrication process. During the KOH etching step to release

the membrane, if either the <111> plane is etched, or there is some misalgnment to the features on the topside of the wafer, the cantilever's clamped end will be supported by a section of silicon of the same thickness as the beam itself. The width of this "rim" varies from wafer to wafer and even depends on which side the cavity opening the cantilever is located and is likely the main source of frequency error in the FEM simulations. Device thickness variations, on the other hand, will only have a minor effect on the in-plane resonance frequency.

5.3 Mechanical Characterization of Prismatic Cantilevers

In total, 73 unique cantilever geometries were characteried in both air and water. Tables 5.3-5.6 summarize the measured results for four different cantilever thicknesses (5, 8, 12 and 20 μm) and 20 lateral geometries. The metrics of interest were the quality factor and the resonant frequency of the fundamental in-plane resonant mode in both air and water. Q is of interest because the Q of the resonance is related to the short-term frequency stability, and the noise floor of the cantilever sensors operated in closed-loop is defined by their short-term frequency stability. Thus, Q will give an indication of the sensor resolution (i.e., sensors with a higher Q will give a better short-term frequency stability and a lower noise floor).

Table 5.3: Measured resonant frequency and quality factors for the first in-plane flexural mode for cantilevers with a silicon thickness of 5 μm.

Width (μm)	Length (μm)	f_o Air (kHz)	Q Air	f_o Water (kHz)	Q Water
45	200	1124.7	2314.3	1054	29.5
45	400	337.5	1288.4	312.9	14.4
45	600	155.4	1220	140.8	12.3
45	800	87.8	663.6	78.6	7.1
45	1000	57.8	599.8	50.6	4.2
60	200	1553.2	1409.4	1484.8	36.8
60	400	440.6	1643.4	410.2	14.2
60	600	203.5	1370.1	189.8	10.7
60	800	116.9	855.9	105.1	9.9
60	1000	76.3	639.8	67.5	N/A
75	200	1628.4	1706.2	1562.2	36.8
75	400	509.1	1902.7	483.6	22
75	600	238.2	1415.8	225.3	14.5
75	800	141.1	1168.6	129.4	10
75	1000	87.2	281.9	77.6	9.1
90	200	N/A	N/A	N/A	N/A
90	400	617.2	2724.1	589.4	24.2
90	600	N/A	N/A	N/A	N/A
90	800	182.7	530.6	176.3	25.9
90	1000	111.2	1120.1	102.5	9

The resonant frequency is significant for two reasons. First, measuring the resonant frequency of the first in-plane mode (and other modes) gives an indication of how well the designed excitation and detection scheme is working. Second, comparing the first in-plane mode frequency in air and water gives a measure of how much mass loading the cantilever experiences from the surrounding fluid. A smaller reduction in frequency from air to water indicates less mass loading. Lower mass loading means better sensitivity as will be discussed further in Section 5.7.

Table 5.4: Measured resonant frequency and quality factors for the first in-plane flexural mode for cantilevers with a silicon thickness of 8 μm.

Width (μm)	Length (μm)	f_o Air (kHz)	Q Air	f_o Water (kHz)	Q Water
45	200	1212	2140	1132.8	43.8
45	400	336.4	1654	309.2	21.8
45	600	156.7	1328.8	141.7	13.1
45	800	89.3	1020.6	79	10.1
45	1000	58.4	787.3	51.5	7.2
60	200	1506.1	1203.1	1426.3	53.2
60	400	431.8	2353.3	402.7	27.1
60	600	203.6	1494.7	187.9	16.9
60	800	116.6	1272.3	111.7	16.3
60	1000	77	1029.7	70	9.2
75	200	1797.7	835.7	1722.5	61.6
75	400	530.1	1034.2	502.2	29.5
75	600	247.6	1379.7	231.3	18.1
75	800	146.1	1725.2	135.5	15
75	1000	94.5	1474.8	85.6	10.9
90	200	1905	338.4	1816.6	17.5
90	400	N/A	N/A	N/A	N/A
90	600	291.7	2253.1	276.2	23.6
90	800	N/A	N/A	N/A	N/A
90	1000	N/A	N/A	N/A	N/A

Table 5.5: Measured resonant frequency and quality factors for the first in-plane flexural mode for cantilevers with a silicon thickness of 12 μm.

Width (μm)	Length (μm)	f_o Air (kHz)	Q Air	f_o Water (kHz)	Q Water
45	200	1226.3	3613.3	1124.7	54.9
45	400	341.7	2474.9	313.6	26.4
45	600	157.7	1592.9	140.5	16.2
45	800	88.9	1219.6	80.6	11.3
45	1000	59.6	977.2	51.9	8.6
60	200	1575.9	2153	1426	56.7
60	400	453.1	3332.5	410.5	31.2
60	600	214.8	937.6	186.2	18.1
60	800	117.2	1740	105.9	15.7
60	1000	76.3	859	62.3	9.9
75	200	1819	2880	1726.3	60
75	400	557.9	1537	520.9	33.9
75	600	251.8	1205.9	232.9	23.5
75	800	146.4	2126.9	142.1	11
75	1000	96.1	1649.2	88.5	12.6
90	200	204.5	1203	1968	66.8
90	400	622.7	4291.5	588	36.8
90	600	298.7	3230.3	275.6	27.4
90	800	171	2592.9	159.2	13.2
90	1000	112	1944	103.4	17.6

Table 5.6: Measured resonant frequency and quality factors for the first in-plane flexural mode for cantilevers with a silicon thickness of 20 μm.

Width (μm)	Length (μm)	f_o Air (kHz)	Q Air	f_o Water (kHz)	Q Water
45	200	1228.5	2869.6	1148.9	20.1
45	400	364.7	3194.2	322.6	32.7
45	600	157.4	1944.5	136.5	4.7
45	800	95.3	1607.7	83	15.4
45	1000	58.9	1244.6	N/A	N/A
60	200	1539.1	948.1	1410.5	68.1
60	400	437	2982.7	396	39.1
60	600	211.1	1670.4	190.2	25.7
60	800	120.5	2168.5	107.5	20.1
60	1000	77.7	1672.2	68.7	14.9
75	200	1724.3	345.8	1604.3	86.8
75	400	532.1	2355.4	489.6	42.4
75	600	256.5	2486.2	234.3	30.6
75	800	153.7	2385.6	145.4	25
75	1000	96.1	2200	87	18.8
90	200	2066	593.7	N/A	N/A
90	400	617.3	3263,6	575.4	54.9
90	600	300.5	2155.8	278.9	36
90	800	176.7	1224	162.8	28.4
90	1000	116.8	2696.8	106.6	21.5

5.4 Quality Factors and Resonant Frequencies in Air

Although this work focuses on liquid-phase sensor development, the cantilevers were characterized in both air and water. Characterization in the gas-phase is important for several reasons. First, the FEM simulations discussed in Section 5.2 assume that the beam vibrates in air only (the simulations actually assume vacuum operation, but the frequency change by the surrounding air is minimal). Thus, to ensure that the electrothermal excitation and piezoresistive detection preferentially excite the first in-plane flexural mode, testing in air is necessary. Second, to determine the effect of liquid-phase operation on the cantilever's resonance (through e.g. mass-loading or viscous damping) testing in air is needed as a baseline for comparison. Third, there are many applications for biochemical sensors in the gas-phase, such as detection of toxins or

breath analysis for disease detection [132]. In addition to liquid-phase operation, the cantilevers designed here can be employed as effective gas-phase sensors.

In air, generally several resonant peaks are visible in the transfer characteristic of the piezoresistive sensing signal, not just the first in-plane mode as desired. Comparison to FEM data was used to identify each mode. In addition, the spacing between modes can be used to ensure that the desired modes are being excited correctly. An open-loop frequency transfer characteristic for the first in-plane mode of a 45 μm wide, 200 μm long, 8 μm thick resonator is presented in Figure 5.6. From the 3-dB bandwidth of the resonance, a Q-factor in air of 2140 can be found for this beam dimension.

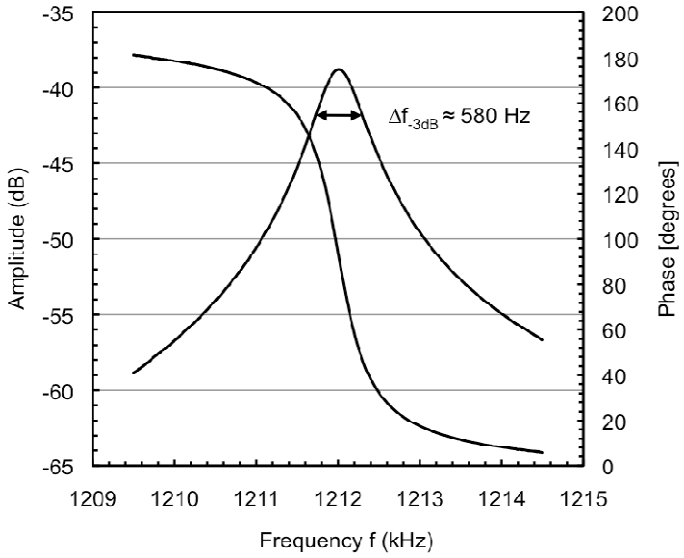

Figure 5.6: Amplitude and phase transfer characteristic for a 45μm wide, 200μm long and 8μm thick cantilever in air.

As mentioned in Section 5.2, the cantilever fabrication process leads to a non-ideally clamped boundary condition for the beams. Figure 5.7 shows a comparison between the simulated and experimentally measured in-plane resonant frequencies of 8 μm and 12 μm thick beams in air. The experimental results deviate considerably from

frequency values estimated by Equation 3.3 for two reasons: (i) short and wide cantilevers exhibit shear deformation in addition to bending deformation, and (ii) the micromachined silicon support structure is compliant compared to an ideal clamped boundary. In Figure 5.7, the dashed-dotted and dashed lines represent the simulated frequencies for ideally clamped cantilevers and cantilevers with a realistic silicon support structure, respectively. The silicon support structure includes the micromachined etch cavity and a 20 µm wide silicon rim (see Figure 5.5).

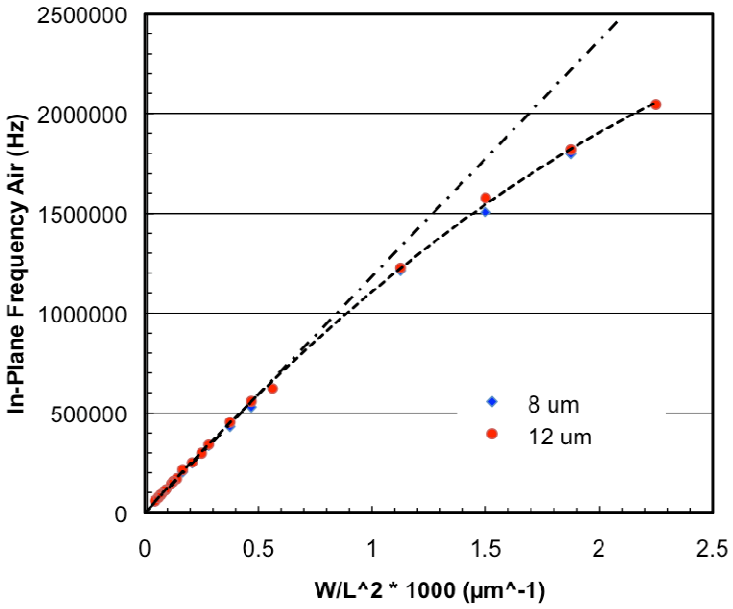

Figure 5.7: In-plane resonance frequency in air as a function of the width over length-squared ratio; symbols represent experimental data for cantilevers with silicon thicknesses of 8 and 12 µm. The dashed-dotted line represents FEM simulation results for an ideally clamped cantilever, the dashed line represents FEM simulation results for cantilevers with a silicon support structure as shown in Figure 5.5.

Figure 5.8 shows the Q-factor of the fundamental in-plane flexural mode in air as a function of the length-to-width (L/W) ratio for 12 µm thick cantilevers. Similar to cantilevers vibrating in their out-of-plane bending mode [5], an optimal L/W ratio appears to exist, with air damping reducing Q for larger L/W and support loss reducing Q for

smaller L/W. The highest measured quality factor of 4300 in air was obtained for a 90 µm wide, 400 µm long, 12 µm thick beam, i.e. for L/W ≈ 5. The measured Q-factors in air are approximately a factor of 3 larger than the one's for cantilevers with similar dimensions vibrating in the out-of-plane mode [5]. The reason why certain cantilevers around the "optimal" L/W ratio exhibit distinctly lower Q's is not understood yet and subject to further investigation; possibly, a close-by resonance mode lowers the measured Q for these cantilevers.

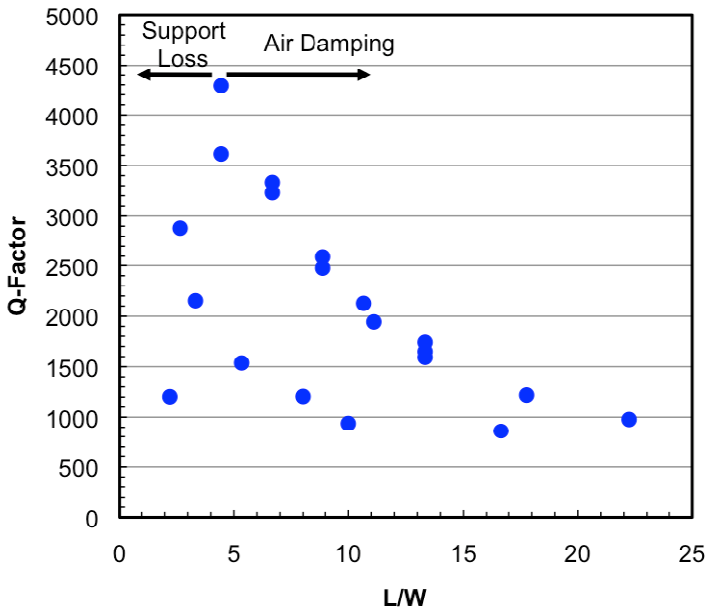

Figure 5.8: Q-factor of in-plane bending mode for cantilevers with 12 µm silicon thickness in air as a function of the length-to-width ratio.

Figure 5.9 shows the dependence of Q in air on the resonance frequency for two different cantilever widths (for various L values), again limited by air damping and support loss. The 90 µm wide devices reach a regime where they are support loss limited, which is why the Q drops dramatically for the shortest, i.e. highest frequency beam. The 45 µm wide cantilevers, on the other hand never reach a support loss limited region, and

thus maintain high Q at the higher frequencies. Thus, in particular 45 µm wide cantilevers with in-plane resonance frequencies in the low MHz range are expected to perform well as gas-phase chemical sensors.

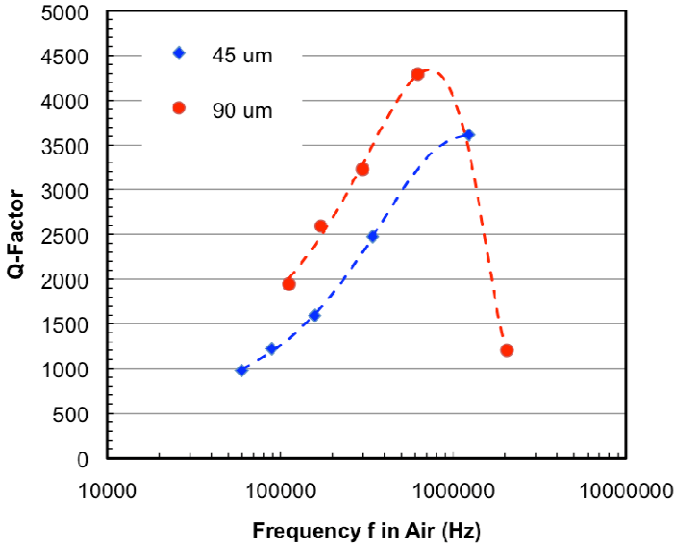

Figure 5.9: Quality factor of the in-plane mode in air as a function of the resonance frequency for 12 µm thick cantilevers in air. Results for both, 45 µm and 90 µm wide cantilevers are shown.

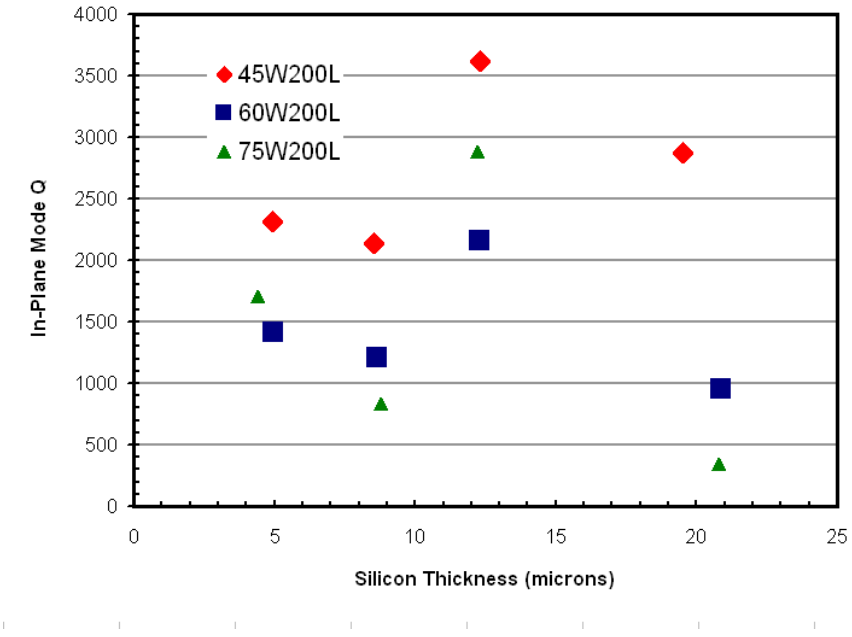

Figure 5.10: In-plane mode quality factor in air as a function of silicon thickness for 200 µm long cantilevers.

Further discussion will focus on the shortest and widest cantilevers, which were found to give the lowest limit-of-detection (LOD) when applied as sensors (see also Section 5.5). Figure 5.10 gives the cantilever Q-factor in air as a function of beam thickness for 200 μm long cantilevers of different widths and Figure 5.11 shows the same, but for beams that are 400 μm long.

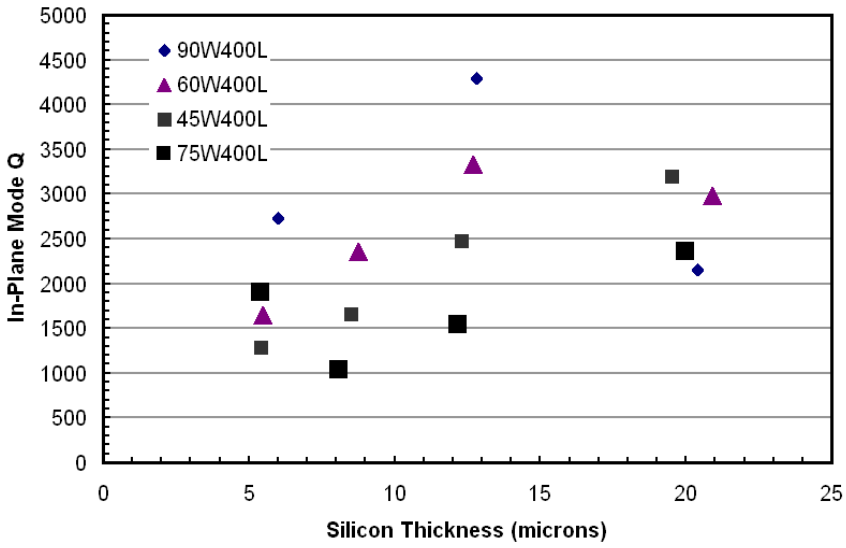

Figure 5.11: In-plane mode quality factor in air as a function of silicon thickness for 400 μm long cantilevers.

One effect visible from Figures 5.10 is that for the 200 μm long cantilevers, the 45 μm wide beams appear to exhibit the highest Q. This is somewhat counter intuative, one would expect to the widest beams to have higher Q because they store more energy per cycle (see Equation 3.1). Again, there is a tradeoff between energy storage in the beam's stiffness and energy loss through the anchor. The narrowest beams loose less of their energy through their clamped end, giving them a higher Q. In Figure 5.11 the 90 μm wide beams have the highest Q. The longer beams (400 μm instead of 200 μm) exbibit a

comparatively smaller energy loss through the anchor, i.e. the viscous loss becomes more dominant and the wider (and thicker) cantilevers show the largest Q-factors.

It should be noted that besides frequency stability (and thus Q-factor), the sensor limit-of-detection is affected by the sensor's sensitivity, i.e. the frequency change for a given amount of analyte loading on the resonator's surface (see Chapters 3 and 6). Thinner beams will exhibit a higher sensitivity because they have a lower starting mass. Thus, there will be an optimal silicon thickness for each lateral beam geometry (length and width) that optimizes the LOD. Sensor design considerations will be discussed in detail below (see Section 5.5)

5.5 Quality Factors and Resonant Frequencies in Water

The measured frequency transfer characteristic of the fundamental in-plane flexural mode for a 200 μm long, 45 μm wide, and 8 μm thick cantilever operated in water is given in Figure 5.12. For the same cantilever, the fundamental in-plane resonance frequency in air is 1212 kHz with a Q-factor of 2140 (see Figure 5.6); in water, the frequency drops by only 6.5 % to 1133 kHz with a Q-factor of 44 (determined from the 3-dB width of the amplitude transfer characteristic). While the Q-factor is reduced by a factor of ≈ 50 when immersing the cantilever in water, its value in water is significantly larger than those typically obtained for cantilevers vibrating in their out-of-plane flexural mode [24]. The measured resonant frequency in air and in water (Figure 5.12) is lower than that predicted by simple beam bending theory without fluid effects (see Equation 3.3); as discussed previously (see also Figure 5.7), this is expected because of the compliant support and the importance of shear deformations in addition to beam bending.

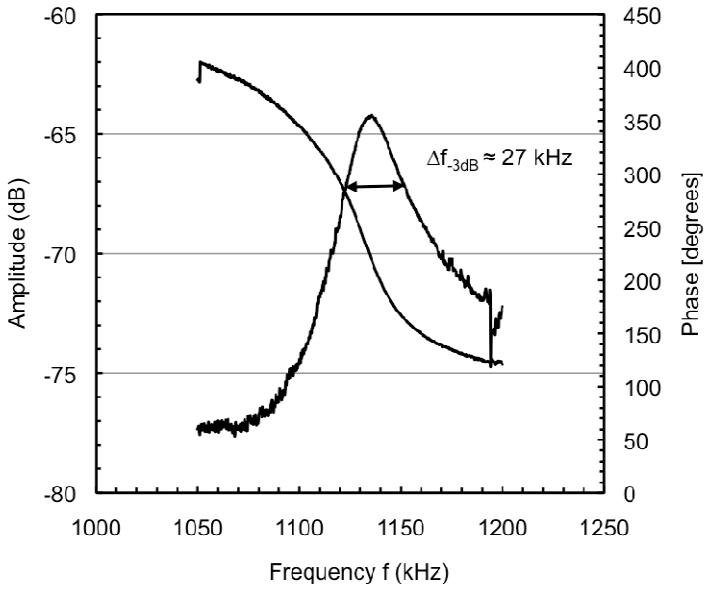

Figure 5.12: Amplitude and phase transfer characteristic for a 45 µm wide, 200 µm long and 8 µm thick cantilever in water.

Figure 5.13 summarizes the quality factor in liquid for all cantilever sizes tested. For a given device thickness, the Q-factor increases proportional to the square-root of the resonant frequency, i.e., proportional to $b^{1/2}/L$, as is predicted under the assumptions that viscous damping by the surrounding fluid is the dominating loss mechanism and that the non-ideal clamping and rotational effects are negligible [116, 133] (see Equation 3.17). Furthermore, for a constant in-plane resonance frequency (i.e., constant in-plane cantilever geometry), the Q-factor increases with increasing device thickness, again as expected from theory [116, 133]. The highest Q-factor of 86 was measured for a 200µm long, 75µm wide and 20µm thick cantilever. In summary, short, wide and thick cantilevers (i.e. the beams with the highest resonant frequencies) yield the highest Q-factors for the flexural in-plane mode in water. Because of the much larger viscous damping in water compared to the device operation in air, anchor losses play only a minor role in liquid for the cantilever dimensions investigated in this work.

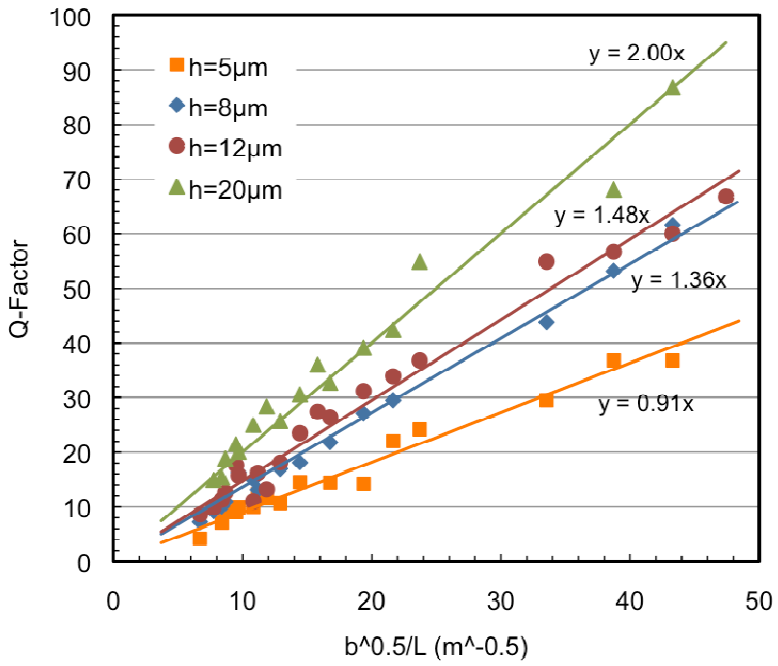

Figure 5.13: Q-factor of in-plane bending mode for cantilevers with 5, 8, 12 and 20 µm silicon thickness in water as a function of the square-root of the resonance frequency (square-root of beam width divided by length). (Lines are curve fits to the experimental data for a given device thickness.)

Figure 5.14 shows the observed frequency shift when immersing the cantilevers in water as a percentage of the resonant frequency in air as a function of the cantilever length divided by the square root of width (for all tested cantilevers). While there appears to be a general trend of reduced mass loading for higher-frequency devices (i.e. devices with smaller $L/b^{0.5}$ ratio), the mass loading by the surrounding fluid will be discussed in more detail in the following.

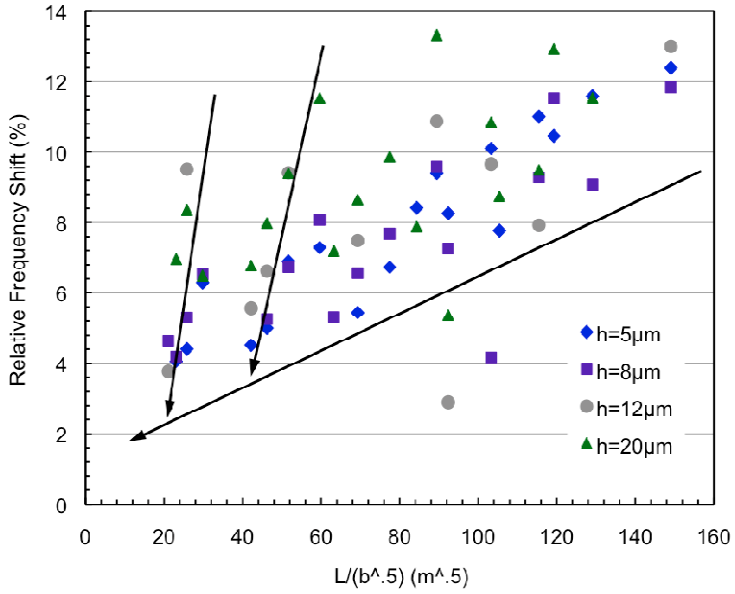

Figure 5.14: Relative frequency shift of the first in-plane flexural mode when immersed in water (compared to value in air) as a function cantilever length divided by the square-root of the cantilever width. Data are presented for cantilevers with silicon thicknesses of 5,8,12 and 20 µm.

While Figure 5.15 only shows data for cantilevers with a silicon thickness of 8 µm, Figure 5.16 summarizes the observed frequency shift for 400 µm long cantilevers having different widths and thicknesses. One can see that for both Figure 5.15 and Figure 5.16 the frequency shifts are linear when plotted against the cantilever length divided by the square root of the width; this is what is expected from theoretical models [133]. The experimental data show that short, wide and thin cantilevers exhibit the smallest frequency shift when immersed into water, i.e., the smallest added fluid mass. Put differently, as the cantilevers get wider and shorter, their resonance frequency increases, thus as the cantilever resonance frequency increases the amount of mass loading from the surrounding fluid decreases.

While the Q-factor affects the short-term frequency stability and thus the sensor resolution (see Eq. (1)), the frequency shift due to mass loading by the surrounding liquid

is an important consideration because it reduces the sensor sensitivity. Assuming that the resonance frequency is proportional to the square root of the effective mass-to-stiffness ratio for the particular resonant mode, the frequency change due to mass binding of a target substance on the surface of a gravimetric sensor is given by [23]

$$\Delta f = -\frac{1}{2}\frac{\Delta m}{m} f \qquad (5.5)$$

where Δf is the observed frequency shift due to the analyte's mass, Δm is the (effective) added mass associated of the target substance, m is the original effective mass of the resonator, and f is the original resonance frequency of the device (prior to mass uptake). Having a lower starting mass improves (increases) the observed frequency shift due to the analyte that one wished to detect. Thus, minimizing the mass loading on the beam by the surrounding fluid is important and is one of the main motivations for using in-plane rather than out-of-plane flexural modes. Measurements of the first out-of-plane mode with these devices show a frequency change on the order of 30-50% going from air to water. While the out-of-plane flexural mode is generally difficult to detect in liquid (due to the arrangement of the detection resistors), a small peak could be observed in liquid for some cantilevers, but its amplitude was too small to define the quality factor. By contrast, the relative frequency drop (from air to water) is as low as 4% for the in-plane mode (Figure 5.14).

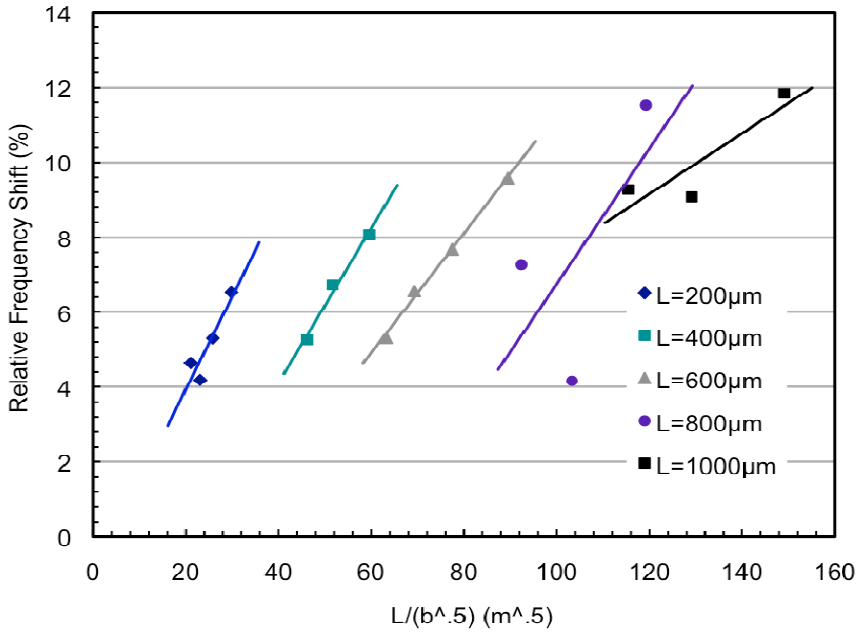

Figure 5.15: Percentage frequency shift of the first in-plane flexural mode when immersed in water (compared to value in air) as a function of the cantilever length divided by the square-root of the cantilever width for different lateral (in-plane) dimensions of cantilevers with an 8 µm silicon thickness.

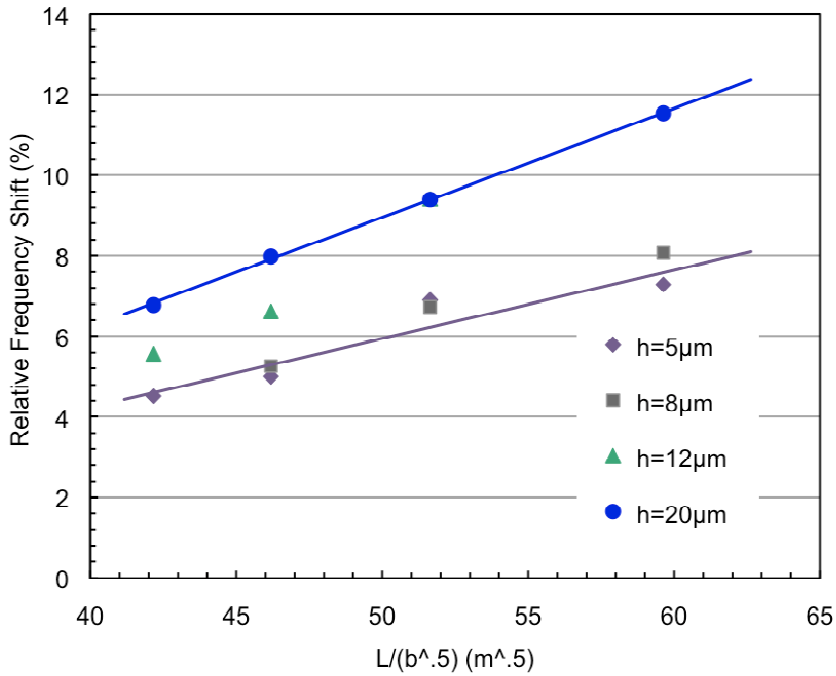

Figure 5.16: Percentage frequency shift of the first in-plane flexural mode when immersed in water (compared to value in air) as a function of the cantilever length divided by the square-root of the cantilever width for cantilevers with a length of 400 µm.

5.6 Special Cantilever Geometries: Hammerheads and Tuning Forks

In addition to standard cantilever beams with uniform cross-section, the tuning fork and hammerhead geometries presented in Chapter 3 were investigated. The motivation for the hammerhead design was originally that the larger wing area would provide a larger surface area for analyte binding. Subsequently it has been demonstrated that the normalized chemical sensitivity (i.e., the frequency shift normalized be the resonator's frequency) for any in-plane mode of a resonant microstructure with uniform layer structure is independent of the resonator's lateral geometry and only depends on the device thickness and layer stack [134]. Thus, the original motivation for investigating the hammerhead design was not supported by the experimental evidence. Yet, especially the smaller area hammerhead design (termed F150) exhibits a resonant frequency around 800 kHz, i.e. in the range where devices with good sensitivity and quality factor in liquid are generally located, making them excellent candidates for use as liquid-phase sensors (see Section 5.7 for further discussion). An additional advantage of the hammerhead structures is that they provide a large surface area outside of the high stress region (during cantilever bending) for ligand attachment. If a polymer is used as the sensitive film, placing the polymer only on the wing (and not on the support beam) can help reduce damping by the viscoelastic polymer film itself.

The motivation behind the investigation of the tuning fork structure was to first see if a tuning fork mode, where the tines vibrate against each other, could be excited using a thermal excitation and (preferentially) detected using a piezoresistive detection scheme. The tuning fork mode in theory allows for very little anchor loss because the motion of the tines cancels at the anchor meaning that less energy leaves the device

through the anchor. Thus, the second motivation for the tuning fork was to minimize the anchor loss compared to a similarly sized single cantilever.

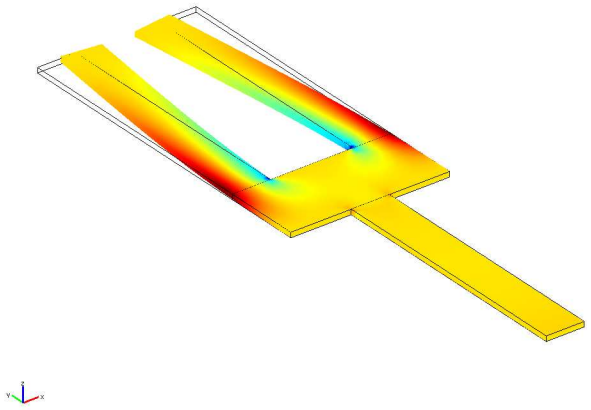

Figure 5.17: COMSOL simulation showing the vibrations of the tuning fork mode. The colors correspond to the y-directed stress distribution in the structure.

Tuning forks have found applications in micromachined quartz resonators [50, 119]. Thus, it was thought that they could also be successfully implemented in silicon. It was found that these devices can give a quality factor improvement of up to 30% in air over a cantilever with the same dimensions as the tines of the tuning fork.

FEM simulations, piezoresistive measurements, and laser vibrometer measurements were all used to characterize both the tuning forks and the hammerheads. Figure 5.18 shows the measured piezoresistive transfer characteristic of a 20µm thick F150 hammerhead device (see Chapter 4 for device shape and Appendix 6 for detailed dimensions), again clearly showing the effectiveness of the readout scheme for the desired in-plane mode compared to both lower-frequency out-of-plane and torsional modes. Tables 5.7 summarizes the resonant frequencies extracted from eigenmode analysis of the F150 hammerheads. Again, simulated and measured resonance frequencies match within 5%. Optical investigation of the in-plane resonance mode of a

20µm F150 hammerhead show Q-factors around 5000 in air and an in-plane vibration amplitude of 430 nm (at the device corner) for V_{AC} = 2 V and V_{DC} = 2 V. The measured out-of-plane vibration component at the in-plane resonance frequency of 796.8 kHz is about 10 nm for the same excitation voltages, i.e. at least a factor of 40 smaller than the in-plane amplitude. The Q-factor of the in-plane mode is more than a factor of 7 higher than that of the fundamental out-of-plane mode of the same device (Q = 650 at 511.6 kHz) and almost double the value of the first torsional mode (Q = 2880 at 464.3 kHz).

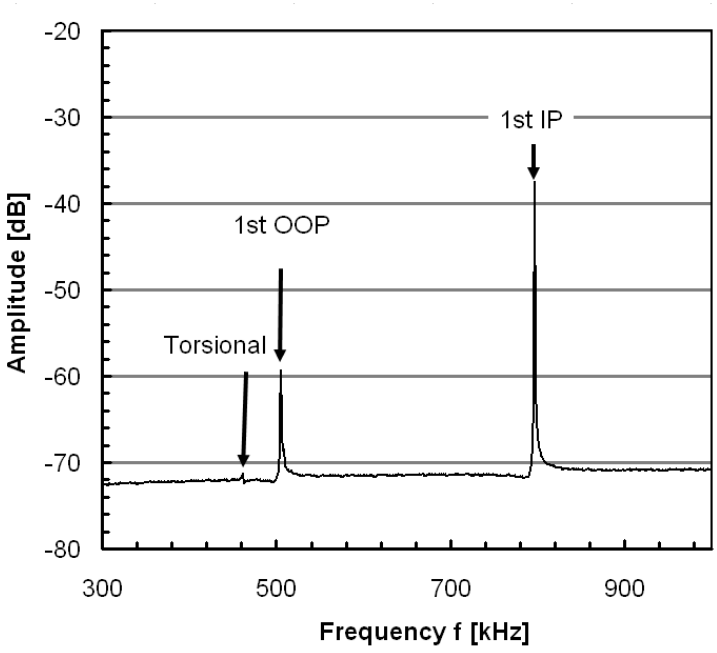

Figure 5.18: Piezoresistive transfer characteristic of an F150 hammerhead structure in air measured using the piezoresistive Wheatstone bridge.

Table 5.7: Simulated eigenfrequencies of a 20 µm thick F150 hammerhead in the range of 100-1200 kHz.

Mode	**1st Torsional**	**1nd OOP**	**1st IP**	**2nd OOP**
Frequency (kHz)	457.2	488.8	746.9	1136.9

More detailed measurements of the hammerhead structures were performed in both air and water for 8 µm thick F150S devices (the F150S design was preferred over

the F150 design for liquid testing). The tested resonators had a 3000 Å gold film on the surface for functionalization during biosensor testing. This gold film lowers the (in-plane) resonance frequency. Figure 5.19 shows the piezoresistive amplitude and phase transfer characteristic for the first in-plane mode in air. From the 3-dB bandwidth a Q of 3250 is extracted at the resonance frequency of 735 kHz. This Q-factor is smaller than the value of 5000 measured optically, because of the smaller device thickness and resulting lower inertia. A similar measurement performed in water yields an in-plane resonance frequency of 712 kHz (i.e. only a 3% reduction in frequency compared to the in-air data) with a Q-factor of 36.

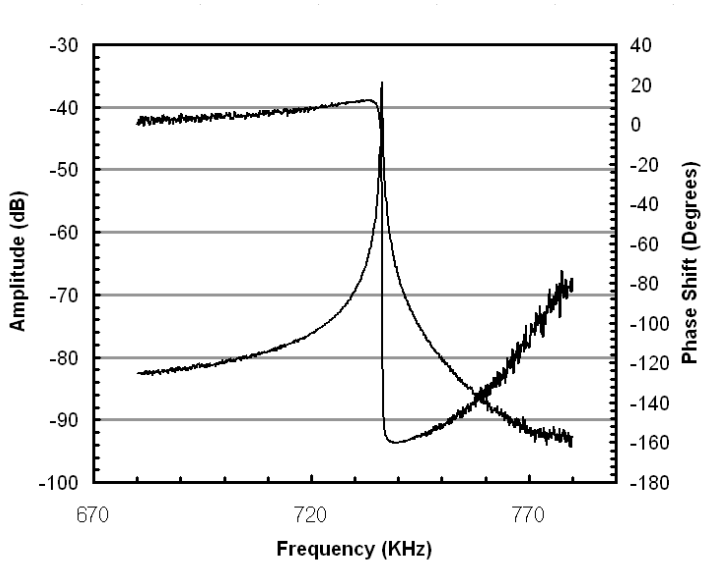

Figure 5.19: Transfer characteristic of in-plane mode of an F150S hammerhead structure in air measured using the piezoresistive Wheatstone bridge. This device has a 3000 Å thick gold layer on its surface for biochemical sensing applications. The Q-factor extracted from the 3-dB bandwidth of the resonance is 3250.

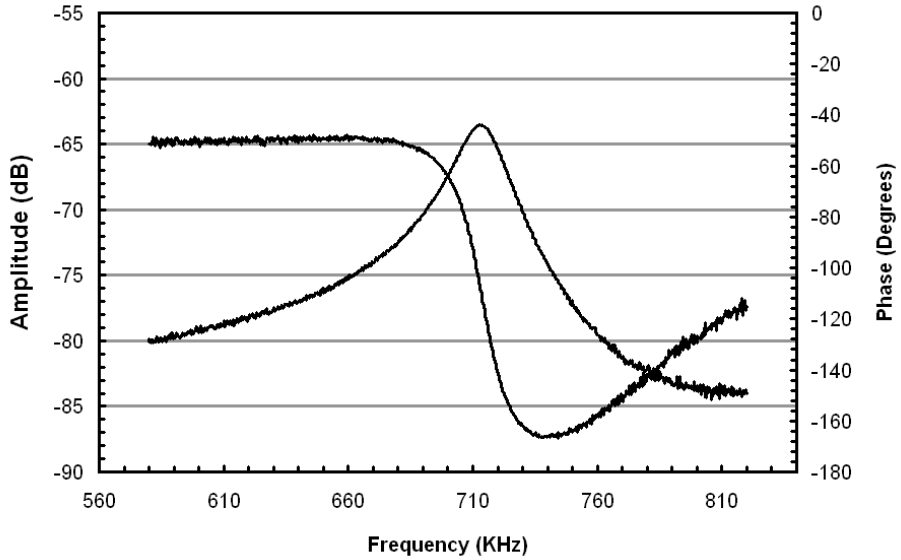

Figure 5.20: Transfer characteristic of in-plane mode of an F150S hammerhead structure in water measured using the piezoresistive Wheatstone bridge. This device has a 3000 Å thick gold layer on its surface for biochemical sensing applications. The Q-factor extracted from the 3-dB bandwidth of the resonance is 36.

Similar measurements that were performed for the hammerhead structures were also performed for the tuning forks. Figure 5.21 gives the piezoresistive transfer characteristic for a long and narrow tuning fork with an 8 μm silicon thickness (detailed dimensions can be found in Table 4.1 and Appendix 6) and Table 5.8 summarizes the simulated resonant frequencies for an 8 μm thick tuning fork. One drawback of the designed tuning fork structure is that they exhibit several resonant modes at frequencies lower than the desired tuning fork mode. More importantly, an out-of-plane and a torsional mode are close in frequency to the tuning fork mode. While the tuning fork mode still shows the strongest piezoresistive signal (see Fig. 5.21), these nearby modes can make it more difficult to excite the structure at the desired frequency and mode. Optical measurements using the Polytec MSA-500 were again used to investigate the vibration amplitudes: for a 20μm thick tuning fork, an in-plane vibration amplitude at the beam tip of 670nm was measured at the tuning fork mode (f = 419 kHz) for V_{AC} = 2 V

and V_{DC} = 2V. From the 3-dB bandwidth, a Q-factor of 4100 was extracted. The out-of-plane vibration component at the in-plane resonance mode was found to be less than 1nm, clearly demonstrating the effectiveness of exciting the desired tuning fork mode.

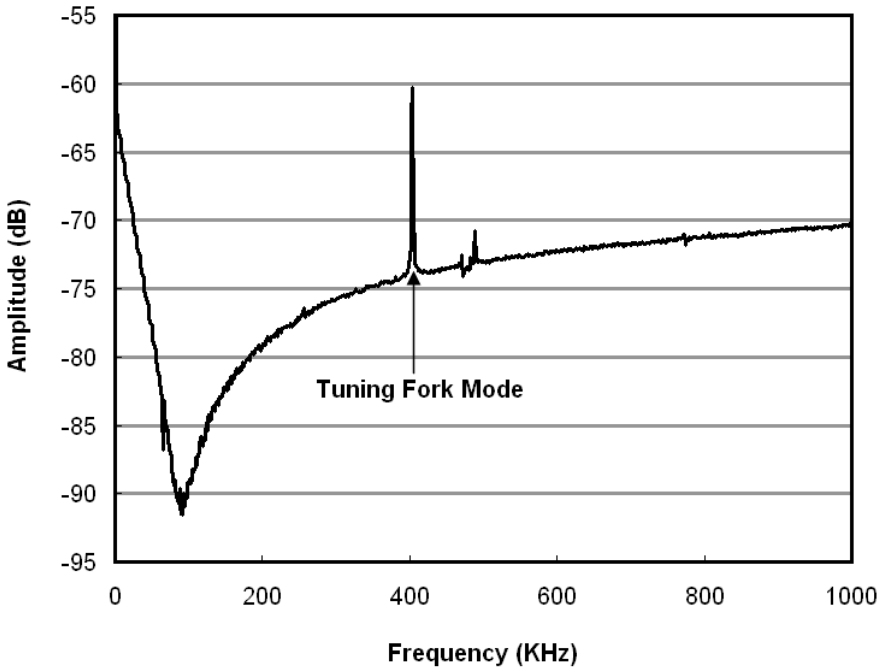

Figure 5.21: Amplitude transfer characteristic for an 8 μm thick, long and narrow tuning fork structure in air, measured using the piezoresistive Wheatstone bridge.

Table 5.8: Simulated eigenmodes of the narrow and long tuning fork structure (8μm thick). Not all of the modes are list here, just selected ones.

Mode	**1st OOP**	**1st Torsional**	**1st IP**	**3rd Torsional**	**TF Mode**	**4th Torsional**
Frequency (kHz)	8.84	46.3	65.5	391.8	402.4	410.5

Figure 5.22 shows the piezoresistive transfer characteristic of the tuning fork mode for an 8 μm thick, long and narrow tuning fork in air. This device has a Q of 2299 in air. A device with the same dimensions was characterized in water and the transfer characteristic is given in Figure 5.23. This structure has a Q of 29 in water, but also has 3000 Å of gold on the surface for sensor functionalization. Because the device tested in

water had a gold coating while the device tested in air had no gold coating, the resonant frequencies of both measurements cannot be directly compared.

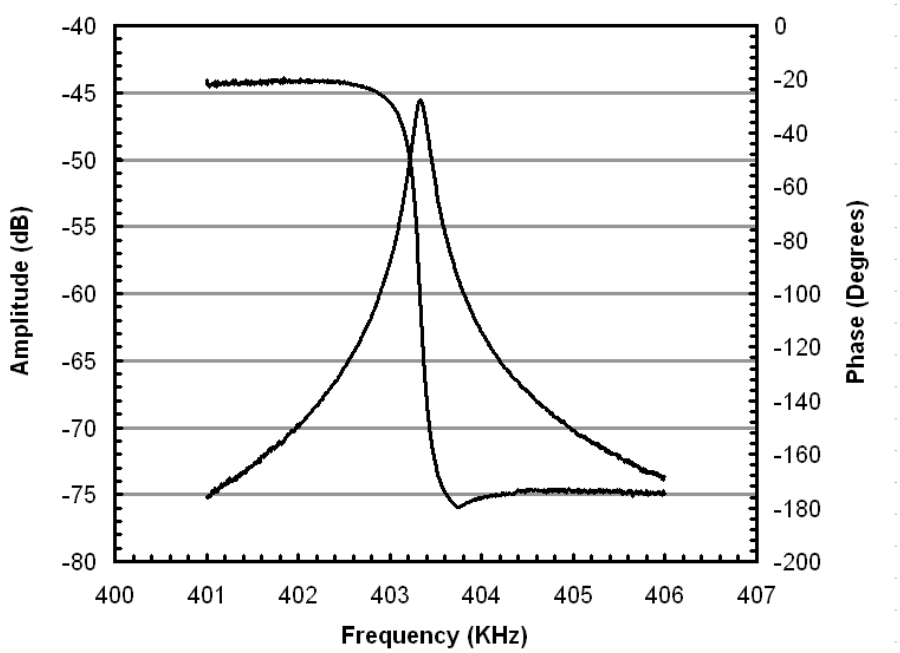

Figure 5.22: Amplitude and phase transfer characteristic for the tuning fork mode of a 8 μm thick, long and narrow tuning fork structure in air. The Q-factor extracted from the 3-dB bandwidth of the resonance is 2299.

The investigated hammerhead and tuning fork structures show that tailoring the lateral device geometry can in fact be useful in obtaining high quality factors for in-plane mode resonators. Although the designed tuning fork structures do resonate at the correct frequencies, they are too large and break easily. Further optimization of these resonators would be needed for the creation of robust liquid-phase sensors. Yet, the smaller area hammerhead structures do provide favorable characteristics for liquid phase sensors and will be discussed further in Section 5.7 below.

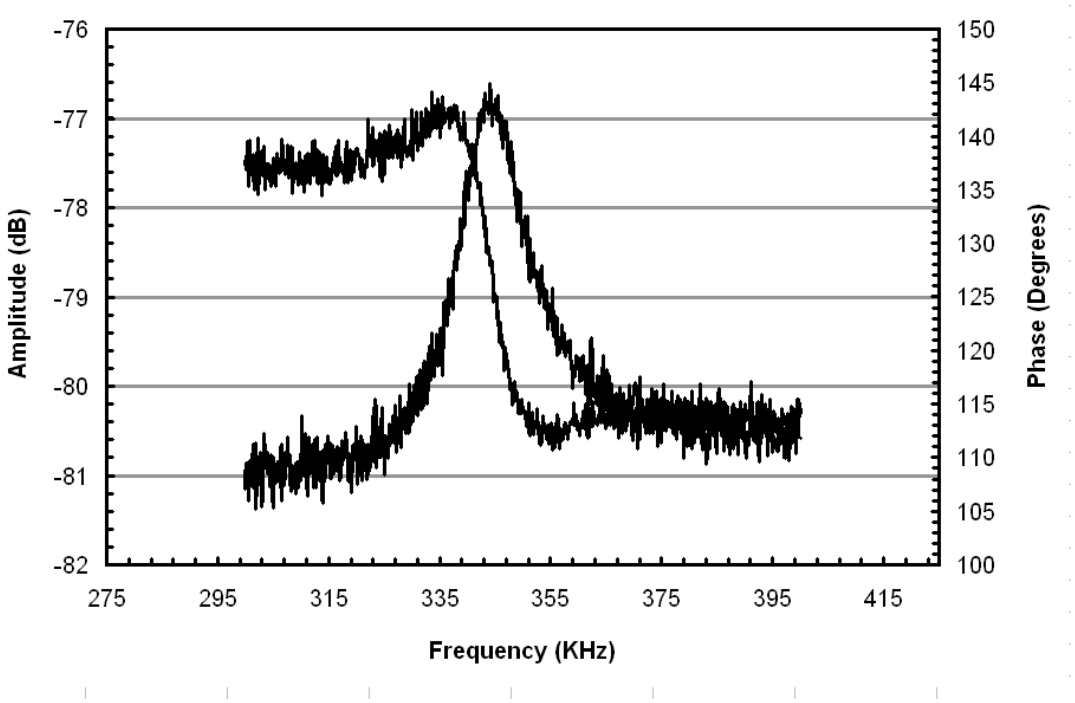

Figure 5.23: Amplitude and phase transfer characteristic for the tuning fork mode of a 8 μm thick, long and narrow tuning fork structure in water. This device has a 3000 Å thick gold layer on its surface for biochemical sensing applications. The Q-factor extracted from the 3-dB bandwidth of the resonance is 29.

5.7 Sensor Design Considerations

The quality-factor and frequency change due to mass loading in liquid do not give the entire picture when it comes to fabricating effective resonant sensors (for liquid-phase operation). As shown in Equation 3.18, the limit of detection for closed-loop operation is a function of both the short-term frequency stability (which is correlated with the resonator quality factor) and the sensor (chemical) sensitivity. The chemical sensitivity is the product of the gravimetric sensitivity G and the analyte sensitivity S_A, the latter depending only on the characteristics of the analyte sensitive layer. The gravimetric sensitivity G of the cantilevers has been simulated using the finite element software COMSOL. Using modal analyses, the in-plane resonance frequencies of cantilevers with different dimensions coated with a 2 μm polymer layer (density of 840 kg/m^3) have been

obtained and the gravimetric sensitivity was extracted by changing the polymer density (see Figure 5.24). It should be noted that the thermal oxide and PECVD passivation layers were not included in the simulations, nor were the effects of the surrounding fluid. The simulations show that shorter, wider and thinner beams yield the best gravimetric sensitivities.

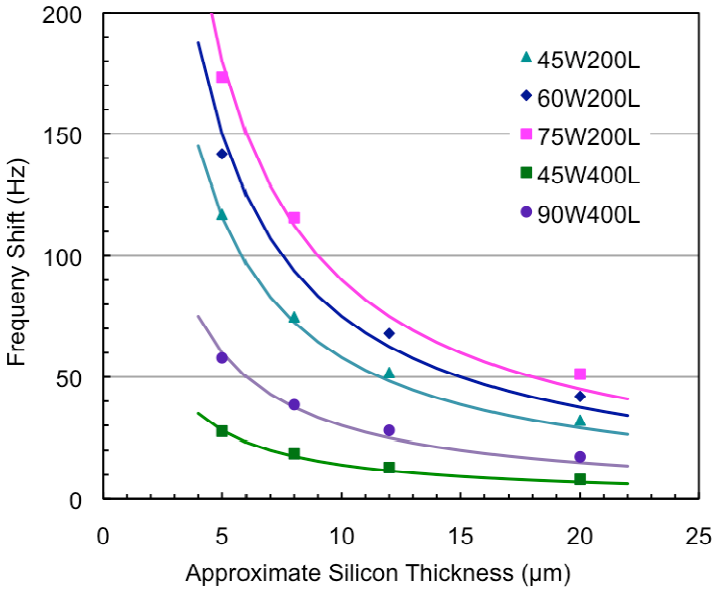

Figure 5.24: Simulated frequency shift as a function of silicon thickness for 200µm and 400µm long beams with different widths. The cantilevers were coated with a 2µm thick polymer film with a density of 840 kg/m^3. The gravimetric sensitivity of the devices was extracted from modal analyses performed using the finite element software COMSOL.

Wider and shorter cantilevers (i.e., those that are higher in frequency) have a higher quality-factor and lower frequency shift when immersed in water (indicating less mass-loading by the surrounding fluid). In addition, from Figure 5.24, it is evident that the shorter and wider beams also have a higher gravimetric sensitivity G. (As mentioned earlier, it should be noted that the relative gravimetric sensitivity G_R for the in-plane mode, i.e., the frequency shift per unit change in coating density, normalized by the

resonant frequency, is only a function of the layer thicknesses and not the lateral cantilever geometry, assuming devices with uniform layer sandwich [134].)

Figure 5.24 also indicates that thinner cantilevers will give a larger frequency drop for the same mass loading, i.e., the thinner beams have higher sensitivity than thicker ones (when comparing cantilevers of the same length and width). Thus, thinner cantilevers will improve both absolute and relative gravimetric sensitivity. However, from experimental data, we know that making the cantilevers thinner will degrade Q, which can have a large effect on the frequency stability and thus sensor resolution. For example, a 45 μm wide, 200 μm long cantilever with a measured Q of 36 in water has a measured short-term frequency stability of 2.9 Hz, while a 45 μm wide by 800 μm long cantilever (Q = 9.6) has a short-term frequency stability of approximately 70 Hz. The short-term frequency stabilities were measured using the Allan Variance method [117] at a gate time of 1 second. A general guideline from our experimental data is that *a Q of at least 25-35 is required for stable closed-loop operation in water*. The 8 μm thick devices have higher Q values than the 5 μm thick ones, which is a possible advantage of the slightly thicker beams. Nevertheless, examining the measured Q values (see Figure 5.13), some of the 5 μm thick devices could also be employed as liquid-phase sensors. The 200 μm long devices show the highest Q-factors in liquid; the measured quality factor plotted as a function of the silicon thickness for the three different widths of the 200 μm-long cantilevers is presented in Figure 5.25. In addition to the 200 μm long cantilevers, the F150 hammerhead structures with a radius of 150 μm show promise for use as liquid-phase biochemical sensors. These devices have a Q in the needed range with a silicon thickness of 8 μm. Since it can be shown that the gravimetric sensitivity of the 1st in-

plane mode is independent of the lateral geometry for a given layer sandwich, devices that have a resonant frequency in the 700-1500 kHz range give good properties for liquid-phase sensing (i.e. good sensitivity and quality factor).

Further, when considering the length and width dimensions, it appears that the shortest and widest cantilevers are best for sensor applications using the in-plane mode, i.e., a 75W200L cantilever would be preferred for liquid-phase sensing (see Figures 5.24 and 5.25). However, the higher stiffness of the shorter and wider beams, which is responsible in large part for their higher Q and frequency values, has its negative aspects as well: since all of the excitation resistors have the same resistance, each will dissipate the same amount of power as heat for the same heating voltage, and thus apply the same amount of bending force. Therefore, the wider and shorter beams (which have a higher stiffness) have a lower vibration amplitude when excited. This lower amplitude may make closed-loop operation far more difficult, if not impossible.

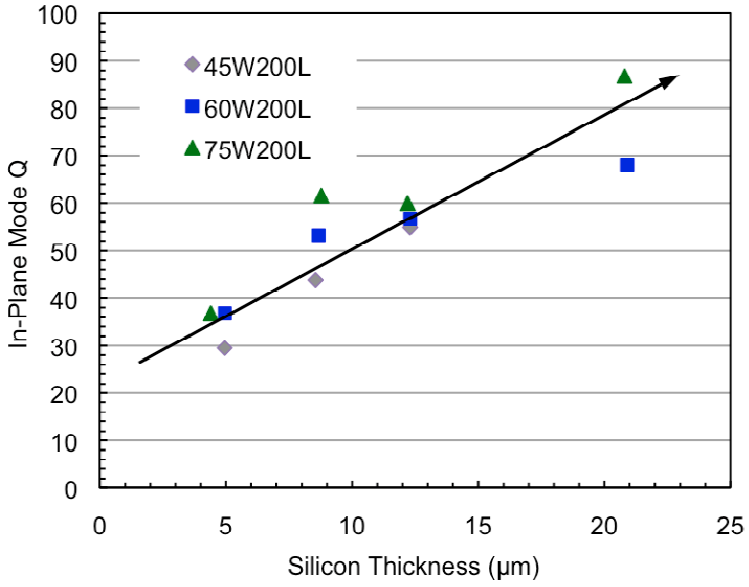

Figure 5.25: Quality factor as a function of silicon thickness for 200µm long cantilevers operated in water.

Higher heating powers could be used in order to excite stiffer cantilevers, yet this is undesirable for two reasons: (1) higher heating power would increase the power consumption of the devices, which is undesirable for in-situ applications; (2) temperature increase along the length of the cantilever is problematic for sensing applications because high temperatures can denature proteins and lower the partition coefficients of analytes in polymers used for chemical sensing. COMSOL (Stockholm, Sweden) simulations based on the currently used $1.5V_{pp}$ AC excitation and ±3V DC biases show a maximum temperature rise of ≈10 ˚C above room temperature on the cantilever surface.

In conclusion, twenty different cantilever length and width combinations were tested in water for the purpose of determining their resonant properties in in-plane flexure and their potential for liquid-phase chemical sensing applications utilizing this mode. For each of the length/width combinations, up to four different silicon thicknesses were tested. Using the measured frequency and Q-factor data and considering resonant sensor design objectives, it was determined that shorter, wider and thinner beams give the best sensing characteristics. Of the cantilevers and hammerheads tested here, the ones most promising for sensing applications are those having (in-plane) resonant frequencies in the 700-1200 kHz range, as evidenced by their combination of high quality factor and gravimetric sensitivity, while exhibiting stiffnesses sufficiently low that they could be excited thermally in liquid. In terms of thickness, the 5 μm- and 8 μm-thick beams demonstrated the greatest potential for sensing; however, one must ensure that the chosen device has a sufficiently large Q for stable closed-loop operation. Theoretical and experimental results indicate that, of the cantilevers tested, the 45 μm wide and 200 μm long devices with 5 μm or 8 μm thicknesses should yield the lowest limits of detection.

CHAPTER 6

CANTILEVER LIQUID-PHASE BIOCHEMICAL SENSOR TESTING

6.1 Testing Setup

For liquid-phase biochemical testing, cantilevers were fabricated and packaged using the methods described in Chapter 4.Two sample injection schemes are used to deliver analyte to the flow cell. In the first, luer-lok fittings are used to connect the flow cell to a three-way "T" that is connected to two syringe pumps (Figure 6.1). In the second, liquid is directly injected in the flow cell via a syringe attached to the top manifold (Figure 6.2).

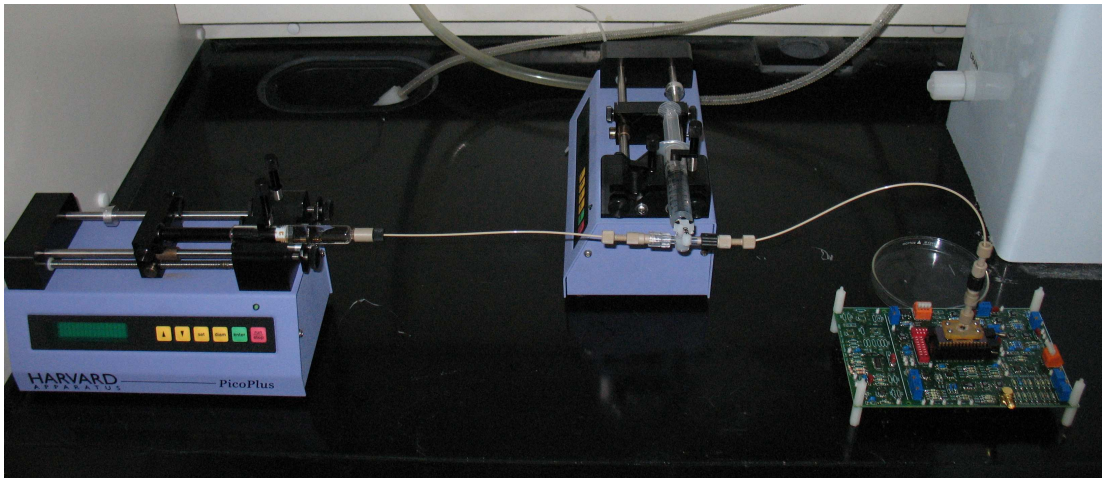

Figure 6.1: Flow cell connected to the measurement system with two syringe pumps.

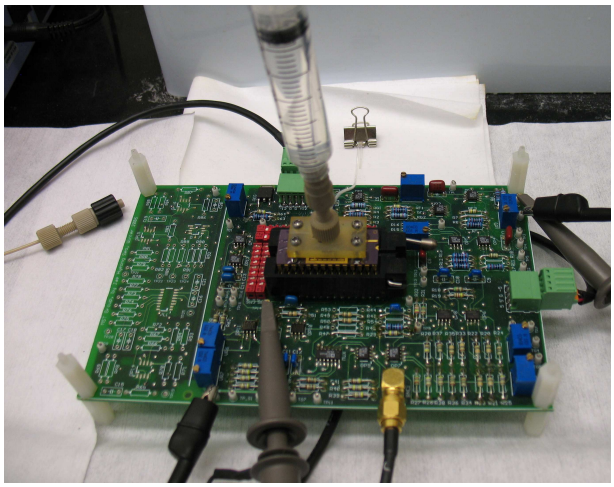

Figure 6.2: Flow cell connected to the closed-loop testing board. In this configuration fluid is injected by hand from a syringe.

6.2 Surface Functionalization

Depending on the biochemical sensing application, several different surface functionalization methods exist. The chosen method will depend on what type of film or molecule is needed on the device surface. Different chemistries are used to detect different types of analytes and the designer needs to choose the appropriate surface functionalization.

6.2.1 Polymer Films

Rubber-like polymers, such as polyisobutylene (PIB), polydimethylsiloxane (PDMS), or polyepichlorohydrin (PECH) enrich volatile organics and have long been used for chemical sensors [24, 81, 86]. In this work PIB and ethylene-propylene copolymer (EPCO) are used to detect volatile organics in the liquid-phase. The polymers are first dissolved in a solvent to facilitate placement on the resonator surface. The polymer solutions can be applied to the cantilever surface by spray coating using an air brush. For coating the cantilevers with polymer, the following procedure was used: a drop

of hexamethyldisilazane (HMDS) acting as an adhesion promoter was placed on the resonator die surface and allowed to dry. The cantilevers were then spray-coated on both sides with a 1% polymer solution using toluene as the solvent. Test samples were simultaneously coated for polymer thickness measurement. After coating, the dies were annealed for five minutes in a saturated toluene atmosphere to improve the film uniformity. The bond pads were masked off using tape during spray coating. For the liquid-phase chemical testing described in this work, the glue-on ring (see Chapter 4) was first placed on each die. After coating the dies were wire bonded into the package with the acrylic manifolds. Measurements of the obtained polymer thickness were performed on the test samples (blank pieces of silicon); the PIB coating was around 0.25µm thick on both sides, and the EPCO coating was 2µm thick on both sides (confirmed with an SEM). In contrast to PIB, it was found that EPCO layers could be applied up to a thickness of 2µm without delamination.

6.2.2 Protein Attachment

There are many available methods for surface functionalization of microdevices for biochemical sensing. In particular, two popular choices are silane chemistry [106] and gold-thiol chemistry [61, 135, 136] . Silane chemistry can be used to attach molecules to the surface of silicon [137], glass/dielectric [106, 138] materials and several other types of surfaces. Silane chemistry is versatile, but is not particularly selective with regards to the surface that it will attach molecules to. On the other hand the use of self-assembled monolayers (thiol chemistry) to attach proteins to gold is a highly selective strategy. If patterned gold surfaces are used then one can end up with a patterned protein or antibody

surface. Extensive work has been done on the creation of self-assembled monolayers (SAMs) on metals using organic compounds [139]. Since self-assembled monolayers from thiolated organic compounds will only form on a gold surface, gold can be deposited on the area of the cantilever that should be functionalized and the surrounding areas of the cantilever and the die itself ideally should not see any protein attachment. This helps to ensure maximum sensor signal because analyte will only attach to parts of system that are sensitive to it. For this reason, a gold-thiol chemistry was chosen for cantilever functionalization.

The developed functionalization protocol utilizes the formation of a carboxyl terminated SAM layer on a gold surface, followed by activation with N-(3-Dimethylaminopropyl)-N′-ethylcarbodiimide hydrochloride (EDC) and N-Hydroxysuccinimide (NHS). Finally, the activated carboxyl will bind to any amine group [140]. This strategy can be used to directly attach proteins, antibodies, or other biomolecules to the surface of cantilevers. In the case of antibodies, preserving the bioactivity is essential, and thus the antibody needs to be attached in the correct orientation. This can be accomplished by first attaching protein A to the surface. Protein A selectively binds to the FC region at the base of the antibody thus anchoring the antibody to the surface [135]. On the other hand, DNA or other nucleotides can be thiolated at one end and directly attached to a gold surface using gold-thiol chemistry. In addition, aptamers are an increasingly important class of nucleotide-based receptor molecules [7]. They are nucleotides with the correct sequence so that they selectively bind to a protein of interest. These receptors show high selectivity and are far more stable than protein based chemistries [7]. Aptamers could be attached to the cantilevers using

the strategies outlined above.

The implemented functionalization protocol is outlined below, currently proteins and antibodies are attached to the beam surface, and thus in biosensor tests the antibody to the attached protein is detected. The protocol was developed starting from [135, 136, 140] with modification, functionalization experiments were performed on 5 cm by 5 cm silicon squares with a 2000 A thick gold layer on top of a 100 A thick titanium film (for adhesion). In particular, the incubation time for each reagent, the concentrations of the NHS and EDC and the pH of the NHS/EDC solution needed to be adjusted. Confocal microscopy images of a functionalized gold substrate (treated with BSA-FITC) and a control (which was treated with protein only) are shown below in Figure 6.3. The images were taken with a 40x objective, and have a footprint of roughly 230μm by 230μm, and the control and the experimental sample were imaged using the exact same microscope settings. The microscope was focused on each sample separately before imaging. (This same method was used to capture all of the confocal images shown below). One can see that compared to the control, the functionalized sample shows protein attachment. Further analysis with X-ray photoelectron spectroscopy (XPS) has also been performed to confirm protein attachment.

Materials

Thioctic acid (99%), Phosphate buffered saline (PBS), fluorescein isothiocyanate conjugated bovine serum albumin (BSA-FITC), Bovine Serum Albumin (BSA) (>98%), Anti-BSA, (N-(3-Dimethylaminopropyl)-N′-ethylcarbodiimide hydrochloride (EDC) (BioXtra), N-Hydroxysuccinimide (NHS) (98%), and 2-(N-Morpholino)ethanesulfonic

acid hydrate, 4-Morpholineethanesulfonic acid (MES)(Biotechnology Performance Certified 99.5%), IgG and anti-IgG FITC were all obtained from Sigma-Aldrich(St. Louis, MO). Acetone, methanol and isopropanol were supplied by Georgia Tech's NRC cleanroom. 200 proof ethanol (99.5% ACS reagent) was obtained from Acros Organics(Geel, Belgium). All chemicals were used as supplied.

I. SAM Formation.

1. Pre-clean gold samples: 10 min in acetone, 2 min in methanol, 2 min in isopropanol, dry with nitrogen. Treat for 5 min in oxygen plasma at 100 sccm in the plasma cleaner.
2. Incubate gold substrates in a 250mM Thioctic Acid in absolute ethanol solution(200 proof ethanol) for 24 hrs. Substrates are placed directly into the SAM solution after cleaning in the oxygen plasma, there is not a significant amount of time between cleaning and placing the substrates into solution.
3. Rinse substrates with 200 proof ethanol from a squirt bottle, dry with nitrogen.

II. Crosslinking of SAM Layer

4. Treat Substrate with a Solution of 15mM of NHS + 75mM EDC + 40mM NaCl in .1M MES buffer for 1 hour. Solution pH should be around 5.7. (8.6mg NHS, 72mg EDC, 97.6mg MES, and 11.7 mg NaCl in 5ml of DI H_2O)

III. Protein Attachment

5. Immerse substrates in 0.4mg/ml protein (BSA or Protein A) in (phosphate

buffered saline) PBS for 2 hours at 2-4 °C. The solution pH was 7.4)

6. Rinse substrates in DI water and dry. (This step is performed only on samples to be imaged.)

(a) 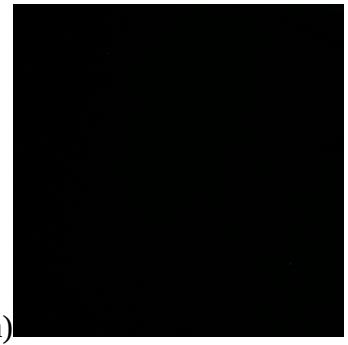 (b) 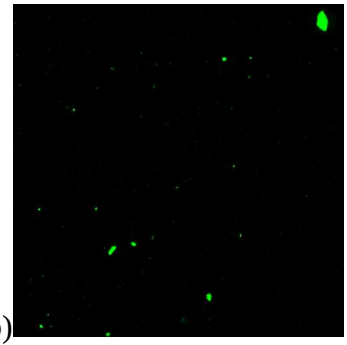 (c) 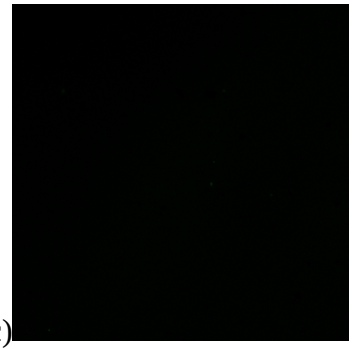

Figure 6.3: Confocal microscopy images of functionalized gold surfaces. (a) treated with SAM and crosslinker, (b) treated with SAM, crosslinker and BSA-FITC, and (c) treated with BSA-FITC only. The images are approximately 230 μm on each side.

Table 6.1: XPS results from a surface functionalization experiment. The presented data are the integrated area under each XPS peak from a survey scan. The area numbers given above are proportional to the amount of each element on the gold surface. The XPS samples are the same samples shown in the confocal images in Figure 6.3.

	Blank	**SAM only**	**SAM+ Crosslinker**	**SAM+Crosslinker + BSA-FITC**	**BSA-FITC only**
C1s	530167	31627	240628	564710	378183
N1s	81931	0	54193.55	174935	154525
O1s	524528	730869	435266	743968	809813
S2p	0	136162	65115	91761	0

As mentioned above, the functionalization has been verified using confocal microscopy and XPS. The combination of the confocal images and XPS results show that protein is being conjugated to the surface. (The confocal images show a more dramatic difference between samples on a full screen in a dark room.) The confocal images show fluorescent protein on the sample treated with the functionaliztion protocol, while very little fluorescence is visible on the sample treated with crosslinker, but without protein,

and also on the sample treated with protein only (all the images were taken with the exact same microscope settings). This indicates that the crosslinker treatment does not fluoresce and also that there is little non-specific binding of the protein to a gold surface. Further evidence that the functionalization attaches protein to a gold surface is shown below in Figure 6.4. In this image the mean fluorescent intensity is measured inside the red circle for both the functionalized and control samples (the control was treated with protein only). The functionalized sample has a mean fluorescent intensity of 10.1 at a standard deviation of 15.5, while the control has a mean fluorescent intensity of 2.3 at a standard deviation of 1.4

(a) 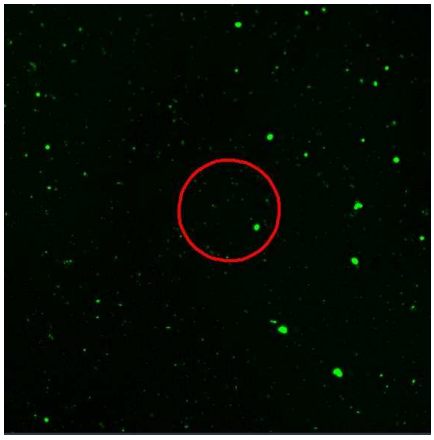 (b) 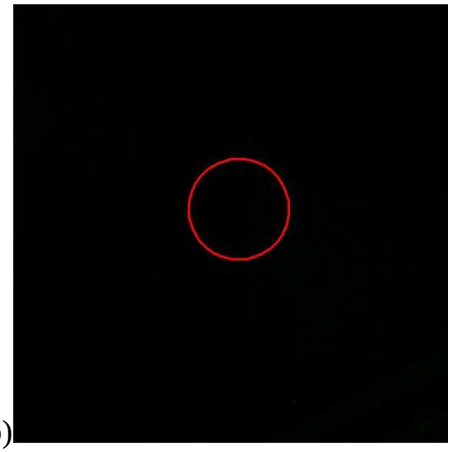

Figure 6.4: (a) Confocal microscope image of a sample treated with the protocol outlined above and (b) a control sample treated with BSA-FITC only

.

The XPS results (see Table 6.1) indicate that the fluorescent objects on the sample treated with the functionalization protocol are protein. The larger nitrogen and carbon peaks from the functionalized sample in comparison to both the crosslinked sample and the sample treated with protein only suggest that what is seen on the surface of the functionalized sample is protein. The oxygen measurement in the XPS data shows a larger peak on the protein-only sample compared to the functionalized sample; this is

somewhat unexpected, as proteins contain oxygen and one might expect the functionalized sample to also have a larger oxygen peak. One possible explanation is that some of the oxygen on the functionalized sample is in a different bonding state than that would show up in a O1s peak, making the signal smaller. (These additional oxygen peaks may not be significant on the survey scans used to collect this data.) Some sort of contamination may also be possible. (This may also explain the somewhat larger than expected N1s peak.) It is also possible that the buffer used for protein incubation somehow oxidizes the bare gold surface.

As indicated by the experimental results, it is important that multiple techniques are used to confirm protein attachment. Using one technique, such as confocal microscopy, could lead to false results because some materials will auto-fluoresce giving a false positive. Alternatively, XPS is more time consuming to use, and surface contamination can lead to inaccurate results. The advantage of XPS is that it gives elemental information so that it can be used to confirm that the SAM formation or crosslinking (both of which do not fluoresce) is working. Ultimately, the combination of approaches allows the investigator to have some redundancy and multiple ways to confirm that the functionalization is working.

The efficiency of the EDC-NHS crosslinking system is pH dependant (Sigma-Aldrich Data Sheet). Thus, selecting the correct pH for the reaction is essential for good surface coverage. The crosslinking reaction works best in acidic solution, with a pH range between 4 and 6. To achieve this, an acid buffer (morpholino)ethanesulfonic acid (MES) is chosen; the 0.1 M MES buffer solution by itself has a pH of 3.5, and sodium chloride (NaCl) can be added to the buffer to adjust the pH upwards. (The chlorine in the NaCl is

a weak base.) In order to investigate the effect of pH on the crosslinking reaction, six different 0.1 M MES solutions were prepared with different sodium chloride concentrations. The pH based on the NaCl concentration can be calculated using the Henderson-Hasselbalch [25] equation and the results are summarized in Table 6.2.

Table 6.2: Tested NaCl concentrations and the corresponding calculated MES buffer pH values.

Solution #	**NaCl Conc, (mM)**	**pH**
Solution 1	0	3.55
Solution 2	2	4.4
Solution 3	10	5.1
Solution 4	40	5.7
Solution 5	150	6.28

Table 6.2 gives the different sodium chloride concentrations that were tried and the pH of the resulting crosslinking solution calculated using the Henderson-Hasselbalch equation. For the experiment, each sample was treated the same for the SAM formation and protein attachment steps, but for the crosslinking step each sample was placed in a different crosslinking solution for one hour. An unfunctionalized control was also used. Figure 6.5 shows confocal microscopy images giving the results of the experiment. As a result of this experiment, a sodium concentration of 40mM was chosen for the functionalization protocol given above.

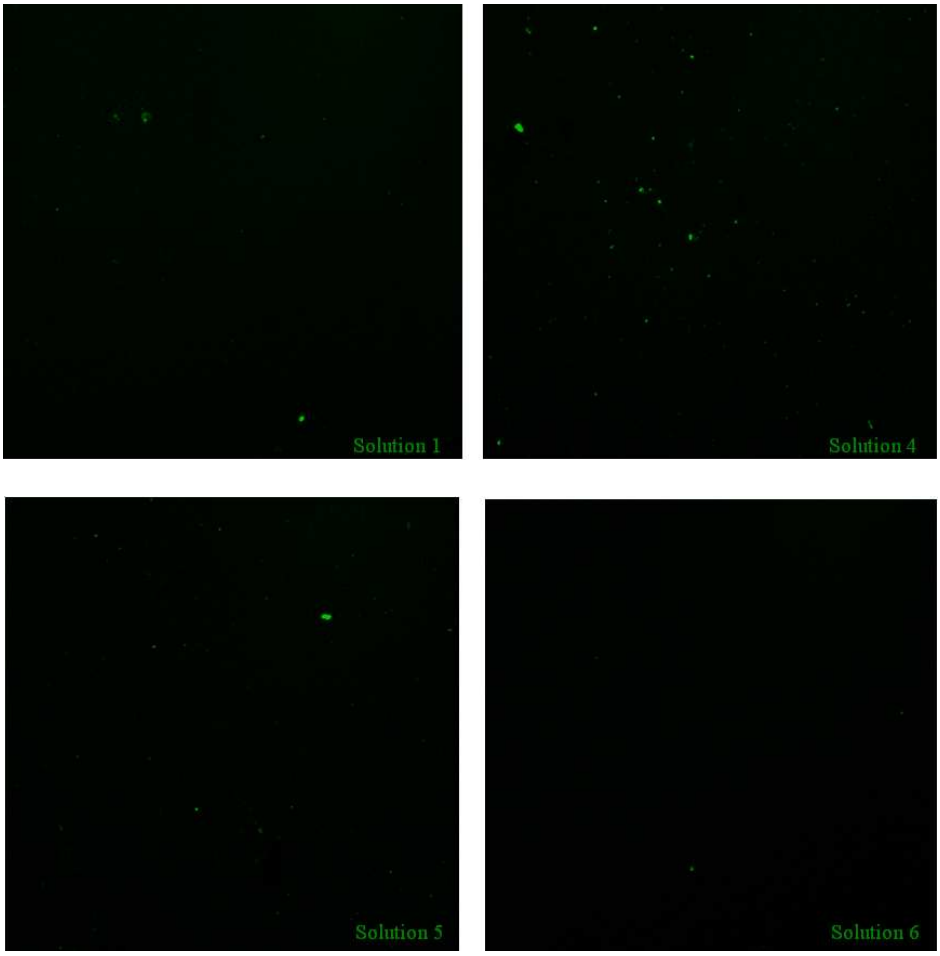

Figure 6.5: Images from the pH optimization experiment (described above). The pH of each solution is given in Table 6.2. Solution 4 clearly gives the best surface coverage as evidenced by the fluorescent signal.

In addition to optimization of the pH, there is also an optimal concentration for the protein solution in the protein attachment step. If the protein solution is too dilute, activated molecules on the SAM layer will not be bound with protein. Conversely, if the protein solution is too concentrated, then the surface will be saturated with non-specifically bound proteins. Non-specifically bound proteins can cause inconsistent results because analytes will be bound to a layer this is not well controlled. For optimization of the protein solution concentration, five different protein solutions were made, and samples were functionalized using the protocol above, with each sample

receiving the same treatment during the SAM formation and crosslinking steps, but with each sample being incubated in a different protein solution. The results were analyzed using confocal microscopy. (Nonspecifically bound protein appears as large clumps in the confocal images.) Based on the results a protein solution concentration of 0.4 mg/ml was chosen.

A surface functionaliztion protocol has been developed, but there is ample room for further improvement. The results (see Figures 6.3-5) show that the presented protocol does work but more optimization is needed. To further improve the functionalization protocol a more quantitative method of analyzing the experimental results is needed. This could be either via comparing the number of counts for nitrogen, carbon, and sulfur from the XPS, or finding a more quantitative method of analyzing the confocal microscopy results such as measuring the light intensity at different locations on the experimental samples and comparing them to the control. An additional possibility is doing AFM analyses at several locations on the gold surface to determine the surface coverage of the protein. More details on what has been tried regarding surface functionalization can be found in Appendix 1.

6.2.3 Enhancement Using Carbon Nanotubes

SAM formation on a gold surface is a common method of ligand attachment for the creation of sensors. A major advantage of this method over other methods is that it allows for protein attachment to only the portion of the device where the gold is deposited. A drawback is that SAM formation is only a two-dimensional process, and does not allow attachment of thicker layers of protein. Thus, a SAM layer will bind far

less analyte from solution than a 3-dimensional structure, limiting sensitivity. To allow ligand attachment in three dimensions without needing to incorporate the molecule into some sort of matrix (e.g., a polymer), carbon nanotubes (CNTs) can be grown on the surface of the resonators. The ligands can then attach to the CNTs, which are three dimensional, increasing the amount of receptor molecules on the device's surface. In addition, if a functionalization chemistry that is selective for carbon is chosen, then the protein will only attach to areas of the die that contain CNTs, in a similar fashion to the gold-thiol chemistry. In fact, functionalization protocols have been developed for carbon nanotubes that rely on activation of the carbons comprising the CNT's [25, 141]. The activation forms carboxyl groups from these carbons and subsequent crosslinking of those carboxyl groups using the same EDC-NHS chemistry from Section 6.2 can allow for protein attachment to the CNTs. A second method of ligand attachment entails designing molecules that wrap around the tubes themselves [142]. In the present research, CNT growth has been demonstrated on the in-plane cantilevers making this functionalization strategy possible. To be compatible with the in-plane resonators, the CNT growth has be performed at temperatures below 450 °C.

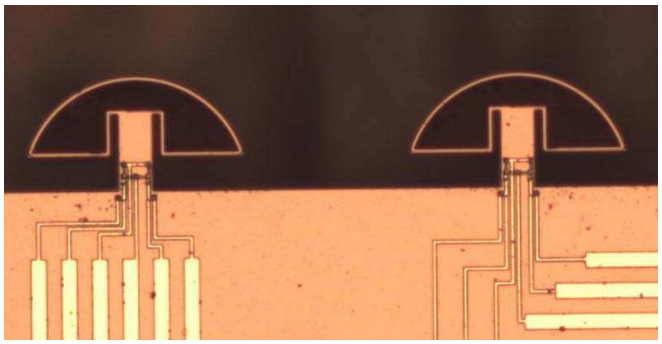

Figure 6.6: Photograph of hammerhead structures with CNTs deposited on the wing area, (seen in black on resonator wing).

To prepare for the CNT growth, two modifications were needed to the bulk micromachining process presented in Chapter 4. First, the SiO_2/SiN_x passivation stack deposited by plasma enhanced chemical vapor deposition (PECVD) needed adjustment. Since this film is deposited at a lower temperature than the CNT growth, the subsequent higher temperature processing could potentially alter the stress distribution in the individual PECVD layers, resulting in bent cantilevers after the CNT processing. To prevent this from happening, the PECVD oxide and nitride layers were annealed at 450°C after deposition. The stress in both films was measured after annealing using the wafer curvature method. Because oxide and nitride films have opposite stress signs, the layer thicknesses could be chosen to give approximately zero total stress in the passivation film. The second process modification was the deposition and patterning of a nickel film as catalyst for the CNT growth on top of the hammerhead structures.

The low-temperature CNT growth was performed in an AIXTRON Black Magic PECVD system using a nickel catalyst at 450°C (Figure 6.6). The catalyst was deposited using e-beam evaporation and patterned using lift-off prior to the KOH etching step used to release the microstructures (see Chapter 4.). Prior to CNT growth the wafer was diced, and individual dies were placed in the Black Magic PECVD, instead of the entire wafer. For CNT growth, individual dies were first annealed in an H_2 plasma at 450°C; then the plasma was turned off and the CNTs were grown in a flow of pure acetylene at 450°C for 75 minutes (growth process similar to [143]). The resulting CNT layer was roughly 0.5-1μm thick (Figure 6.7).

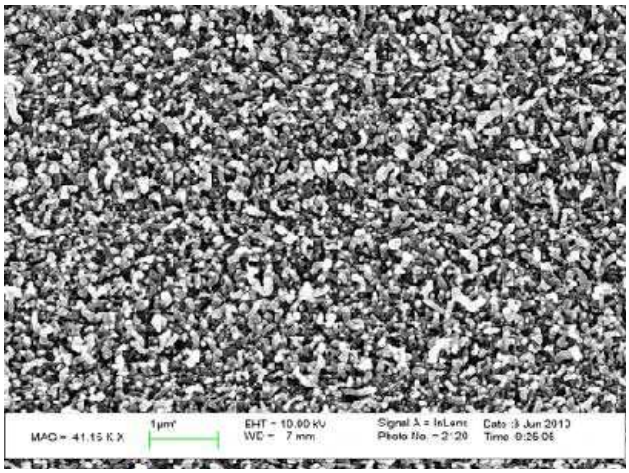

Figure 6.7: SEM image of carbon nanotubes grown using a low-temperature process at 450˚C.

To demonstrate a gas-phase chemical sensor using the CNT cantilevers, the CNTs could be functionalized with different peptide sequences to make them sensitive to different volatile organics (VOCs). The cantilevers were functionalized with specific peptide sequences designed to select between different VOCs based on their polarity. The peptides have two regions, one region is meant to bond with the CNT and the other region is a repeating sequence of identical amino acids (i.e. threonine). For CNT functionalization, the peptides were dissolved in distilled water at a concentration of .24 µg/µl. A nanoliter quantity of peptide solution was placed on a cantilever in the Bioforce Nanoenabler. For peptide functionalization of the CNTs, the cantilever in the tool deflects against the die surface depositing a drop of fluid. Because such a small quantity of peptide was used, measures must be taken to prevent evaporation during the deposition process. These steps included using an atmosphere of 75% humidity in the Bioforce and also adding 10% v/v glycerol to the peptide solution. To facilitate the chemical reaction between the section of the peptide that interacts with the CNT and the nanotubes themselves the cantilevers were annealed in 75% humidity for at least 15 minutes after coating. Before use, each cantilever die was rinsed in pure DI water and dried. For testing,

each die was wire-bonded into a 28 pin DIL package. The devices were used the same day that the peptide functionalization was performed in order to avoid possible issues with peptide degradation.

6.3 Chemical Sensor Testing Results

Once fabricated and diced, the devices were sprayed coated on both sides as described in Section 6.2.1. The dies were then wire-bonded and packaged using acrylic manifolds as described in Chapter 4. As shown in Figure 6.1 luer-lok fittings are used to connect the flow cell to a three-way "T" that is connected to two syringe pumps. Fluid exits the flow cell through a piece of silicone tubing routed through the top manifold.

For electrical operation during liquid-phase chemical testing, the cantilevers were placed in an amplifying feedback loop that has previously been described [103]. Phase adjustments and signal gain adjustments are set to ensure device oscillation. A Schmidt trigger at the output of the circuit creates a square wave that allows the frequency to be read using a digital counter. A gate time of one second is used for measurement, but further averaging using MATLAB (MathWorks, Natick, MA) allows studying the effects of varying the gate time. All of the measurements were done using 75μm wide, 400μm long, and 7.5μm thick cantilevers covered by an approximately 1.2μm thick silicon dioxide and silicon nitride passivation layer and a 0.6 μm thick thermal oxide layer; the cantilevers also had an approximately 300nm thick gold layer deposited at the surface. For liquid operation, the heating resistors were biased with 4V DC, which was superposed with a 1.6 V peak-to-peak AC signal; the bias used for the Wheatstone bridge was 2V (See Fig. 3.1.b.1). The two excitation resistors and four Wheatstone bridge resistors all have a resistance of approximately 500-700 Ω. The quality factor of the

EPCO-coated cantilever was measured in water after packaging and was determined to be around 40.

M-xylene (99.9+%, HPLC grade), trichloroethylene (99.5+%, HPLC grade), benzene (99.5% HPLC grade), dichloropropane (99.5% HPLC grade), epichlorohydrin (99.5% HPLC grade), dichlorobenzene (99.5% HPLC grade), tetrachloroethylene (99.5% HPLC grade), ethylbenzene (99% GC grade) and chlorobenzene (99.5+%, HPLC grade) were purchased from Sigma-Aldrich (St. Louis, MO). Chloroform (99.5% spectraphotometric grade) was purchased from Alpha Aesar (Ward Hill, MA). Toluene (ACS grade) was purchased from EMD (Gibbstown, NJ). Carbontetrachloride (certified ACS grade) was purchased from Fisher Scientific (Houston, TX). All chemicals were used as supplied. Deionized water (R = 18.2 MΩ·cm at 25 °C) was used for preparation of all solutions and for equilibration/regeneration of the sensing membranes. Poly(isobutylene) (PIB) and poly(ethylene-co-propylene) (EPCO) were purchased from Sigma-Aldrich (St. Louis, MO). Toluene (J.T. Baker HPLC grade) was used as a solvent to prepare the polymer solutions. 100% hexamethyldisilazane (HMDS) was purchased from Shin-Etsu MicroSi (Phoenix, AZ), and was used as supplied.

The sample solutions were individually prepared just prior to analysis by dissolving known amounts of the volatile organics in degassed and deionized water. The 1% (w/v) PIB and EPCO polymer solutions used in this work were dissolved in toluene at constant stirring for 4 hrs.

Figure 6.8 presents the effect of the flow rate on the sensor sensitivity. For these measurements a 75 ppm m-xylene solution was injected at various flow rates ranging from 40 to 200 μL/min and the sensitivity was extracted from the sensor response. The

measurements were performed using an EPCO-coated cantilever and a 75 ppm m-xylene solution. The sensitivity increases with increasing flow rate, and finally levels off at higher flow rates. The data in Figure 6.8 suggests that at lower flow rates mass delivery to the measurement chamber is not fast enough to compensate for absorption by the packaging materials.

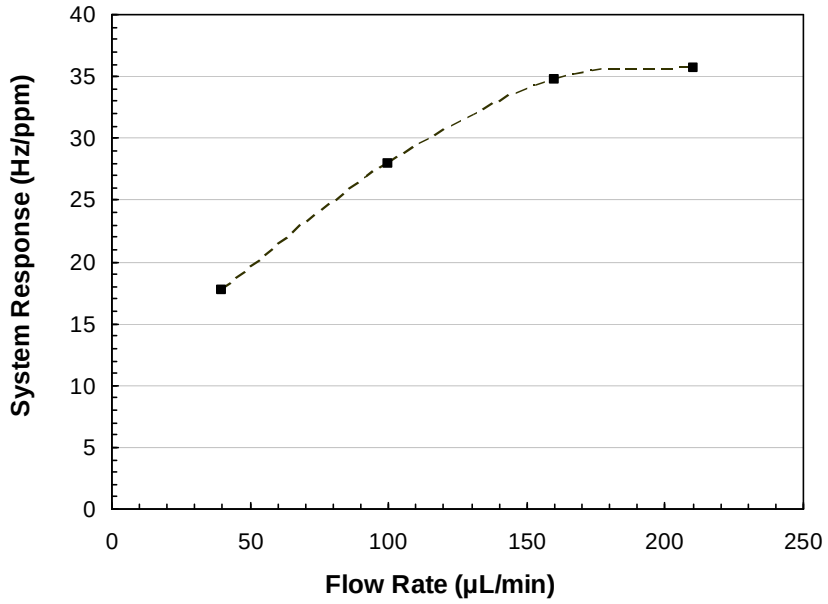

Figure 6.8: Sensor sensitivity as a function of the analyte flow rate for an EPCO-coated cantilever exposed to a 75ppm m-xylene solution.

During spray coating, not only the cantilever but the entire chip surface is partially coated; thus, the chemically sensitive polymer is present throughout the package, not just at the cantilever surface. Hence, polymer present within the chamber, and possibly also the gasket material at the inlet may absorb analyte, thereby changing the solution concentration encountered by the cantilever. At higher flow rates, mass delivery to the flow cell is sufficiently high to compensate for any absorption within the flow cell, and the sensor sensitivity thus becomes independent of the flow rate. Based on these

results, a flow rate of 200µL/min was selected for all measurements. It should be noted that despite possible analyte enrichment silicone gaskets were used here, as they provide excellent sealing to the die; however, in a final device design the cantilever die would be glued into the manifold and packaged using epoxy, thereby rendering the entire package more chemically inert.

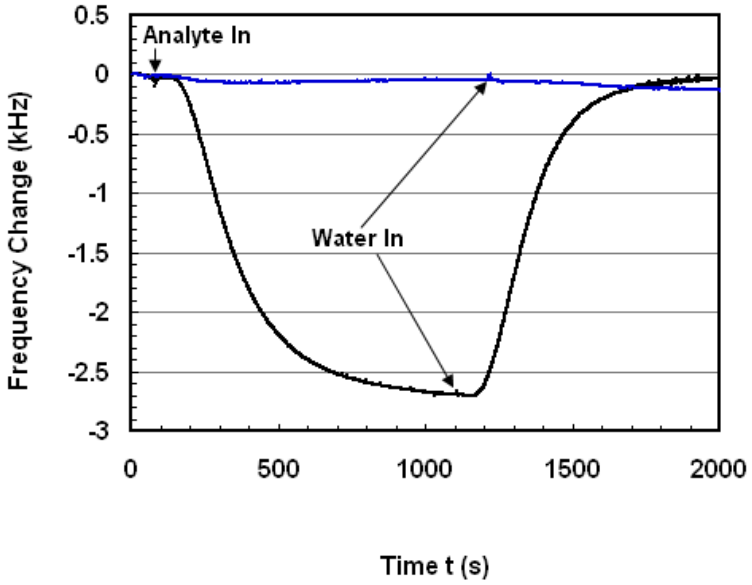

Figure 6.9: Frequency change of an uncoated 45 µm wide, 200 µm long reference cantilever (blue line) and a 75 µm wide, 400 µm long EPCO-coated cantilever to subsequent flow of 75 ppm m-xylene solution (starting at Analyte In) and DI water (starting at DI Water In). The uncoated device had a resonance frequency of 109 0kHz in water and the coated device had a resonance frequency of 426 kHz in water.

Figure 6.9 compares the frequency change of an uncoated 45µm wide, 200µm long and 7.5µm thick cantilever to that of an EPCO-coated (2µm coating on each side of the cantilever) 75µm wide, 400µm long and 7.5µm thick cantilever, each exposed to a 75ppm m-xylene solution at a flow rate of 210µL/min. Clearly, the response of the uncoated cantilever is substantially smaller than that of the coated device, indicating that the measured frequency changes are caused by analyte partitioning into the polymeric

sensing material, and not due to e.g. a density or viscosity change of the surrounding fluid. The small frequency drift evident for the uncoated reference cantilever is most likely a thermal drift.

Figure 6.10 shows a sample measurement for the EPCO-coated cantilever, i.e. the frequency change of the cantilever following two subsequent exposures to a 5ppm tetrachloroethylene solution. After exposing the sensor to the analyte solution for approx. 800sec, the measurement chamber is flushed with DI water for approx. 800sec. When conducting these measurements, the syringe pumps were switched from analyte solution to DI water and vice versa once the measured frequency change was <30Hz within 3min indicating that the analyte concentration in the polymer layer had almost reached equilibrium.

The recorded data shows the signal transients during analyte absorption and desorption cycles. The baseline drift is mainly caused by temperature effects, and may be considered negligible compared to the magnitude of the analyte response. Thermal drifts may be further minimized by appropriate measures for temperature stabilization, e.g. via thermoelectric heating/cooling. The measured frequency shift in response to a 5ppm tetrachloroethylene solution was approximately 370 Hz, which yields a sensitivity of approximately 75 Hz/ppm. A detailed estimation of the LOD is given below.

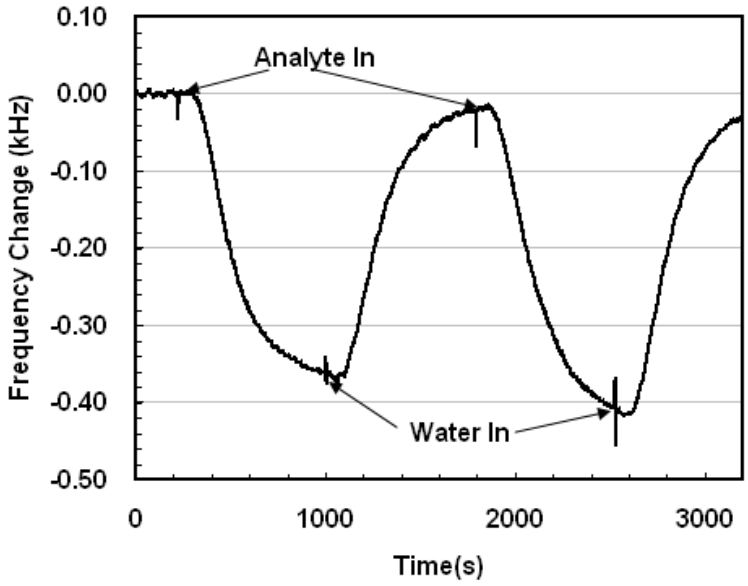

Figure 6.10: Response of EPCO-coated cantilever, i.e. frequency change vs. time, to two subsequent exposures to a 5 ppm tetrachloroethylene solution. The resulting sensitivity is approx. 75 Hz/ppm. The spikes at the top and bottom of the peaks are due to pressure transients when the pumps are switched. The device tested here had a resonance frequency of 426 KHz in water.

For direct quantification of m-xylene, trichloroethylene, and chlorobenzene in water using PIB and EPCO sensing layers, six calibration curves were obtained (Figures 6.11(a), 6.11(b) and 6.11(c)). For each analyte, four concentrations in the range of 0 to 150 ppm(v/v) were analyzed in duplicate with error bars representing the calculated standard deviation. The achieved sensitivities were derived from linear regressions y = m*x with zero intercept, and are provided in Figures 6.11(a), 6.11(b) and 6.11(c). The goodness of the fit (R^2) is typically around 0.99. Evaluating Figures 6.11(a), 6.11(b) and 6.11(c), it appears that the EPCO polymer layer provides superior enrichment properties for the tested analytes in contrast to PIB. However, the EPCO membrane thickness was eight times the PIB membrane thickness due to better film adhesion of EPCO, and thus, the obtained sensitivities need to be normalized by the film thickness for comparison.

Given the experimental results, it is evident that EPCO provides favorable properties as a sensing membrane given the increased membrane thickness that may be applied and the resulting increase in sensitivity. Analyzing Figure 6.11(a), it is evident that the error bars for the highest concentration of m-xylene for both EPCO and PIB layers are significantly larger than the error bars at lower concentrations. This is attributed to the polymer layer approaching saturation, and thus, producing less repeatable results. The error bars for the measurements shown in Figure 6.11(b) and 6.11(c) are minimal, thereby indicating excellent measurement reproducibility. The ability to establish robust calibrations provides evidence that these microresonators may be successfully applied for the quantification of VOCs for *in situ* water monitoring applications.

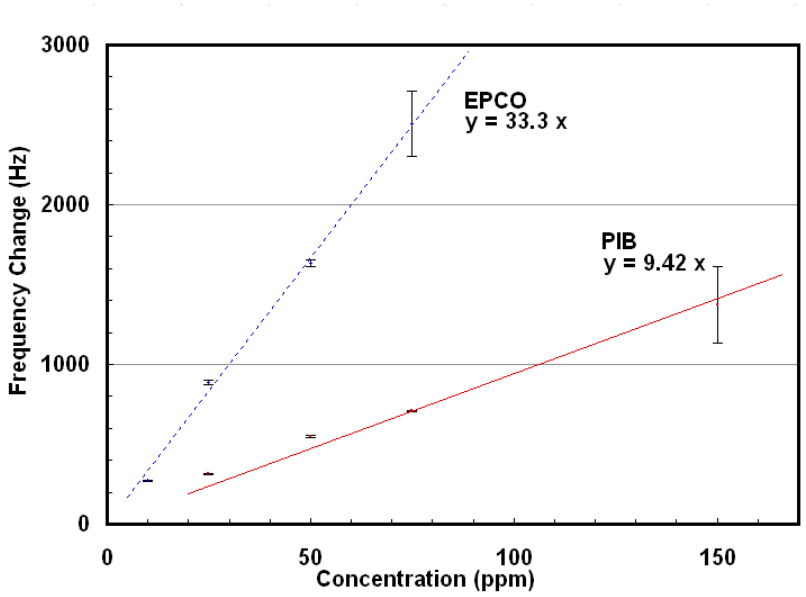

Figure 6.11(a): Measured frequency change of EPCO (blue symbols) and PIB-coated (red symbols) cantilever systems as a function of the m-xylene concentration in water. The lines are linear fits to the measurement data according to the equation given in the graph.

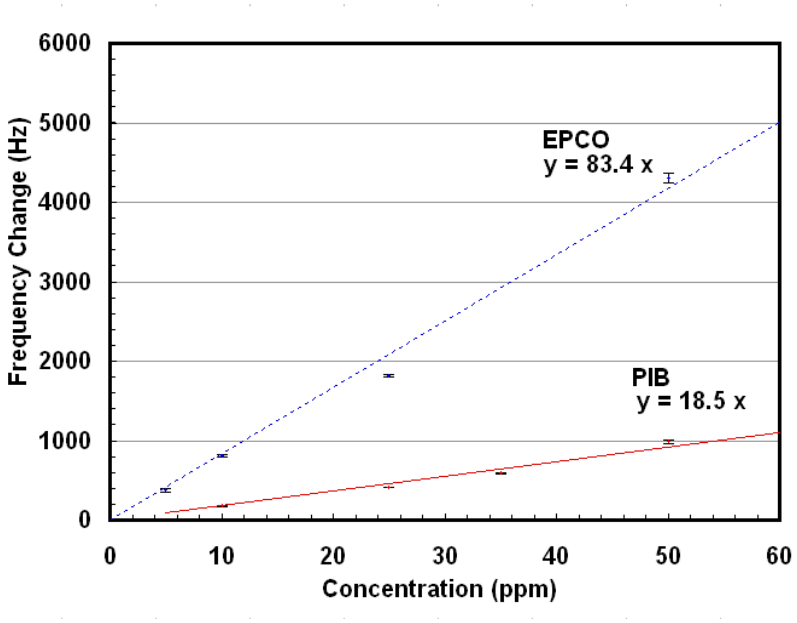

Figure 6.11(b): Measured frequency change of EPCO (blue symbols) and PIB-coated (red symbols) cantilever systems as a function of the tetrachloroethylene concentration in water. The lines are linear fits to the measurement data according to the equation given in the graph.

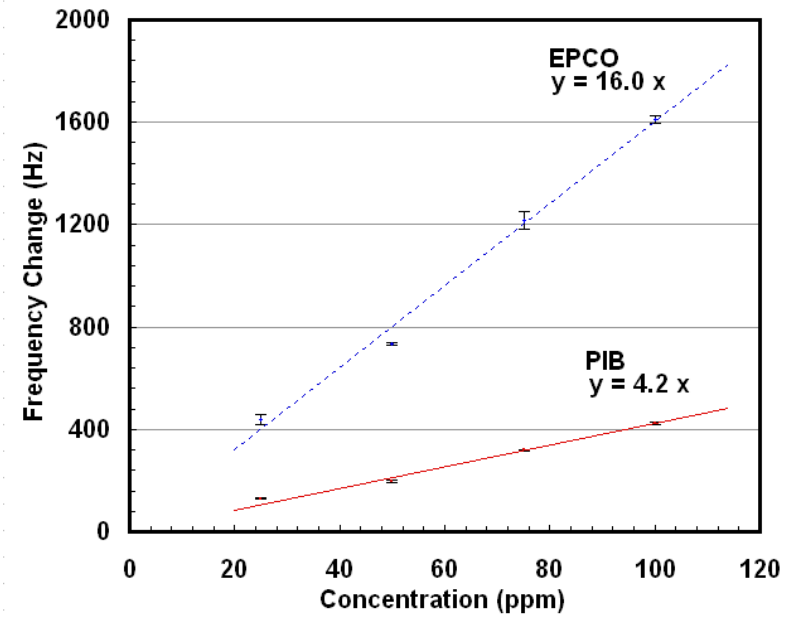

Figure 6.11(c): Measured frequency change of EPCO (blue symbols) and PIB-coated (red symbols) cantilever systems as a function of the chlorobenzene concentration in water. The lines are linear fits to the measurement data according to the equation given in the graph.

The measurements used to create the calibration curves were performed in random order, sometimes with higher concentration solutions being measured before lower concentrations or vice versa. A flow rate of 200 μL/min was used for all the measurements. The random order of the measurement helps to address the concern that the materials used for packaging may be absorbing analyte, and changing the concentrations within the flow cell. If this were the case, linear calibration curves could not be created from the data because if a lower concentration solution were measured after a higher concentration one, then analyte could desorb from the packaging during the lower concentration measurement making the concentration higher than expected and making the response not fit with other measurements.

The obtained experimental results are summarized in Table 6.3.

Table 6.3: Calculated limits of detection for volatile organics measured in water based on the presented measurements.

Chemical	**EPCO LOD (ppb)**	**PIB LOD (ppb)**
m-Xylene	113	289
Tetrachloroethylene	46	170
Chlorobenzene	224	690
Chloroform	3600	5800
Ethylbenzene	144	570
Toluene	376	1100
Epichlorohydrin	10900	25000
Dichlorobenzene	43	(Not Tested)
Trichloroethylene	341	(Not Tested)
Benzene	1400	(Not Tested)
Dichloropropane	980	(Not Tested)
Carbontetrachloride	216	(Not Tested)

The EPCO-coated device provided a frequency stability of 1.1 Hz, and the PIB-coated device had a stability of 1.0 Hz, both determined using the Allan variance method at a

gate time of roughly 4 sec in water. While all the measurements were performed at a gate time of 1 sec, the data was averaged for a 4 sec gate time using MATLAB (Mathworks, Natick, MA).

As further evidence that the presented chemical sensor results are valid and match what is expected, a finite element approach (COMSOL) has been used to model the gravimetric sensitivity of in-plane-mode cantilevers. Using a modal analysis, the in-plane resonance frequency of a polymer-coated silicon cantilever was calculated as a function of the polymer density. For 75 μm wide, 400 μm long, and 6.3 μm thick silicon cantilevers -- as also experimentally used in the present study -- with a 1.2μm SiO_2/SiN_x passivation layer and a 0.3 μm gold coating, the calculated gravimetric sensitivity is 35 Hz/(kg m^{-3}) in the case of a 2 μm EPCO coating at both sides of the cantilever; the simulated first in-plane resonance frequency is 482.2 kHz in vacuum. The simulation does not account for changes in resonator stiffness due to the analyte absorption; while this is a reasonable assumption for the case of thin polymeric films on top of silicon resonators as studied herein, stiffness effects may substantially change the characteristics of a mass-sensitive sensor for other conditions [129].

If the analyte concentration is given in ppm(v/v), the analyte sensitivity S_A may be calculated using Equation 3.21. In the case of chlorobenzene detection (ρ=1.11gcm^{-3}) using an EPCO membrane, a liquid-phase partition coefficient of approx. 320 [144] yields an analyte sensitivity of 0.36 (kg m^{-3})/ppm. Similarly, calculated liquid-phase partition coefficients for PIB and several other analytes have been reported in [145]. For the cantilever tested in this work, the resulting sensitivity becomes 13 Hz/ppm. As is shown (Figure 6.11(c)), this value is close to the experimentally determined sensitivity of

16 Hz/ppm. The discrepancy is likely attributed to a thicker polymer layer on the tested cantilever, or due to a larger than expected partition coefficient. Theoretically, the sensitivity may be improved by using thicker sensing membranes. However, in the case of liquid-phase operation, membrane adhesion limits the possible thickness of the chemically sensitive polymer film. In the case of the EPCO coating used here, the maximum film thickness without loss of adhesion was determined at approximately 2 µm. By coating both sides of the cantilever, the overall film thickness could be doubled without adhesion loss.

Limits of detection were calculated using Equation (3.18). While for the analytes shown in Figures 6.11(a), 6.11(b) and 6.11(c) detailed calibration curves were established, the sensor sensitivity to further analytes was extracted from single concentration measurements. It is important to note that the calculated limits of detection are specific to the system tested here, and further optimization using e.g. alternative cantilever geometries may allow for further lowering the achieved limits of detection.

From the presented data, the distinct advantages of using the in-plane mode are evident. The estimated LODs around 100 ppb represent a roughly one order of magnitude improvement compared to values reported for out-of-plane cantilevers in water [24]. From equation (3.18), the limit of detection for a resonant sensor is a function of the short-term frequency stability divided by the sensitivity; using the first in-plane mode results in a significant improvement in both sensitivity and stability. The measured quality factors in liquid for in-plane mode cantilevers are four times higher than those reported for out-of-plane mode devices in liquid. In addition, as evidenced by the reduced frequency shift in liquid compared to air (10% for the in-plane mode vs. 50% for the out-

of-plane mode), the added fluid mass affects the device performance much less for in-plane mode devices. Thus, compared to out-of-plane cantilevers, the gravimetric sensitivity of the in-plane cantilevers is substantially improved when immersed in water. In summary, the achieved improvement in LOD is attributed to both improved sensor sensitivity and improved frequency stability for in-plane cantilevers in water-based solutions.

6.4 Biosensor Testing Results

The in-plane cantilevers have been successfully employed as liquid-phase chemical sensors. (Mass-sensitive) chemical sensors based on polymer sensing films benefit from stable/reproducible coatings and the (easy) reversibility of the interaction between analyte and enrichment membrane. Developing a proper surface functionalization protocol for the attachment of biomarkers to a (resonant) biosensor can be difficult and because of the nature of the antibody-antigen interaction, sensor responses are generally not reversible. Yet, biosensors operate on the same principles as chemical sensors, the only difference being the surface coating for analyte binding. Once a surface functionalization protocol has been developed (see Section 6.2.2), biosensors can be tested in a similar manner to chemical sensors.

Biosensor testing experiments have been conducted by binding bovine serum albumin (BSA) to the cantilever surface and then detecting the presence of antibodies to BSA in PBS. Similar experiments have also been performed by binding IgG to the surface and then detecting anti-IgG in PBS. In both cases the antibody is detected instead of the antigen; this simplifies the surface chemistry, which is desirable for proof-of-

concept experiments (IgG is in fact an antibody, but in this case it is not used to detect its own antigen, but rather is bound to anti-IgG). The same functionalization protocol could be used to attach antibodies to the device surface by first attaching protein A to the EDC/NHS activated thioctic acid. Protein A preferentially binds to the FC region of an antibody, and thus can be used as a linker for subsequent antibody attachment [135]. In actual clinical applications it may be possible to use either strategy, i.e., attach either the antibody or the antigen to the device surface. In an individual infected with a pathogen, his/her body will contain both the antigens specific to that pathogen and also antibodies produced in response to those antigens. Another advantage of detecting the antibody when using mass-sensitive devices is that the antibodies tend to be heavier than antigens (as much as 3-4 times heavier).

The cantilevers are packaged for biosensor testing as described in Chapter 4, with the exception that instead of using a gasket the devices are directly glued into packages. (This is done to get better reliability from the packaging; since the devices are not re-usable adjustments cannot be made during testing and the permanent gluing of devices is preferred.) The devices go through pre-cleaning and SAM formation (see above) and then are glued into a flow cell for the actual experiment. This is done because the ethanol used for SAM formation dissolves the acrylic manifolds. The remaining functionalization steps are accomplished by injecting solutions through the flow cell. Before testing, the device is thoroughly rinsed by injecting 1x PBS through the flow cell.

As mentioned earlier, there are two possible liquid injection strategies for biosensor testing. For the first approach, a syringe is directly attached to the flow cell (see Figure 6.2) and a single dose of antibody solution is injected through the flow cell all at

once. This method is simple and would be ideal for a point-of-care system. Unfortunately, the analyte injection causes a jump in frequency, likely due to pressure effects, which makes interpretation of the result more difficult. For the second approach, syringe pumps are used to inject the fluid. The identical setup is used as was employed for liquid phase chemical testing (see Section 6.3, Figure 6.1). For biosensor testing one syringe is filled with 1x PBS, while the syringe on the second pump is filled with the antibody solution. It was found that a flow rate of 25 μL/min works well for biosensor testing.

During biosensor experiments, the resonators are operated in 1x PBS for at least 15 minutes to allow for frequency stabilization and to check for reliable device performance. (This time is kept as short as possible because of device lifetime issues.) In the first set of experiments the antibody is subsequently injected by hand into the package using a plastic syringe directly connected to a luer-lok fitting on the top manifold. The antibody solution is allowed to incubate for up to 1 hour with the device running in closed-loop and the frequency being tracked (see Section 6.3). In addition, an unfunctionalized resonator in a separate package (currently, the electronics to run two resonators on the same package simultaneously is not available) is subsequently measured to account for non-specific binding. The control is pre-cleaned and then exposed only to the antibody solution with the resonator operating in closed-loop. In the case that an actual biomarker is used, the control can be functionalized with BSA or some other protein that is not complimentary to the antibody being employed. An additional improvement that can be investigated is the use of silane or pluronic treatments to prevent non-specific adsorption of biomolecules onto the silicon dioxide surface of the die. Figure 6.12 (a), (b) shows the results of an initial biosensor test using direct injection of

the antibody solution; in this measurement an approximately 8 μm thick F150 resonator was used.

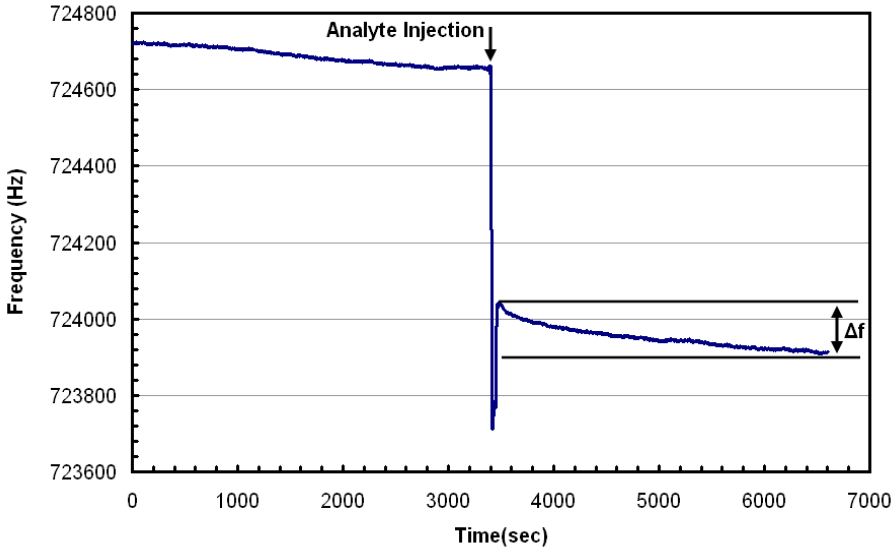

Figure 6.12(a): Response of a BSA functionalized F150 hammerhead resonator to a 10 μg/ml anti-BSA agarose solution in PBS. The frequency jump seen in the graph is due to pressure effect when analyte is injected.

Both the control (unfunctionalized) and experimental (functionalized with BSA) resonators were exposed to a 10 μg/ml solution of anti-BSA agarose in 1x PBS. The anti-BSA contains an agarose tag to make the antibody heavier, amplifying the response. The result from Figure 6.12(a) give roughly a 130 Hz frequency shift due to the analyte binding. The control resonator (see Figure 6.12(b)) gave roughly a 75 Hz frequency shift. Subtracting the two responses, a 55 Hz change is attributed to specific binding of the anti-BSA agarose to the functionalized surface. Using a frequency stability of 0.8 Hz, this gives a limit of detection around 420 ng/ml (using Equation 3.18). The frequency stability of 0.8 Hz is used because from the many biosensor measurements that is the best frequency stability that can be obtained. It is assumed that a device with this optimal Allan variance could be measured with the same sensitivity. A second experiment was

performed identically to the one above with similar results. The large frequency drop – likely due to pressure effects– when the analyte is injected makes interpreting the measurements more difficult because it is difficult to determine at what point to begin measuring the frequency drop. In the present analysis, the frequency shift is taken from the highest point after the injection to the lowest point at the end of the measurement.

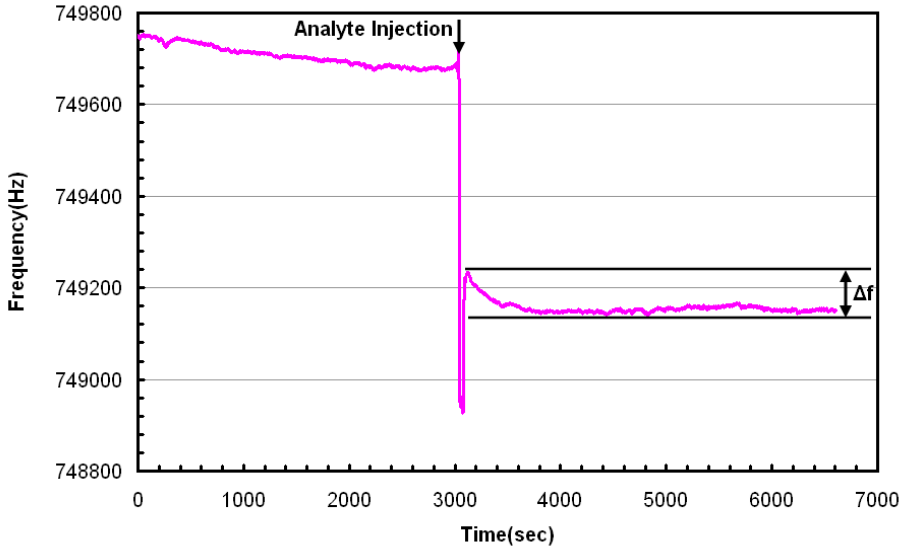

Figure 6.12(b): The response of an unfunctionalized F150 hammerhead device to a 10 μg/ml Anti-BSA agarose solution.

Figure 6.13 (a),(b) show the results of a biosensor experiment using the syringe pump setup. 75 μm wide, 400 μm long, 8 μm (approximate) thick cantilevers were used for this test. These devices were packaged using the wafer-level placement of the silicon ring for creating the flow cell. Both the experimental and control samples were treated with a 25 μg/ml anti-BSA agarose solution applied at 25 μL/min from a syringe pump. The experimental sample was functionalized with BSA as described in Section 6.2. Note: During the measurement in Figure 6.13 (a), the frequency jumped up when the analyte flow was started (in a single time step) and then after 5 min fell back down to the original

level. This jump was most likely due to a small air bubble or a pressure effect and was removed from the measurement in Figure 6.13 (a)

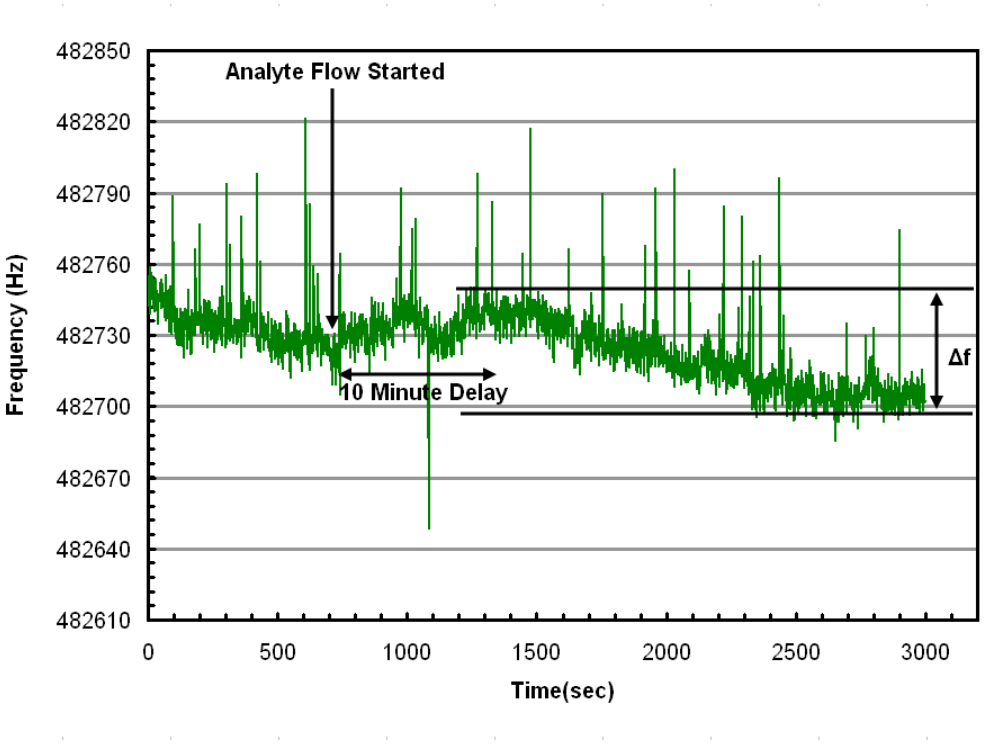

Figure 6.13(a): Response of a BSA functionalized 75 μm wide, 400 μm long, 8 μm (approximate) thick cantilever to a 25 μg/ml Anti-BSA agarose solution.

As expected the undesirable frequency drop due to pressure effects is avoided by using the syringe pumps for fluid injection. In both the experimental and control measurements the analyte was injected after roughly 15 minutes (1x PBS was applied before injecting antibody solution). From calculations using the tubing lengths and diameters, as well as the volume of the flow cell it takes approximately 10 minutes for the antibody solution to reach the flow cell and to replace the volume of fluid inside of it. This is consistent with the experimental result where no shift is seen until about 10 minutes after analyte injection. The control measurement in Figure 6.13(b) does not show any significant frequency shift after approximately 25 min.

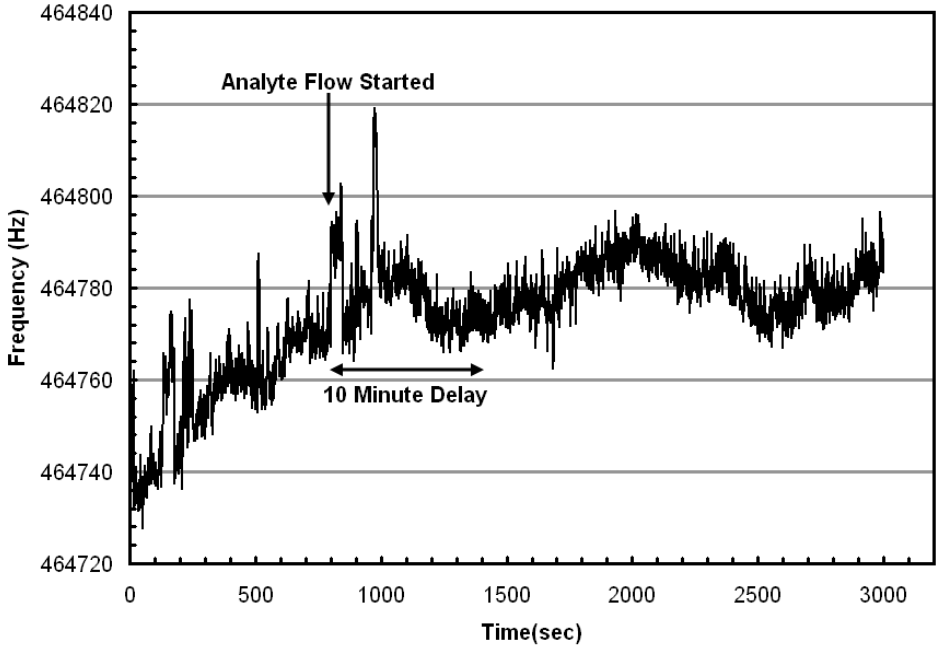

Figure 6.13(b): Response of an unfunctionalized 75 μm wide, 400 μm long, 8 μm (approximate) thick cantilever to a 25 μg/ml Anti-BSA agarose solution.

In the experiment in Figure 6.13(a) the experimental resonator shows a frequency drop of roughly 30-40 Hz (the signal is very noisy, thus it is difficult to determine the exact shift). The noise in the signal is a result of the chosen resonator; it is not always possible to choose an optimal device to measure because of constraints on the number of dies per wafer and other factors. In addition, it was found that the surface passivation was not as repeatable as one would hope, meaning that many devices corrode and fail during measurements. Thus, if a device works for a measurement it is best to measure it regardless of the noise (as long as the noise floor is low enough to see a response).

Additional biosensor measurements were performed with IgG. IgG is a type of immunoglobulin, which is a class of antibodies found in humans [25]. It was chosen because it is inexpensive and readily available. In addition, anti-IgG antibodies could be

obtained with a FITC tag to allow for confocal imaging (the FITC does not add a significant amount of mass to the antibody molecule). For IgG attachment to a gold surface the exact same functionalization protocol outlined in Section 6.2 is used, but IgG is used in the protein incubation step instead of BSA. Figure 6.14(a) shows an IgG functionalized gold surface that was treated with 100 μg/ml anti-IgG FITC in PBS for 15 minutes. Figure 6.14(b) shows an unfunctionalized gold surface treated with 100 μg/ml anti-IgG in PBS (the control). The treated surface shows a larger level of antibody attachment with a mean fluorescent intensity of 7.1 and a standard deviation of 1.2, compared to a mean fluorescent intensity of 0.6 and a standard deviation of 1.2 for the control. Robust antibody binding is observed after only 15 min, and IgG functionalized samples treated for as much as an hour show similar amounts of antibody binding (time points of 15, 30, 45 and 60 min were measured).

(a) (b)

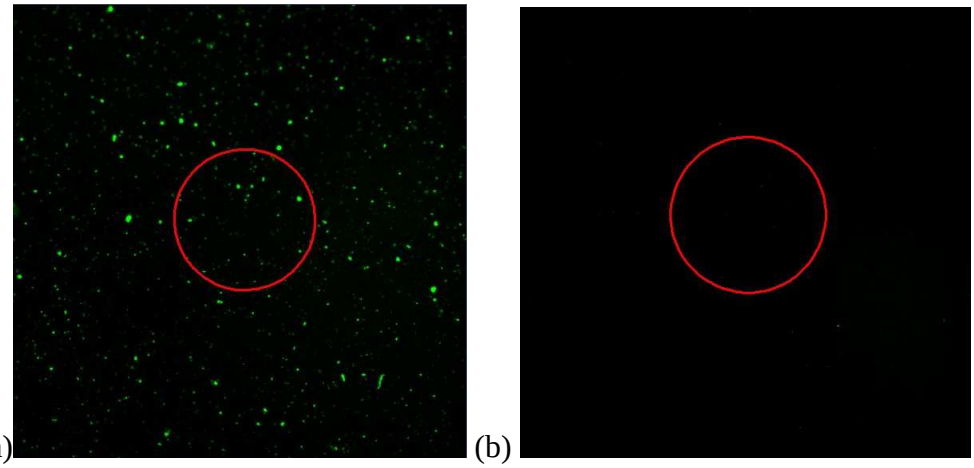

Figure 6.14: (a) Confocal microscopy images of IgG functionalized gold surface after 15 min of incubation with a 100 μg/ml anti-IgG FITC solution. The fluorescent intensity is measured inside the red circle, mean= 7.1, standard deviation 18.1 (b) Unfunctionalized gold surface treated with anti-IgG FITC. The fluorescent intensity is measured inside the red circle, mean .6, standard deviation 1.2. Both of these images are approximately 230 μm on a side.

Biosensor experiments were performed using the same protocol as the

measurements performed with BSA (see above). During surface functionalization IgG was used instead of BSA for protein incubation. F150 hammerhead devices (8 μm silicon thickness) with a 500 Å thick gold layer were functionalized with IgG using the protocol outlined in Section 6.2.2. These devices were packaged by gluing a silicon ring to the device surface (see Chapter 4). The resonators themselves have a slightly different surface passivation made of an approximately 0.36 μm thick PECVD oxide/nitride layer capped with a 50 nm thick ALD ZrO_2/Al_2O_3 nanolaminate. For both measurements a 100 μg/ml anti-IgG FITC solution was used. Antibody was injected after flowing 1x PBS for 15 min. As above, a flow rate of 25 μL/ml was used.

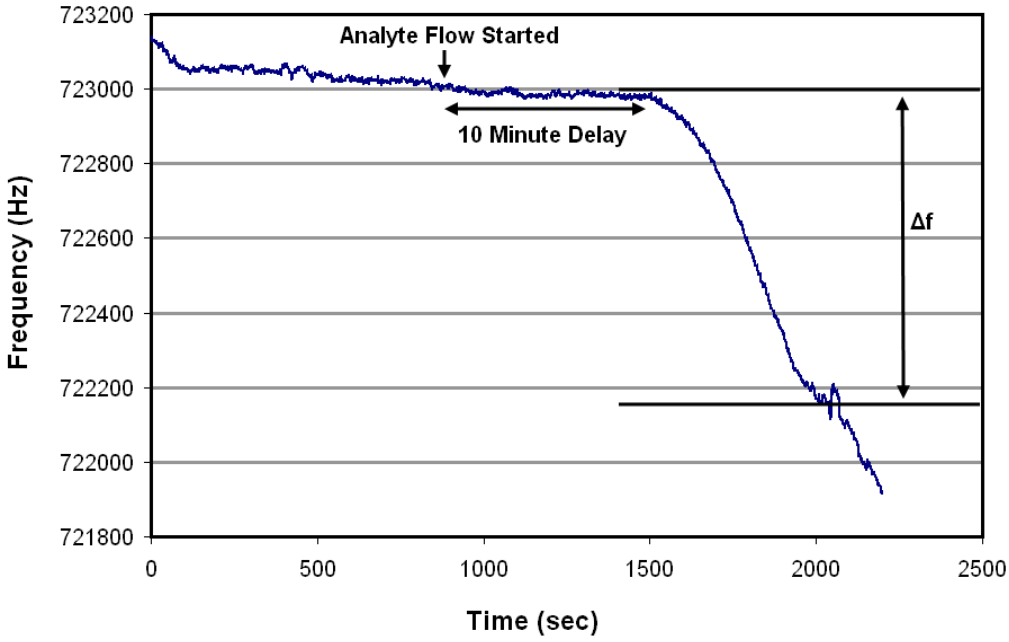

Figure 6.15(a): Response of an IgG functionalized F150 hammerhead device to 100 μg/ml anti-IgG-FITC in 1x PBS.

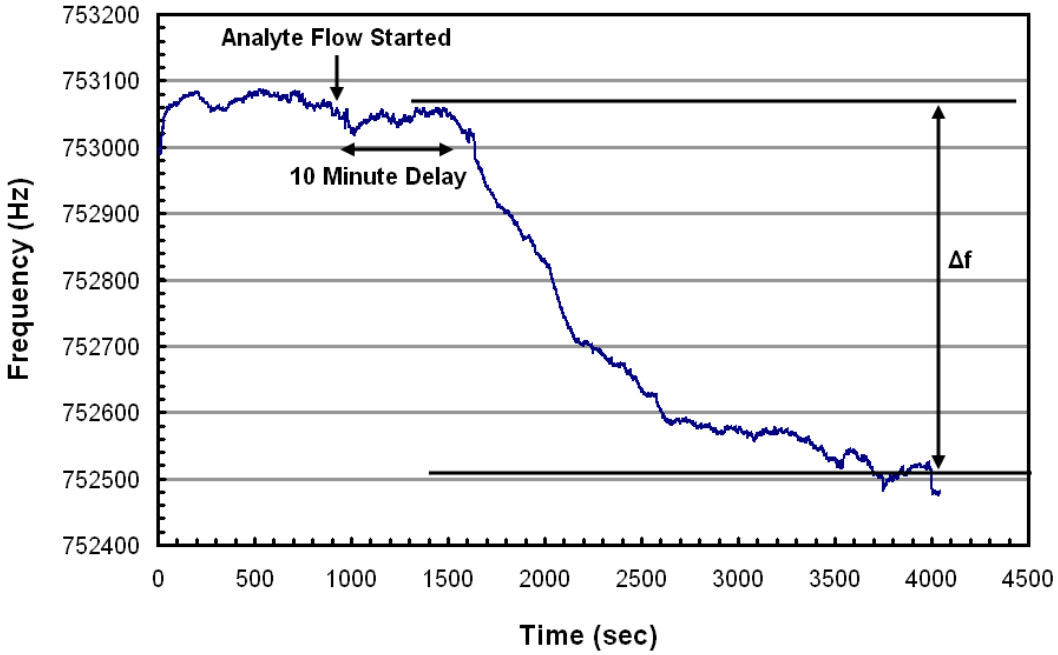

Figure 6.15(b): Response of an unfunctionalized F150 hammerhead device to 100 μg/ml anti-IgG-FITC in 1x PBS.

Figure 6.15(a) plots the response of the functionalized device. At the end of the measurement there is a large downward drift of unknown origin; luckily, the frequency levels off briefly allowing for extraction of the frequency shift. Figure 6.15(b) plots the response of an unfunctionalized resonator to 100 μg/ml anti-IgG-FITC. The frequency of the control drops by about 460 Hz, while the experimental resonator experiences a 815 Hz drop. Assuming that for these devices a frequency stability of around 0.8 Hz can be achieved (see above), the estimated limit of detection for the specific binding of IgG is approximately 680 ng/ml (using Equation 3.18).

Further biosensor experiments were performed with IgG using the same methods as those for the measurements depicted in Figure 6.15(a) and 6.15(b). Figure 6.16(a) and 6.16(b) shows the response of a functionalized F150 hammerhead and an

unfunctionalized control to 25 μg/ml anti-IgG-FITC in 1x PBS. For these experiments the resonators were functionalized and packaged using the exact same methods as the resonators for the measurements in Figure 6.15(a) and 6.15(b). There is a large and rapid frequency drop at approximately 2800 seconds in the control measurement in Figure 6.16(b). This drop is not taken as part of the response to the antibody because it occurs after the resonant frequency has leveled off for a period of time. This drop is most likely due to a particle settling on the surface of the hammerhead, since at the end of the measurement there was a larger particle observed on the surface of the device.

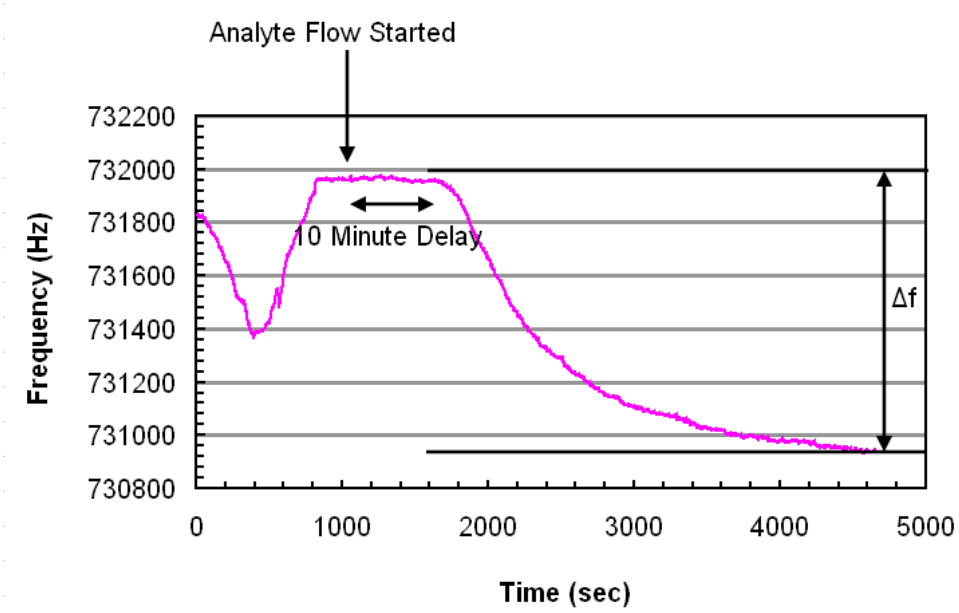

Figure 6.16(a): Response of a IgG functionalized F150 hammerhead resonator to 25 μg/ml anti-IgG-FITC in 1x PBS.

An additional concern is whether or not the response is linear (i.e., is the sensor response to 25 μg/ml anti-IgG FITC four times less than the response to 100 μg/ml anti-IgG FITC). Assuming that the functionalization was equally effective for both measurements a direct comparison is possible. The observed frequency shift response does not scale linearly with the anti-IgG concentration, which is most likely a result of all

of the ligands on the surface of the hammerhead being saturated at both 25 and 100 μg/ml. Actually, the response at 25 μg/ml is larger by almost 150 to 200 Hz, which could indicate issues with repeatability of the attachment of the IgG to the device surface and also possible issues with the large drift at the end of the measurement in Figure 6.15(a), which may have prevented the entire sensor response from being measured.

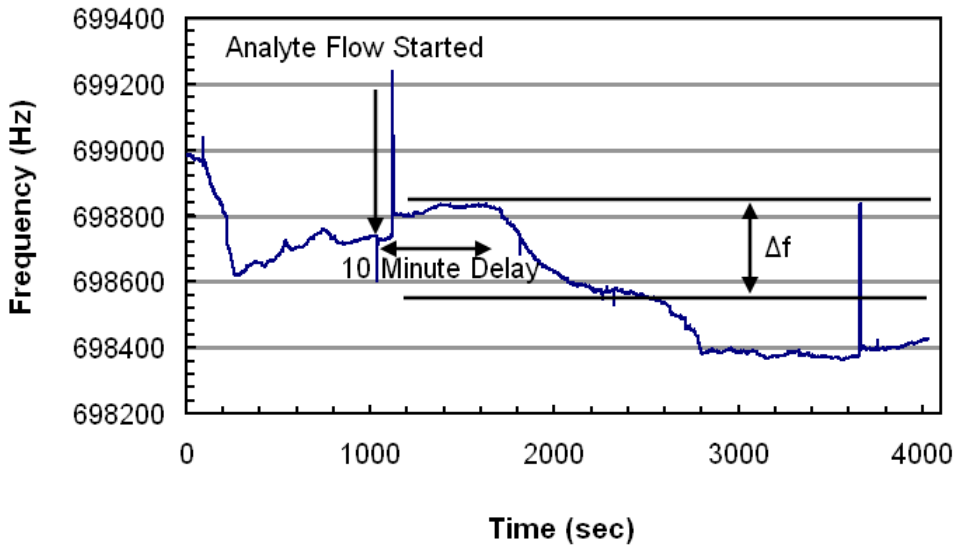

Figure 6.16(b): Response of an unfunctionalized (control) F150 hammerhead resonator to 25 μg/ml IgG-FITC in 1x PBS.

An additional challenge with the biosensor measurements is how to further reduce non-specific binding. Eventually, the goal is to employ these sensors in complex mixtures where the molecules of interest may be embedded in a background of a much greater population of species (cells, proteins, platelets, etc.). In this more physiologically realistic case, preventing non-specific attachment would be paramount. One step that can be taken is to block the surface of the resonator with BSA or some other molecule to try to prevent non-specific binding. In addition, for the functionalized device, there may be NHS-esters that are unbound to IgG, if this is the case then these esters can bind antibody from

solution [135]. This would be in contrast to antibody from solution binding specifically to the IgG on the device surface. Blocking will help to alleviate this issue. BSA is a commonly used blocking agent and was thus employed for this purpose [135]. For the experiments with blocking, the functionalized resonator and the unfunctionalized control were packaged and functionalized identically to the other samples. Before being measured, both resonators were treated with a 1 mg/ml BSA in solution in 1x PBS at 2 ºC (in a refrigerator) for 1 hour. The BSA solution was injected into each package using a syringe. After treatment with BSA the dies were rinsed thoroughly with 1x PBS injected from a syringe into the flow cell. After blocking, the measurements were performed as before by flowing 25 µg/ml anti-IgG FITC in 1x PBS at 25 µl/min through the flow cell. 1x PBS was applied before introducing the analyte in order to allow the resonator to stabilize. The results from the measurements using F150 hammerhead resonators using BSA blocked surfaces are shown in Figure 6.17(a) and 6.17(b).

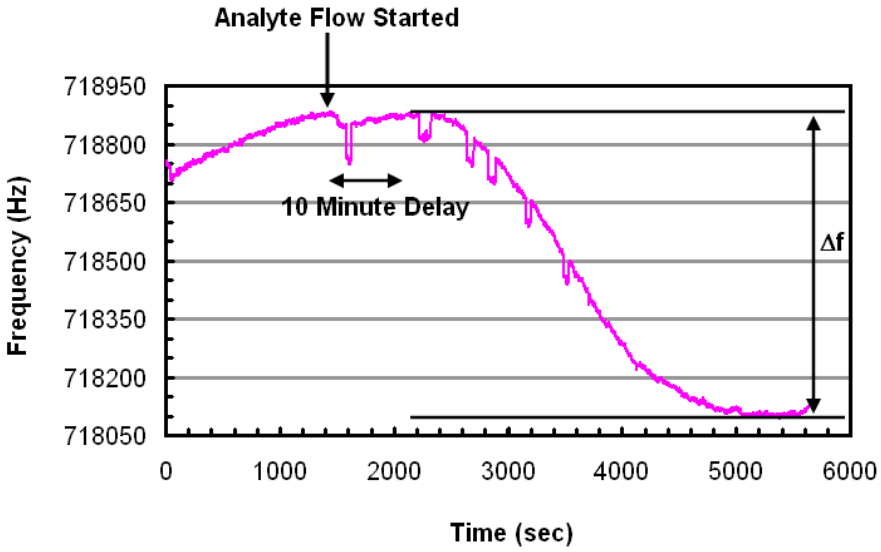

Figure 6.17(a): Response of a functionalized and blocked F150 hammerhead resonator to 25 µg/ml anti-IgG FITC in 1x PBS. The surface of this resonator was blocked with 1 mg/ml BSA in 1x PBS for 1 hour at 2 ºC just prior to measurement.

The control measurement using a BSA-blocked hammerhead shows significantly less non-specific binding than the control measurement with an unblocked surface. This indicates that blocking is a good strategy to mitigate non-specific binding on the resonator surface.

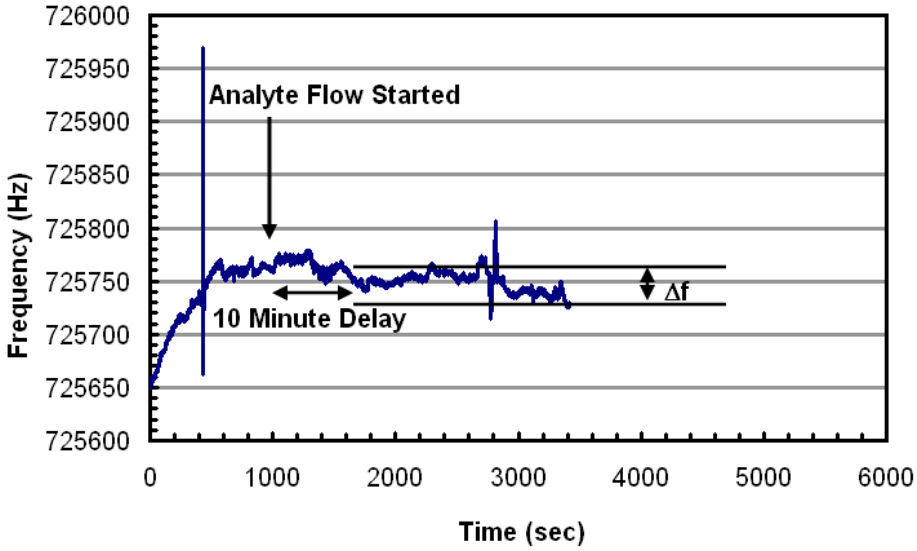

Figure 6.17(b): Response of a blocked unfunctionalized (control) F150 hammerhead resonator to 25 μg/ml anti-IgG FITC in 1x PBS. The surface of this resonator was blocked with 1 mg/ml BSA in 1x PBS for 1 hour at 2 ºC just prior to measurement. A 50 Hz frequency jump that occurred after the time that the analyte flow was started, but before the 10 minute delay when the analyte reaches the flow cell was removed from the measurement.

The results in Figure 6.17(a) show around 770 Hz of frequency shift in response to a 25 μg/ml anti-IgG-FITC solution. This result is roughly consistent with the unblocked measurement. This may indicate (further experiments are required) that the functionalized resonator does not experience a significant amount of non-specific binding. Two unusual features of the measurement in Figure 6.17(a) are the regions where the frequency jumps down (in one frequency step) and then jumps back up. The exact origin of this effect is unknown, but it is thought that the most likely cause is small

air bubbles being trapped near the resonator. Second, it takes about 14-15 minutes for the frequency to being dropping, instead of the anticipated 10-12 minutes. This may be due to the upward drift that occurs after the analyte is added. Additional antibody might need to be bound to the surface in order to overcome the drift before a drop in frequency is observed. Looking at the results of the BSA-blocked measurements, the control drops around 30 Hz, while the experimental resonator drops around 770 Hz. The minimum measured frequency stability for an 8 μm thick F150 devices in water is 0.8 Hz (this device had a thicker passivation and a thicker gold layer giving it about 10% more mass than the devices tested in Figures 6.16 (a),(b) and 6.17 (a),(b)). Assuming that an F150 device with an Allan variance of 1 Hz can be measured with the same sensitivity, a detection limit of 100 ng/ml is estimated, which is close to the required detection limit for many biomarkers in bodily fluid.

An important question for the biosensor measurements is whether or not the observed frequency shifts are reasonable. This issue can be investigated through the use of FEM simulations and information about the size of the IgG molecules that are used for the measurements depicted in Figures 6.16 (a),(b) and 6.17 (a),(b). Using COMSOL the mass-sensitivity of 8μm thick F150 resonators with the relevant surface passivation/gold layer could be extracted. It was found that the mass-sensitivity for this device is 0.8 Hz/pg, assuming that the added mass is uniformly distributed over the gold-coated sensing area. Thus, the roughly 800 Hz frequency shift observed in Figure 6.17(a) corresponds to 1 ng of mass being attached to the device surface. The IgG molecules used in this work have a mass of 150 kDa (per vendor specification) and 1 ng added mass, thus, means that roughly $4 \cdot 10^9$ IgG molecules are attached to the device surface.

Calculating the gold-coated area of the resonator (roughly 19000 μm^2) shows that each IgG molecule that is attached to the surface takes up about 5 nm^2. This is very close to the published dimensions of an IgG molecule of 4 by 5 by 8 nm [146, 147] and indicates basically 100% surface coverage.

In reality, the surface coverage from the IgG is most likely not 100%. One important item to note is that at the concentration of antibody used all of the receptors on the beam's surface are likely saturated (this is supported by the responses to a 100 μg/ml and a 25 μg/ml solution looking very similar; see Figures 6.16 (a),(b) and 6.17 (a),(b)). In addition, clumps of anti-IgG could be attaching to the device, or the IgG could be attaching to the surface in more than a single monolayer. Both of these effects would increase the surface density of ligands. In addition, there are device-related variables that can also affect how well simulated and measured results agree with each other. The tested devices may be thinner (by as much as 10-15 %) than expected and the same goes for the passivation and gold layers. If the beam is thinner than is assumed, then the sensitivity will be higher than expected. Either way, the above theoretical estimations shows that the measured frequency changes are within a reasonable range, and are not orders of magnitude higher or lower than what is expected.

In conclusion, basic biosensor results have been presented. IgG antibodies could be detected with an estimated detection limit close to 100 ng/ml, which approaches those needed for detecting biomarkers for diagnostics. Further measurements at analyte concentrations that do not saturate the receptor molecules on the resonator surface are needed in order to establish the true sensitivity and LOD of the system. In addition, a system with two methods of sample injection has been demonstrated that could possibly

be ported to a hand-held unit. Actually measuring the resonator in the fluid itself greatly simplifies the system and experimental design without the need of extra reagents for washing and drying. This simplicity is a major advantage for in-the-field or point-of-care applications. Finally, further improvements can be made by (1) using a blocking agent (e.g. BSA) on the resonators to help prevent non-specific binding, (2) by improving the consistency/repeatability of the protein attachment to the resonator surface, and (3) by enhancing the surface area for ligand attachment to the resonator through the growth and functionalization of CNTs on the cantilever surface as outlined above (see Section 6.2).

CHAPTER 7

SPRING-SOFTENING SENSOR CONCEPT AND DESIGN

The device concept presented here offers a possible alternative and/or improvement to current liquid-phase resonant sensor topologies. It does this by isolating the resonator from the fluid, offering advantages in terms of resolution and reliability. In the broadest sense, the operation of this sensor can be understood as the combination of capacitive and resonant sensing concepts. Essentially, a capacitive transducer is read-out by the resonator, with the resonator acting as an analog-to-digital converter (ADC), converting the analog signal from the capacitor to a digital frequency signal.

One obvious question with such a configuration is: since the sensing concept is more complex than either a resonator or capacitive system by itself what advantages does it offer over either of these systems alone? The advantages of the proposed system are threefold: (1) capacitive sensors often require very thick electrodes (10's of microns), small electrode spacing, or large electrode areas to produce measureable signals [40, 148]. The proposed structure has a smaller footprint (micron scale) and could be integrated with a CMOS fabrication process. (2) The resonator provides a digital output signal which only requires a counter for read-out, in contrast to a capacitive sensor which can require more complex circuitry based on e.g. switched capacitors [38]. (3) An issue with many possible liquid-phase biochemical sensor topologies is their sensitivity to properties of the solution (e.g., pH or salt concentration) that contains the analyte, instead of only the analyte within the solution. For the proposed topology it may be possible to implement a compensation for changes in solution properties, if a device with two fluid

channels is used.

7.1. Motivation for Developing a Decoupled Sensor

In order to address some of the concerns with liquid-phase resonator operation, including (1) their significant viscous damping limiting resolution and (2) device reliability challenges associated with direct contact between the resonator and the fluid, an alternative sensing scheme has been investigated that enables liquid-phase sensing without resonator immersion. This technique potentially offers high resolution because it utilizes an electrostatic resonator that can be operated in vacuum with submicron transduction gaps. In addition, because the resonator itself is not in solution, issues of metal line corrosion and resonator breakage are less of a concern.

The basic device is shown in Figure 7.1 and consists of a cantilever beam with two sets of electrodes. One set of electrodes is placed on either side of the resonator and is separated from the beam by an air gap. The second set of electrodes is placed on either side of a fluid channel that is formed between this second set of electrodes and the first set of electrodes. Thus, the electrodes form two capacitors, one between the outer electrodes and the electrode next to the beam, and another capacitor between the beam and the inner electrodes (the electrodes across the air-gap from the beam). The sample fluid is in contact with the electrodes but not with the resonator itself. The beam is fixed at a DC voltage and the two outer electrodes are placed at a different DC voltage or at ground.

For operation of electrostatically actuated resonators, a DC voltage is superimposed with an AC voltage. This DC voltage prevents frequency doubling during

closed-loop operation, but also affects the beam's frequency via the spring-softening effect. In the design in Figure 7.1, electrostatic spring-softening is used to change the resonator's frequency upon analyte binding. The sensor generates an output signal in the following way: the electrodes that are closest to the beam are at a floating DC potential and form the center electrode of a capacitive voltage divider that is formed between the fluid channel capacitance and the air-gap capacitance. During sensor measurements, the dielectric constant within the fluid channel will change as analyte enters and binds to ligands in the channel. Analyte binding alters the fluid channel capacitance, and thus the voltage on the floating electrode that biases the beam. Since the DC bias on the beam is altered, the resonant frequency will change via the electrostatic spring-softening effect (see Section 7.2). A similar sensing concept has recently been investigated for determining the humidity content of air [149].

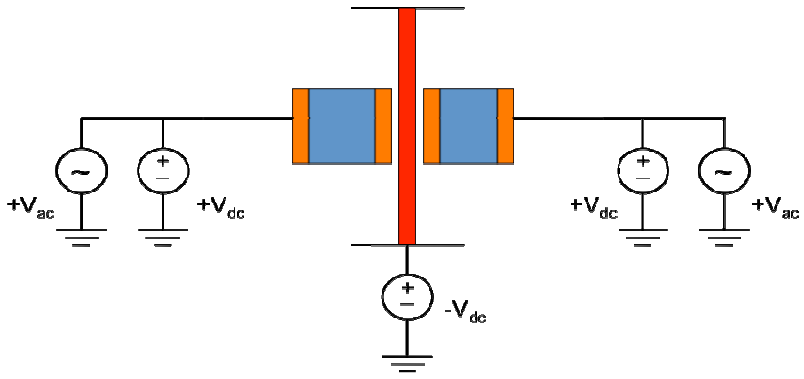

Figure 7.1: Basic configuration of the spring-softening sensor. The beam can be seen in red in the middle, the electrodes are shown in orange next to the beam and on the outside of the fluid channels (shown in blue).

7.2 The Spring-Softening Effect

The electrostatic spring-softening effect is a nonlinear phenomenon that has been extensively investigated for radio-frequency (RF) applications, such as tunable filters

[150, 151]. During electrostatic resonator operation, the beam moves closer to and further away from the drive electrodes as a results of its vibrations. The resonator has a mechanical stiffness determined by its dimensions and material properties; the beam itself can be modeled as a spring. The displacement of the cantilever alters the capacitance between the cantilever and the drive electrodes, and consequently the electrostatic force on the beam. As the resonator moves closer to the drive electrode the electrostatic force on the beam increases because the gap between the resonator and drive electrode is narrowed (see Equation. 7.2).

For a purely mechanical spring, as it is displaced it applies a larger and larger restoring force making further displacement more difficult (see Equation. 7.1). The restoring force resulting from the beam's stiffness is

$$F = -k_m x, \qquad (7.1)$$

where k_m is the mechanical spring constant and x is deflection of the spring from its equilibrium position. The force is negative in sign because the spring applies a force that is in the opposite direction of its displacement. For electrostatic resonators, in contrast to a simple mechanical spring, the net restoring force (the electrostatic force minus the mechanical force from the beam's stiffness) is lower than expected (for a simple linear spring) because the electrostatic force increases with further displacement.

Based on purely mechanical reasoning, it is expected that it would require more force to displace the cantilever towards the drive electrodes as it is displaced further (see Equation. 7. 1). The difference here is that in contrast to a simple mass-spring system, the applied force displacing the spring also increases, so the net force increases, allowing the beam to displace further than expected from purely mechanical reasoning. Another way

of looking at this increase in net force oriented towards the drive electrode, is to say that the mechanical stiffness of the beam is reduced, allowing it to displace further for the same applied force. In electrostatic resonators, this increase in net force in the direction of the drive electrode can be modeled as a reduction in the effective spring constant of the resonator and is termed the "spring-softening" effect. The relevant equations describing this phenomenon are presented below.

The capacitance of a parallel plate capacitor (the beam and the drive electrodes form parallel plate capacitors) can be written as

$$C = \frac{Q}{V} = \frac{\varepsilon_o \varepsilon_r A}{g}, \qquad (7.3)$$

Where Q is the amount of charge stored on the plates, V is the applied voltage, ε_0 is the dielectric permittivity of free-space, ε_r is the relative dielectric permittivity of the material between the capacitor plates, A is the area of the capacitor plates, and g is the distance between the capacitor plates. The resulting electrostatic force acting on the electrodes can be derived as:

$$F_{el} = QE = \frac{1}{2}\frac{\varepsilon_r \varepsilon_0 A V^2}{g^2}, \qquad (7.4)$$

Where E is the electric field that exists between the beam and drive electrode (the two plates of the capacitor). The total net force, resulting from the interaction of mechanical and electrical effects can be expressed as (assuming two electrodes)

$$F_{net} = \frac{1}{2}\frac{\varepsilon_r \varepsilon_0 A V^2}{(g-x)^2} - \frac{1}{2}\frac{\varepsilon_r \varepsilon_0 A V^2}{(g+x)^2} - k_m x, \qquad (7.5)$$

As in Equation 7.1, x is the deflection of the beam. For a mass-spring system, the derivative of the net force will give the spring constant, k. Differentiating Equation 7.5,

one obtains the form:

$$k = \frac{dF_{net}}{dx} = \frac{\varepsilon\varepsilon_0 A V_1^2}{(g-x)^3} + \frac{\varepsilon\varepsilon_0 A V_2^2}{(g+x)^3} - k_m, \qquad (7.6)$$

For a clamped-clamped beam the magnitude of the spring-softening effect can be found by examining Equation 7.6, and has the form [151]:

$$k_e = \left[\frac{V_1^2 \varepsilon_a A}{g^3}\right] + \left[\frac{V_2^2 \varepsilon_a A}{g^3}\right], \qquad (7.7)$$

with V_1 and V_2 being the voltages on the floating conductors, and A being the area of the floating conductors (this equation assumes the beam is at ground). Once the electrostatic spring constant k_e has been determined, the relative shift of the resonance frequency of the beam is given by [152]:

$$\frac{\Delta f}{f} = \sqrt{1 - \frac{k_e}{k_m}}, \qquad (7.8)$$

with the mechanical spring constant k_m of the clamped-clamped beam.

7.3 Concept of the Spring-Softening Sensor

The electrostatics of the device shown in Fig.7.2 can be modeled as two capacitors in series, whereby the biochemical analyte modifies the dielectric properties inside the fluid channel or induces a surface charge on the (functionalized) electrodes.

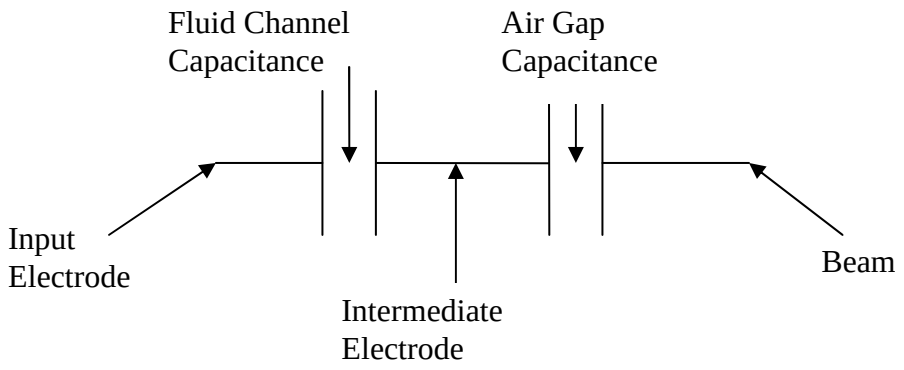

Figure 7.2: A diagram of the electrical operation of the spring softening sensor, with the two capacitances and the three electrodes labeled.

The voltage on the floating electrode(s) (the electrode across the air-gap from the beam) results from the capacitive divider between the fluid channel and air-gap capacitance and is given by

$$V = V_{dc} \frac{\varepsilon_f g - \varepsilon_a d_f}{\varepsilon_f g + \varepsilon_a d_f}, \qquad (7.9)$$

where V_{dc} is the voltage on the fixed electrodes, ε_f is the dielectric constant of the fluid, ε_a is the dielectric constant of the air, g is the width of the air gap and d_f is the width of the fluid channel. As shown in Equation 7.9 changing the dielectric properties of the fluid channel will alter the voltage on the floating electrode across the air-gap from the beam (altering the dielectric properties changes the fluid channel capacitance). If the DC voltage on the electrode next to the beam changes, the electrostatic spring constant, and thus the beam's resonant frequency will change.

7.4 Spring-Softening Sensor Design and Simulation

To further investigate the sensing concept and device topology described in the preceding sections, analytical and numerical modeling was performed. The dimensions

and layout of the device that was modeled by hand and simulated is given below in Figure 7.3.

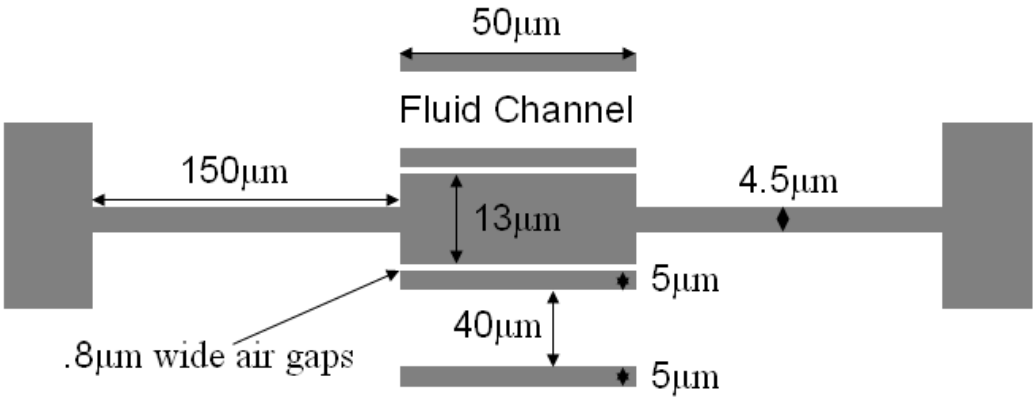

Figure 7.3: Beam layout for the hand calculations and simulations.

To model the frequency shift that would occur for changes in the dielectric constant within the fluid channels, both analytical and numerical models were used. A two-stage modeling strategy was employed, where first the electrostatics were modeled and the voltage on the floating electrode was calculated. Subsequently, the frequency of the clamped-clamped beam resonator was calculated using the DC drive voltage determined in the first step.

For the hand calculations, Equation 7.9 was used to determine the voltages on the floating electrode. The beam dimensions for the simulations are given in Figure 7.3. For the electrostatic calculations and simulations both the input electrodes were held at 15 V and the beam (the conductor on the opposite side of the air gap from the floating electrode in the case of the electrostatic simulations) was held at -15 V. For the hand calculations, once the electrostatics had been modeled to determine the potential on the floating electrode, the magnitude of the electrical spring-constant (k_e) could be determined using Equation 7.7. The beam's mass could be calculated from its volume and

the density of silicon and its mechanical spring constant (k_m) could be determined from textbook equations for the case of clamped-clamped beam [96].

$$k_m = \left(\frac{\pi^4}{6}\right)\left(\frac{EWH^3}{L^3}\right), \qquad (7.10)$$

where E is the Young's modulus of the beam, W is the width of the beam, H is the thickness of the beam, and L is the length of the beam. For determining the mechanical stiffness, L was taken to be 2*150μm, a better approximation of the spring constant probably could be made, and this is a possible source of discrepancy between the hand calculations and the simulations (see below). From the effective mass of the beam and the effective mechanical spring-constant, the resonant frequency without an electrostatic spring-softening can be calculated:

$$f_0 = \frac{1}{2\pi}\sqrt{\frac{k_m}{M}}, \qquad (7.11)$$

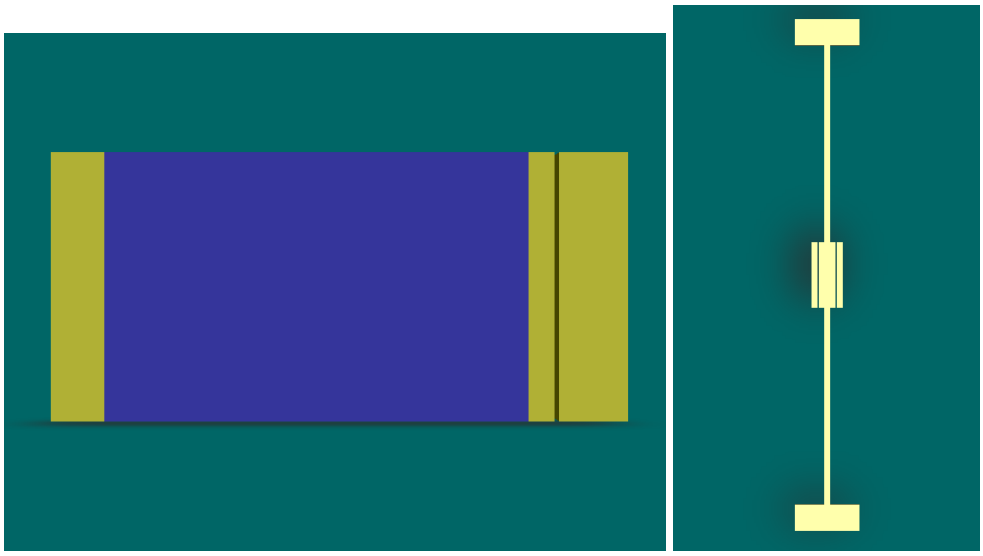

Figure 7.4: Images of the structures used to simulate the spring-softening sensor in Coventorware. (a) the beam resonator, (b) the structure used for electrostatic simulations.

Finally, since k_{el} and k_m are known the resonant frequency of the device with

electrostatic spring-softening can be calculated using Equation 7.8, where M is the mass of the beam.

The FEM simulations were performed in Coventorware (Coventor, Cary, NC), using a similar strategy to the hand calculations. (The same beam and electrode dimensions were used for both the hand calculations and the simulations (Figure 7.3)). First, the electrostatics were simulated using Coventorware's electrostatics module to determined the potential on the floating electrodes (see Figure 7.4 (a)). Next, Coventorware's "cosolve" was used in which a mechanical eigenfrequency simulation is done at the same time as an electrostatics simulation (See Figure 7.4 (b)). When this type of simulation is performed, Coventor includes frequency changes due to the spring-softening effect. The resonant frequency as a function of dielectric constant obtained from both hand calculations and simulation are given in Table 7.1.

The frequency results found by simulation and hand calculation match to roughly 15%. One possible reason for the discrepancy is the method that was used to calculate the mechanical spring constant of the beam. Second, the FEM simulations may be more accurate at calculating the voltages on the floating electrode (the hand calculations are a simplification). Consequently, the frequencies determined by hand may not be as accurate as those from the eigenfrequency analysis. The FEM simulations will take these effects into account and thus the obtained voltages, on the floating electrodes, will differ between the hand calculations and the simulations.

Table 7.1: Simulated and calculated frequency changes for different dielectric constants in the fluid channel.

ε_r	**Simulated Δf (Hz)**	**Calculated Δf (Hz)**
80	2.827705*10^5	3.305057*10^5
80.005	.4	.7
80.007	.6	1
80.01	1	1.5
80.05	5.5	7.2
80.07	7.8	10.1
80.1	11.2	14.4
80.2	22.3	28.7
80.3	33.6	42.9

As an example, using V_{dc} = 15 V, a change of the dielectric constant in the fluid channel from 80 to 80.3 (i.e., 0.375%) results in a simulated frequency change of 33 Hz at a base frequency of approx. 300 kHz. While a change of the dielectric constant of 0.375% appears large, one has to consider that the short-term frequency stability of silicon-based resonators (even if operated in air) is of the order of 10^{-8} or better [131], i.e. in the above case frequency changes as small as 0.01 Hz can be resolved. In theory, these numbers can be improved if the resonator is operated in vacuum or at least in a controlled environment (as is the case with the concept presented here). Under this assumption, dielectric constant changes down to 1 ppm become measurable, not taking into account any enrichment of analyte in a sensing membrane. Note: for the modeling it is simpler to think of the proposed structure as a chemical sensor because the dielectric properties of different polymers and organic analytes are well know. This is not the case for different biomolecules where their dielectric constants have not generally been well characterized.

7.4.1 Spring-Softening Device Layout Considerations

Different variations of the spring-softening sensor were drawn in Cadence (the

layout editor). In total, 42 unique devices layouts were designed, and a total of 330 dies were created in the mask layout. The device footprint itself is roughly 500 μm by 500 μm; each die contains 4 individual resonators in two sets, with each set sharing fluid channels. The die size is 4mm by 4mm. In terms of device operation, the resonators were designed to be fabricated on an SOI (silicon on insulator) wafer with a degenerately doped device layer. The highly conductive silicon helps to avoid capacitive charging effects and allows for longer electrodes to be used (this eases the required fabrication tolerance). One drawback is that the highly conductive layer increased the amount of crosstalk between the input electrodes.

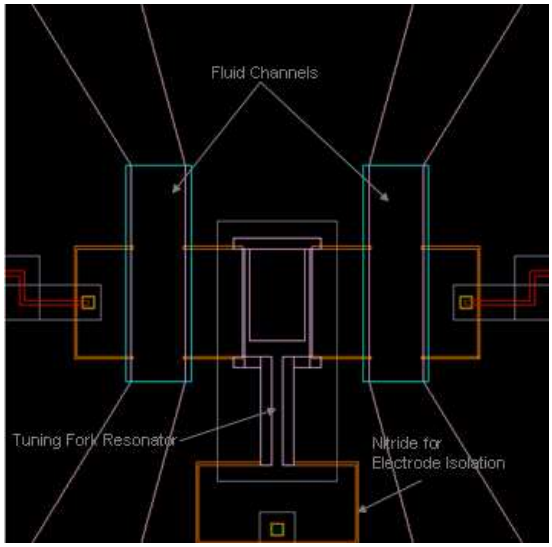

Figure 7.5: Tuning fork with the silicon nitride filled trenches used to isolate electrodes labeled as well as the fluid channels and the resonator itself.

To prevent shorting, silicon nitride was used to isolate the electrodes from the rest of the device layer. Patterned metal lines were drawn to connect the electrodes on each device to bond pads, which were used for electrical connections to a DIL package. Through-wafer holes with a 200μm diameter are used for microfluidic packaging. By placing the die in a manifold and sealing the fluid channels from the top using a wafer

bonding technique, fluid can be injected up through the holes, into the fluid channels and exit through the second set of holes on the opposite end of the die (see Chapter 8). The manifold can easily be fabricated using stereolithography. A variety of resonator shapes were incorporated into the layout, including clamped-clamped beams, clamped-free beams and also tuning forks (see Figures 7.5, 7.6).

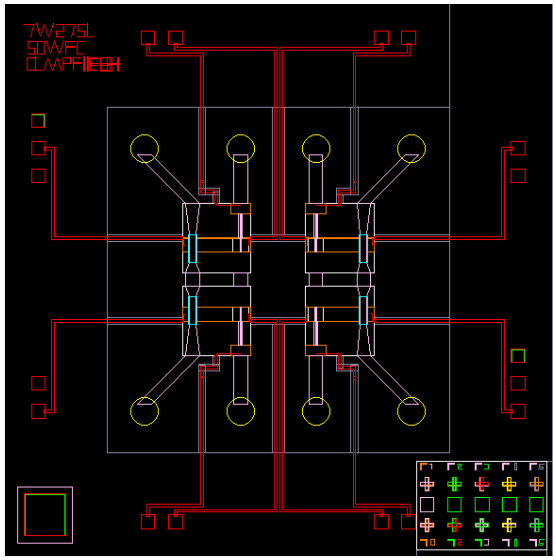

Figure 7.6: Die layout for the spring-softening sensor concept for a die with 7μm wide, 275μm long cantilevers. The through holes for the fluid are shown in yellow and the metal lines are shown in red.

In an effort to reduce noise, and also lower the voltages needed for actuation, the resonators were designed so that they could be fabricated with submicron transduction gaps. In addition, several variations on the same device were drawn, including: (i) having one or two fluid channels, (ii) having wider or narrower fluid channels, (iii) having wider conduction gaps and electrodes, different sizes of the same basic beam resonator dimensions, and different configurations allowing the resonators to be packaged by hand if need be. Finite element simulations were used to find beam shapes that had a range of resonance frequencies from 100 KHz to 1 MHz, and FEM simulations were also

employed to find the best dimensions for the capacitive electrodes and fluid channels. Eventually, the devices need to be packaged using a hermetic process such as eutectic bonding. The device layout leaves at least 25μm from the edge of the resonator electrodes to the fluid channel edge to allow for misalignment during bonding.

Besides the standard devices with two fluid channel, also devices that only require a single fluid channel were included in the layout. For resonator operation and sensor testing (described in detail in Chapter 8) an input electrode and a sense electrode is required. For sensing purposes a signal can be obtained by situating the drive (input) electrode on the edge of the fluid channel, so that it biases a floating electrode, while the sense electrode is directly located across the air gap from the resonator (See Figure 7.7). Doing this helps to reduce signal attenuation across the device's capacitances and also simplifies the electrical connections to the sensor.

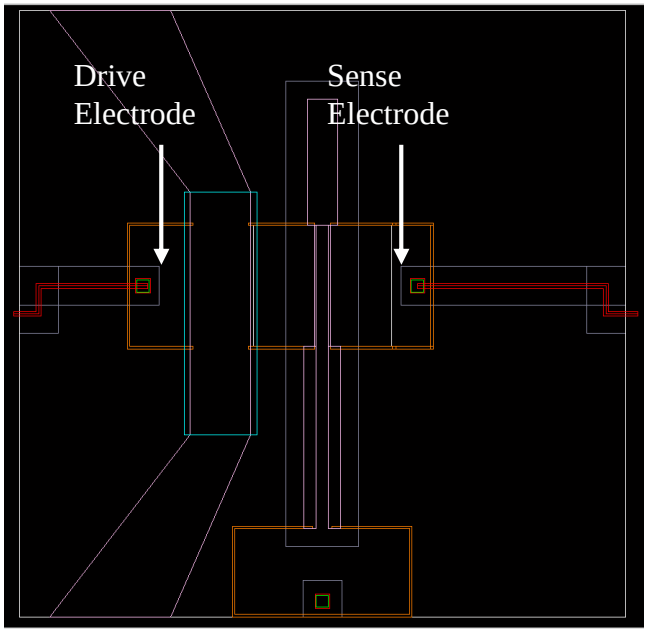

Figure 7.7: Spring-softening sensor with only one fluid channel; instead of a second fluid channel the sense electrode is directly coupled to the output via an air gap.

CHAPTER 8

SPRING SOFTENING SENSOR FABRICATION, PACKAGING AND TESTING

To create working spring-softening sensors, a new fabrication process that is different from the established cantilever process flow needed to be designed, tested and implemented. The key parameters for successful sensor operation are (1) the nitride isolation to prevent electrode shorting, (2) the width of the transduction gaps and, (3) the implementation of a vacuum packaging method.

For the fabrication of spring-softening resonators, a surface micromachining process on SOI wafers was used. The process begins by creating trenches to isolate the electrodes (this is necessary because the device layer is degenerately doped). Also, there can be no voids in the materials which enclose the fluid channel and the resonator cavity, or else the channels will not hold fluid and the resonator cannot be vacuum sealed. For electrical isolation, trenches were first ICP etched down to the BOX (buried oxide) layer of an SOI wafer and then backfilled with LPCVD nitride. It was found that the nitride as deposited was too conductive to provide effective isolation, so in subsequent processing a thermal oxide was grown to aid in isolation. The next steps are aimed at creating submicron transduction gaps, which is done using an oxidation process to narrow the openings in an etch mask, similar to the process presented in [153]. After the mask is created and the gaps are narrowed the transduction gaps are ICP etched into the device layer of the SOI wafer. The use of a trench closure process with oxidation precludes the need for expensive, non-parallel processes such as electron-beam lithography.

The final steps of the process involve patterning polysilicon on the wafer surface in preparation for wafer bonding, and then etching contact openings through the nitride and oxide that remains on the surface of the device layer. Metal is evaporated and patterned using liftoff and ports (circular openings) are etched through the wafer from the backside to allow for fluid injection. The devices are released in BOE. The final step of the process is bonding a Borofloat wafer to the wafer containing the devices to both vacuum seal the resonators and to seal the topside of the fluid channels.

For the implementation of submicron transduction gaps using an etch process (as opposed to i.e. a HARPSS process [151]), a method is needed to etch submicron gaps in silicon without scalloping. Scalloping is a result of the standard BOSCH ICP etching process, where the SF_6 plasma isotropically etches silicon, leaving scalloped sidewalls. An STS Pegasus tool was used for narrow trench etching. With this piece of equipment it is possible to reduce the cycle time for the passivation and etch steps in the BOSCH process to around 2 seconds each. This helps reduce sidewall scalloping because although the SF_6 still etches anisotropically, the amount of etching in any direction is reduced because of the reduced cycle time, thus reducing scalloping. The entire process flow is summarized below.

8.1 Spring-Softening Sensor Fabrication Process Outline

This section summarizes the major steps in the spring-softening sensor fabrication process. The steps outlined below were first tested as much as possible on prime wafers. They were then combined and tested together on SOI wafers. The process was performed on SOI wafers with a p-type device layer having a resistivity of 0.001 to

0.005 Ω-cm. Two device layer thicknesses were used, 10 μm and 15 μm. The BOX layer was 2 μm thick. The handle wafers were between 525 and 620 μm thick and had a resistivity of 10 to 20 Ω -cm. A detailed process flow for fabricating the spring-softening sensors can be found in Appendix 4. The cross-sections shown below and also those in Section 8.1.2 are taken across the width of a single resonator. The through wafer etching is shown in the same cross-section to illustrate the process but only occurs at the ends of the die where the through-wafer fluidic ports are created (See Figure 8.1(j)).

The starting substrate is an SOI wafer with a 10-15μm thick degenerately doped p-type device layer, a 2μm thick BOX layer and a 500μm thick p-type handle layer.

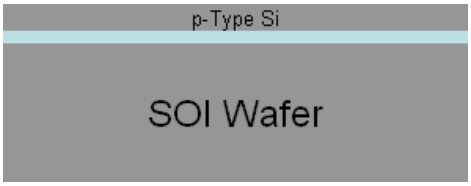

Figure 8.1(a): SOI wafer starting material for spring-softening sensor fabrication.

1. Pattern and ICP etch trenches into the silicon in order isolate electrodes.

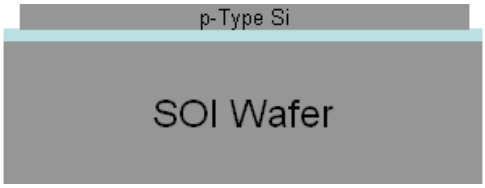

Figure 8.1(b): SOI wafer with trenches etched for electrode isolation.

2. Grow 300 nm of thermal oxide(wet) to improve electrical isolation.
3. Backfill trenches with 1.5-2 μm of LPCVD nitride.
4. ICP Etch back nitride on surface until 400-600 nm remain.
5. Strip nitride from wafer backside using ICP etching. (Doing this makes ensuring that the etch mask for the fluidic holes (see below) is actually etched to the bare silicon on the SOI wafer backside.)

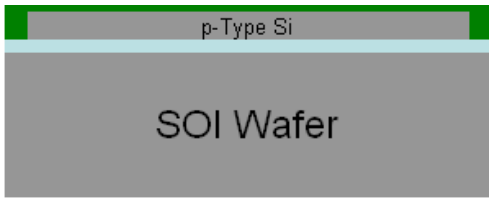

Figure 8.1(c): Spring-softening wafer with the isolation trenches refilled with silicon nitride (shown in green).

6. Deposit 2-2.5 μm of LPCVD polysilicon on wafer. (There is also polysilicon on the wafer backside, for simplicity this polysilicon is not shown in the cross-sections.)

7. Pattern and ICP etch the polysilicon on the topside of the wafer using the BOSCH process. A tool that has very short cycle times must be used to minimize scalloping This mask defines the resonator geometry, but not the submicron gaps.

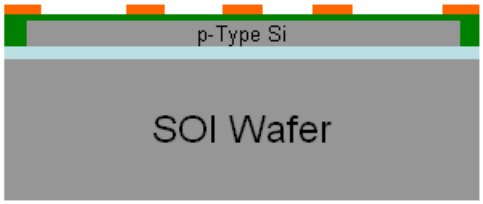

Figure 8.1(d): Spring-softening wafer after polysilicon deposition (shown in orange) and patterning.

8. Grow 1.7-2 μm of oxide using wet thermal oxidation. Oxidizing the polysilicon closes the gaps defined by the polysilicon etching, forming submicron gaps.

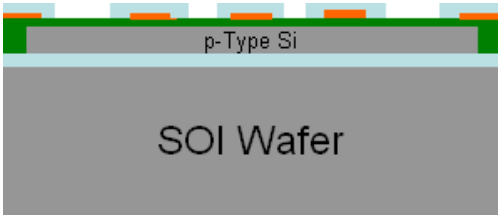

Figure 8.1(e): Spring-softening wafer after polysilicon oxidation for trench narrowing. The grown oxide is shown in blue.

9. ICP etch the silicon nitride.

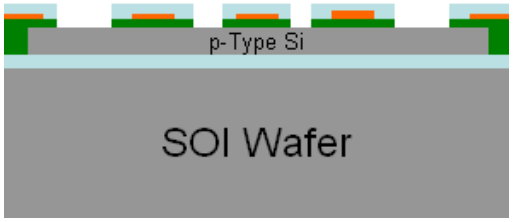

Figure 8.1(f): Spring-softening wafer after etching of the underlying silicon nitride exposing the silicon on the device layer.

10. Strip thermal oxide from backside with BOE, protect topside oxide with photoresist.
11. Etch the device layer using the BOSCH process, using a tool that has very short cycle times to minimize scalloping.
12. Strip thermal oxide from polysilicon on the topside of the wafer.

Figure 8.1(g): Spring-softening wafer after etching of the device layer in order to define the resonators and fluid channels.

13. Pattern topside polysilicon for packaging in subsequent steps. Again, a tool that has very short cycle times must be used to minimize scalloping in the trenches that have already been etched. (Even if eutectic bonding is not used, the packaging etch must be done to prevent metal line shorting by the polysilicon.)
14. Deposit 4 μm of PECVD oxide on wafer backside using the STS PECVD. (This forms the SiO_2 etch mask for the through-wafer for the microfluidic holes.)
15. Pattern and ICP etch PECVD oxide on backside. The PECVD oxide will serve as an etch mask for the through-wafer fluidic ports (see Section 8.1.2).

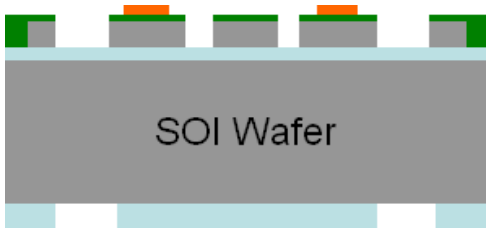

Figure 8.1(h): Spring-softening wafer after deposition and patterning of a PECVD silicon dioxide etch mask on the wafer backside. The PECVD layer is shown blue.

16. Pattern and etch contacts through the nitride on the wafer topside.

17. Clean wafer in Pirhana for 10 min and 5 cycles in a dump rinser.

18. Coat wafer topside with negative resist and pattern with a mask defining the metal-line lift-off.

19. Deposit 400 nm of gold on wafer in an electron-beam evaporator, lift-off gold. Chromium is used as an adhesion layer.

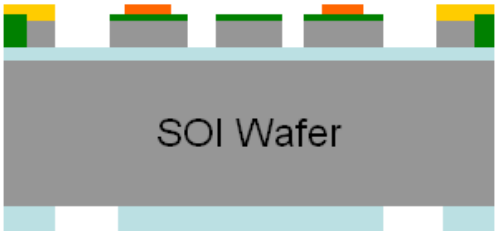

Figure 8.1(i): Spring-softening wafer after etching of contact opening and gold deposition for making electrical connections to the bond pads. The gold layer is shown in gold.

20. Clean wafer thoroughly with Pirhana and DI water.

21. ICP etch through-wafer holes from the backside.

Figure 8.1(j): Spring-softening wafer after etching of fluid ports from the wafer backside.

22. Release the dies by wet etching the BOX layer, check the release with an IR microscope.

Figure 8.1(k): Spring-softening wafer after resonator release in BOE.

*For initial experiments, gold was chosen as the metallization; gold is not etched by BOE or sulfuric acid allowing for device release after dicing and also more thorough cleaning of the wafer with Pirhana after metallization. Eventually, the process could be implemented using aluminum metallization.

8.1.1 Wafer-Level Packaging Scheme

The wafer-level packing process used for the spring-softening sensors is based on a gold-eutectic bonding process [154]. Gold-eutectic bonding is chosen for three main reasons: (1) it is readily implemented with available materials (i.e. gold and polysilicon), (2) it is a hermetic process allowing for vacuum packaging of the resonators, and (3) it can tolerate some degree of surface roughness, gold-eutectic can be made fairly reliable, as opposed to anodic bonding which cannot tolerate any surface roughness. The wafer surface should generally be pretty smooth, but the areas of the wafer that are re-filled with LPCVD nitride for electrical isolation of the electrodes have on the order of .5-1 μm of surface roughness. A Borofloat glass (Schott, Elmsford, NY) (very similar to Pyrex) wafer is chosen for the capping wafer because (1) Borofloat glass has a similar thermal expansion coefficient to that of silicon, minimizing thermal stress, (2) Borofloat glass is clear which makes bond alignment possible without an IR microscope. (Borofloat glass is also relatively inexpensive.)

To facilitate the gold-eutectic bonding it is desired to have at least a 1 μm thick polysilicon layer available for bonding. The polysilicon thickness is determined by both the original thickness of the deposited polysilicon and also by the amount of polysilicon consumed during the gap closing oxidation step (see above). In the process, the poly layer should be thicker than the gold metal lines to prevent the gold from contacting the Borofloat cap wafer. In addition, when the gold-silicon eutectic forms enough polysilicon must be available to form the eutectic liquid during bonding and it was found that 1 μm of poly was adequate for this purpose.

For bonding, the preparation of the wafers is essential; both the device wafer and packaging wafer need to be cleaned thoroughly, and also be as particle free as possible. The uniformity of the deposited gold layer on the Borofloat wafer is also important for bonding and will effect the uniformity of the bonded interface. The Unifilm Sputterer was used for gold deposition because it has a rotating sample holder and deposits at three different sample plate positions to achieve the best uniformity possible. Finally, a method is needed to separate the dies after wafer bonding and to expose the bond pads. A dicing step through most of the depth of the upper Borofloat wafer allows for a section of that wafer to be removed exposing the bond-pads. This step was also tried by dicing part way through the Borofloat wafer before bonding, and then the rest of the way after bonding. It was found that doing this leads to particles on the wafer surface that are very difficult to clean off, greatly reducing the bond yield.

A summary of the on-chip packaging process for the spring-softening sensors is given below:

1. Deposit 400 A of chromium and 7500 A of gold on a 600-800 μm thick Borofloat

wafer. The deposition is done in a sputterer with a rotating sample holder to try and get the best uniformity possible. The Borofloat wafer is cleaned before the metals are sputtered.

Figure 8.2 (a): Packaging wafer (shown in blue) with a sputtered gold layer.

2. Pattern and wet-etch the gold.

Figure 8.2 (b): Packaging wafer with a patterned gold layer.

3. Bond the SOI wafer with devices to the Borofloat in the Karl Suss bonder. Although the alignment tolerances are on the order of 20 μm's the alignment can still be done by hand using a microscope and the clamps from the bond fixture to steady the two wafers. The bonding is done under vacuum at 430 °C for 2.5 hrs, with 28 psi of pressure.

Figure 8.2 (c): Packaging wafer and device wafer after bonding.

4. Dice most of the way through the Borofloat wafer, this creates cracks allowing the glass to be broken away (after dicing) exposing the bond pads.

Figure 8.2 (d): Bonded device wafer and packaging wafer with notches cut into the packaging wafer using a dicing saw. The notches allow for the packaging wafer to be broken away exposing the bond pads.

5. Dice through the Borofloat wafer and the SOI wafer to singulate the wafer.
6. Apply ALD TiO_2 or ZrO_2 passivation, using exposure mode (This allows the precursor to sit in the chamber for 10-20 seconds without being pumped out so that it has time to diffuse). The exposure mode allows for coating the inside of the channels which have a high aspect ratio. This step can be done at the die level after dicing.

As with the packaging process for the cantilevers there are some important layout considerations for successful eutectic bonding. First, at least 450 μm must be left between the edge of the bonded structure and the bond pads. Doing so ensures that there is enough space for the width of the wire-bonder's wedge allowing it to contact the bond pads. Secondly, the packaging and device wafer must be aligned by hand, and some tolerance must be left for misalignment. In the spring-softening sensor layout at least 25 μm was left between the edge of the fluid channels and the resonator cavity. Although this is a small tolerance for alignment by hand, by using one or more of the bond fixture clamps during alignment it is possible to restrain the wafer enough to allow for alignment.

8.1.2 Spring-Softening Sensor Flow-Cell Design

The packaging concept used for the spring-softening sensors is very similar to

that of the cantilevers. Both use an on-chip packaging step to facilitate further packaging in an acrylic manifold constructed using SLA. The much smaller tolerance (on the order of 30μm for the spring-softening resonators compared to roughly 300μm for the cantilevers) means that a different approach is needed for the on-chip packaging step (as discussed above). With the much smaller tolerances, a wafer level capping step is selected because (1) it has the potential to hermetically seal the resonator, (2) a wafer level process allows for more accurate alignment which is necessary with the tighter tolerances. The packaging concept is diagramed below in Figure 8.3.

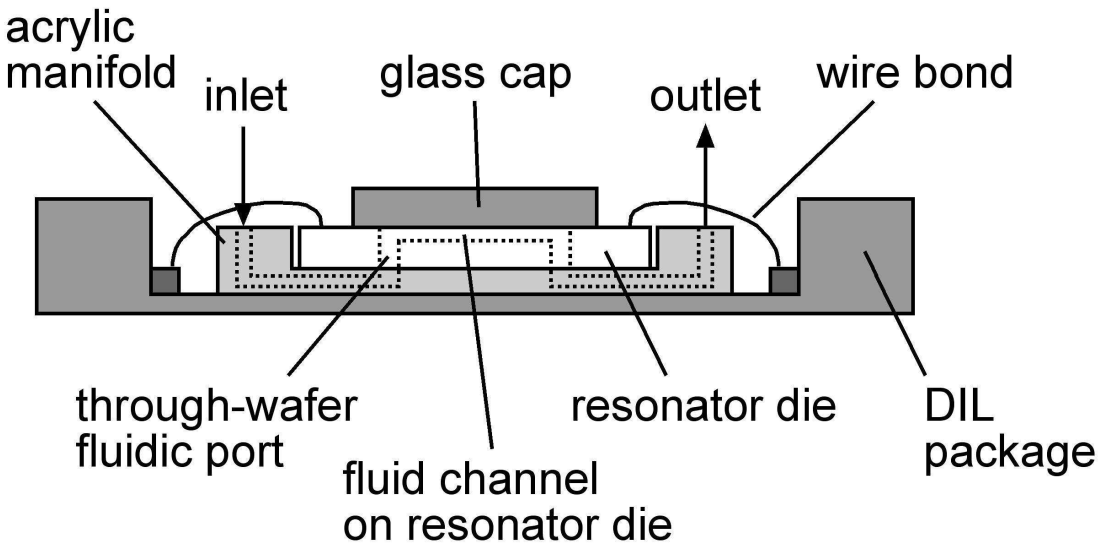

Figure 8.3: Illustration of the packaging concept for the spring-softening sensor with the cap wafer on the die and fluid flow from the inlet, up into the fluid channels on the die and back down and out through the outlet.

Figure 8.4 shows a CAD drawing of the manifold used for creating a flow cell for the spring-softening sensors. The flow cell is created by interfacing the circular ports on the die with the fluid channels on the manifold allowing for fluid flow as depicted in Figure 8.3.

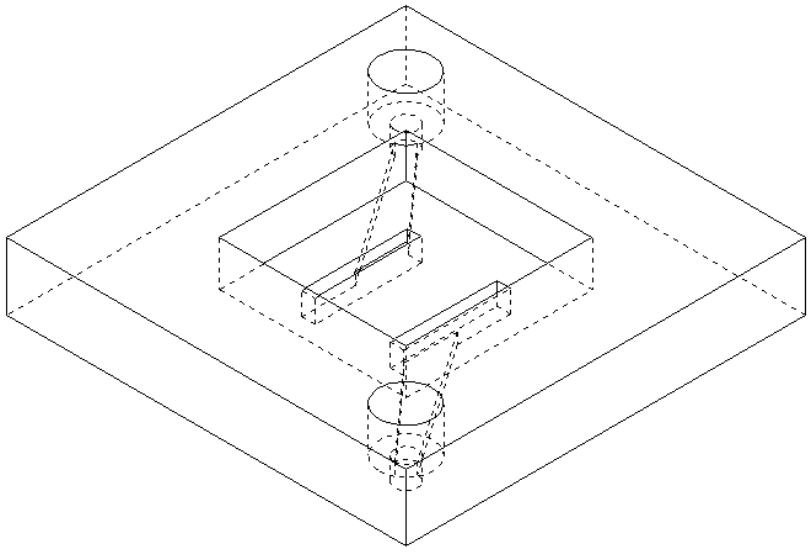

Figure 8.4: Lower manifold used for spring-softening resonator packaging. The two circular holes are for fluid flow to and from the manifold. Fluid flows from these two circular openings, to the rectangular slots, through the fluid ports (large circular openings) on the die, into the fluid channels on the device layer and then back out through the other set of ports into the other side of the manifold.

The bottom manifold is attached to a ceramic DIL package using epoxy (see Figure 8.4). The die itself has a glass cap, which seals the fluid channel and also the through wafer fluid ports on the top. Fluid is injected through tubing inserted into the bottom manifold; the same silicone to PEEK tubing connection used for the cantilevers can be used to make a secure fluidic connection to the bottom manifold (see Chapter 5). Fluid flows from the manifold, through the fluidic ports on the die, to the fluid channel on the die, out through the other set of fluid ports, and finally out through the tubing at the opposite side of the manifold.

8.1.3 Process Characterization Results

The fabrication process outlined in Section 8.1 was applied to the fabrication of the spring-softening resonator structures. Figure 8.5 is an SEM image of an entire

clamped-clamped beam resonator. The target gap width for the fabricated resonators was .6-.8 μm, it was found that these gaps could reliably be created. With the oxidative trench closure process the gap width can be adjusted using the same mask set simply by varying the polysilicon oxidation time

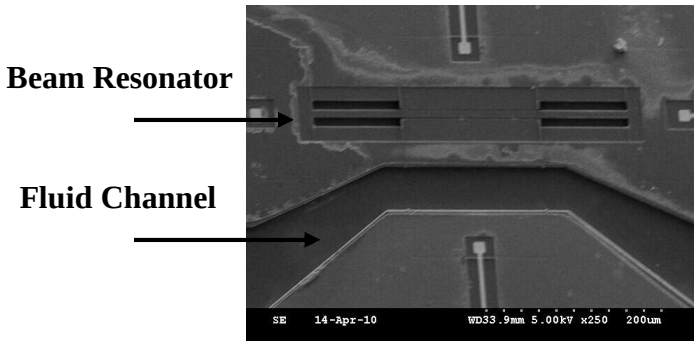

Figure 8.5: Fabricated spring-softening sensor with clamped-clamped beam resonator, fluid channel, and all four electrical connections.

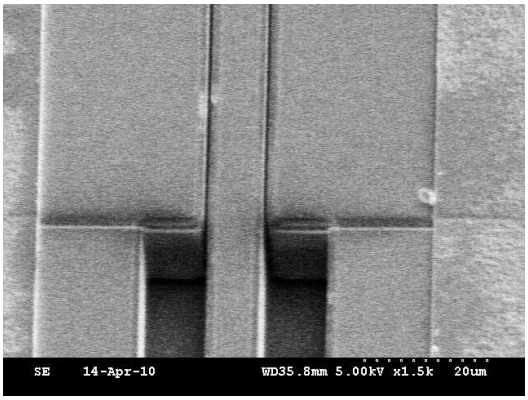

Figure 8.6: SEM image of spring-softening sensor with submicron transductions gaps between the floating electrodes and the resonators.

Figure 8.6 shows a completed device with submicron transduction gaps. Figure 8.7 is an SEM image of the nitride isolation at the base of a released beam. The overlap of the nitride with the resonator cavity is visible indicating that the nitride does in fact isolate the beam from the substrate and the other electrodes.

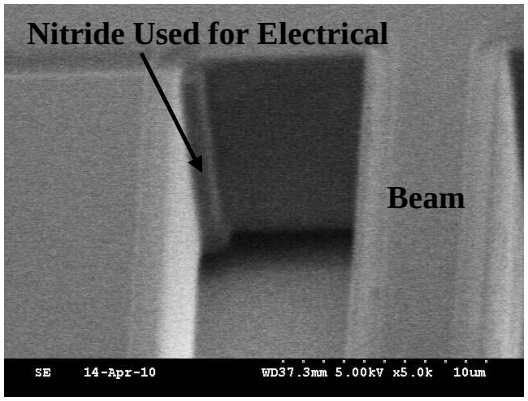

Figure 8.7: The nitride isolation on a beam resonator. The nitride extends 2μm past the corner of the trench at the base of the resonator.

Figure 8.8 is an infrared (IR) microscope image of a released clamped-clamped beam resonator. Silicon is transparent in the infrared region of the electromagnetic spectrum, and thus imaging the devices in the IR allows one to look below the silicon device layer. In this case, the infrared image allows one to see if the beams are released. One can see the white areas around the edges indicating that the oxide is etched, under etching the silicon areas. The beam has a different color than the surrounding silicon indicating that is has been released. Further, the areas next to the beam, particularly those adjacent to the submicron gaps, are under etched (as demonstrated by the white color). If the oxide in these areas is etched there is nothing that will prevent the beam from being released. In additional to IR microscope images, resonators have been broken off by hand, and from doing so it can be seen that there is no oxide left under the beams.

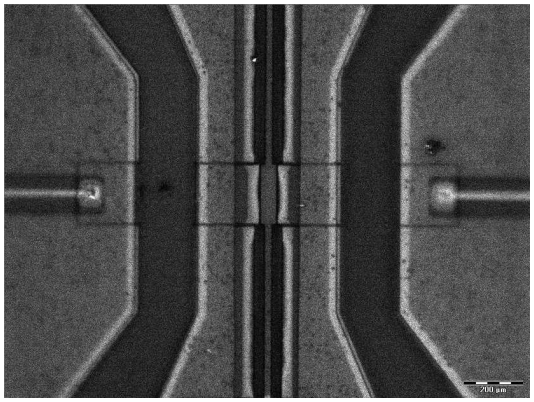

Figure 8.8: Infrared microscope image showing that the resonators are in fact released.

Figures 8.9-8.11 are optical images depicting the wafer-level packaging process flow. Figure 8.9 shows a die before packaging (after dicing from a wafer that was not actually bonded to a glass wafer); the polysilicon area for eutectic bonding can be seen in gray on the die's surface. Figure 8.10 shows a successfully bonded die from a wafer where bonding was performed. The wafer was diced and this image shows the die with cuts made part way through the capping wafer. These cuts allow the glass over the bond pads to be snapped off, exposing the bond pads. (Unfortunately, there was an issue with the metallization on this wafer and the bonded devices could not be tested.) In Figure 8.11 the glass has been removed from the top of the bond pads.

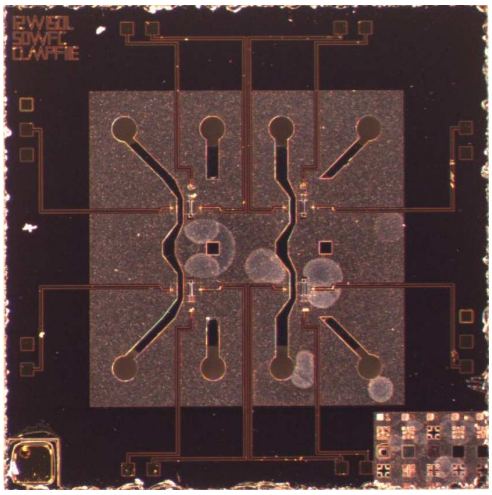

Figure 8.9: Optical microscopy image of an unbonded spring softening die.

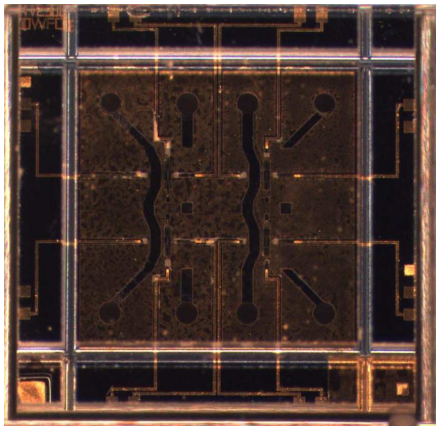

Figure 8.10: Optical microscopy image of wafer-level packaged spring-softening resonator before the scored glass wafer is broken off at the edges exposing the bond pads.

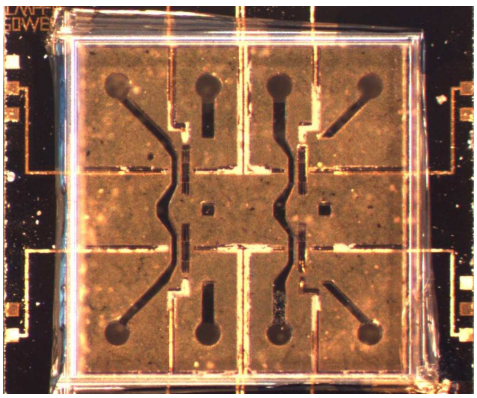

Figure 8.11: Optical microscopy image of a Borofloat wafer eutectically bonded to the SOI device wafer after breaking off access pieces to access the bond pads.

Figure 8.12 is an optical microscopy image of a clamped-free beam. The nitride isolation can be seen as dark lines on the die surface. A probe station was used to confirm that there is electrical continuity across the metal lines that cross the nitride trenches. The color streaks in the silicon nitride over the beam and on the edges of the resonator cavity are a result of the resonator release and show where the buried oxide has been etched from under and around the beam.

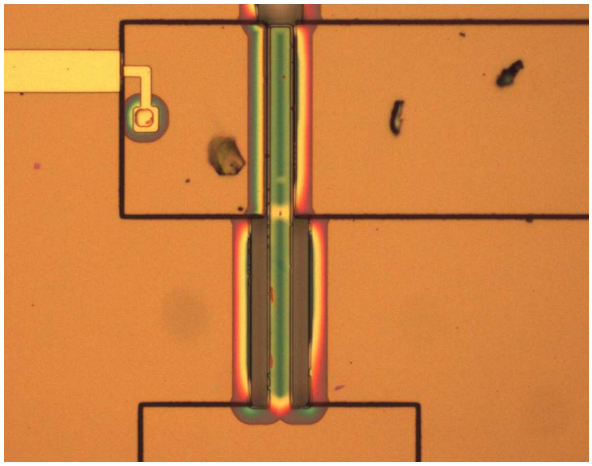

Figure 8.12: Optical image of a clamped-free beam fabricated using the spring-softening process.

The images presented above show that the fabrication process as implemented can achieve the above mentioned goal of creating submicron transductions gaps with the designed structures. In addition, the combination of a thermal oxide layer in addition to an LPCVD nitride layer allowed the device's three electrodes to be isolated from each other to the extent that the resistance between them was too large to be measured with a digital multi-meter (the resistances are in the 10^9 Ω range).

There are further improvements that can be made to the mask design and the fabrication process. First, for the mask design, a larger overlap should be left at the base of the resonators (next to the beam's anchor) between the trenches that are etched for electrode isolation and the mask that is used to define the resonator geometry. This will allow for more reliable fabrication because there will be (1) more alignment tolerance allowing for more error, (2) thicker oxides can be used during the polysilicon oxidation step without overlapping with the isolation trenches preventing proper etching and causing shorts. A second improvement would be to have fingers in the fluid channel. Fingers will increase the capacitive coupling between the electrodes and also increase the surface area for analyte binding. A third and final improvement would be to completely

backfill the isolation trenches with spin-on glass. To do this, a thin oxide layer would be grown, on top of that LPCVD nitride would be deposited, then spin-on glass would be deposited, cured, polished back to the surface, and finally capped with nitride. Using spin-on glass would help to reduce the surface roughness around the trenches making it easier for metal lines to bridge the trenches and also helping to make the wafer-bonding process more reliable.

8.2 Spring-Softening Device Testing Setup and Characterization Results

Figure 8.13 below shows the basic electrical connections of the spring-softening resonator for testing. As indicated in Figure 8.13, the devices were connected to a transimpedance amplifier for testing, which converts the resonator output current to a voltage that can then be read by a spectrum analyzer. For testing, the spring-softening resonators were electrically connected to an external circuit in one of three ways: (1) wire-bonding to a 28-pin DIL package, (2) using a probe station to contact the bond pads, or (3) by directly wire-bonding the dies to a custom PCB board containing the transimpedance amplifier. It is thought that this third method of directly wire-bonding the devices to a custom PCB board is best because it reduces parasitic capacitances.

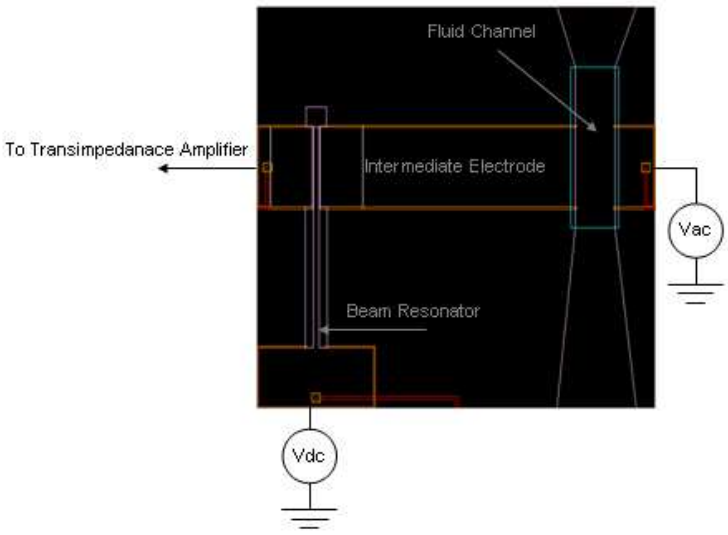

Figure 8.13: Schematic of CAD layout of spring-softening sensors with electrical connections used for testing. The electrode labeled intermediate electrode is the node that changes DC voltage in response to a dielectric constant change within the fluid channel.

The phase and frequency response of a 7 μm wide, 275 μm long, 10 μm thick cantilever with 2 μm transduction gaps is shown in Figure 8.14. The presented measurement has the crosstalk between the input and output signals removed using MATLAB (Mathworks, Natick MA). The simulated resonance frequency for the tested device is 126.6 KHz, assuming a silicon density of 2330 kg/m^3, a Young's modulus of 167 GPa, and a Poisson ratio of 0.07. The simulated and measured responses are similar, with the measured result showing a frequency of 129.9 KHz. The extracted Q-factor for the device operating in air is approximately 6.3. For the test shown in Figure 8.14 a 15V DC bias was applied to the beam. For this measurement there was no nitride and electrical probes were directly connected to the intermediate electrodes to make the electrical connections shown in Figure 8.13.

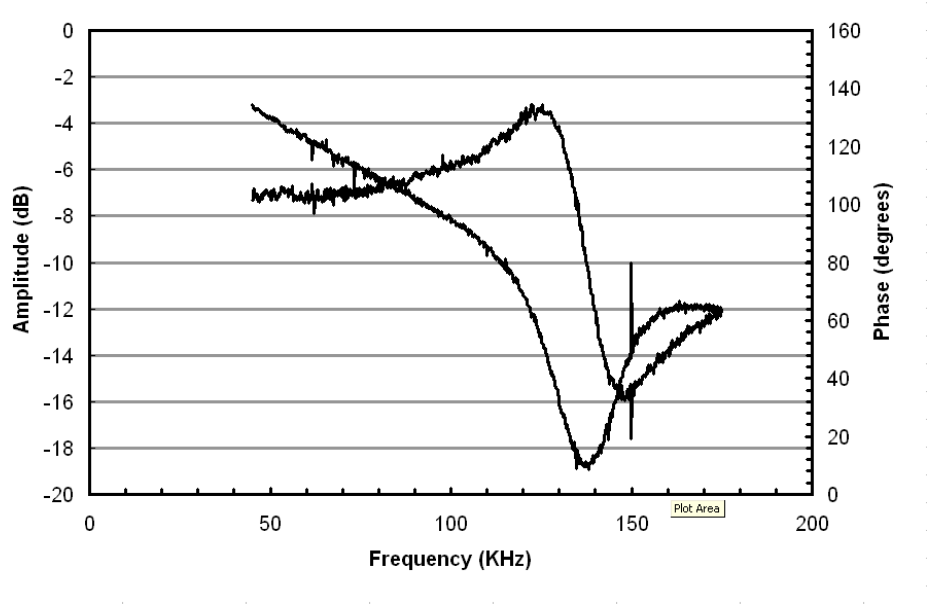

Figure 8.14: Amplitude and phase transfer characteristic of a 7μm wide 275μm long 10μm thick clamped-free beam.

Further analysis was also performed using a Polytech MSA-500 motion analyzer. Unfortunately, this instrument was found to be not sensitive enough in its in-plane sensing capability to resolve the small vibration amplitude of the in-plane mode. Despite this, an out-of-plane mode was observed for a 15 μm thick device (10 μm thick beams were not tested with the vibrometer). The presence of an out-of-plane mode at least indicates that the beams were fabricated and released in such a way that resonance is possible.

As mentioned above, based on the preliminary fabrication and testing results, two changes could be made to the device layout that would improve performance. First, instead of having fluid channels with straight walls, interdigitated fingers could be added into the fluid channels to increase the capacitive coupling between the input and floating electrodes, giving a better signal to noise ratio and a higher surface area for analyte binding. This strategy is commonly used in purely capacitive sensors to increase

sensitivity [38]. Second, trenches could be etched around the anchor for each beam (leaving only a small bridge to route a metal line); this would give better electrical isolation between the electrodes leading to less crosstalk between electrodes and improving SNR. Finally, with the current layout, only two microns of overlap was left between the nitride line at the base of the resonator and the resonator cavity. In future iterations, this overlap could be increased, which would improve the fabrication yield. Currently, many of the fabricated devices have with the resonator and input electrode shorted due to this issue.

A device concept and fabrication process has been developed for a spring-softening sensor that decouples resonator operation from the surrounding media. Unfortunately, with the desired and fabricated submicron gap size, the resonators may be too damped to operate in air [155]. A more robust vacuum packing concept requiring further process development is necessary to actually demonstrate these devices as liquid-phase sensors. A candidate process may involve the use of a sacrificial polymer packaging process that has been demonstrated for packaging of electrostatic resonators [156].

CHAPTER 9

CONCLUSIONS OUTLOOK AND FUTURE WORK

The purpose of this work is the development of resonant MEMS-based liquid-phase biochemical sensors. Of particular interest are systems that can be batch manufactured, reducing the cost per unit. Two systems have been investigated: one using bulk-micromachined thermally excited, piezoresistively detected single-crystal silicon cantilevers and the other utilizing surface-micromachined electrostatically actuated single-crystal silicon resonators.

A thermal actuation and piezorestive detection scheme has been implemented, allowing for excitation of the fundamental in-plane mode of a cantilever beam. Subsequently, the cantilevers have been fabricated and thoroughly characterized in both air and water. The mechanical characterization has allowed for conclusions to be drawn about which cantilever geometries make the most effective liquid-phase biochemical sensors. In addition, the in-plane cantilevers have been implemented as both chemical sensors and biosensors in liquid. For liquid-phase testing a flow cell has been designed. A wafer-level packaging process has been developed allowing part of the structure needed for the creation of the flow to cell to be placed on each die at the wafer level. Chemical testing results indicate that the cantilevers can be used as liquid-phase sensors achieving ppb-range limits of detection for volatile organics in the liquid phase. This represents an order of magnitude improvement compared to previously demonstrated liquid-phase sensors based on cantilevers vibrating in their out-of-plane mode.

For biosensors, the goal of this work was a proof-of-concept demonstration of a

biosensing system using an in-plane cantilever operated in liquid. A surface functionalization protocol has been developed allowing for the attachment of proteins to a gold surface on each beam. In addition, a low-temperature CNT growth process has been developed enabling CNT growth on the cantilevers. The CNTs create a large surface area for ligand attachment, which in the future could be used to improve sensitivity. Biosensor testing has indicated that the cantilevers are capable of limits of detection in the hundreds of ng/ml range. The lowest limit of detection measured was around 100 ng/ml, which is close to the range needed for biomarker detection in clinical applications.

In order to further improve the reliability and possibly the detection limit of liquid-phase resonant biochemical sensors, a new sensing concept has based on the spring-softening effect has been devised. The proposed design has been modeled and a fabrication process has been developed and implemented for the creation of the spring-softening resonators. Basic device testing has been performed indicating that the fabrication process does in fact create devices that can resonate. A packaging scheme has been designed for the creation of a flow cell for the spring-softening sensors. Further a wafer level packaging method has been implemented and tested indicating that such a process could be used to package these sensors.

In the future, several possible directions are possible for both sensing concepts. As chemical sensors, the cantilevers demonstrate good sensitivity, but still require improvements for water monitoring applications. Perhaps even more importantly, a better method is needed to create selectivity between different volatile organics. This could possibly be accomplished by using peptide functionalized CNTs, which has recently been investigated for the same purpose in the gas-phase. For biosensor implementation, the

detection limit must be brought into the low ng/ml range for clinical applications. Going forward the detection limit could be improved by (1) increasing the surface coverage using the current functionalization method, or by (2) creating a larger area to functionalize by using CNTs on the device surface (see Chapter 6).

The spring-softening sensor concept has been developed and initial devices have been fabricated. Despite this, preliminary proof-of-concept results are still lacking. A key component to achieving these results will be improving the packaging methods to allow for both encapsulation of the fluid channels for flow cell creation and vacuum packaging of the resonator to allow for high-Q resonances to be observed.

In conclusion, while both of the investigated systems cannot promise to give as low detection limits as benchtop instruments or some other semi-integrated systems, their strength is in both the simplicity of their design and their ability to be fabricated using the same tooling as CMOS circuits. Both systems investigated here are simple and compact enough to find their way into in-field measurement systems if the detection limits can be improved further.

APPENDIX 1

NOTES ON SURFACE FUNCTIONALIZATION

The same functionalization protocol presented in Chapter 6 is presented below. Notes are added to the protocol that describe what has been tried in improving the surface coverage. It should be noted that the real metric of interest is not the surface coverage, but rather the bioactivity of the molecules that are conjugated to the surface. Future investigations using SPR or antibody attachment studies to the functionalized surface should be used to compare the bioactivity obtained with changes to the protocol.

=> One general note is that it is very important to determine how the chemicals used for functionalization need to be stored (i.e., frozen at 0 C, frozen at -20 C, at 2-8 C). The storage temperature and conditions will be specified on the datasheet or on the chemical container itself.

I. SAM Formation.

1. Pre-clean gold samples: 10 min in acetone, 2 min in methanol, 2 min in isopropanol, dry with nitrogen. Treat for 5 min in oxygen plasma at 100 sccm in the plasma cleaner.

=> If there are particles on the surface as a result of contamination from dicing or other wise the dies can be sonicated in DI H_2O to remove particles. Sonicating the samples for too long can cause the resonators to snap off. No more than 10 min of sonication at one time is recommended.

=> A 30 second pirhana (3:1 H_2SO_4: H_2O_2 @ 120 C) can be done if needed.

2. Incubate gold substrates in a 250mM Thioctic Acid in absolute ethanol solution(200 proof ethanol) for 24 hrs. Substrates are placed directly into the SAM solution after cleaning in the oxygen plasma, there is not a significant amount of time between cleaning and placing the substrates into solution.

=> A 10mM Mercaptundecanoic acid (MUA) was also used. The same protocol can be used with MUA. Thioctic acid was ultimately chosen based on the results of contact angle measurements. A gold surface treated with 10mM MUA for 18 hours gave a contact angle of 44.4 degrees, while a gold surface treated with a 250mM thioctic acid solution gave a contract angle of 64.5 degrees. The larger contact angle for the sample treated with thioctic acid means the surface is more hydrophobic and that the surface coverage is better for the thioctic acid than the MUA.

=> During the SAM formation step the vial containing is filled with dry nitrogen by spraying the opening from a nitrogen gun. The vial is then closed and sealed with parylene.

3. Rinse substrates with 200 proof ethanol from a squirt bottle, dry with nitrogen.

=> With the resonator dies, they are placed in a plastic boat containing 200 proof ethanol for 2 min. This is done twice.

II. Crosslinking of SAM Layer

1. Treat Substrate with a Solution of 15mM of NHS + 75mM EDC + 40mM NaCl in .1M MES buffer for 1 hour. Solution pH should be around 5.7. (8.6mg NHS, 72mg EDC, 97.6mg MES, and 11.7 mg NaCl in 5ml of DI H_2O)

=> The EDC/NHS reaction works best at a pH of 4-6. The pH needs to be adjusted based on the starting pH of the buffer or salt solution used (the pKa or pH will be specified by the vendor.)

=> The EDC has a lifetime of only 1-3 months depending on the number of times it is opened. It breaks down due to the presence of water. The EDC needs to be stored at – 20 C, nitrogen should be sprayed over the bottle opening (from a house nitrogen gun) and then the vial should be sealed with parylene. Optimal storage for the EDC would be dessicated at -20 C (per vendor specification).

=> The NHS has a lifetime of 9-12 months. The NHS should be stored at 2-8 C.

III Protein Attachment

1. Immerse substrates in .4 mg/ml protein A in (phosphate buffered saline) PBS for 2 hours at 2-4 degrees C.(PH 7.4)

=> Protein solutions ranging in concentration from .1 to 1 mg/ml were used to determined what concentration gives the best surface coverage without too much non-specific binding on a control sample.

=>The PBS that was used was DPBS without calcium or magnesium.

2. Rinse substrates in DI water, dry. (This step is performed only on samples to be imaged.)

=> *For measurements, the resonators are rinsed with 1X PBS. DI water would cause the proteins to denature.*

=> If a protein solution is made and aliquoted beforehand it should be stored at – 20 C at a concentration of at least 1 mg/ml. A protein or antibody solution should NOT go through multiple freeze thaw cycles (i.e., it should not be frozen, thawed and then re-frozen).

=> Antibody solutions were prepared with in 1X PBS. When using antibodies it is essential to look at the certificate of analysis to determine the concentration of the stock solution.

APPENDIX 5

MECHANICAL DRAWINGS OF PACKAGING MANIFOLDS

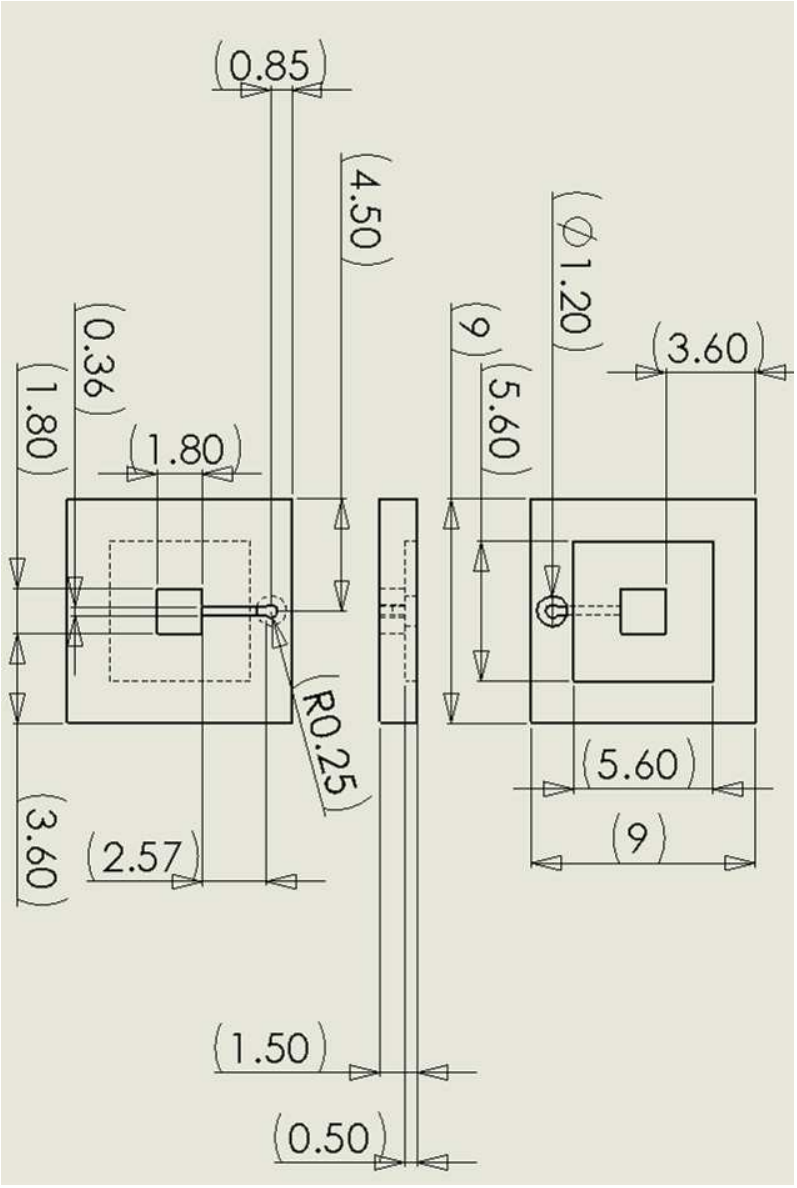

Figure A5.1: This is a drawing with dimensions of the bottom manifold used for packaging the in-plane cantilevers for liquid operation. All units are in millimeters. The dimensions given are for gluing the die into the manifold. This manifold is attached to a DIL packaged using Epoxy and epoxy is also used to attach a piece of hard tubing to the outlet hole.

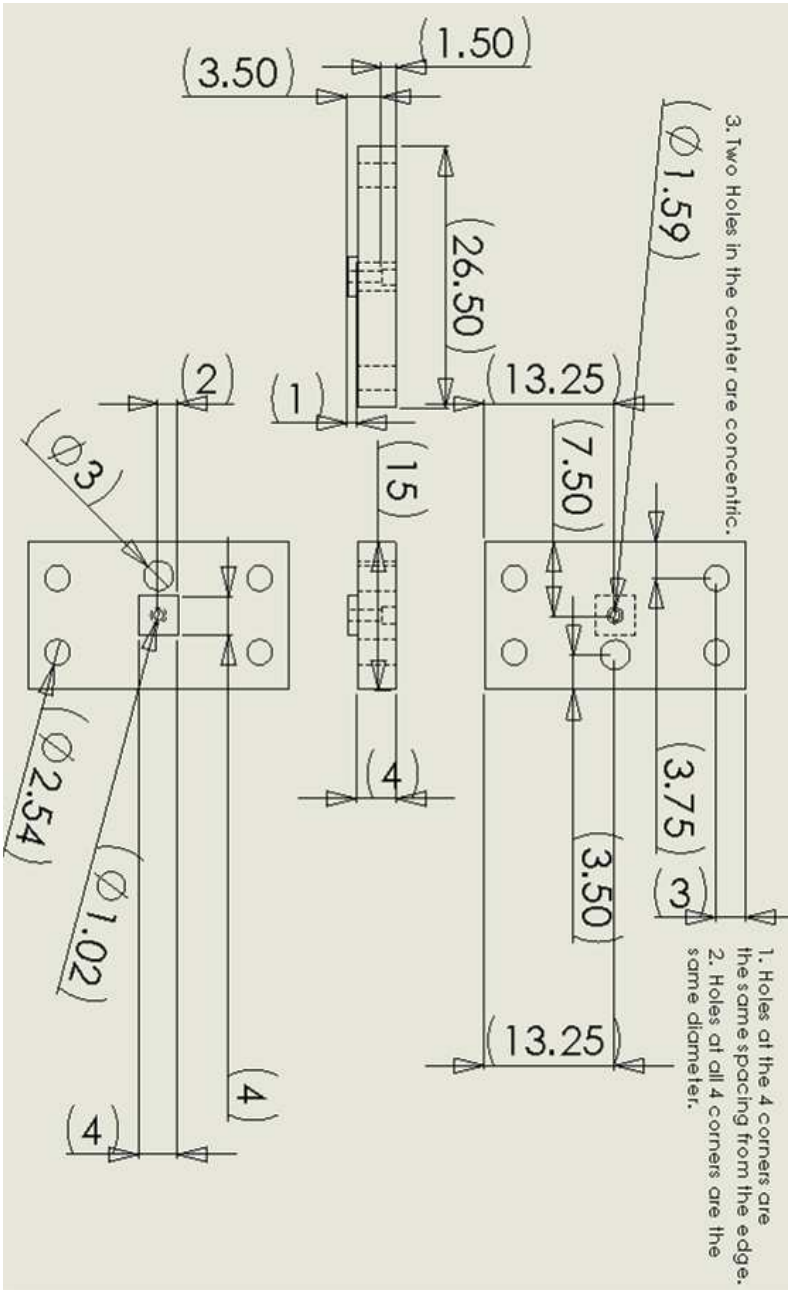

Figure A5.2: This is a drawing with dimensions of the top manifold used for packaging the in-plane cantilevers for liquid operation. All units are in millimeters. This manifold is meant for use with a 500μm thick gasket. Thermoplastic inserts are attached to a DIL package with epoxy allowing the manifold to screw down creating a flow cell.

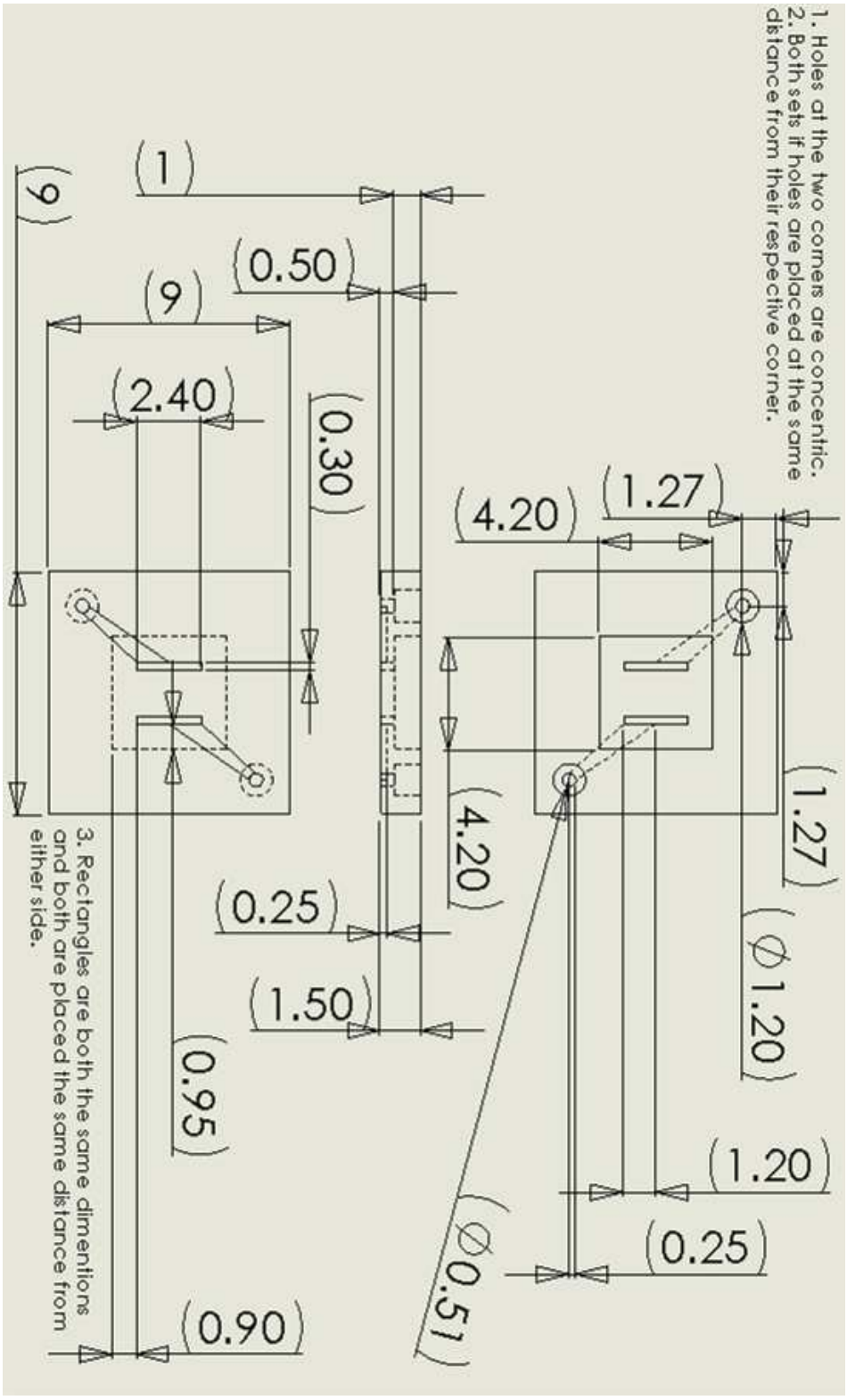

Figure A5.3: This is a drawing with dimensions of the top manifold used for packaging the spring-softening sensors for liquid operation. All units are in millimeters. This manifold is meant to have the chip glued into it (using epoxy) and is attached to a DIL package with epoxy.

Table A5.1: Packaging parts with descriptions.

Vendor	Part #	Description	Application
JB Weld	JB Kwik	Fast Setting Epoxy	Epoxy used for packaging assembly.
IDEX	1569	1/32” X .02” X 5ft PEEK Tubing	Tubing glued into the bottom cantilever manifold outlet.
Upchurch	1538	1/16” X .04” X 5 ft PEEK Tubing	Tubing used at the inlet to the top cantilever manifold and also to make connections to the syringe pumps.
VWR		.02” X .037” X .008 (wall) Silicone Tubing	Silicone tubing used at the outlet to the cantilever manifold.
Upchurch	F-330NX	1/16 to 10-32 fitting	Fitting used to seal the adapters to the PEEK tubing.
Upchurch	P-656	10-32 female to male luer adapter	Adapter used to connect PEEK tubing to luer fittings.
Upchurch	P-659	10-32 female to female luer adapter	Adapter used to connect PEEK tubing to luer fittings.
World Precision Instruments	14035-10	3-way stopcock valve	3-way valve used to connect 2 syringe pumps to a single piece of tubing leading to the flow cell.
Mcmaster-Carr	R700549PK	.02” thick silicone rubber. (40 durometer)	Gasket material used under the cantilever dies and also to seal the top manifold to the ring on the cantilever die.
Mcmaster-Carr		2-56 X 1/4 screws	Screws used to hold down the top manifold used to create the cantilever flow cell.
Mcmaster-Carr	93365A110	2-56 X .115” Brass Thermoplastic Insert	Thermoplastic inserts glued to the DIL packaged allowing the top manifold to be screwed into place.

APPENDIX 6

DIMENSIONS OF SPECIAL STRUCTURES

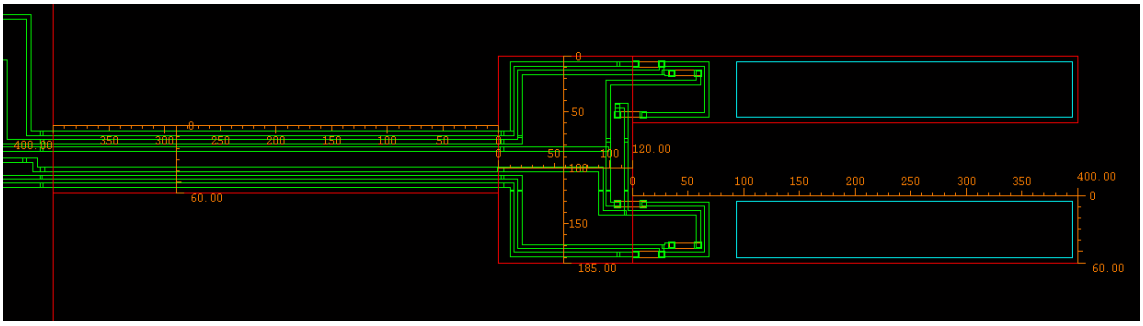

Figure A6.1: Dimensions of the long and narrow tuning fork structure. The numbers shown are in microns.

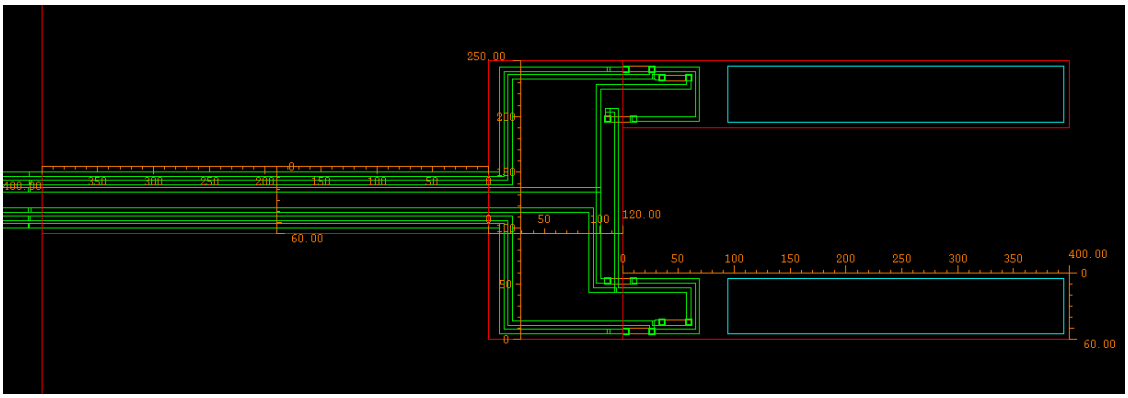

Figure A6.2: Dimensions of the long and wide tuning fork structure. The numbers shown are in microns.

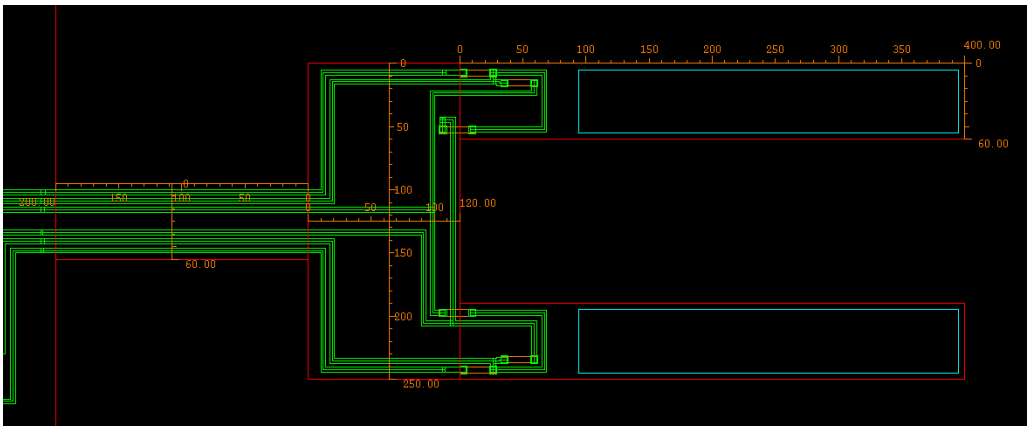

Figure A6.3: Dimensions of the short and wide tuning fork structure. The numbers shown are in microns.

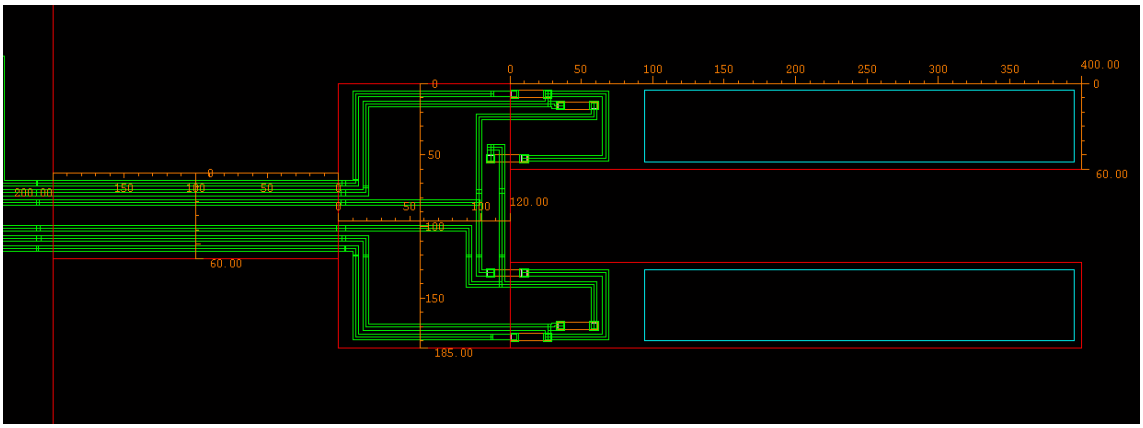

Figure A6.4: Dimensions of the short and narrow tuning fork structure. The numbers shown are in microns.

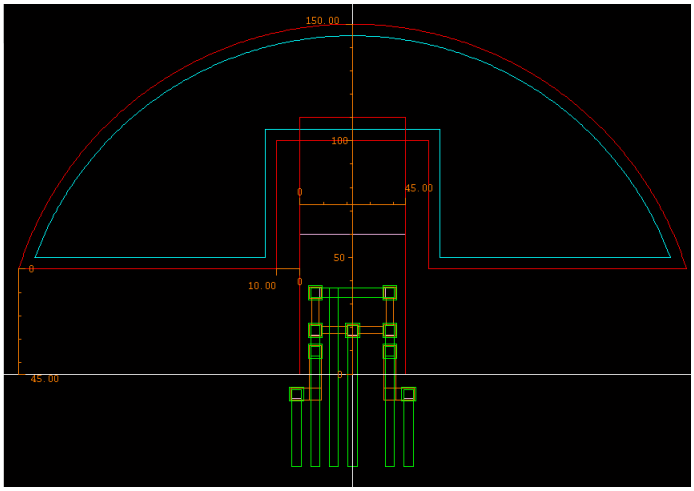

Figure A6.5: Dimensions of the F510 hammerhead structure. The numbers shown are in microns.

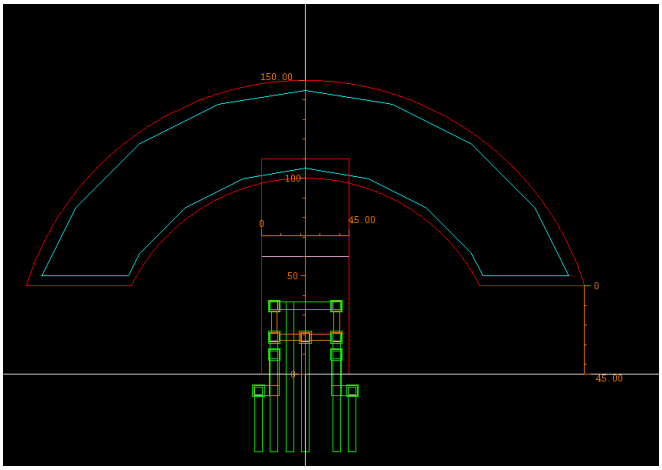

Figure A6.6: Dimensions of the F510S hammerhead structure. The numbers shown are in microns.

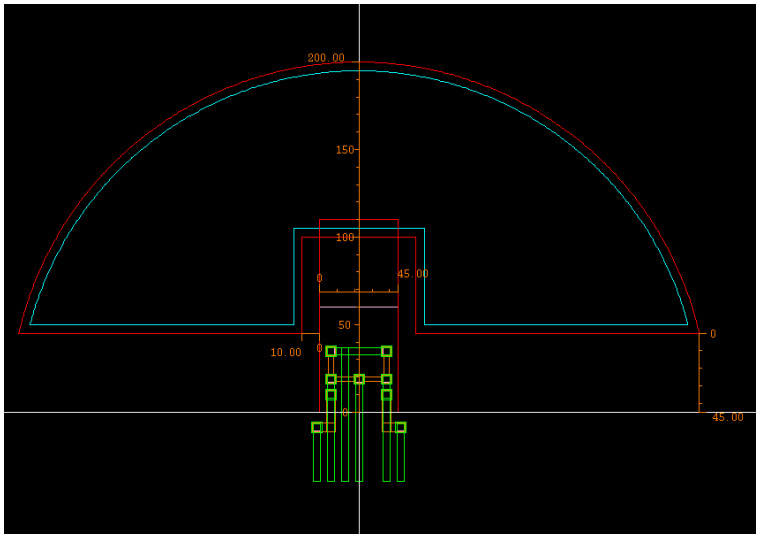

Figure A6.7: Dimensions of the F200 hammerhead structure. The numbers shown are in microns.

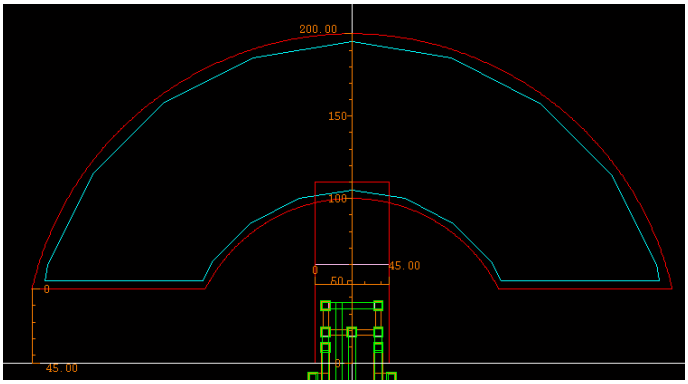

Figure A6.8: Dimensions of the F200S hammerhead structure. The numbers shown are in microns.

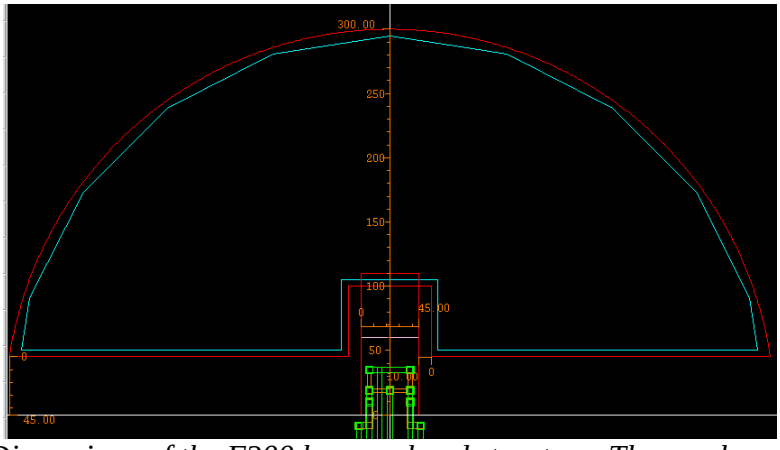

Figure A6.9: Dimensions of the F300 hammerhead structure. The numbers shown are in microns.

REFERENCES

[1] C. K. Ho, A. Robinson, D. R. Miller, and M. J. Davis, "Overview of Sensors and Needs for Environmental Monitoring," *Sensors,* vol. 5, pp. 4-37, 2005.

[2] R. A. Kerr, E. Kintisch, L. Schenkman, and E. Stokstad, "Five Questions on the Spill," *Science,* vol. 328, p. 963, 2010.

[3] E. Schleicher, "The clinical chemistry laboratory: Current status, problems and diagnostic prospects," *Analytical and Bioanalytical Chemistry,* vol. 384, pp. 124-131, 2006.

[4] T. Velten and M. Biehl, "Gaps and Challenges of Point-of-Care Technology," *IEEE Sensors Journal,* vol. 8, pp. 593-600, 2008.

[5] U. Friess and M. Stark, "Cardiac markers: A clear cause for point-of-care testing," *Analytical and Bioanalytical Chemistry,* vol. 393, pp. 1453-1462, 2009.

[6] J. J. Gooding, "Biosensor technology for detecting biological warfare agents: Recent progress and future trends," *Analytica Chimica Acta,* vol. 559, pp. 137-151, 2006.

[7] A. Warsinke, "Point-of-care testing of proteins," *Analytical and Bioanalytical Chemistry,* vol. 393, pp. 1393-1405, 2009.

[8] (June 2010). *Milken Institute Study of the Economic Burden of Chronic Diseases in the US*. Available: www.chronicdiseaseimpact.org

[9] G. A. Posthuma-Trumpie, J. Korf, and A. Van Amerongen, "Lateral flow (immuno)assay: Its strengths, weaknesses, opportunities and threats. A literature survey," *Analytical and Bioanalytical Chemistry,* vol. 393, pp. 569-582, 2009.

[10] C. A. Burtis, E. A. Ashwood, and D. E. Bruns, Eds., *Tietz Textbook of Clinical Chemistry and Molecular Diagnostics*. St. Louis: Elsevier Saunders, 2005.

[11] L. N. Plummer, E. Busenberg, S. M. Eberts, L. M. Bexfield, C. J. Brown, L. S. Fahlquist, B. G. Katz, and M. K. Landon, "Low-Level Detections of Halogenated Volatile Organic Compounds in Groundwater: Use in Vulnerability Assessments," *Journal of Hydrologic Engineering,* vol. 13, Nov 2008

[12] P. A. Lieberzeit and F. L. Dickert, "Sensor technology and its application in environmental analysis," *Analytical Bioanalytical Chemistry,* vol. 387, Jan 2007.

[13] J. Kaiser, "Panel Finds Environmental Risks Neglected," *Science,* vol. 328, p. 802, 2010.

[14] (2010). Available: http://www.epa.gov/safewater/contaminants/index.html

[15] I. Urbina, "Chemicals Were Injected Into Wells, Report Says," in *New York Times*, ed. New York, 2011.

[16] S. Zamplli, I. Elmi, F. Mancarella, P. Betti, E. Dalcanale, G. C. Cardinali, and M. Severi, "Real-time monitoring of sub-ppb concentrations of aromatic volatiles with a MEMS-enabled miniturized gas-chromatograph," *Sensors and Actuators B,* vol. 141, pp. 322-328, Aug 2009.

[17] G. Serrano, H. Chang, and E. T. Zellers, "A micro gas chromatograph for high-speed determinations of explosive vapors," presented at the Transducers 15th International Conference Solid State Actuators and Microsystems, Denver, 2009.

[18] M. Mehta, C. S. Hanumanthaiah, P. A. Betala, Z. Hong, R. SaeWeon, W. Buttner, W. R. Penrose, J. R. Stetter, and V. H. Perez-Luna, "Detection of proteins and

bacteria using an array of feedback capacitance sensors," *Biosensors and Bioelectronics,* vol. 23, pp. 728-34, 2007.
[19] D. A. Hall, R. S. Gaster, T. Lin, S. J. Osterfeld, S. Han, B. Murmann, and S. X. Wang, "GMR biosensor arrays: a system perspective," *Biosensors and Bioelectronics,* vol. 25, pp. 2051-7.
[20] L. Gorton, Ed., *Biosensors and Modern Biospecific Analytical Techniques* Comprehensive Analytical Chemistry. Amsterdam: Elsevier, 2005.
[21] M. J. Wenzel, "Polymer-Coated and Polymer-Based Microcantilever Chemical Sensors: Analysis and Sensor Signal Processing," PhD, Marquette University, Milwaukee, 2009.
[22] O. Brand, "Microsensor Integration Intro Systems-on-Chip," *Proceedings of the IEEE,* vol. 94, pp. 1160-1176, June 2006.
[23] P. S. Waggoner and H. G. Craighead, "Micro- and nanomechanical sensors for environmental, chemical, and biological detection," *Lab Chip,* vol. 7, pp. 1238-1255, Oct 2007.
[24] C. Vancura, Y. Li, J. Lichtenberg, K. U. Kirstein, A. Hierlemann, and F. Josse, "Liquid-phase chemical and biological detection using fully integrated magnetically actuated complementary metal oxide semiconductor resonant cantilever sensor systems," *Analytical Chemistry,* vol. 79, pp. 1646-1654, Jan 2007.
[25] D. L. Nelson and M. M. Cox, *Lehinger Principles of Biochemistry*, 4th ed. New York: W.H. Freeman Company, 2005.
[26] G. Gauglitz, "Direct optical sensors: Principles and selected applications," *Analytical and Bioanalytical Chemistry,* vol. 381, pp. 141-155, 2005.
[27] S. Andreescu and O. A. Sadik, "Trends and challenges in biochemical sensors for clinical and environmental monitoring," *Pure and Applied Chemistry,* vol. 76, pp. 861-878, 2004.
[28] M. Louden, *Organic Chemistry*, 4th ed. New York: Oxford University Press, 2002.
[29] J. B. Haun, C. M. Castro, R. Wang, V. M. Peterson, B. S. Marinelli, H. Lee, and R. Weissleder, "Micro-NMR for Rapid Molecular Analysis of Human Tumor Samples," *Science Translational Medicine* vol. 3, p. 71ra16, 2011.
[30] I. Barman, C.-R. Kong, G. P. Singh, R. R. Dasari, and M. S. Feld, "Accurate Spectroscopic Calibration for Noninvasive Glucose Monitoring by Modelding the Physiological Glucose Dynamics," *Analytical Chemistry,* vol. 82, pp. 6104-6114, 2010.
[31] K. Mercer and K. Kerly, "PTSD Genetics LAB Presentation," ed, 2009.
[32] Artemis. (2010). Available: http://www.artemishealthinc.com/technology/artemis_healths_microfluidic_technology/
[33] Y.-C. Kim, K.-H. Lee, S. Sasaki, K. Hashimoto, K. Ikebukuro, and I. Karube, "Photocatalytic sensor for chemical oxygen demand determination based on oxygen electrode," *Analytical Chemistry,* vol. 72, pp. 3379-3382, 2000.
[34] O. A. Sadik, A. O. Aluoch, and Z. Ailing, "Status of biomolecular recognition using electrochemical techniques," *Biosensors and Bioelectronics,* vol. 24, pp. 2749-65, 2009.

[35] K. Dill, D. D. Montgomery, A. L. Ghindilis, and K. R. Schwarzkopf, "Immunoassays and sequence-specific DNA detection on a microchip using enzyme amplified electrochemical detection," *Journal of Biochemical and Biophysical Methods,* vol. 59, pp. 181-187, 2004.
[36] S. R. Nugen, P. J. Asiello, J. T. Connelly, and A. J. Baeumner, "PMMA biosensor for nucleic acids with integrated mixer and electrochemical detection," *Biosensors and Bioelectronics,* vol. 24, pp. 2428-33, 2009.
[37] H. Suzuki, N. Nashida, W. Satoh, and J. Fukuda, "Electrochemical immunoassay on a microfluidic device with sequential injection and flushing functions," *Biosensors and Bioelectronics,* vol. 22, pp. 3167-73, 2007.
[38] E. Ghafar-Zadeh, M. Sawan, and D. Therriault, "CMOS based capacitive sensor laboratory-on-chip: A multidisciplinary approach," *Analog Integrated Circuits and Signal Processing,* vol. 59, pp. 1-12, 2009.
[39] M. I. Prodromidis, "Impedimetric immunosensors-A review," *Electrochimica Acta,* vol. 55, pp. 4227-4233.
[40] C. Berggren, B. Bjarnason, and G. Johansson, "Capacitive Biosensors," *Electroanalysis,* vol. 13, pp. 173-180, 2000.
[41] O. Gul, E. Heves, M. Kaynak, H. Basaga, and Y. Gurbuz, "Label-free, capacitive immunosensor for protein detection," in *IEEE Sensors 2006,* Daegu, Korea, 2006, pp. 600-3.
[42] A. R. Varlan, J. Suls, W. Sansen, D. Veelaert, and A. De Loof, "Capacitive sensor for the allatostatin direct immunoassay," *Sensors and Actuators, B: Chemical,* vol. B44, pp. 334-340, 1997.
[43] C. Hagleitner, A. Hierlemann, D. Lange, A. Kummer, N. Kerness, O. Brand, and H. Baltes, "Smart single-chip gas sensor microsystem," *Nature,* vol. 414, pp. 293-296, Nov 2001.
[44] C. F. Sanchez, A. M. Gallardo-Soto, K. Rawson, O. Nilsson, and C. J. McNeil, "Quantitative impedimetric immunosensor for free and total prostate specific antigen based on a lateral flow assay format," *Electrochemistry Communications,* vol. 6, pp. 138-43, 2004.
[45] C. K. Ho and R. C. Hughes, "In-Situ Chemiresistor Sensor Package for Real-time Detection of Volatile Organic Compounds in Soil and Groundwater," *Sensors,* vol. 2, pp. 23-34, 2002.
[46] P. R. Nair and M. A. Alam, "Design considerations of silicon nanowire biosensors," *IEEE Transactions on Electron Devices,* vol. 54, pp. 3400-8, 2007.
[47] Y. Cui, Q. Wei, H. Park, and C. M. Lieber, "Nanowire nanosensors for highly sensitive and selective detection of biological and chemical species," *Science,* vol. 293, pp. 1289-1292, 2001.
[48] V. Xuan Thang, R. Stockmann, B. Wolfrum, A. Offenhausser, and S. Ingebrandt, "Fabrication and application of a microfluidic-embedded silicon nanowire biosensor chip," *Physica Status Solidi A,* vol. 207, pp. 850-7.
[49] A. Hodge-Miller, F. K. Perkins, M. Peckerar, S. Fertig, and L. Tender, "Gateless depletion mode field effect transistor for macromolecule sensing," *2003 IEEE International Symposium on Circuits and Systems*. 2003, pp. 918-21.
[50] G. T. A. Kovaks, *Micromachined Transducers Sourcebook*. Boston: McGraw-Hill, 1998.

[51] C. R. Tamanaha, S. P. Mulvaney, J. C. Rife, and L. J. Whitman, "Magnetic labeling, detection, and system integration," *Biosensors and Bioelectronics,* vol. 24, pp. 1-13, 2008.
[52] K. Taton, D. Johnson, P. Guire, E. Lange, and M. Tondra, "Lateral flow immunoassay using magnetoresistive sensors," *Journal of Magnetism and Magnetic Materials,* vol. 321, pp. 1679-82, 2009.
[53] P. A. Besse, G. Boero, M. Demierre, V. Pott, and R. Popovic, "Detection of a single magnetic microbead using a miniaturized silicon Hall sensor," *Applied Physics Letters,* vol. 80, pp. 4199-201, 2002.
[54] J. Homola, "Surface plasmon resonance biosensors: advances and applications," in *20th International Conference on Optical Fibre Sensors(Proceedings of SPIE),* Edinburgh, Scotland, 2009, p. 75030P (4 pp.).
[55] K. Kneipp, W. Yang, H. Kneipp, L. T. Perelman, I. Itzkan, R. R. Dasari, and M. S. Feld, "Single molecule detection using surface-enhanced Raman scattering (SERS)," *Physical Review Letters,* vol. 78, pp. 1667-70, 1997.
[56] J. D. Ryckman, M. Liscidini, J. E. Sipe, and S. M. Weiss, "Porous silicon structures for low-cost diffraction-based biosensing," *Applied Physics Letters,* vol. 96, p. 171103 (3 pp.).
[57] M. E. Bosch, A. J. R. Sanchez, F. S. Rojas, and C. B. Ojeda, "Recent Development in Optical Fiber Biosensors," *Sensors,* vol. 7, pp. 797-859, 2007.
[58] X. Fan, I. M. White, S. I. Shopova, H. Zhu, J. D. Suter, and Y. Sun, "Sensitive optical biosensors for unlabeled targets: A review," *Analytica Chimica Acta,* vol. 620, pp. 8-26, 2008.
[59] (7/2010). *Raman Spectroscopy*. Available: http://en.wikipedia.org/wiki/Raman_spectroscopy
[60] T. K. Gaylord, "ECE 6771 Optoelectronics Class Notes," 2010.
[61] T. Yu-Chia, Y. Yi-Wen, T. Woo-Hu, and Y. Tsong-Rong, "Side-polished fiber immunosensor based on surface plasmon resonance for detection of Legionella pneumophila," *Proceedings of SPIE,* vol. 6852, pp. 685206-1, 2008.
[62] A. J. Haes, W. P. Hall, C. Lei, W. L. Klein, and R. P. Van Duyne, "A localized surface plasmon resonance biosensor: first steps toward an assay for Alzheimer's disease," *Nano Letters,* vol. 4, pp. 1029-34, 2004.
[63] T. Springer, M. Piliarik, and J. Homola, "Surface plasmon resonance sensor with dispersionless microfluidics for direct detection of nucleic acids at the low femtomole level," *Sensors and Actuators, B: Chemical,* vol. 145, pp. 588-591.
[64] A. Densmore, M. Vachon, D. X. Xu, S. Janz, R. Ma, Y. H. Li, G. Lopinski, A. Delage, J. Lapointe, C. C. Luebbert, Q. Y. Liu, P. Cheben, and J. H. Schmid, "Silicon photonic wire biosensor array for multiplexed real-time and label-free molecular detection," *Optics Letters,* vol. 34, pp. 3598-600, 2009.
[65] J. Tschmelak, G. Proll, and G. Gauglitz, "Verification of performance with the automated direct optical TIRF immunosensor (River Analyser) in single and multianalyte assays with real water samples," *Biosensors and Bioelectronics,* vol. 20, pp. 743-52, 2004.
[66] F. Baldini, L. Bolzoni, A. Giannetti, M. Kess, P. M. Kramer, E. Kremmer, G. Porro, F. Senesi, and C. Trono, "A new procalcitonin optical immunosensor for

POCT applications," *Analytical and Bioanalytical Chemistry,* vol. 393, pp. 1183-1190, 2009.
[67] G. Gauglitz, "Optical sensors in water monitoring," *Proceedings of SPIE,* vol. 6633, pp. 663319-8, 2007.
[68] T. Ye, W. Wenhui, A. Chery, Jr., W. Nan, C. Guthy, and W. Xingwei, "Label-free detection of biomolecules using a tapered optical fiber sensor," *Proceedings of SPIE,* p. 767307 (7 pp.).
[69] B. Mizaikoff, "Reviewed: Mid-IR Fiber Optic Sensors," *Analytical Chemistry,* vol. 75, pp. 258A-267A, June 2003 2003.
[70] H. Zhu, J. D. Suter, I. M. White, and X. Fan, "Aptamer Based Microsphere Biosensor for Thrombin Detection," *Sensors,* vol. 6, pp. 785-795, 2006.
[71] K. De Vos, P. Debackere, T. Claes, J. Girones, W. De Cort, E. Schacht, R. G. Baets, and P. Bienstman, "Label-free biosensors on silicon-on-insulator optical chips," *Proceedings of SPIE,* vol. 7397, p. 739710 (8 pp.), 2009.
[72] I. M. White, "Optofluidic biosensing for the study of disease at the molecular level," *Proceedings of SPIE,* vol. 7606, pp. 760609-1.
[73] C. Liu, X. Qiu, S. Ongagna, D. Chen, Z. Chen, W. R. Abrams, D. Malamud, P. L. A. M. Corstjens, and H. H. Bau, "A timer-actuated immunoassay cassette for detecting molecular markers in oral fluids," *Lab on a Chip,* vol. 9, pp. 768-76, 2009.
[74] C. Hou and A. E. Herr, "Ultrashort separation length homogeneous electrophoretic immunoassays using on-chip discontinuous polyacrylamide gels," *Analytical Chemistry,* vol. 82, pp. 3343-3351.
[75] A. K. Ellerbee, S. T. Phillips, A. C. Siegel, K. A. Mirica, A. W. Martinez, P. Striehl, N. Jain, M. Prentiss, and G. M. Whitesides, "Quantifying colorimetric assays in paper-based microfluidic devices by measuring the transmission of light through paper," *Analytical Chemistry,* vol. 81, pp. 8447-8452, 2009.
[76] X. Y. Liu, C. M. Cheng, A. W. Martinez, K. A. Mirica, X. J. Li, S. T. Phillips, M. Mascarenas, and G. M. Whitesides, "A Portable Microfluidc Paper-Based Device for ELISA," in *24th IEEE MEMS Conference,* Cancun, Mexico, 2011, pp. 75-78.
[77] H. J. Lee, K. K. Park, P. Cristman, O. Oralkan, M. Kupnik, and B. T. Khuri-Yakub, "A Low-Noise Oscillator Based On A Multi-Membrand CMUT For High Sensitivity Resonant Chemical Sensors," in *22nd IEEE MEMS,* Serrento, Italy, 2009, pp. 761-764.
[78] S. Tadigadapa and K. Mateti, "Piezoelectric MEMS Sensors: State-of-the-Art and Perspectives," *Measurement Science and Technology,* vol. 20, p. 92001, Jul 2009.
[79] R. Lucklum and P. Hauptmann, "Quartz crystal microbalance: mass sensitivity, viscoelasticity and acoustic amplification," *Sensors and Actuators, B: Chemical,* vol. 70, pp. 30-36, 2000.
[80] R. Lucklum and P. Hauptmann, "Acoustic Sensors the Challenge Behind Microgravimetry," *Analytical Bioanalytical Chemistry,* vol. 384, pp. 667-682, Feb 2006.
[81] Z. Li, Y. Jones, J. Hossenlopp, R. Cernosek, and F. Josse, "Analysis of Liquid-Phase Chemical Detection Using Guided Shear Horizontal-Surface Acoustic Wave Sensors," *Analytical Chemistry,* vol. 77, pp. 4595-4603, Nov 2005.

[82] K. Lange, B. E. Rapp, and M. Rapp, "Surface acoustic wave biosensors: A review," *Analytical and Bioanalytical Chemistry,* vol. 391, pp. 1509-1519, 2008.
[83] O. Tigli, L. Bivona, P. Berg, and M. E. Zaghloul, "Fabrication and characterization of a surface-acoustic-wave biosensor in cmos technology for cancer biomarker detection," *IEEE TRANSACTIONS ON BIOMEDICAL CIRCUITS AND SYSTEMS,* vol. 4, pp. 62-73, 2010.
[84] M. Weinberg, C. E. Dube, A. Petrovich, and A. M. Zapta, "Fluid Dampling in Resonant Flexural Plate Wave Devices," *Journal of Microelectromechanical Systems,* vol. 12, pp. 567-576, 2003.
[85] I. Y. Huang and M. C. Lee, "Development of a FPW allergy biosensor for human IgE detection by MEMS and cystamine-based SAM technologies," *Sensors and Actuators: B. Chemical,* vol. 132, pp. 340-8, 2008.
[86] D. Lange, C. Hagleitner, A. Hierlemann, O. Brand, and H. Baltes, "Complementary metal oxide semiconductor cantilever arrays on a single chip: mass-sensitive detection of volatile organic compounds," *Analytical Chemistry,* vol. 74, pp. 3084-3095, Jul 2002.
[87] D. Jeutter, F. Josse, M. Johnson, M. Wenzel, J. Hossenlopp, and R. Cernosek, "Design of a portable guided SH-SAW chemical sensor system for liquid environments," in *Proceedings of the IEEE International Frequency Control Symposium and Exposition*, Vancouver, BC, Canada, 2005, pp. 59-68.
[88] Y. Song and B. Bhushan, "Atomic Force Microscope Dynamic Modes: Modeling and Applications"," *J. Phys.: Condens. Matter,* vol. 20, p. 225012, May 2008.
[89] K. M. Goeders, J. S. Colton, and L. A. Bottomley, "Microcantilevers: sensing chemical interactions via mechanical motion," *Chemical Reviews,* vol. 108, pp. 522-542, Feb 2008.
[90] R. Datar, S. Kim, S. Jeon, P. Hesketh, S. Manalis, A. Boisen, and T. Thundat, "Cantilevers: Nanomechanical Tools for Diagnostics," *MRS Bulletin,* vol. 34, pp. 449-454, Feb 2009.
[91] Y. Nemirovsky, A. Shemesh, and S. Stolyarova, "NEMS/MEMS Cantilever-Based Biosensors: Addressing the Open Issues," *Proceedings of SPIE,* vol. 6993, pp. 699302-1-699302-12, May 2008.
[92] J. H. Lee, K. H. Yoon, K. S. Hwang, J. Park, S. Ahn, and T. S. Kim, "Label free novel electrical detection using micromachinged PZT monolithic thin film cantilever for the detection of C-reactive Protein," *Biosensors and Bioelectronics,* vol. 20, pp. 269-275, 2004.
[93] Y. Min, J. C. Stachowiak, L. Henry, R. Datar, R. Cote, and A. Majumdar, "Label-free protein recognition two-dimensional array using nanomechanical sensors," *Nano Letters,* vol. 8, pp. 520-4, 2008.
[94] R. Mukhopadhyay, M. Lorentzen, J. Kjems, and F. Besenbacher, "Nanomechanical sensing of DNA sequences using piezoresistive cantilevers," *Langmuir,* vol. 21, pp. 8400-8408, 2005.
[95] S. S. Bedair and G. K. Fedder, "CMOS MEMS oscillator for gas chemical detection," in *IEEE Sensors Conference 2004*, Vienna, Austria, pp. 955-8.
[96] S. D. Senturia, *Microsystems Design*. New York: Springer, 2001.

[97] D. Then, A. Vidic, and C. Ziegler, "A highly sensitive self-oscillating cantilever array for the quantitative and qualitative analysis of organic vapor mixtures," *Sensors and Actuators B,* vol. 117, pp. 1-9, Sept 2006.
[98] M. Zimmermann, T. Volden, K. U. Kirstein, S. Hafizovic, J. Lichtenberg, O. Brand, and A. Hierlemann, "A CMOS-based integrated-system architecture for a static cantilever array," *Sensors and Actuators B: Chemical,* vol. 131, pp. 254-264, 2008.
[99] G. Wu, R. H. Datar, K. M. Hansen, T. Thundat, R. J. Cote, and A. Majumdar, "Bioassay of prostate-specific antigen (PSA) using microcantilevers," *Nature Biotechnology,* vol. 19, pp. 856-860, 2001.
[100] A. Boisen and T. Thundat, "Design fabrication of cantilever array biosensors," *Materials Today,* vol. 12, pp. 32-8, 2009.
[101] X. Li, H. Yu, X. Gan, X. Xia, P. Xu, J. Li, M. Liu, and Y. Li, "Integrated MEMS/NEMS Resonant Cantilevers for Ultrasensitive Biological Detection," *Journal of Sensors,* 2009.
[102] Y. Liu, X. Li, Z. Zhang, G. Zuo, Z. Cheng, and H. Yu, "Nanogram per milliliter-level immunologic detection of alpha-fetoprotein with integrated rotating-resonance microcantielvers for early-stage diagnosis of hetocellular carcinoma," *Biomedical Microdevices,* vol. 11, pp. 183-191, 2009.
[103] J. H. Seo and O. Brand, "High Q-factor in-plane mode resonant mircrosensor platform for gaseous/liquid environment," *Journal of Microelectromechanical Systems,* vol. 17, pp. 483-493, Apr 2008.
[104] A. Rahafrooz and S. Pourkamali, "Resonant MEMS sensors for detection of aqueous heavy metal ions with sub-ppm resolution," in *2008 IEEE International Conference on Electron Devices and Solid-State Circuits,* Hong Kong, China, 2008.
[105] A. Rahafrooz and S. Pourkamali, "Rotational Mode Disk Resonators for High-Q Operation in Liquid," in *IEEE Sensors Conference,* Waikoloa, Hawaii, 2010, pp. 1071-1074.
[106] C. Ricciardi, G. Canavese, R. Castagna, I. Ferrante, A. Ricci, S. Luigi Marasso, L. Napione, and F. Bussolino, "Integration of microfluidic and cantilever technology for biosensing applications in liquid environment," *Biosensors & Bioelectronics,* vol. 26, pp. 1565-1570, 2010.
[107] H. Urey, E. Timurdogan, E. Ermek, I. H. Kavakli, and B. E. Alaca, "MEMS Biosensor for Parallel and Highly Sensitive and Specific Detection of Hepatitis," in *24th IEEE MEMS Conference,* Cancun, Mexico, 2011, pp. 920-923.
[108] C. P. Cheney, A. Wig, D. L. Hedden, A. Gehl, A. L. Lereu, R. H. Farahi, S. R. Hunter, and T. L. Ferrell, "Ethanol vapor detection in saline solution using piezoresistive microcantilevers," *Review of Scientific Instruments,* vol. 77, pp. 95101-1, 2006.
[109] T. P. Burg, M. Godin, S. M. Knudsen, W. Shen, G. Carlson, J. S. Foster, K. Babcock, and S. R. Manalis, "Weighing of biomolecules, single cells and nanoparticles in fluid," *Nature,* vol. 446, pp. 11066-11069, April 2007.
[110] J. Lee, R. Chunara, W. Shen, K. Prayer, K. Babcock, T. P. Burg, and S. R. Manalis, "Suspended Microchannel resonators with piezoresistive sensors," *Lab on a Chip,* vol. 11, pp. 645-651, 2011.

[111] V. Agache, G. Blanco-Gomez, M. Cochet, and P. Caillat, "Suspended Nanochannel in MEMS Plate Resonator for Mass Sensing in Liqudi," in *24th IEEE MEMS Conference*, Cancun, Mexico, 2011, pp. 157-160.
[112] J. Park, S. Nishida, H. Kawaktsu, and H. Fujita, "Novel Type of Microcantilever Biosensor Resonating at the Interface Between Liquid and Air," in *24th IEEE MEMS Conference*, Cancun, Mexico, 2011, pp. 948-951.
[113] J. E. Sader, "Frequency response of cantilever beams immersed in viscous fluids with applications to the atomic force microscope," *Journal of Applied Physics*, vol. 84, pp. 64-76, 1998.
[114] C. Vancura, I. Dufour, S. M. Heinrich, F. Josse, and A. Hierlemann, "Analysis of resonating microcantilevers operating in a viscous liquid environment," *Sensors and Actuators A: Physical*, vol. 141, pp. 43-51, 2008.
[115] O. Brand, "Micromachined Resonators For Ultrasound Based Proximity Sensing," PhD, Physics, Swiss Federal Institute of Technology, Zurich, 1994.
[116] S. M. Heinrich, R. Maharjan, I. Dufour, F. Josse, L. A. Beardslee, and O. Brand, "An Analytical Model of a Thermally Excited Microcantilever Vibrating Laterally in a Viscous Fluid," in *IEEE Sensors Conference*, Waikoloa, Hawaii, 2010, pp. 1399-1404.
[117] D. W. Allan and J. A. Barnes, "A Modified Allan Variance with Increased Oscillator Characterization Ability," in *35th Annual Frequency Control Symposium*, Philadelphia, 1981, pp. 470-475.
[118] L. A. Beardslee, A. M. Addous, S. M. Heinrich, F. Josse, I. Dufour, and O. Brand, "Thermal Excitation and Piezoresistive Detection of Cantilever In-Plane Resonance Modes for Sensing Applications," *Journal of Microelectromechanical Systems*, vol. 19, pp. 1015-1017, 2010.
[119] M. Tanaka, "An overview of quartz MEMS devices," in *International Frequency Control Symposium*, San Fransisco, California USA, 2010, pp. 162-167.
[120] M. F. Zaman, A. Sharma, Z. Hao, and F. Ayazi, "A Mode-Matched Silicon-Yaw Tuning-Fork Gyroscope With Subdegree-Per-Hour Allan Deviaton Bias Instability," *Journal of Microelectromechanical Systems*, vol. 17, pp. 1526-1536, 2008.
[121] Z. Y. Guo, L. T. Lin, Q. C. Zhao, Z. C. Yang, H. Xie, and G. Z. Yan, "A Lateral-Axis Microelectromechanical Tuning-Fork Gyroscope With Decoupled Comb Drive Operating at Atmospheric Pressure," *Journal of Microelectromechanical Systems*, vol. 19, pp. 458-468, 2010.
[122] K. Azgin, C. Ro, A. Torrents, T. Akin, and L. Valdevit, "A Resonant Tuning Fork Force Sensor With Unprecedented Combintaion Of Resolution and Range," in *24th IEEE International Conference on Micro Electro Mechanical Systems*, Cancun, Mexico, 2010, pp. 545-548.
[123] Y. Taur and T. H. Ning, *Fundamentals of Modern VLSI Devices*. Cambridge: Cambridge University Press, 1998.
[124] S. A. Campbell, *The Science and Engineering of Microelectronic Fabrication*. New York: Oxford University Press, 2001
[125] L. Yu, C. Iliescu, F. E. H. Tay, and B. Chen, "SU8 Adhesive Bonding using Contact Imprinting," in *Internation Semiconductor Conference*, 2006, pp. 189-192.

[126] C. Iliescu, D. P. Poenar, M. Carp, and F. C. Loe, "A microfluidic device for impedance spectroscopy analysis of biological samples," *Sensors and Actuators B,* vol. 123, pp. 168-176, 2007.
[127] J. Lu, T. Ikehara, Y. Zhang, T. Mihara, and R. Maeda, "Mechanical Quality Factor of Cantilevers for Mass Sensing Applications," *Proceedings of SPIE,* vol. 6800, pp. 68001Y-1-668001Y07, 2007.
[128] S. A. Chandorkar, R. N. Candler, A. Duwel, R. Melamud, M. Agarwal, K. E. Goodson, and T. W. Kenny, "Multimode Thermoelastic Dissapation," *Journal of Applied Physics,* vol. 105, p. 043505, Feb 2009.
[129] R. Cox, F. Josse, M. J. Wenzel, S. M. Heinrich, and I. Dufour, "Generalized Model of Resonant Polymer-Coated Microcantilevers in Viscous Liquid Medium," *Analytical Chemistry,* vol. 80, pp. 5760-5767, Aug 2008.
[130] K. Naeli and O. Brand, "Dimensional Considerations in Achieving Large Quality Factors for Resonant Silicon Cantilevers in Air," *Journal of Applied Physics,* vol. 105, p. 014908, Jan 2009.
[131] J. H. Seo, "Silicon-Based Resonant Microsensor Platform for Chemical and Biological Applications," PhD, Electrical and Computer Engineering, Georgia Institute of Technology, Atlanta, 2007.
[132] G. W. Hunter and R. A. Dweik, "Applied breath analysis: an overview of the challenges and opportunities in developing and testing sensor technology for human health monitoring in aerospace and clinical applications," *Journal of Breath Research,* vol. 2, p. 037020, 2008.
[133] S. M. Heinrich, R. Maharjan, L. Beardslee, O. Brand, I. Dufour, and F. Josse, "An Analytical Model for In-Plane Flexural Vibrations of Thin Cantilever-Based Sensors in Viscous Fluids: Applications to Chemical Sensing in Liquids," in *International Workshop on Nanomechanical Cantilever Sensors*, Banff, Canada, 2010, p. FP5.
[134] L. A. Beardslee, S. Truax, J.-J. Su, S. M. Heinrich, F. Josse, and O. Brand, "On the Relative Sensitivity of Mass-Sensitive Chemical Microsensors," in *Transducers 2011*, Beijing, China, 2011, pp. 1112-1115.
[135] E. Briand, M. Salmain, C. Compere, and C.-M. Pradier, "Immobilization of Protein A on SAMs for the elaboration of immunosensors," *Colloids and Surfaces B: Biointerfaces,* vol. 53, pp. 215-224, 2006.
[136] L.-S. Jang and H.-K. Keng, "Modified fabrication process of protein chips using a short-chain self-assembled monolayer," *Biomedical Microdevices,* vol. 10, pp. 203-211, 2008.
[137] G. K. Towarfe, R. J. Composto, I. M. Shapiro, and P. Ducheyne, "Nucleation and growth of calcium phosphate on amine-, carboxyl- and hyrdroxyl-silane self-assembled monolayers," *Biomaterials,* vol. 27, pp. 631-642, 2006.
[138] A. Tlili, M. Ali Jarboui, A. Abdelghani, D. M. Fathallah, and M. A. Maaref, "A novel silicon nitride biosensor for specific antibody-antigen interaction," *Materials Science and Engineering C,* vol. 25, pp. 490-495, 2005.
[139] J. C. Love, L. A. Estroff, J. K. Kriebel, R. G. Nuzzo, and G. M. Whitesides, "Self-Assembled Monolayers of Thiolates on Metals as a Form of Nanotechnology," *Chemical Reviews,* vol. 105, pp. 1103-1169, 2005.
[140] G. T. Hermanson, *Bioconjugate Techniques*. San Diego: Academic Press, 1996.

[141] A. Felton, C. Bittencourt, J. J. Pireaux, G. Van Lier, and J. C. Charlier, "Radio-frequency plasma functionalization of carbon nanotubes surface O2, NH2 and CF4 treatments," *Journal of Applied Physics,* vol. 90, p. 074308, 2005.
[142] Z. Kuang, S. N. Kim, W. J. Crookes-Goodson, B. L. Farmer, and R. R. Naik, "Biomimetic Chemosensor: Designing Peptide Recognition Elements for Surface Functionalization of Carbon Nanotube Field Effect Transistors," *ACS Nano,* vol. 4, pp. 452-458, 2009.
[143] M. Cantoro, S. Hofmann, S. Pisana, V. Scardaci, A. Parvez, C. Ducati, A. C. Ferrari, A. M. Blackburn, K.-Y. Wang, and J. Robertson, "Catalytic chemical vapor depostion of single-wall carbon nanotubes at low temperatures," *Nano Letters,* vol. 6, pp. 1107-112, 2006.
[144] H. Steiner, "In-situ monitoring of landfill related contaminants in soil and water by mid-infrared chemical sensors," PhD, Technical University Vienna, Vienna, 2005.
[145] Y. K. Jones, Z. Li, M. M. Johnson, F. Josse, and J. Hossenlopp, "ATR-FTIR spectroscopic analysis of sorption of aqueous analyte into polymer coatings used with guided SH-SAW sensors," *IEEE Sensors Journal,* vol. 5, 2005.
[146] B. Alberts, A. Johnson, J. Lewis, M. Raff, K. Roberts, and P. Walter, *Molecular Biology of the Cell*, 4th ed. New York: Garland Science, 2002.
[147] L.-I. Larsson, *Immunocytochemistry: theory and practice*. Boca Raton: CRC Press, 1988.
[148] A. Frey, M. Schienle, and H. Seidel, "CMOS based sensors for biochemical analysis," in *Transducers 2009*, Denver, Colorado, 2009, pp. 1670-1673.
[149] R. G. Hennessy, M. M. Shulaker, R. Melamud, N. Klejwa, S. Chandorkar, B. s. Kim, J. Provine, T. W. Kenny, and R. T. Howe, "Vacuum Encapsulated Resonators for Humidity Measurement," in *Hilton Head Solid-State Sensors, Acuators and Microsystems Workshop,* Hilton Head, SC, 2010.
[150] F. D. Bannon, J. R. Clark, and C. T.-C. Nguyen, "High-Q HF Microelectromechanical Filters," *IEEE Journal of Solid-State Circuits,* vol. 35, pp. 512-526, 2000.
[151] S. Pourkamali, A. Hashimura, R. Abdolvand, G. K. Ho, A. Erbil, and F. Ayazi, "High-Q Single Crystal Silicon HARPSS Capacitive Beam Resonators With Self-Aligned Sub-100-nm Transduction Gaps," *Journal of Microelectromechanical Systems,* vol. 12, pp. 487-496, 2003.
[152] J. H. Zhao, G. E. Bridges, and D. J. Thomson, "Direct evidence of "spring-softening" nonlinearity in micromachined mechanical resonator using optical beam deflection technique," *Journal of Vacuum Science and Technology A,* vol. 24, pp. 732-736, 2006.
[153] R. Abdolvand and F. Ayazi, "A gap reduction and manufacturing technique for thick oxide mask layers with multiple-size sub-m openings," *Journal of Microelectromechanical Systems,* vol. 15, pp. 1139-44, 2006.
[154] S. Lani, A. Bosseboeuf, B. Belier, C. Clere, C. Gousset, and J. Aubert, "Gold metallizations for eutectic bonding of silicon wafers," *Microsystems Technology,* vol. 12, pp. 1021-1025, 2006.
[155] S. A. Chandorkar, M. Agarwal, R. Melamud, R. N. Candler, K. E. Goodson, and T. W. Kenny, "Limits Of Quality Factor In Bulk-Mode Micromechanical

Resonators," in *22nd IEEE International Conference on Micro Electro Mechanical Systems*, Tucson, AZ USA, 2008, pp. 74-77.

[156] P. J. Joseph, P. Monajemi, F. Ayazi, and P. A. Kohl, "Wafer-Level Packaging of Micromechanical Resonators," *IEEE Transactions on Advanced Packaging,* vol. 30, pp. 19-26, 2007.